Processing and Optical Uses of Van der Waals Layered Materials

by

Seong Soon Jo

B.S. and M.S. in Materials Science and Engineering
Yonsei University, 2014
M.S. in Materials Science and Engineering
Massachusetts Institute of Technology, 2018

Submitted to the Department of Materials Science and Engineering
in partial fulfillment of the requirements for the degree of

Doctor of Philosophy in Materials Science and Engineering

at the

MASSACHUSETTS INSTITUTE OF TECHNOLOGY

May 2022

Author .....
Department of Materials Science and Engineering
February 28, 2022

Certified by .....
Rafael Jaramillo
Thomas Lord Associate Professor of Materials Science and Engineering
Thesis Supervisor

Accepted by .....
Frances M. Ross
Ellen Swallow Richards Professor in Materials Science and Engineering
Chair, Departmental Committee on Graduate Studies

Processing and Optical Uses of

Van der Waals Layered Materials

by

Seong Soon Jo

Submitted to the Department of Materials Science and Engineering
on February 28, 2022, in partial fulfillment of the
requirements for the degree of
Doctor of Philosophy in Materials Science and Engineering

Abstract

This thesis is mainly divided into two parts: processing and optical uses of (1) transition metal dichalcogenides and (2) group IV-VI monochalcogenides.

We first study processing of large-area polycrystalline MoS_2 and TiS_2 film for photonics and microelectronics, which mainly focus on lowering processing temperature by controlling oxygen concentration. We identify opposite roles of oxygen during the sulfurization process as a reaction catalyst or an inhibitor, for MoS_2 and TiS_2 formation respectively. In MoS_2, O_2 promotes the crystallization of MoS_2 at lower temperature (as low as 400 °C). On the other hand, the kinetic barrier of replacing Ti-O bonds by Ti-S bonds increases with adoption of oxygen in the system. Thus we design the system to lower oxygen background, enabling to lower sulfurization temperature as low as 500° and then form smooth film by suppressing roughening.

Beyond investigating roles of oxygen during thin film growth, it is crucial to thoroughly understand the processing and properties of native oxide for designing semiconductor devices. Combining modeling with experimentation, we calculate the oxidation rate and uncover the mechanisms of spontaneous oxidation of bulk single crystals of ZrS_xSe_{2-x} alloys and MoS_2. ZrS_xSe_{2-x} alloys oxidize rapidly, and the oxidation rate increases with Se content. Oxidation of basal surfaces is initiated by favorable O_2 adsorption and proceeds by a mechanism of Zr-O bond switching, that collapses the van der Waals gaps, and is facilitated by progressive redox transitions of the chalcogen. The rate-limiting process is the formation and out-diffusion of SO_2. In contrast, MoS_2 basal surfaces are stable due to unfavorable oxygen adsorption. Furthermore, we investigate the role of various processing parameters involved in thermal oxidation and non-thermal oxidation, revealing the growth mechanism.

In the second part, new switching mechanism for light-controlling-light is examined in IV-VI monochalcogenides and black phosphorous for photonic integrated circuits. This work is inspired by recent theoretical work suggesting that the in-plane crystal

orientation in such materials can be switched through an ultra-fast, displacive (i.e. non-diffusive), non-thermal, and lower-power mechanism by strong electric fields, due to in-plane dielectric anisotropy. We use numerical device modeling to study device concepts based on switching the crystal orientation of SnSe and bP in photonic integrated circuits. Furthermore, we experimentally observe a preliminary switching behavior in bulk single crystal SnSe using single THz pump-probe spectroscopy.

Thesis Supervisor: Rafael Jaramillo
Title: Thomas Lord Associate Professor of Materials Science and Engineering

Acknowledgments

Firstly, I would like to acknowledge the efforts of my advisor, Professor Rafael Jaramillo, in giving me the opportunity to research on all the work presented in this thesis. Since the day one, he has helped research projects move forward and been always open for scientific discussions. It has been amazing that he could answer almost all fundamental questions right away, which has motivated us. Also his passion for research has been inspirational. Thanks to him, I have developed both of soft skills and hard skills. He taught me analytical, collaborating, writing and communication skills, which enabled me become an independent researcher. I would not have come this far without his support. I am truly grateful that I pursued my PhD under his mentorship along with the best labmates at MIT. I would also like to thank my thesis committee members Profs. Frances M Ross and Juejun Hu, for their insightful questions and comments, which made me explore other possibilities and enriched my project. I enjoyed sharing my research progress in committee meeting and collaboration with both group. Not only from the academic viewpoint, but also they have been willing to make time for me and hear me out whenever I had concerns. I appreciate their kindness.

I feel grateful to all the members of the Jaramillo's group, past and present. With the benefit of small group, we shared almost everything. Whenever I had a bad day, they offered to talk a walk, get a coffee or tea. They carefully heard me out and became a great company. Special thanks to very first members of 2D phase change subgroup Yifei and Akshay, we did so many things together, lab set-up, numerous experiments and the road trip. I would never forget. I want to thank my office mates Kevin, Jack and Wouter for brightening the office and having active research discussion from time to time. The past group members Allan and Stephen, I thank them to hear my concern and support me to run across the finish line. I also want to thank my numerous collaborators for constructive discussions and teaching me their research field.

I would like to thank my friends, DMSE incoming class of 2015, KGSA and friends

in Korea. Special thanks to Takian, Yusu and Eric, we probably consumed more than few hundreds cups of coffee and tea in the graduate lounge. They thought about my work as if it were their work. Even when my English was not fluent enough, they patiently listened to me and helped me with the countless emails in early years at MIT. Life savers! Also thanks for inviting me to multicultural parties and events. I also thank Jiyoun Chang and Ahhyun Nam they helped me settle and survive at MIT and thank Kyung Yun Choi, Minjung Son, Soo Yeon Kim, Byong Ha Kang, Seung Kyun Ha, Sang-ho Lee and many more for their wonderful friendship and making MIT/Boston more homey. Although my friends in Korea are not in the same time zone nor continent, we talked almost every day and they made me feel I am not alone. Some of them even came to Boston just to see me, it meant a lot to me. I cannot list all names but thank Minjoo Kim, Sera Yu, Hyojin Choi, Yun Cho, Seo Yeon Jo, Sejin Park, Eun Jae Jo, Jae Ryung Choi and Meche class 4 friends for encouraging me and memorable time we spent together every time I visited Korea.

If I have to choose one of wonderful things happened during my PhD, I would definitely choose Phil Inagaki. He brought lots of joys and love in my PhD life. Even when I felt lost, he has given me confidence and guided me to become the best version of myself. He has showed his faith in me and made me feel that I am a good enough person.

Finally, I thank my family for their unwavering support and unconditional love through my life. Thank you for believing in me, and for always being by my side no matter what choice I make.

Contents

List of Figures

List of Tables

Chapter 1

Introduction

Sections of text and illustrations are reprinted with permission from ref. [12].
Singh, A., **Jo, S.S.**, Li, Y., Wu, C., Li, M., Jaramillo, R., "Refractive Uses of Layered and Two-Dimensional Materials for Integrated Photonics", *ACS Photonics* **7**, 3270−3285 (2020), Copyright 2020 American Chemical Society.

The purpose of this chapter is to give a brief summary of important background, helping readers understand overall content of this thesis. In the first Section 1.2, we introduce van der Waals (vdW) layered materials (LMs) as an emerging class of photonic materials and discuss the correlation of the unique structure and novel properties (mainly optical properties). Then various processing techniques of this material class is reviewed with regard to ongoing challenges, advantages and disadvantages. The second Section 1.3 of this chapter covers phase change materials for integrated photonics and the corresponding switching fundamental principles. By discussing aforementioned aspects, we motivate the work discussed in the remainder of this thesis. Lastly, we briefly review the outline of the thesis.

1.1 Motivation

Integrated photonic system transports information signals imposed on optical wavelengths, mostly in the infrared regime. Similar to integrated electronic systems use

electrons, photons are utilized as information carriers in the photonic systems. Modulation of signal light using a control light is a key fundamental to build optical communication networks and optical computing systems [13]. By the concept of light-controlled-by-light, optical switch can be regarded as one of important photonic devices in photonic integrated circuits (PIC) as like transistors in integrated electronic systems. The ideal optical switch for PIC should have fast switching time (defined as the transition time between on/off states), high switching efficiency (defined as the reflection or transmission contrast between on/off states, low threshold control power and nanoscale feature size [14–16].

Mature technologies for optical phase-shifters - such as carrier injection in silicon, or the Pockels effect in $LiNbO_3$ - are based on perturbative changes to the refractive index. In nearly all cases, the refractive index modulation Δn is ~ 0.01 or smaller, equivalent to an absolute change of $0.1 - 0.5\%$ [17–19]. In this thesis we consider two types of LMs that can provide strong, non-perturbative optical phase modulation: transition metal dichalcogenides (TMDs) and group IV-VI monochalcogenides.

1.2 Van der Waals Layered Materials

1.2.1 Properties

LMs are studied widely due to their diverse physical properties, which become particularly rich in the two-dimensional (2D) limit of individual monolayers. LMs typically have weak vdW bonding between layers, and strong bonding within layers, resulting in highly-anisotropic optical and electronic properties. In Figure 1-1 we illustrate representative crystal structures for the LMs discussed here: dichalcogenides (MX_2), monochalcogenides (MX) (M: metal, X: chalcogen), and black phosphorus (bP). bP is included in the study due to its prevalence in the 2D research and structural and functional similarities with some MX (GeS-type with crystal structure of P_{nma}). LMs are strongly biaxial (*i.e.* birefringent) due to their layered structure. Many also feature in-plane anisotropy, making them triaxial. LMs can often be prepared with

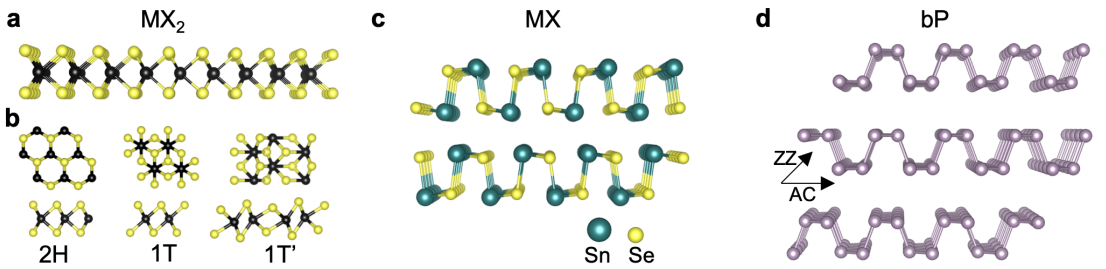

Figure 1-1: **Representative crystal structures of the LMs discussed in this thesis.** LMs with band gap in the visible and near-infrared (VIS-NIR) regime and strong light-matter interaction. (a) Side view of a monolayer in the trigonal prismatic (so-called 2H) phase common to many TMDs with stoichiometry MX_2. (b) Top-views (top row) and side views (bottom row) of common TMD polymorphs: 2H, 1T (tetragonal coordination), and 1T' (distorted 1T). (c) Monochalcogenides MX generally form as puckered layers with substantial in-plane anisotropy; here we show two layers of SnSe. (d) bP also adopts a puckered structure with high in-plane anisotropy; zigzag (ZZ) and armchair (AC) directions are indicated. The structure diagrams were generated using VESTA 3 software [1].

varying layer count, all the way down to individual monolayers. The electronic structure can vary strongly with layer count; a well-known example is that of 2H-MoS_2, which as a bulk crystal has an indirect band gap with energy (E_g) of 1.3 eV, but as a 2D monolayer has a direct band gap of E_g = 1.8 eV [20]. LMs usually feature strong exciton absorption resonances and large exciton binding energy, which result from the weak dielectric screening for out-of-plane electric fields, which in turn follows from layered crystal structure. LMs also feature notable mechanical properties such as high flexibility and facile inter-layer sliding; MoS_2 is widely used as a dry lubricant (*e.g.* trademarks MOLY-MIST and Never-Seez Blue Moly). Their structure and opto-electronic properties can be controlled by chemical doping, surface modification, the underlying substrate, and by stimuli such as electric fields and mechanical strain [21]. Many LMs have E_g in the range of 1 – 2 eV, making them attractive for refractive NIR applications [3, 22].

LMs feature E_g ranging from 0 eV (metallic or semi-metallic, such as graphene and TiS_2) to 6 eV (hexagonal boron nitride, hBN). We illustrate this distribution in Figure

Table 1.1: **Crystal structure, anisotropy and linear optical properties for materials discussed in this review. The crystal structure is related to the anisotropy, which relates to the different optical properties for in-plane (IP) and out-of-plane (OP) directions.**

Materials	Crystal structures	Anisotropy	Refractive index (n), in-plane (IP) and out-of-plane (OP)
MoS_2, $MoSe_2$, WSe_2, WS_2	$P6_3/mmc$; known as 2H; trigonal, prismatic coordination	Biaxial	2-4 (IP)[23], 1-2 (OP, calculated)
ZrS_2,$ZrSe_2$; TiS_2, $TiSe_2$	$P\bar{3}m1$; known as 1T, or the $Cd(OH)_2$ structure type; tetragonal coordination	Biaxial	3∼3.5 (IP)[24]; TiS_2 3.9∼4.9 [23]
GeS, GeSe; SnS, SnSe	Pnma	Triaxial	GeS 3.3∼3.9[25] ; SnS 3.7-4.6[26]
bP	Cmce	Triaxial	bP 2∼4[27]

1-2. For some materials, we also illustrate the range of E_g achievable by varying the layer count. Several trends are apparent in the data. For a given metal element, E_g increases as the chalcogen varies from Te, to Se, to S. The band gap often changes from indirect to direct with decreasing layer count. Chemical alloying can tune E_g, traversing the difference between pure phases; examples include the $HfSe_2$-HfS_2, the SnS_2-$SnSe_2$, and the ZrS_2-$ZrSe_2$ systems [24, 28, 29].

The complex refractive index (n - ik) is related to the dielectric permittivity ε by n = Re($\sqrt{\varepsilon}$) and k = -Im($\sqrt{\varepsilon}$), and k is related to absorption coefficient α by $\alpha = 4\pi k/\lambda$. For integrated photonics, materials with large n are preferred to improve optical confinement and reduce mode leakage. There exists an extensive body of work measuring n for LMs, dating back decades, focused mainly on spectral reflectivity and transmission in the visible range from basal faces of bulk LM crystals [24, 30, 31]. Measurements of (n,k) in the VIS-NIR of few- and monolayer samples have appeared more recently, and reveal notable differences from bulk properties [23, 32–34].

1.2.2 Processing

Using LMs in photonic integrated circuits will require reliable methods to make and pattern uniform, wafer-scale thin films. Wafer-scale photonic integrated circuitry will be built on established material platforms, including Si, Si_3N_4, and InP, using planar processing methods. It is important to be able to insert LMs into these process

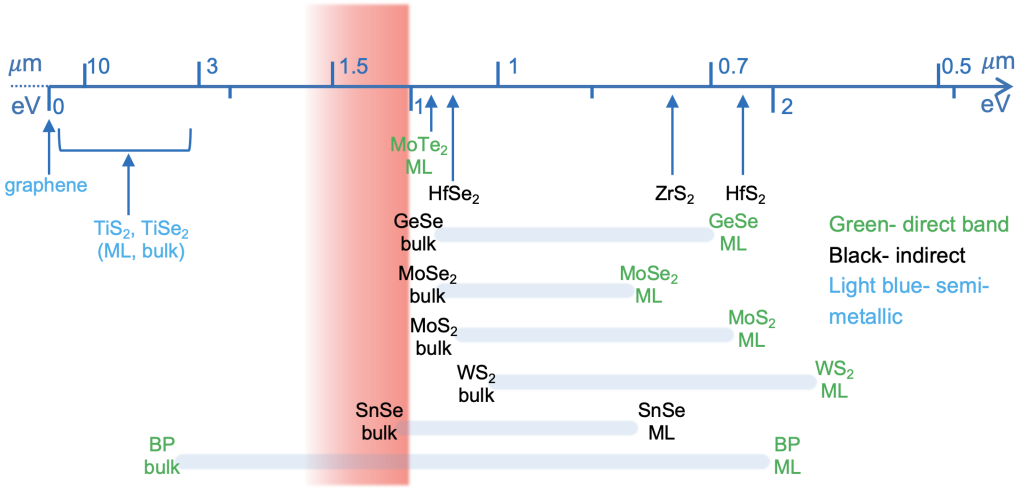

Figure 1-2: **Distribution of experimentally measured band gap (E_g) for LMs discussed here.** For some materials, we also present the variation of E_g with layer count between the bulk and monolayer limits. For some materials the data reported are the exciton absorption resonances, because the fundamental band gap is difficult to determine experimentally. The labels are colored according to the nature of the gap: green = direct, black = indirect, light blue = metallic/semi-metallic. We also illustrate (in red) the NIR spectral range 0.75 – 1 eV relevant to telecommunications. Further details and data citations are presented in Table 1.

flows because even a spectacular material is not viable for commercialization without process compatibility. In this section we review synthesis methods for LMs with chemical formulas MX and MX_2, with emphasis on wafer-scale processing.

Processing temperature is an important consideration for integration due to a strict thermal budget window (*i.e.* within the duration and temperature, the process does not affect on performance) at different integration level. Si photonic integrated circuit wafers with passive waveguides patterned from SiO_2 or Si_3N_4 can withstand at least 800 °C without degradation, which is sufficient for most LM film processing methods. However, the high temperature process become challenging when it comes to CMOS compatibility. If CMOS devices (such as doped modulators or detectors) are present on the wafer, then the processing temperature should be lower than 600 °C at where copper diffusion occurs [35]; this may be a challenge for many LMs. Moreover, the highly doped source and drain region (*i.e.* silicide) with N-type dopant (arsenic (As) and phosphorus (P)-based) in transistors starts to degrade as low as 500 °C by dopant deactivation [36, 37]. The allowable temperature range becomes

more limited as the integration progresses. The thermal budget for back-end-of-line (BEOL) device and materials in modern silicon technology is $\sim$ 550 °C for 2h [38], which can be further limited by selection of metal. For example, aluminum metallization in BEOL limits the thermal budget to 1 h at 450 °C due to low melting temperature of aluminum [39, 40]. Our efforts on low temperature processing of selective LMs will be described in greater detail in Chapter 2 and 3.

Layer transfer methods can decouple the LM film processing temperature from the photonic integrated circuit wafer thermal history: LMs can be synthesized at high temperature and chemically aggressive conditions and then can be transferred onto target wafer. For realistic implementation by the industry, manufacturable transfer process (*i.e.* scalable, fast and cost-effective production) is required for wafer-scale LMs. In this respect, the roll-to-roll transfer technique, both wet [41, 42] and dry transfer [43, 44], has been of interest but limited to graphene or hBN grown on Cu foil.

Thin-film synthesis methods can be grouped according to the phase relation at the surface of the forming film. Here we focus on vapor-phase methods, for which the desired film grows at a vapor-solid interface.

Solid-source chemical vapor deposition (ssCVD): In this process, solid precursors vaporize and react on a substrate to grow a film. This is the most common method for making LM films - the archetypical process is growth of MoS_2 films from powder MoO_3 and S sources - and is usually referred to simply as CVD [45]. However, it is useful to distinguish between gas- and solid-source CVD. Traditionally, CVD implies that sources are delivered to the reactor as gases, which holds important benefits for wafer-scale and reliable deposition. The use of solid sources means that ssCVD is more difficult to scale [46]. A great many LMs can be synthesized by ssCVD. The list includes TMDs with transition metals Ti, Zr, Hf, V, Nb, Ta, Mo, W, Re, Pt, Pd, and Fe, and chalcogens S, Se, and Te [47]; main-group metal chalcogenides GeS and GeSe [48, 49]; bP [50].

Gas-source CVD (CVD) and metal-organic CVD (MOCVD): In gas-source CVD and its variant, metal-organic CVD (MOCVD), gas-phase precursors react on

a substrate to grow a film. Of all the LM thin film synthesis methods demonstrated to-date, MOCVD offers the best combination of process uniformity and scale, layer number control, and material quality [51, 52]. CVD and MOCVD are versatile, but the requirement of gas-source precursors has limited the range of materials made to date, compared to ssCVD. Materials made by CVD and MOCVD include MoS_2, WS_2, WSe_2, TiS_2, SnS, and SnSe [53–57]. A variation on CVD and ssCVD is to use a chalcogen source (*e.g.* H_2S or solid S) to convert a metal thin film to a LM compound thin film [58–60]. These are two-step processes, first involving deposition of the precursor thin film, often by evaporation or sputtering, followed by conversion in a CVD reactor. These two-step methods are mostly utilized throughout this thesis. The advantage of these two-step methods are scalability and reliability but controlibility over layer number and materials quality such as grain size and crystallinity is inferior than ssCVD, CVD or MOCVD.

Atomic layer deposition (ALD): ALD is a variation on MOCVD in which the film growth is kinetically limited by a precursor delivery sequence. ALD growth of LMs MoS_2, WS_2, $MoSe_2$, WSe_2, ZrS_2, HfS_2, TiS_2, SnS, SnSe, GeS, and GeSe have been reported [61–68]. ALD offers excellent control over film morphology and layer number at nm-scale, enabling pin-hole free conformal coating with excellent thickness uniformity on large area substrate even with complex geometry. However, the kinetic control inherent to ALD dictates rather low reaction temperature, and high-temperature post-deposition annealing is often required to improve film material quality. ALD also faces low deposition rate and low precursor utilization efficiency due to its inherent layer by layer deposition [69].

Physical vapor deposition (PVD): PVD covers a number of vacuum deposition methods including thermal evaporation, electron-beam evaporation, sputtering, and pulsed laser deposition. Chalcogenide films deposited by PVD are often anion-deficient, due to the differential re-evaporation of metals and chalcogens. To compensate, an additional chalcogen source may be introduced during film growth, resulting in reactive PVD. PVD is less-widely used for LM film synthesis than ssCVD, CVD, and MOCVD. A number of main-group metal monochalcogenides that evaporate con-

gruently and that have fairly high vapor pressure have been synthesized as thin films by PVD, including SnS, SnSe, GeS and GeSe [70–73]. bP and TMD thin films have been synthesized by PLD and sputtering [74–76].

Molecular beam epitaxy (MBE): MBE is a variant of PVD that emphasizes epitaxy and precise control over film thickness and morphology. MBE growth of many LMs is challenged by the vastly-different thermodynamic properties of transition metals and chalcogens [77]. Taking for instance MoS_2, the high melting point of Mo (2623 °C) means that ad-atom mobility is negligible at substrate temperatures of 800 °C or below. At the same time, the saturation vapor pressure of condensed sulfur at a substrate temperature of 800 °C is well over 1 atm; this implies that the time during which sulfur resides on the heated substrate and may react with the metal is vanishingly short. Despite these challenges, there has been impressive progress such as the growth of monolayer and high-quality $MoSe_2$ on hBN, and the growth of multilayer WSe_2 with grain size ≈ 1 μm [78, 79]. Taking a cue from the history of complex oxide MBE, and lessons learned from MOCVD growth of LMs, it seems promising to revisit MBE growth of LMs using metal-organic precursors [80, 81].

Table 1.2: **Summary of synthesis methods and trade-offs available for making LM thin films for use in photonic integrated circuits.**

	ssCVD	CVD/ MOCVD	ALD	PVD	MBE
Scalability	*Low*	*High*	*High*	*High*	*High*
Range of materials	*High*	*Medium*	*Low*	*High*	*Low*
Deposition rate	*High*	*Low*	*Low*	*High*	*Medium*
Crystal quality and chemical purity	*Medium*	*High*	*Low*	*Medium*	*High*
Film layer number control/smoothness	*Medium*	*High*	*High*	*Medium*	*High*
Conformal coating	*Medium*	*Medium*	*High*	*Medium*	*Low*
Cost (equipment and operation)	*Low*	*Medium*	*High*	*Low*	*High*

1.2.3 Air Stability

Stability in air is a key consideration for any material to be deployed widely in technology. Uncontrolled oxidation can ruin a device, while controlled and self-limited

oxidation can imbue functional properties such as surface passivation [82, 83]. Understanding and controlling the interaction between LMs and oxygen (and water) is just as important for future LM-based photonic integrated circuit technology as it is for processing integrated circuits from legacy semiconductors such as Si and GaAs.

Metal-chalcogen bonds are often easily disrupted by oxygen, becoming more susceptible as the electronegativity difference between oxygen and chalcogen grows. Hence, for chalcogenides of a particular metal, susceptibility to oxidation by oxygen increases as the chalcogen element varies from S, to Se, to Te [82, 84]. Edges and atomic defects accelerate oxidation by providing thermodynamic local minima for oxygen chemisorption, and by reducing the kinetic energy barriers to oxide growth [85–87]. For TMDs, air stability varies with transition metal group and the chalcogen atom. For example, $MoTe_2$ is reactive upon air exposure, but the surface of MoS_2 is stable for long times in ambient conditions [84]. TMDs based on group IV metals Hf and Zr oxidize apparently without limit, and even rather thick films are susceptible to full oxidation [82]. bP is likewise unstable and degrades rapidly upon air exposure [88]. Monolayer and few-layer films are especially susceptible to oxidation due to extreme surface area-to-volume ratios. For instance, monolayer WTe_2 degrades even during the exfoliation process and characteristic Raman peaks disappear 17 – 18 min after exfoliation [89]. The correlation between crystal defects and oxidation complicate the interpretation of such experiments; controlled studies of thickness-dependent oxidation would be most useful. Native oxidation of TMDs is governed by air stability in ambient condition as will be discussed in Chapter 4. An understanding of mechanisms that controls morphology and crystal quality of native oxide is crucial to design devices for microelectronics. This involves an investigation of processing techniques including various parameters such as annealing temperature, oxygen pressure, the presence of plasma and etc, as will be discussed in Chapter 5.

1.3 Phase Change Materials for Integrated Photonics

Phase change materials (PCMs) have been regarded as promising candidates for the photonic applications including optical switches and optical data storage devices in the infrared regime. PCMs have two stable phases at room temperature such as amorphous/crystalline states, 2H/1T phases and so on [14]. Each phase exhibits different optical properties because structural transformations give rise to change in diverse material properties; dielectric constant, refractive index, light reflection, transmission and optical absorption [90]. The phase transition can be induced by external energy source such as light, heat, and electric field, by reducing energy barrier in between two phases. In this section, We first introduce the well-known PCM, for instance Ge-Sb-Te alloys (we use GST to refer to the commonly used composition of $Ge_2Sb_2Te_5$, throughout this thesis), that provide $\Delta n \sim 1$ by virtue of order-disorder transformations. In addition to GST, we consider the outlook for LMs to combine strong optical phase modulation with other desirable attributes including low optical loss and fast, low-energy switching. Finally, we validate how useful GST and LMs can be in PIC through photonic device simulation which further motivate the research on optical properties in the wavelength regime of optic communication band as well as new phase switching concepts and its fundamental principles.

1.3.1 Thermal Driven Phase Transition

As we mentioned earlier, the most widely used chalcogenide-based PCMs is Ge-Sb-Te alloys [91, 92]. Ge-Sb-Te alloys switch between two solid states through order-disorder transformations [2, 93] in response to an external stimulus, which is accompanied by chemical bond break, atomic diffusion and bond formation. Traditional PCMs using thermal driven phase transition have a long history of development for optical and electrical data storage, and processing for device integration is mature [94]. The phase-change functionality is based on time-temperature processes, and can be

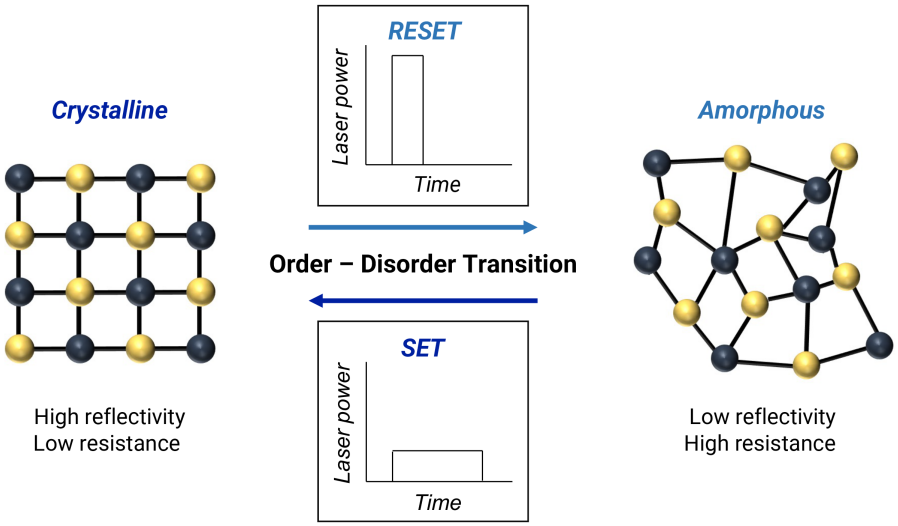

Figure 1-3: **Order (crystalline) – disorder (amorphous) switching, as in the GST system.** Graphical illustration of laser pulse power with time for switching between crystalline (SET) state and amorphous (RESET) state. *(Top)* A high intensity laser short pulse locally heats the crystalline phase change material above its melting temperature followed by rapid cooling to quench the liquid state (*amorphization*). (*Bottom*) For crystallization, a relatively low intensity laser pulse heats the phase change material above the glass transition temperature.

triggered electrically (*electrical current*) and optically (*laser pulse*). Each state corresponds to 1 (SET) and 0 (RESET) respectively. When a laser beam illuminates on small portion of amorphous GST thin film, the exposed part is crystallized due do increase in temperature slightly above its glass transition temperature. A short laser pulse with higher intensity melts the thin film and the laser-exposed crystalline region is transformed into the amorphous phase via melt-quenching process as shown in Figure 1-3

GST alloys have drawbacks that may limit their application as active optical phase shifters in photonic integrated circuits (PICs). The ordered state is often semi-metallic, and the disordered state is a low band gap semiconductor ($E_g \sim 0.5$ – 1 eV). As a result, GST alloys have substantial optical loss, with $k \geq 1$ in one or both phases throughout the NIR as shown in Figure 1-4, although clever device design can mitigate the loss [95]. Switching is based on melt-quench and thermal recrystallization processes, which limit operation to sub-GHz frequencies and are

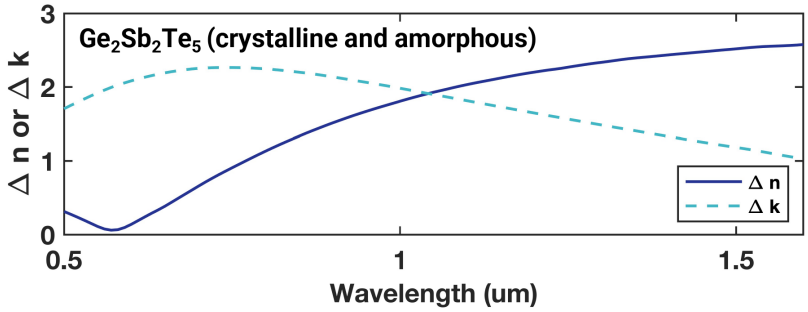

Figure 1-4: **Optical properties of $Ge_2Sb_2Te_5$ alloy.** Change in real (n) and imaginary (k) refractive index across functionally-useful material structure transformations. Order-disorder transformation between crystalline and amorphous phases of GST [2].

inherently energy-intensive [94]. Nanoscale device and materials engineering may extend the frequency range and lower the energy consumption of GST alloys [96]. GST alloys also suffer from fatigue, which limits device life cycles; even state-of-the-art GST alloys for electrical memory are limited to $\sim 10^{12}$ switching events, which may be sufficient for memory applications (including photonic neural networks), but is grossly insufficient for telecommunications [94]. In this respect, desirable PCMs should satisfy these criteria for high performance photonic applications: (1) high speed of phase transition, (2) good stability at room temperature (*i.e.* minimized noise resulted from thermal fluctuation), (3) good data retention (*i.e.* no drift), (4) good reversibility, (5) large erase/write cycles before failure [90].

1.3.2 Diffusion-less Phase Transition

Although the term "phase-change materials" usually refers to chalcogenides such as GST with functionally-useful order-disorder transformations, any material phase transformation may provide strong modulation of optical properties, including order-order transformations in LMs. In materials science, collective atomic displacements that convert between two ordered crystal structures are called martensitic transformations. TMDs feature a panoply of polymorphs (Figure 1-5a) with contrasting electrical and optical properties, and in recent years there has been sustained interest in using martensitic transformations for device [8, 97]. These transformations can be

triggered by electrical fields, charge injection, and strain – these non-thermal mechanisms are exciting for fast and low-power switching [97–99]. The small and collective atomic displacements during switching, facilitated by the layered crystal structure, suggest that material fatigue may be lower and device life cycles may be much longer than for PCMs based on order-disorder transitions [98]. Most of the literature on this topic has focused on transformations between low- and high-conductivity states for electronics and computation [99]. Here we focus instead on proposed applications in photonic integrated devices. In Figure 1-5c we present the difference in refractive index between the 1T' and 2H phases of $MoTe_2$, which has been shown to support fast, non-thermal switching [3, 100].

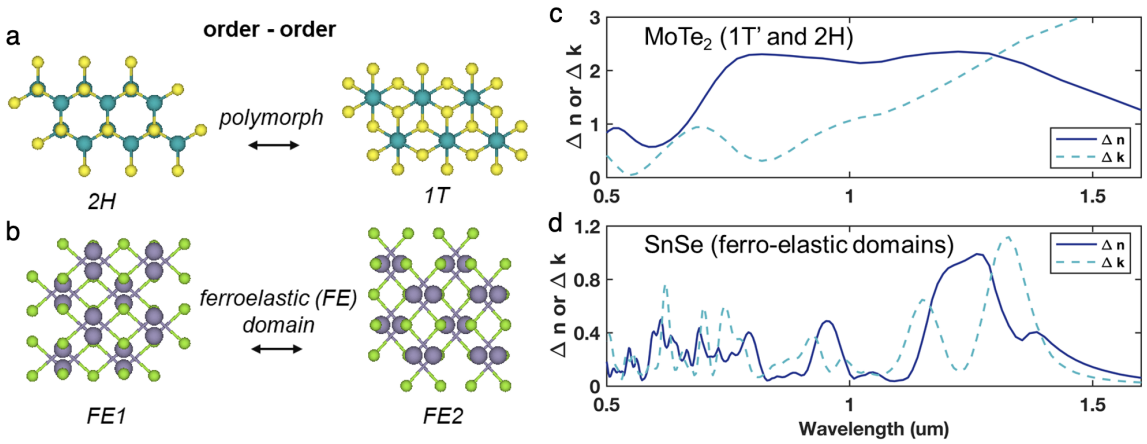

Figure 1-5: **Schematic illustrations of material transformations enabling strong optical phase modulation.** (a) Martensitic, order-order transformation between TMD polymorphs. (b) Ferroelastic domain switching in GeS-type LMs with low in-plane symmetry. (c-d) Change in real (n) and imaginary (k) refractive index across functionally-useful material structure transformations. (c) Order-order transformation between 1T' and 2H phases of bulk $MoTe_2$ [3]. (d) Ferroelastic domain switching in monolayer SnSe [4]. The structure diagrams were generated using VESTA 3 software [1].

Materials with substantial optical and dielectric anisotropy also present opportunities for non-thermal switching between domain orientations, rather than between phases. Crystallographic domain orientation can be switched by an applied electric field, and the optical anisotropy can be used for devices such as mode converters or polarizers. A well-known example of non-thermal, electric field-driven structural

change is ferroelectric domain switching, which is driven by an energy term linear in applied field. Ferroelastic (FE) domain switching is a newer concept that is based on anisotropy in dielectric susceptibility, and is driven by an energy term that varies quadratically with applied field [8, 101]. LMs in the GeS structure-type (Figure 1-5b), have two FE domain variants related by a 90° rotation. Due to dielectric anisotropy $\varepsilon_{xx} \neq \varepsilon_{yy}$, it is predicted that a sufficiently-strong electric field from a pulsed laser can produce barrier-less conversion between FE domains with substantial optical contrast. In Figure 1-5d we reproduce the calculated NIR optical contrast between FE domains in monolayer SnSe; the predicted $\Delta n > 1$ and $k < 0.2$ compares favorably to phase-change materials [4]. Photonic device simulation using large in-plane optical contrast of SnSe and bP will be discussed in Chapter 6, as well as preliminary results demonstrating light-contolling-light concept and calculated parameters for future experiments will be covered in Chapter 7.

1.3.3 Usefulness of LMs in PICs

GST alloys and TMDs offer strong optical phase modulation for applications in photonic integrated devices. Lumerical software is used to simulate results for a prototypical Si_2N_4 ring resonator with a covering patch of active material, as illustrated in Figure 1-6a. Three active materials are chosen for the device simulation and their refractive indices (n,k) data in the wavelength of interest are extracted from the literature: 10 nm-thick GST, 10 nm-thick MoS_2, and monolayer WS_2 [2, 23, 102].

For GST and MoS_2 we simulate a wavelength range in the NIR, below the band gap in the low-loss phase of each material. For WS_2 we simulate results for visible light, at the tunable exciton absorption resonance. GST offers strong optical phase modulation when changing between amorphous and crystalline phases, due to the large Δn, and resulting in a substantial shift in the resonance position. However, the crystalline phase is optically lossy (large k), resulting in a broad resonance and substantial insertion loss. MoS_2 also offers strong optical phase modulation when it changes between crystalline phases (*i.e.* the 2H and 1T polymorphs). Compared to GST, MoS_2 has reduced loss and a sharper resonance in the lossy phase (crystalline

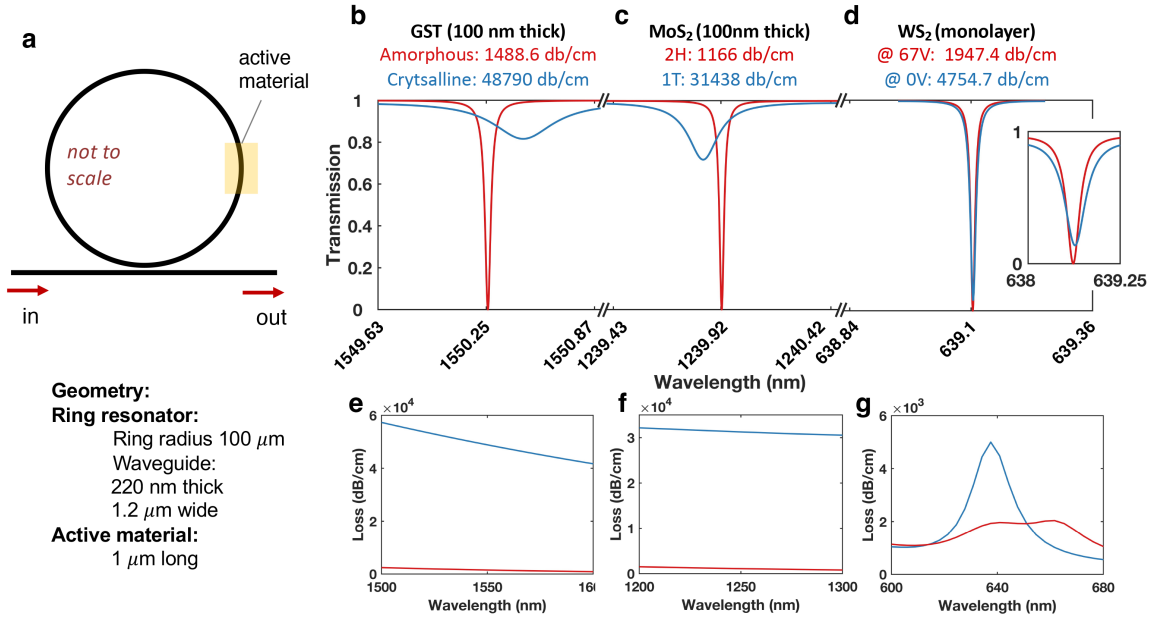

Figure 1-6: **Role of materials offering strong optical phase modulation for photonic integrated devices, illustrated by simulated ring-resonator devices.** (a) Schematic and key dimensions of simulated devices, showing location of the patch of active material that is laid on top of the Si_3N_4 waveguide. (b-d) Transmission spectra for active materials $Ge_2Sb_2Te_5$, MoS_2, and WS_2; see text for details. The axes titles report loss figures on-resonance. (d, inset) Transmission spectra for WS_2 with interaction length increased to 8 μm. (e-g) Loss spectra corresponding to panels (b-d). The loss data report loss (in dB) per length of active material (in cm).

for GST, 1T for MoS_2). Monolayer WS_2 has a much weaker effect on the simulated device performance, due to the small interaction volume. The resonance is sharp, but barely shifts even for a very large electrostatic gate bias. If the interaction volume is increased with a longer interaction length, then the resonance becomes less sharp due to the strong absorption at the exciton resonance (Figure 1-6d, inset). These simulations – and recent experimental results on WS_2 optical phase shifters [103] – motivate continued research on refractive applications of TMDs for photonic integrated devices, and the focus on phase-change functionality.

1.4 Thesis Outline

Given the advantages of vdW LMs and PICs, the aim of this thesis is (1) to develop wafer-scale synthesis and processing method of LMs at low temperature, (2) to investigate native oxides of layered semiconductor by establishing a simple metrology and optical model as well as to develop processing for conformal native oxides and reveal structure and composition of resultant oxides, (3) to propose novel photonic platforms integrated with tri-axial LMs and show preliminary results of new concepts of light-controlling-light. Accordingly, the thesis is organized as follows:

Part I: Transition Metal Dichalcogenides

Synthesis and Processing of LMs: Chapter 2 and 3 discuss roles of oxygen gas in the sulfurization of pre-deposited Mo and Ti thin films and strategies for reduced processing temperature and large area deposition on arbitrary substrates, allowing easy integration on modern silicon integrated circuits.

Native Oxide of LMs: Chapter 4 explains that how spectroscopic ellipsometry can be adapted for native oxide metrology and reveals oxidation mechanisms of ZrS_xSe_{2-x} alloys, MoS_2 and other LMs. The quantitative study on oxidation rate is done in ambient condition. Chapter 5 demonstrates native oxidation mechanism on MoS_2 in different processing condition of temperature, oxygen pressure, and presence of plasma.

Part II: Group IV-VI Monochalcogenides

Photonic Applications of LMs: Chapter 6 investigates new switching mechanism for light-controlling-light in MXs and bP for photonic integrated circuits, suggesting that the in-plane crystal orientation in such materials can be switched through an ultra-fast, displacive (*i.e.* non-diffusive), non-thermal, and lower-power mechanism by strong electric fields, due to in-plane dielectric anisotropy. Numerical device modeling is used to validate device concepts. In Chapter 7, we experimentally observe a preliminary switching behavior in bulk single crystal SnSe using single THz pump-probe spectroscopy.

Chapter 8 summarizes the findings in this thesis and discusses prospects for the future.

Chapter 2

Processing of Large Area of MoS_2 Films: Oxygen as Catalyst

This chapter is reproduced from ref. [59].

Jo, S.S., Li, Y., Singh, A., Kumar, A., Frisone, S., LeBeau, J.M., Jaramillo, R., "The Formation of Large-Area MoS_2 Thin Films by Oxygen-Catalyzed Sulfurization of Mo Thin Films", *J. Vac. Sci. Technol. A.* **38**, 013405 (2020), with the permission of AIP Publishing.

While transition metal dichalcogenide (TMD) thin films are most commonly synthesized by vapor transport using solid metal oxide precursors, directly converting metal thin films to TMDs may be more scalable and controllable, *e.g.*, to enable large-area coating by vacuum deposition. Moreover, low temperature processing is required for industrial use (See Section 1.2.2) which has strict thermal budget at each integration level. It also increases the reliability and endurance of the chips by reducing thermal stress. In the following two chapters, we show that oxygen gas (O_2) can play opposite roles in the sulfurization of pre-deposited Mo and Ti thin films in H_2S gas furnace. The thermodynamics are favorable for MoS_2 formation from Mo in sulfur-rich environments, but sulfurization tends to be slow and the product is highly-dependent on the chemical pathway taken. In Chapter 2, we study the formation of MoS_2 from Mo films in H_2S vapor, between 350 – 500 °C and with varying

levels of O_2. We find that the presence of trace levels of O_2 accelerates the crystallization of MoS_2 and affects the layer orientation, without changing the kinetics of mass transport or the final film composition. O_2 acts as a catalyst to promote the crystallization of MoS_2 at lower temperatures than otherwise possible. On the other hand, O_2 acts as an inhibitor in TiS_2 formation resulting into high sulfurization temperature of 900 °C. In Chapter 3, we report the synthesis of large-area TiS_2 thin films at temperature as low as 500 °C by significantly reducing oxygen background during sulfurization. This dependence arises because Ti-O bonds present a substantial kinetic and thermodynamic barrier to TiS_2 formation. Lowering the sulfurization temperature is important to make smooth films, and to enable integration of MoS_2 and TiS_2 into device technology.

2.1 Project Introduction

As mentioned in the introduction to this thesis, TMDs have been widely-studied due to their remarkable electronic and optical properties, and the existence of polymorphs with contrasting physical properties [104, 105]. These materials have been explored for a variety of applications including optoelectronic devices, field-effect transistors, catalysts, and chemical sensors [106–116]. MoS_2 is naturally-occurring as the mineral molybdenite, and is the prototypical TMD. MoS_2 is a semiconductor with a thickness-dependent bandgap ranging from 1.3 eV (indirect) to 1.9 eV (direct) [107, 117–119]. Developing methods to make MoS_2 thin films has become an important area of research [120].

It is challenging to make homogenous, large-area MoS_2 thin films at low processing temperature. This is because refractory metals are slow to sulfurize [121, 122]. Low temperature processing, however, is necessary to make MoS_2 a practical candidate for many proposed applications, for example those requiring deposition on inexpensive and temperature-sensitive substrates, or integration with sensitive electronic components. Therefore, there is interest in developing low-temperature processing for large-area MoS_2 thin films.

Large-area TMD films are made by techniques including chemical vapor deposition (CVD), metal-organic CVD (MOCVD), and atomic layer deposition (ALD). CVD is the most widely-used technique. The most common precursors to form MoS_2 are solids, such as MoO_3 and S. Both substances are volatile and deliver sufficient vapor pressure to enable film growth in conventional tube furnaces [123]. However, solid-source CVD is difficult to scale: solid metal oxide precursors are poisoned by sulfur and become depleted, requiring frequent replacement, and achieving wafer-scale continuous films with controllable thickness is challenging [53]. These challenges motivate research on MOCVD and ALD methods using all-vapor-phase precursors for easier wafer-scale deposition and run-to-run repeatability [124, 125]. MoS_2 films processed by ALD at low temperature (*e.g.* below 400 ^{o}C) are typically amorphous as-deposited and require annealing at high temperature (*e.g.* 800 – 1000 ^{o}C) for crystallization [125–130]. The processing temperature for crystalline MoS_2 film growth by ALD can be substantially reduced, to as low as 300 ^{o}C, by plasma-assistance and judicious precursor selection [123, 131]. MOCVD can make high-quality TMDs, but also requires high temperature and slow growth rates that may not be practical for many applications [124, 132, 133].

We focus on a two-step synthesis, deposition of Mo metal thin film followed by sulfurization in H_2S gas. Well-established physical vapor deposition (PVD) methods can achieve excellent metal thin film uniformity over large areas [120, 134–136]. Metal thin-film PVD and H_2S processing are industrially-scalable methods. Although MoS_2 films obtained by sulfurization of Mo metal films have small grain size and likely will never match the crystalline quality of films obtained by high-temperature MOCVD, the two-step approach is of interest for applications where cost, flexibility, throughout, and large-area uniformity are higher priorities than crystal quality.

The overall goal of the work presented in this chapter is to investigate the role of oxygen in sulfurzation process and thus lower the processing temperature of MoS_2 thin film. We hypothesize that trace amounts of O_2 can lower the temperature of MoS_2 formation from Mo metal thin films via sulfurization in H_2S. Although MoS_2 degrades in an oxygen environment above $\sim$300 ^{o}C, several recent studies have also

suggested that O_2 can aid MoS_2 formation [137, 138]. Hong *et al.* predicted using molecular dynamics simulations that Mo oxysulfide intermediates catalyze Mo-S-Mo bond formation in gas-phase sulfur environment [135, 139]. Chen *et al.* reported that trace O_2 in a CVD process improves the electron mobility of MoS_2 films, which suggests that the presence of oxygen lowers the concentration of defects that act as traps for electron transport [137]. These results highlight the opportunity to study the influence of O_2 on MoS_2 formation by Mo metal sulfurization, and motivate our experimental design including the use of well-controlled mixtures of H_2S and O_2 gas.

In this chapter, we sulfurize Mo metal films in mixtures of H_2S and O_2 and varying temperature. We characterize the composition, phase, and crystallinity of the synthesized films using scanning transmission electron microscopy (STEM), Raman spectroscopy, X-ray diffraction (XRD), and X-ray photoelectron spectroscopy (XPS). We find that adding trace quantities of O_2 during sulfurization accelerates MoS_2 crystallization at reduced temperature, without affecting sulfur diffusion or overall film composition; O_2 also affects the MoS_2 layer orientation. O_2 therefore acts as a catalyst to lower the processing temperature for MoS_2 film synthesis by the two-step method of Mo metal film sulfurization.

2.2 Experimental Methods

2.2.1 Two-Step Growth Process

We deposit Mo metal precursor films on SiO_2 (100 nm thermal oxide)/Si substrates, which we pre-clean by sequential treatments with methanol, acetone and isopropyl alcohol. We deposit Mo metal using an electron-beam (e-beam) source (Telemark) in a molecular beam epitaxy chamber (Mantis Deposition). The e-beam deposition current is typically 178 mA, and the chamber base pressure and process pressure are approximately 10^{-9} and 10^{-8} torr, respectively. For certain studies we intentionally use relatively thick Mo precursor films (16 and 34 nm) to clearly see the sulfur diffusion front, to distinguish the kinetics of mass transport through the film (*i.e.* diffusion)

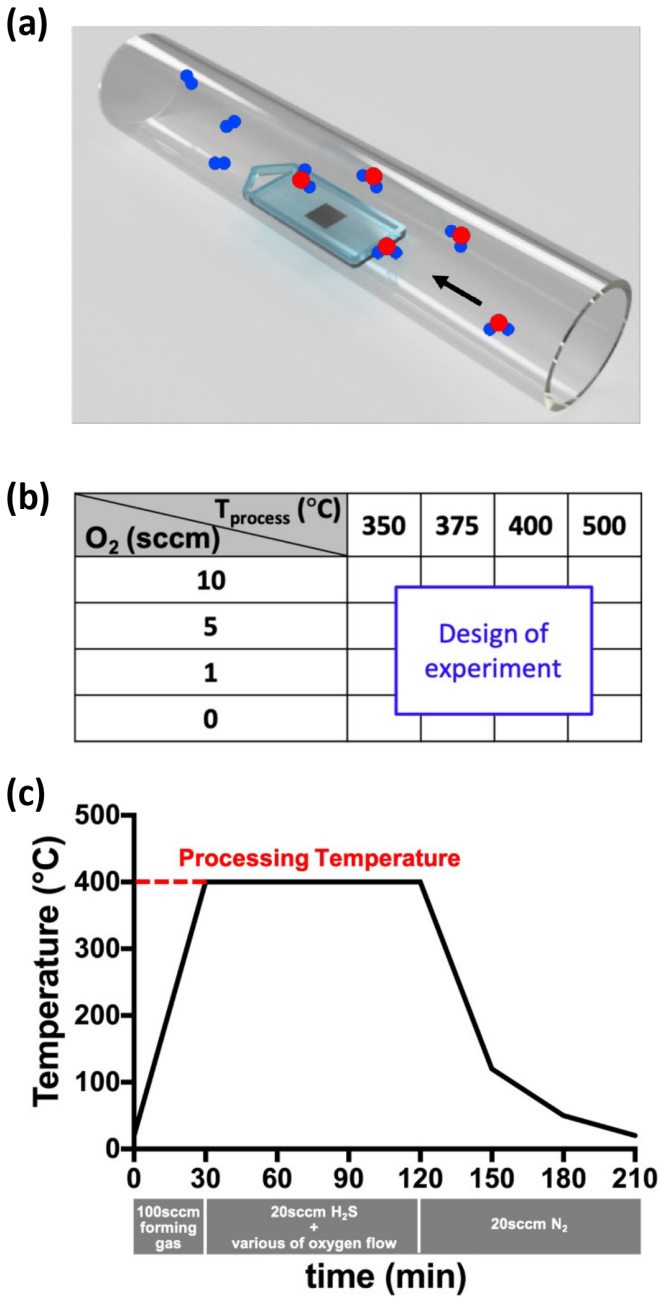

Figure 2-1: **A schematic of sulfurization process and design of experiment.** (a) Pre-deposited Mo (silver) is loaded at the center of 3-inch quartz tube in the three zone tube furnace system. Black arrow indicates the direction of H_2S gas flow. Thermally decomposed sulfur (S) reacts with the Mo thin film to form MoS_2 thin film. Red: S atom, Blue: H atom. (b) Matrix shows the design-of-experiment with two variables, $T_{process}$ and O_2 flow rate. (c) Schematic of sulfurization process. The time-temperature profile is constant for all experiments except for varying processing temperature. The bar on the bottom shows the gas flows. Heating: 100 sccm forming gas (5% H_2 in 95% N_2). Sulfurization: 20 sccm H_2S and varying O_2. Cooling: 20 sccm N_2.

from the kinetics of sulfurization and MoS_2 crystallization reactions. These experiments are designed to result in multi-phase films, with MoS_2 above unreacted Mo. In separate studies we use thinner Mo precursors (1 nm) to produce single-phase MoS_2 films. While the results reported here may inform processing conditions to make ultra-thin (*e.g.* monolayer) MoS_2 films, our focus is instead on sulfurization kinetics.

We sulfurize the Mo metal films while varying O_2 concentration and processing temperature, holding other conditions constant, in order to measure the effects of O_2 on the kinetics of MoS_2 formation as depicted in Figure 2-1b. We place the Mo metal film samples in the center of a 3-inch quartz tube, hot-wall, low-pressure furnace (base pressure $\sim$0.1 Torr) (Figure 2-1a). The leak rate from the ambient into the reactor near base pressure is < 1 sccm, corresponding to < 0.2 sccm of O_2. We determine this leak rate by analyzing steady-state and transient-rise pressure data under varying gas flow conditions. Therefore, the total flow of O_2 into our reactor is the flow controlled by the O_2 mass flow controller (MFC), plus this extra leak rate. For simplicity, below we report only the MFC rates; considering also the leak rate does not affect our results or conclusions. In Figure 2-1c we show the time-temperature profile and gas flows of our process. We ramp from room temperature to the processing temperature at a rate of 8 °C/min, in a flow of 100 sccm of forming gas (5% H_2, 95% N_2) to inhibit the MoO_x formation, and a total pressure of 8 torr. Once the target temperature is reached, we stop the forming gas and introduce H_2S gas at 20 sccm, along with varying flow rates of O_2 (0, 1, 5, 10 sccm). We maintain the processing temperature for 90 min, and then allow the furnace to cool to room-temperature in 20 sccm N_2. It takes 20 – 30 min to cool from the processing temperature to 100 °C. Appendix 2.5 shows experiments conditions we have performed to study O_2 effect on sulfurization of refractory Mo metal.

2.2.2 Photolithography

To fabricate photonic devices with integrated MoS_2 on the top (See Section 2.3.5), maskless lithography is done using Heidelberg MLA 150, a high speed direct write lithography tool with a nominal 1μm resolution. Two kinds of solid state diode laser

are available as a light source in MLA 150, which are 2.8W at 375 nm or 8W at 405 nm. This maskless system is applicable to most of photoresist except for thick SU 8 process.

The process flow is as follow:

(1) The sample (ring resonator and Mach–Zehnder interferometer (MZI) fabricated by our collaborator) is spin-coated with PMGI SF5 at 3500 rpm and soft-baked at 230 °C for 6 min. The reason of soft baking is to improve adhesion between photoresist and the substrate through dehydration. PMGI is photo-insensitive and isotropic, enabling to develop faster than SPR700. PMGI is the underlayer in bi-layer photoresist stack to intentionally make undercut for ease of lift-off.

(2) The second layer of SPR700 is spin-coated at 3500 rpm and pre-baked at 95 °C for 6min.

(3) The pattern is exposed into the photoresist stacks using MLA 150 with the 375 nm laser and a exposure dose of 160 $\frac{mJ}{cm^2}$.

(4) The exposed positive photoresist is developed in CD-26 developer for 75 s and the UV-light exposed parts where is soluble in the developer is removed.

After developing step, 1 nm Mo thin film is deposited on patterned photoresist where sit on Si_3N_4 ring resonator and MZI by AJA electron beam evaporator with a base pressure of 7 x 10^{-6} Torr at deposition rates of 0.5 Å/s at ambient temperature. After deposition, the polycrystalline Mo thin film is patterned by lift-off process using resist strippers. The sample is soaked in a warm NMP (1-Methyl-2-pyrrolidon) solution for 10 min. As a following step, we sulfurize the patterned Mo in CVD tube furnace at 400 °C with 20 sccm of H_2S and 5 sccm of O_2. Figure 2-2 shows the patterned MoS_2 on photonic devices. It is rarely visible because the thickness of MoS_2 is quite thin, $\sim$ 3 nm. This process flow facilitates a reliable lift off for metal which thickness is $\leq$ 300 nm.

2.2.3 Characterization Method

We characterize the MoS_2 phase and crystallinity using Raman spectroscopy (Reinshaw Invia Reflex Micro Raman) at room temperature. We use a 532 nm laser

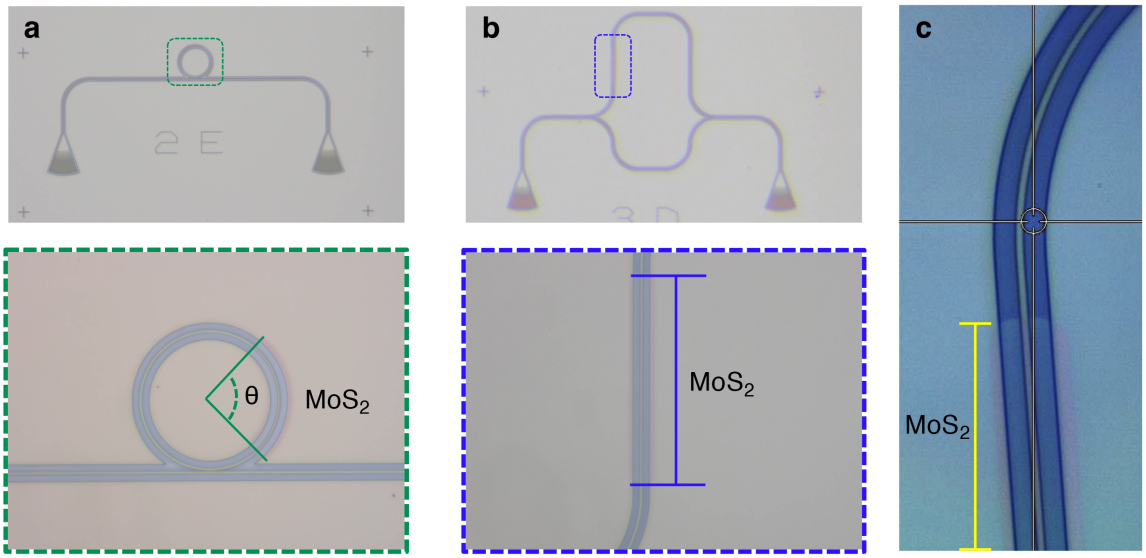

Figure 2-2: **Optical images of patterned MoS_2.** CVD MoS_2 integrated on (a) ring resonator and (b) MZI. (c) Magnified region where MoS_2 is patterned on. The yellow bar indicates the pinkish MoS_2.

excitation source with an optical intensity of 6.5 $\mu W/\mu m^2$. We characterize composition and chemical states using XPS (Physical Electronics Versaprobe II), with a monochromatic aluminum Kα source, and pass energy of 187.85 eV and 117.40 eV for survey scans and for high-resolution scans, respectively; we also perform higher-resolution scans with a pass energy of 55 eV using a Thermo Scientific Nexsa. We measure XPS spectra as a function of depth through the film by sputter etching, using an Ar ion source with 3 kV ion energy, and raster area of 2 x 2 mm^2. We use STEM to measure crystal phase and to visualize the MoS_2 formation process. Cross-sectional TEM samples are prepared by mechanical polishing and final thinning by Ar-ion milling from 1.0 to 0.1 kV. We perform four-dimensional (4D) STEM with a probe-corrected FEI Titan G2 60-300 kV operating at 200 kV with a beam current of 80 pA in microprobe mode and a probe semi-convergence angle of 4.1 mrad. We collect 4D STEM data with an electron microscope pixel array detector (EMPAD) [139]. We carry out high-resolution transmission electron microscopy (HRTEM) on a Thermo Fisher Scientific Talos F200X using an 8.87 mrad collection angle defined by an objective aperture. We use X-ray fluorescence (XRF, Bruker Trace III-SD) before and after sulfurization to detect Mo loss, for instance due to evaporation of volatile

MoO_3. We measure surface morphology using optical microscopy and atomic force microscopy (AFM, Veeco dimension 3100).

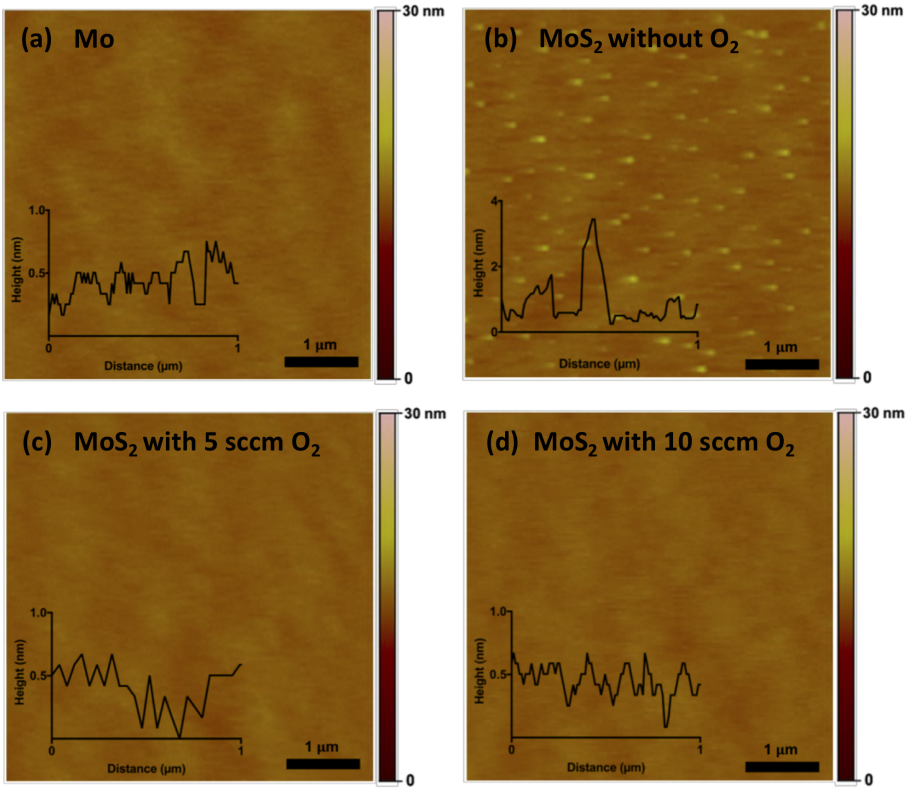

Figure 2-3: **AFM surface scan images and line profiles** (a) the pre-deposited Mo film, and MoS_2 films sulfurized at 400 °C with varying O_2 concentration: (b) no O_2 flow, (c) 5 sccm O_2, and (d) 10 sccm O_2. The Mo precursor film is smooth and homogenous, with RMS roughness of 0.36 nm. MoS_2 films synthesized with O_2 are also smooth, with RMS roughness of 0.30 nm for both 5 and 10 sccm O_2. In contrast, the MoS_2 film sulfurized without O_2 shows small bumps (bright dots) approximately 3 nm tall on an otherwise smooth surface. The RMS roughness of this film is 0.52 nm.

Table 2.1: **The corresponding root-mean-square roughness of AFM image in Figure 2-3.**

Sample	(a)	(b)	(c)	(d)
RMS roughness (nm)	0.36	0.52	0.30	0.30

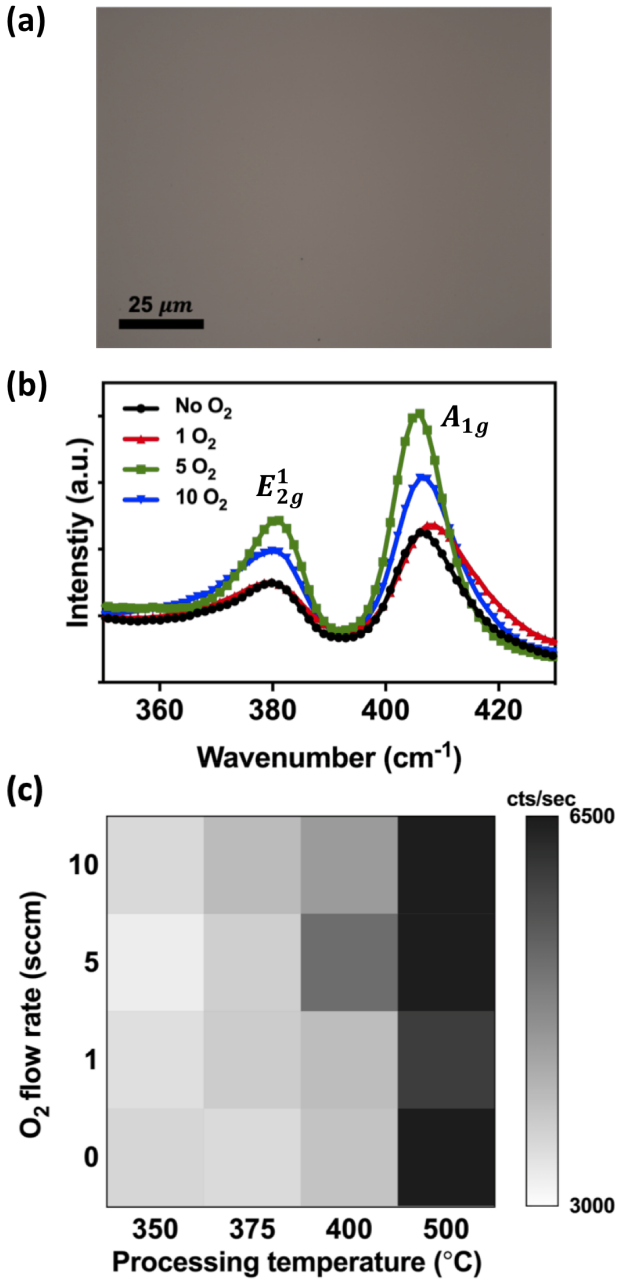

Figure 2-4: **Characterizing MoS_2 films made by sulfurizing Mo films under varying conditions.** (a) Optical image of a MoS_2 thin film sulfurized in 5 sccm O_2 at 400 °C. The film is continuous, smooth and homogenous. (b) Raman spectra of MoS_2 which is processed at 400 °C with a different O_2 concentration; 0, 1, 5 and 10 sccm O_2 flow. The Raman modes $E_{2g}{}^1$ and A_{1g} correspond to in-plane vibration and out-of-plane vibration, respectively. The spacing between two vibrational modes is approximately 28.7 cm^{-1}. (c) Color map of A_{1g} peak intensity for different O_2 flow rate and processing temperature. The grid of processing conditions is the same as in the design-of-experiment in Figure 2-1c.

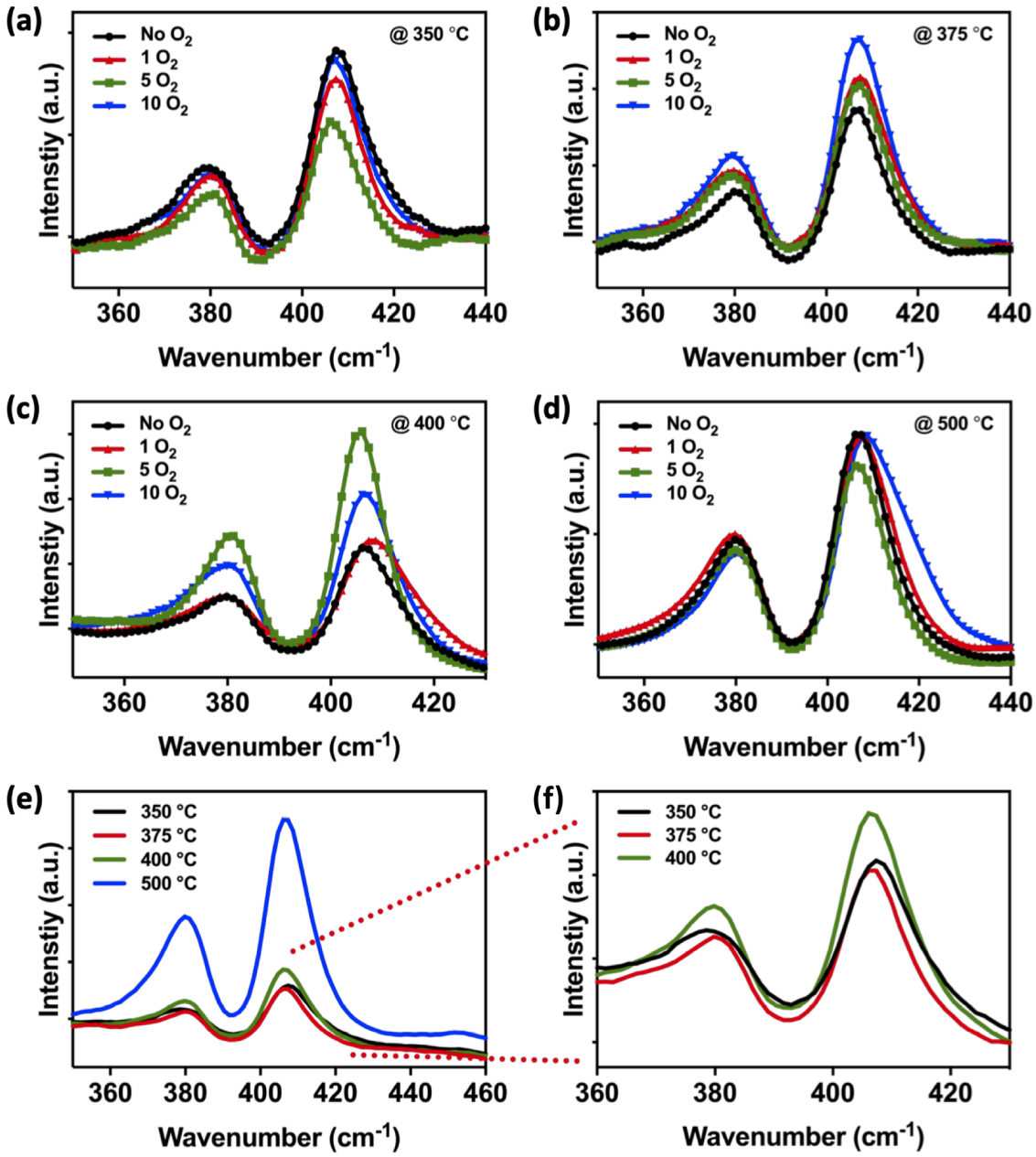

Figure 2-5: **Raman spectra of MoS_2 films sulfurized at various temperature.** Raman spectra of MoS_2 films sulfurized at (a) 350 °C, (b) 375 °C, (c) 400 °C, and (d) 500 °C. In each case we show data for films sulfurized in the presence of no additional O_2 (black), 1 sccm O_2 (red), 5 sccm O_2 (green), and 10 sccm O_2 (blue). (e) MoS_2 synthesized at different temperatures without O_2 flow. (f) Magnified plot includes Raman spectra of 350°C, 375°C and 500°C, as in (e).

2.3 Results and Discussion

2.3.1 Effect of Temperature and Oxygen Pressure

As described in 2.2.1, we intentionally use relatively thick Mo metal precursor films to distinguish diffusion and reaction kinetics. Hong *et al.* has reported that Mo oxysulfide intermediates catalyze Mo-S-Mo bond formation in gas-phase sulfur environment using molecular dynamics simulations [135, 139]. However, diffusion of oxygen atom in Mo thin film is highly unknown. Because sulfurization could be limited either by diffusion or reaction kinetics, we hypothesize that thick Mo film of 34nm shows oxygen diffusion front at various sulfurization temperature and O_2 pressures. This decision results in multi-phase films, with MoS_2 on top and unreacted Mo underneath. The MoS_2 films appear smooth and continuous under an AFM and an optical microscope (Figure 2-3cd and 2-4a). Films sulfurized in the presence of O_2 have root-mean-square (RMS) roughness of approximately 0.3 nm, measured by AFM (Table 2.1 and Figure 2-3cd). The small roughness arises from reduced mobility of species on the surface at low processing temperature. However, MoS_2 films sulfurized without O_2 are speckled by small islands, approximately 3 nm tall, on an otherwise-smooth surface as shown in Figure 2-3b. We hypothesize that O_2 impedes the agglomeration and growth of protruding crystallites due to the known etching effect, thereby improving film morphology [135].

In Figure 2-4b we show Raman spectra of MoS_2 prepared at 400 °C in different O_2 flow rates (0 – 10 sccm). In order to study catalytic effect of O_2 at different sulfurization temperature (350°C, 375°C, 400°C, and 500°C), Raman spectra on MoS_2 film sulfurized at a range of different sulfurization and oxygen flow rate are measured as shown in Figure 2-5. We fit the data using Gaussian curves as described in Figure **??**. We observe the characteristic Raman peaks ${E_{2g}}^1$ and A_{1g}, corresponding to 2H phase of crystalline MoS_2. The ${E_{2g}}^1$ peak is asymmetric with a shoulder on the low-energy side for all samples measured. The A_{1g} peak is more symmetric, but develops a shoulder on the high-energy side for certain O_2 flows. Asymmetric ${E_{2g}}^1$ and A_{1g} peaks of this type have been attributed to the coexistence of multilayer and single-

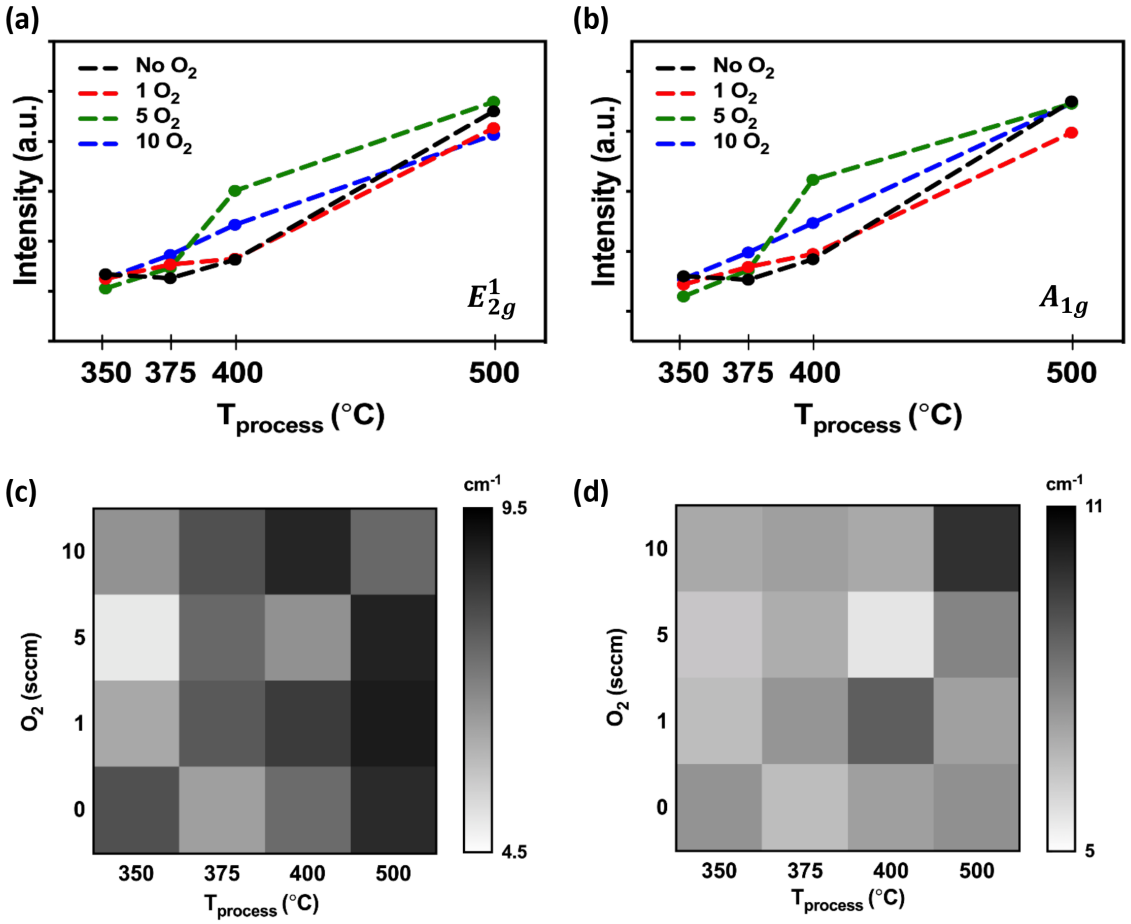

Figure 2-6: **Summary of Raman peak intensity and peak width of processed MoS_2.** Maximum Raman peak intensities for MoS_2 films with varying processing temperature and O_2 flow. (a) $E_{2g}{}^1$ peak intensity. (b) A_{1g} peak intensity. The intensity values are derived from the fit models. Heat map of (c) $E_{2g}{}^1$ peak width and (d) A_{1g} peak width for MoS_2 films synthesized in varying processing temperature and O_2 flow. The grid of processing condition is the same as in the design-of-experiment in Figure 2-1.

layer MoS_2, but it is unclear how relevant this explanation is to our synthesized films [140]. In Figure 2-4c we summarize the extent of MoS_2 crystallization for all processing conditions by reporting the A_{1g} peak intensity. The effect of O_2 is most evident at 400 °C, for which the effect of O_2 is non-monotonic: O_2 enhances MoS_2 formation up to 5 sccm, but additional O_2 is counterproductive. At lower temperature, the effect of O_2 on MoS_2 formation is less clear. For 375 °C, the Raman signal is maximal for the maximum O_2 flow measured (10 sccm). For 350 °C there is no apparent effect. At higher temperature (500 °C) the Raman peaks are stronger, as expected (due to

improved crystallinity), and O_2 has no significant effect. The data suggest that O_2 at low concentrations acts as a catalyst for the formation of MoS_2, while at high concentrations it is detrimental to film formation, presumably due to the effect of etching. For sufficiently high temperature, the catalytic effect is negligible. This is similar to the effect of O_2 observed during the growth of MoS_2 by solid-source CVD [135].

2.3.2 Kinetics of Sulfurization

We use XPS depth profiling to characterize the composition and chemistry of the sulfurized films. In Figure 2-7a we show the Mo, S and O concentrations for films sulfurized with and without O_2. Adding O_2 to the process somewhat increases the O concentration and decreases the S concentration in the resulting film. The similarity of the S depth-profiles with and without O_2 suggest that the presence of O_2 may affect H_2S dissociation and S incorporation at the film-gas interface, but does not affect the diffusion of S through the solid state. The presence of O_2 has negligible effect on the Mo concentration. All films are sulfur-rich at the surface (S:Mo ratio is greater than 2). Deeper into the film, the concentration of unreacted Mo increases and the concentration of sulfur decreases. Figure 2-7b shows the S-2p peak as a function of sputter depth for a film sulfurized in 5 sccm O_2 at 400 °C. The peak position is as-expected for S^{2-} in MoS_2 at all depths, and there is no evidence for other sulfur-containing compounds, such as sulfates. Therefore, O_2 does not affect the sulfur oxidation state in the resulting film.

In Figure 2-8 we show XPS results for the oxidation state of Mo for three films processed at 400 °C with varying O_2 flow. As with S (Figure 2-7b), we see no significant effect of O_2 on the oxidation state of Mo, or its depth-dependence. The dominant oxidation state near the film surface is Mo^{4+}, consistent with MoS_2, while deep in the film Mo remains in its metallic Mo^0 state with lower binding energy. There is no evidence of Mo^{6+}, which would be expected if MoO_3 were present. Therefore, it is unlikely that MoO_3 was formed during sulfurization, with or without added O_2. The expected binding energies for Mo^{6+} in MoO_3, for Mo^{4+} in MoS_2, and for Mo^0 are

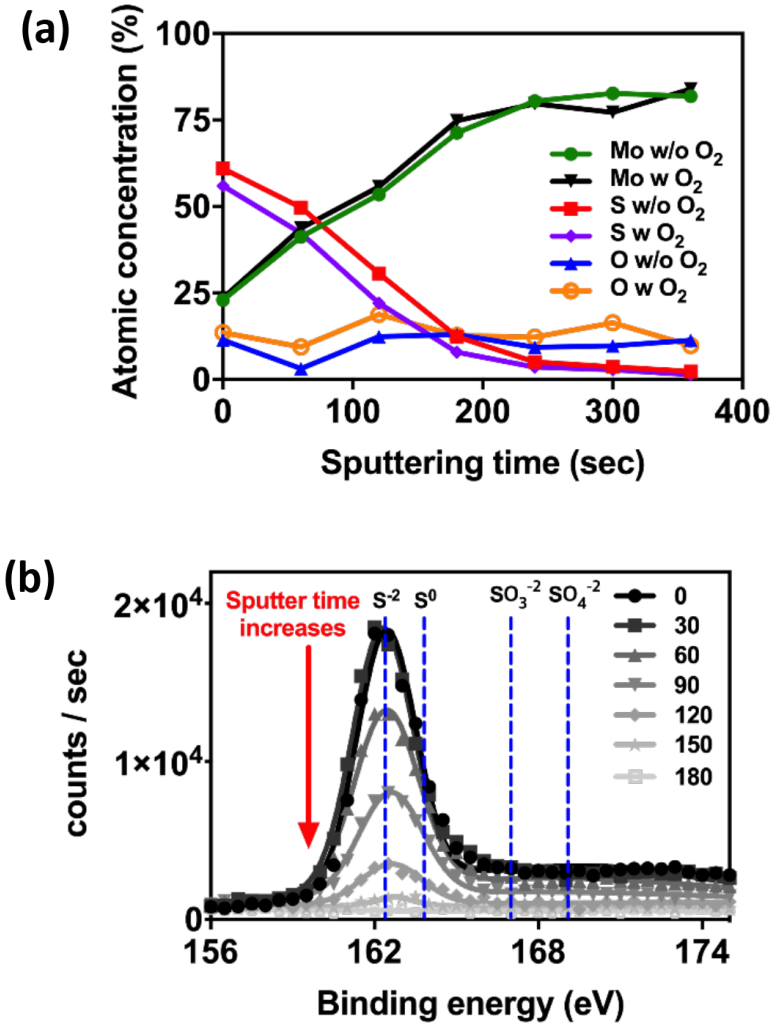

Figure 2-7: **XPS depth profiles and high resolution scan.** XPS data showing atomic concentrations and S oxidation state through a MoS_2 film sulfurized in 5 sccm O_2 at 400 °C. (a) Atomic concentrations of Mo, S, and O as a function of depth through the film, as measured by XPS with sputter depth profiling (0 sec sputter time indicates the surface of as-synthesized MoS_2 film). Concentrations are converted from intensity of Mo-3p3/2, S-2p, and O-1s peaks. (b) S-2p peak for MoS_2 film sulfurized at 400 °C in 5 sccm O_2 flow for varying sputter time, between 0 – 180 sec. The red arrow indicates increasing sputtering time. The blue dotted lines indicate the binding energy expected for various chemical states: 162.3 eV for MoS_2 (S^{2-}), 164 eV for sulfur (S^0), 167 eV of sulfite (SO_3^{2-}), and 169 eV for sulfate (SO_4^{-2}).

398.5 eV, 395.3 eV and 394 eV, respectively, as noted in the Figure 2-8 [141–143]. Additionally, we note that XRF measurements show no sign of Mo loss with increasing processing temperature or O_2 flow (Figure 2-9b). MoO_3 is volatile, and the formation of MoO_3 due to O_2 flow could result in measurable loss of Mo from the film. The facts that we see no Mo loss in XRF and no sign of Mo^{6+} in XPS suggest that the MoO_3 phase does not form during processing.

Considering the XPS results for the S and Mo oxidation states (Figures 2-7b and 2-8), it seems that O_2 does not affect the formation of Mo-S bonds, which can exist in both amorphous and crystalline phases. The Raman and XPS data suggest that O_2 specifically supports the formation of crystalline MoS_2 by catalyzing the formation of Mo-S-Mo bridging bonds, as suggested by molecular dynamics simulations [138].

2.3.3 Effect of Oxygen on Crystallinity

To characterize the crystallinity of films grown with and without O_2 flow, we performed 4D STEM and HRTEM. In Figure 2-10 we present data for samples processed at 400 °C in 0 and 5 sccm O_2 flow. Bright-field images generated from 4D STEM datasets indicate the position of the MoS_2 layer at the surface of the Mo film. The thickness of the sulfur-rich layer is approximately 10 nm in both samples, which is consistent with the XPS depth-profiles that show O_2 does not affect the sulfur mass transport. Convergent beam electron diffraction patterns extracted from the 4D STEM datasets show the effect of O_2 on MoS_2 crystallinity. In the case of sample grown without O_2 flow, the Mo layer shows clear diffraction spots (Figure 2-10a, ii) while only a weak, diffuse ring is visible in the MoS_2 (Figure 2-10a, i). In contrast, the sample grown with 5 sccm O_2 flow shows diffraction spots corresponding to MoS_2 2H phase (Figure 2-10b, iii). Investigation with HRTEM (Figure 2-10c-d) further shows that MoS_2 grown without O_2 is comprised of small, vertically aligned crystallites, whereas MoS_2 grown with O_2 has more horizontal alignment and larger crystallite size. The difference in MoS_2 crystal orientation may result from the effect of oxygen etching that can reduce nucleation density [135].

XRD provides further support for improved crystallinity due to processing in O_2.

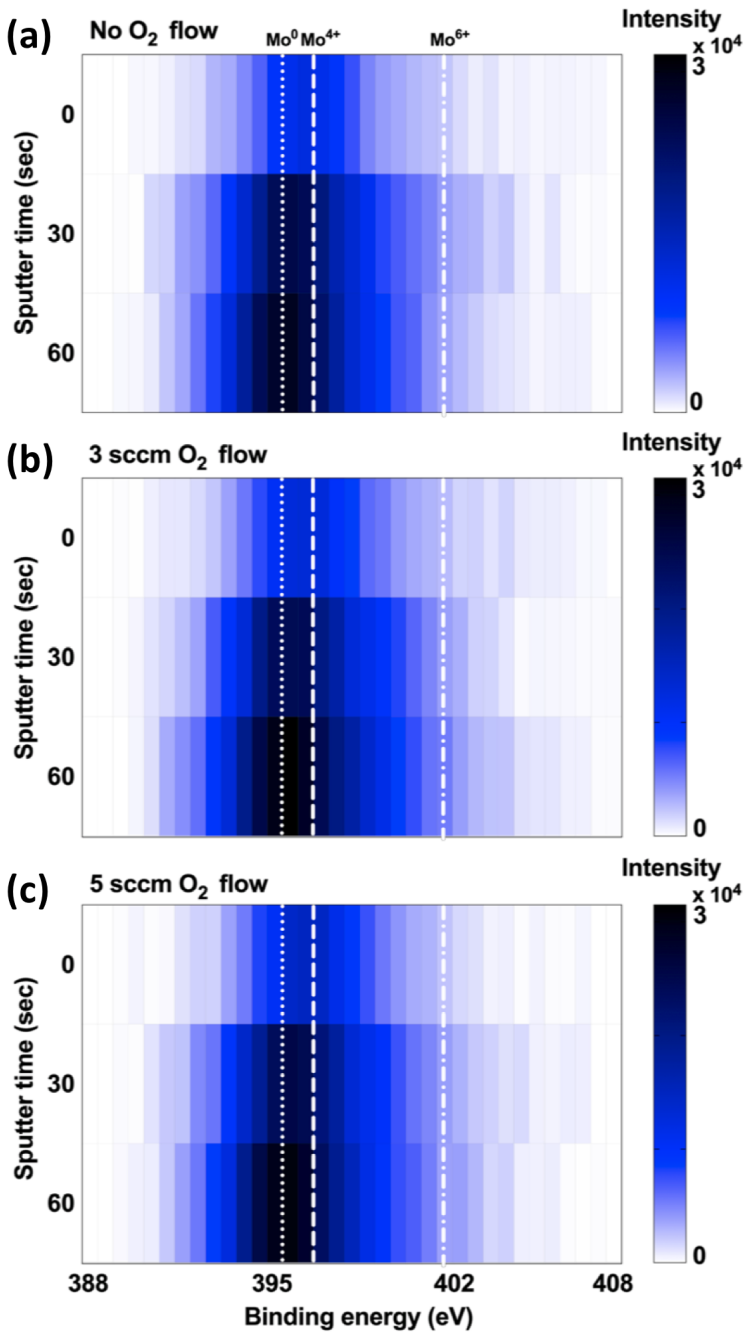

Figure 2-8: **Heat map of Mo-3p$_{3/2}$ XPS peak.** As a function of depth (*i.e.* sputter time) for MoS_2 thin films that are sulfurized at 400 °C with varying O_2 flow. (a) no O_2 flow, (b) 3 sccm O_2, and (c) 5 sccm O_2. In all cases, the top layer has converted from Mo^0 into Mo^{4+}, while the underlying Mo remains metallic as Mo^0. There is no sign of Mo^{6+} as in the MoO_3 phase.

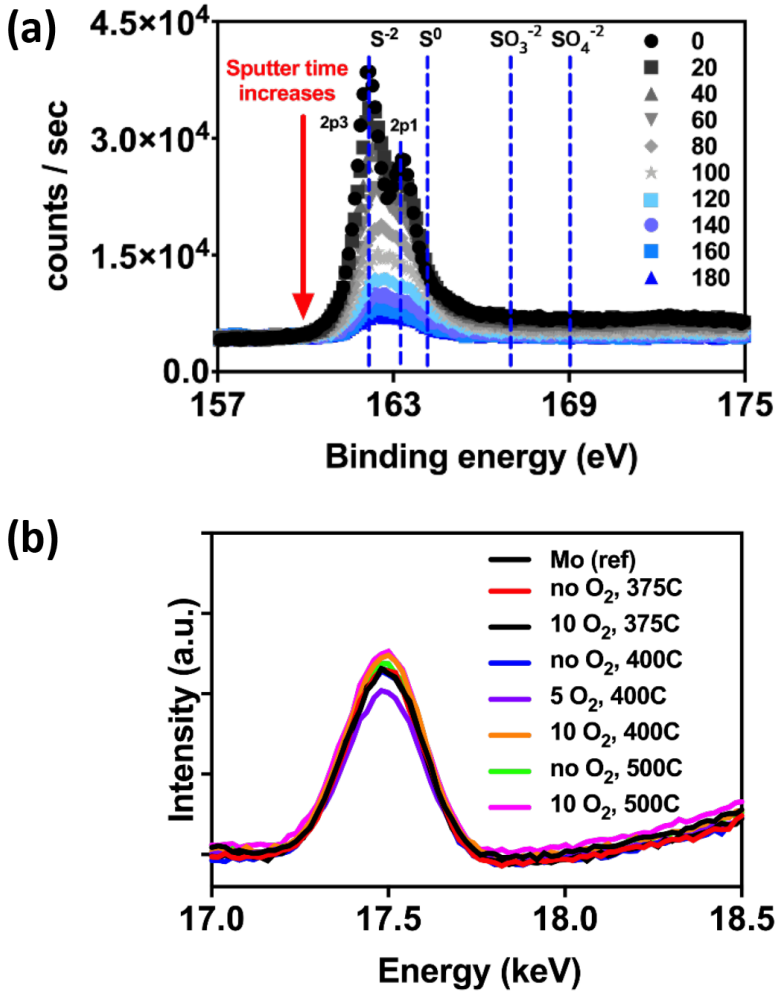

Figure 2-9: **XPS depth profilng of S-2p peak with smaller pass energy and XRF spectra.** (a) S-2p peak for MoS_2 film sulfurized at 400 °C in 5 sccm O_2 flow for varying sputter time, between 0 – 180 sec. We used a pass energy of 55 eV for this high-resolution scan, compared to 117.40 eV used for the data in Figure 2-7b. With this smaller pass energy we can see the splitting of S-2p peak of MoS_2 (S^{2-}) into $S2p_{3/2}$ and $2p_{1/2}$ peaks. The blue dotted lines show the location of each peak and the red arrow indicates the increase in sputter time. (b) XRF spectra showing the Mo Kα characteristic emission for MoS_2 films synthesized in varying processing temperature and O_2 flow, all with Mo precursor films 16 nm thick. XRF is sensitive to the overall amount of Mo present in the sample, independent of the phase. The films are very thin relative to the X-ray attenuation length, and self-absorption is negligible, therefore XRF is sensitive to the whole film thickness. The curve labeled "Mo (ref)" is the precursor before sulfurization. The overlap between spectra shows that there is no significant Mo loss during sulfurization.

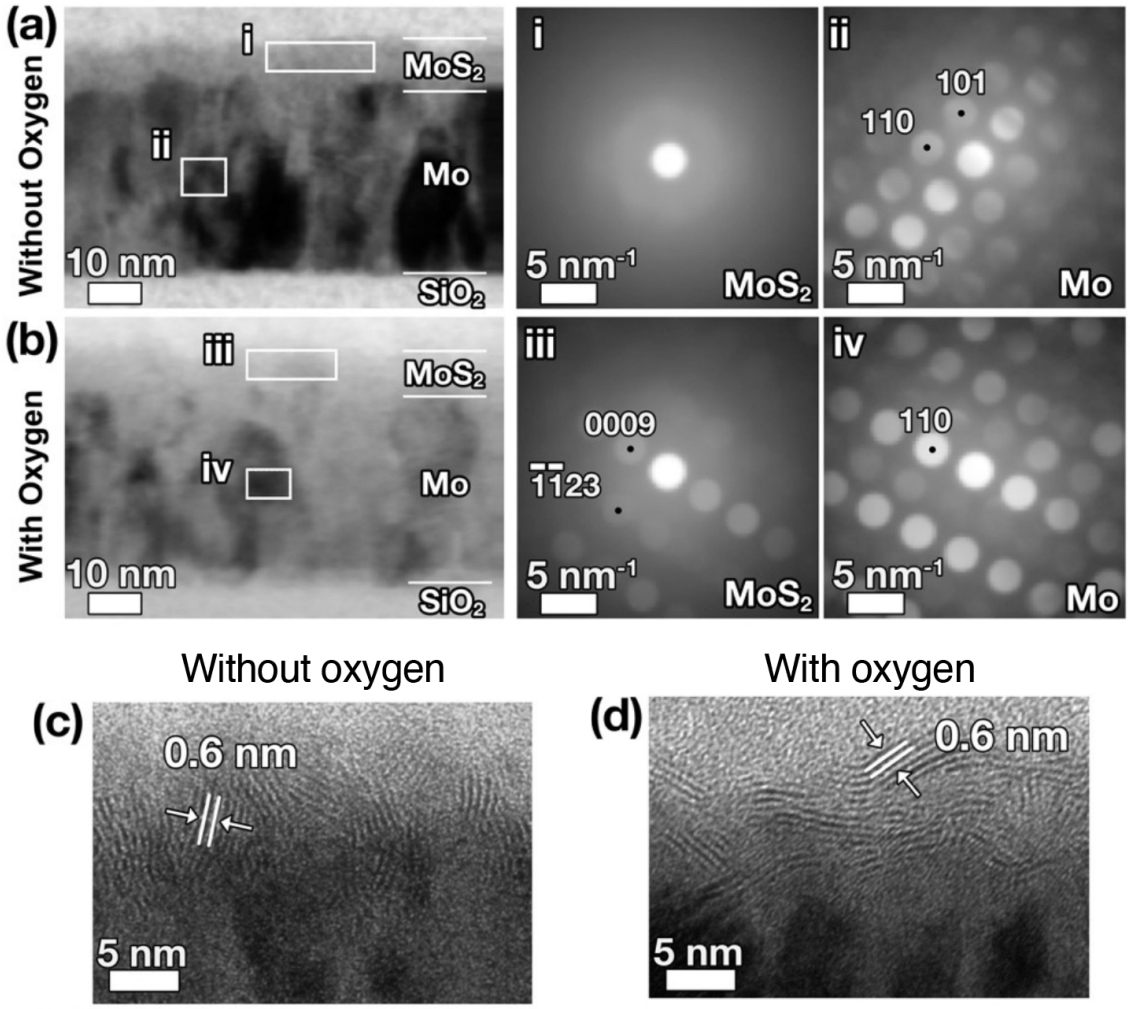

Figure 2-10: **4D STEM images and HRTEM images of MoS_2 synthesized with/without O_2.** (a) Virtual bright-field STEM images generated from 4D STEM dataset from Mo metal film sulfurized at 400 °C with and without 5 sccm O_2 flow as indicated. (b) Convergent beam electron diffraction pattern formed by averaging 4D STEM data collected in the correspondingly labeled areas in (a). i and iii are from within the MoS_2 layer while ii and iv are from the Mo thin film. (c) and (d) HRTEM images showing the differences in crystallinity between the MoS_2 layers with and without oxygen.

In Figure 2-11a we present out-of-plane grazing-incidence XRD spectra for MoS_2 films sulfurized at 375 °C with and without O_2. We observe the (002) and (110) peaks from 2H-MoS_2, at 13.7° and 58.9°, respectively, and the (110) peak from the unreacted, metallic Mo. The very broad peak at 21.6° contains contributions from both the amorphous SiO_2 substrate and the amorphous phase fraction of the MoS_2 film (see

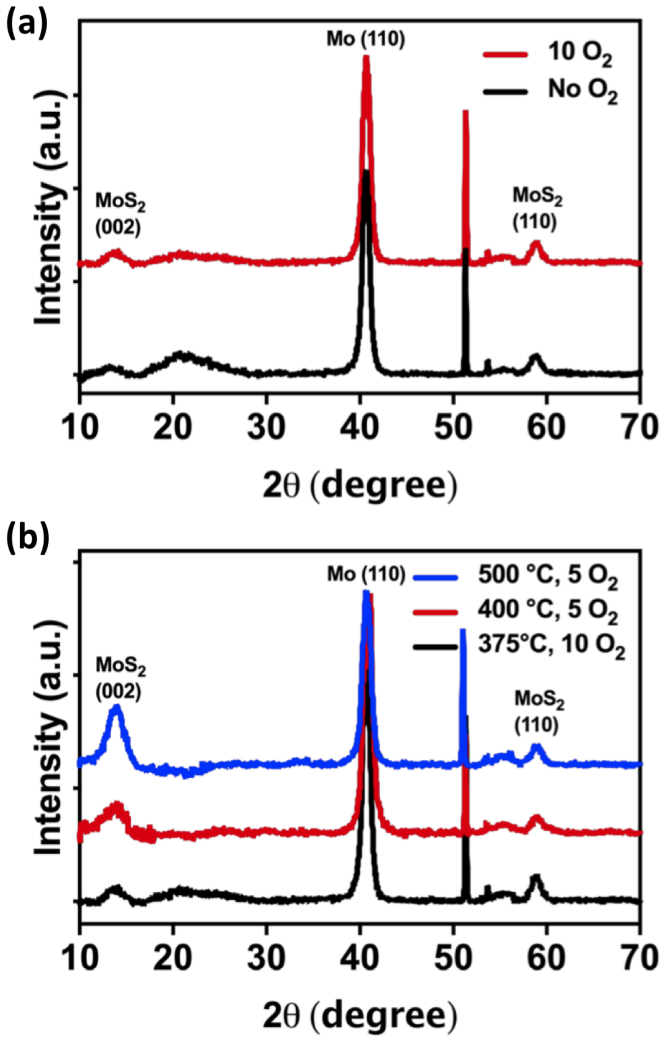

Figure 2-11: **Out-of-plane grazing incidence XRD spectra for sulfurized MoS_2 thin films.** Characteristic peaks assigned to the (002) and (110) reflections of 2H-MoS_2 are observed at 13.7° and 58.9°, respectively. The broad peak at 21.6° contains contributions from amorphous MoS_2 and the amorphous SiO_2 substrate. The substrate contribution has been subtracted from the data presented here, see Figure 2-12 for a full presentation of the data and analysis. (a) Films sulfurized at 375 °C without (black) and with (red) O_2 flow. (b) Films sulfurized in 10 sccm (black) and 5 sccm (red, blue) O_2 flow at processing temperature between 375 °C and 500 °C.

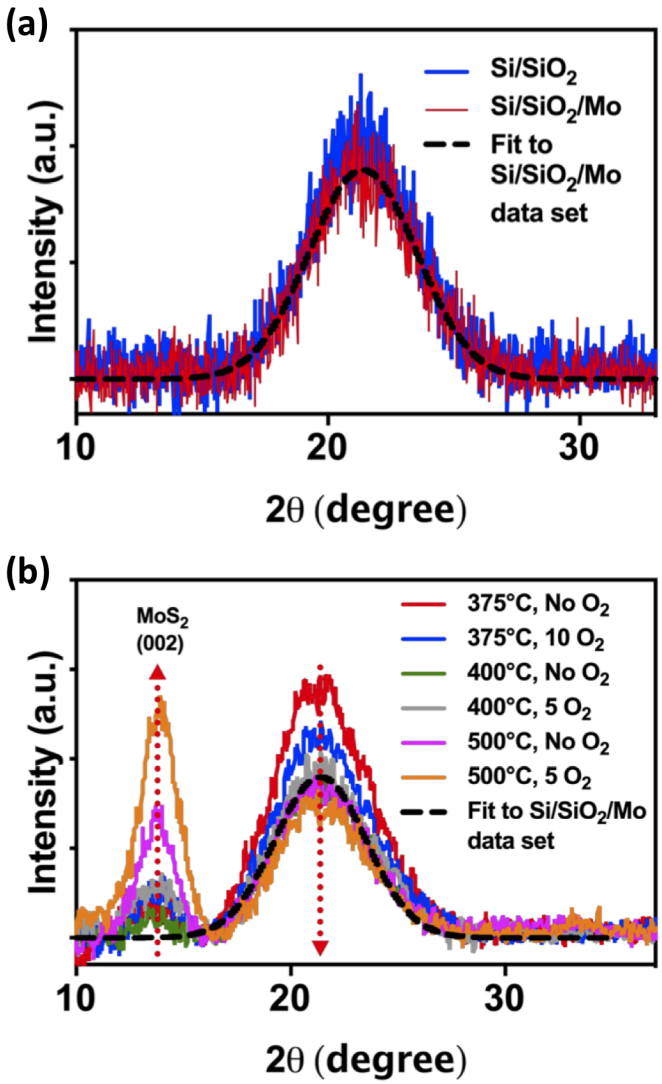

Figure 2-12: **Detailed analysis of the broad XRD peak at 21.6°.** The broad XRD peak at 21.6° is attributed to both amorphous MoS_2 and the amorphous SiO_2 substrate. All data are measured in out-of-plane grazing incidence configuration, with an incidence angle of 1°. (a) XRD spectra measured for a bare Si/SiO_2 wafer, and a wafer after depositing a Mo film (16 nm) but before sulfurization. The broad peak comes from the substrate, and the Mo film is thin enough to be X-ray transparent. The dashed black curve shows a Gaussian fit to the data measured on the $Si/SiO_2/Mo$ sample, which fit we use to subtract the substrate contribution to the data presented in Figure 2-11. (b) XRD spectra measured for a series of samples after sulfurization, showing that the 2H-MoS_2 (002) peak intensity grows as the intensity of the amorphous peak shrinks. We also show the fit profile for the data measured on the $Si/SiO_2/Mo$ sample, from panel (a). We attribute the excess contribution to the broad peak above this fit to the MoS_2 amorphous phase fraction.

Figure 2-12) [144]. The contribution of MoS_2 to this peak intensity shrinks as the crystalline phase fraction and the (002) peak intensity grow; *i.e.* upon adding O_2 to the sulfurization process, the (002) peak from 2H-MoS_2 grows and the amorphous peak shrinks. As we show in Figure 2-11b, we observe a similar trend due to increasing the processing temperature while holding the O_2 content fixed: the (002) peak grows and the amorphous peak shrinks. Therefore, adding O_2 at lower processing temperature has qualitatively the same effect as increasing the processing temperature. The 2H-MoS_2 peaks are relatively broad, consistent with films made few-layer-thick crystals [145, 146].

2.3.4 Large Area Thin Film Deposition on Arbitrary Substrates

Our two-step synthesis method allows us to grow large area MoS_2 thin films on various substrates, and to control the thickness of MoS_2 by tuning the thickness of Mo precursor.

Above we report results using thick Mo precursors (16 nm) to study the sulfurization mechanism. Now we demonstrate fully-sulfurized MoS_2 films made using thin metal precursors. In Figure 2-14a we show a MoS_2 film deposited across a 2 inch wafer. The Mo metal precursor film is 1 nm thick, and is sulfurized under 20 sccm H_2S and 5 sccm O_2 gas flows at 400 °C. XPS depth profiling shows that the films are uniformly sulfurized throughout (Figure 2-13). The same process can be used to make large-area MoS_2 films on various substrates; in Figure 2-14b we show films grown on Al, glass, and indium tin oxide (ITO). In all cases we confirm the MoS_2 phase identity using Raman spectroscopy, as shown in Figure 2-14c. These results demonstrate a general method for making large-area MoS_2 coatings at low processing temperature and with wide substrate compatibility. This creates possibilities to integrate and pattern MoS_2 films in device fabrication, such as for integrated photonics.

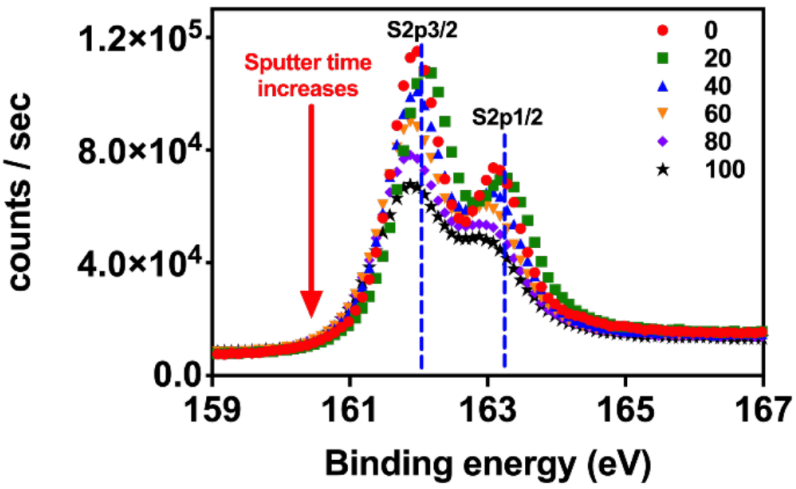

Figure 2-13: **XPS depth profile of MoS_2 sulfurized from 1 nm-thick Mo.** XPS depth profile of fully-sulfurized MoS_2 thin film made from 1 nm-thick Mo metal precursor sulfurized at 400 °C in 5 sccm O_2 and 20 sccm H_2S flows. We show S-2p spectra for depth-profile sputter times between 0 – 100 sec. We used ion gun with energy 500 eV and sputtered for 20 s for each cycle, with 0.03 nm/s estimated sputter rate (calibration based on Ta_2O_5). With the 5-etching cycle, total thickness of sputtering is estimated as 3 nm which is comparable with the MoS_2 thickness expected from sulfurizing a 1 nm-thick Mo film (using the thickness conversion ratio of MoS_2-from-Mo approximately 3.36). The splitting of the S-2p peak of MoS_2 (S^{2-} state) into $S2p_{3/2}$ and $2p_{1/2}$ peaks is clear. The blue dotted lines show the location of each peak and the red arrow indicates the increase in sputter time.

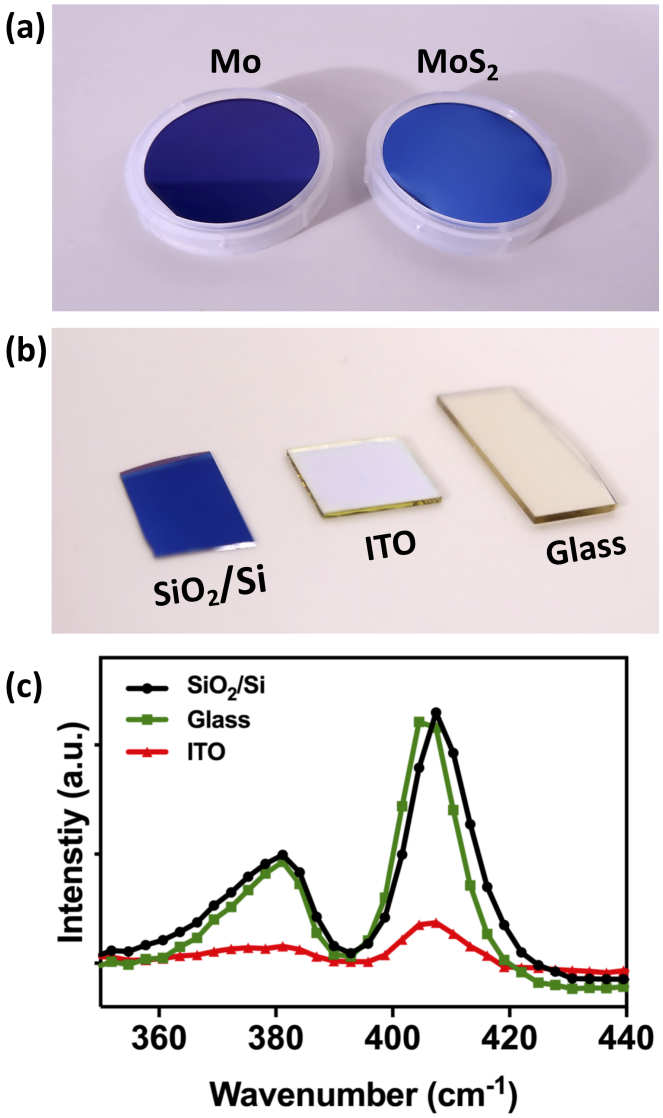

Figure 2-14: **Large area MoS_2 on arbitrary substrates.** Making large-area MoS_2 thin films on various substrates by a low-temperature process catalyzed by oxygen. In all cases films are made by sulfurizing a 1 nm-thick Mo metal film under 20 sccm H_2S and 5 sccm O_2 at 400 °C. (a) Photograph of as-deposited 1 nm Mo metal precursor film and a post-sulfurization MoS_2 film on 2 inch SiO_2/Si wafers. (b) MoS_2 films on various substrates. From left to right: SiO_2/Si, ITO and glass. (Inset) Fully-covered, large-area MoS_2 on Al and glass substrates. (c) Raman spectra of MoS_2 grown on SiO_2/Si (black), glass (green), Al (blue), and ITO (red), respectively.

2.3.5 Optical Properties of MoS_2 on Photonic Devices

Towards all-optical computing, nonperturbative optical switch with strong phase modulation and low insertion loss is an essential component. To achieve good performance device, materials with large Δn and small k are needed. k is a critical parameter in integrated photonics, which is responsible for signal attenuation through travelling. However it is difficult to measure especially below band gap wavelength range, which is attributed to a small signal to noise ratio. Therefore, k values reported in literature have a large range for a given material. Unlike n, which is less sensitive to material processing (unless material density is largely changed through the process), k values in below band gap spectral range strongly depend on measurement method and materials processing. k varies by multiple parameters: (1) implicit defects such as vacancy, dislocation and grain boundary, (2) explicit defects such as impurity, (3) native oxide formation, (4) crystallinity and (5) layer number just to name a few. Using the method we develop for large area coating on any target substrate with good uniformity and continuity, we characterize optical properties of this film and then compare with that of geological MoS_2 sample and calculated values (Table 2.3.5).

Table 2.2: **Refractive index of MoS_2 in the range of NIR.**

@ 1.5 ~1.6 μm	MoS_2	n	k
Calculated	Monolayer	2.32	0.001
	Bulk	3.5	0.01~0.02
Measured	Bulk (naturally-occurring)	4.2	0.2
	CVD film (in this work)	4.2 (assumed)	0.04/0.1

k value of geological, bulk MoS_2 crystal is measured using spectroscopic ellipsometry, which is $\sim$ 0.2 (Figure 2-15a) attributed to native oxide. To understand loss characteristics of our CVD film, we fabricate a series of Si_3N_4 all-pass ring resonator and MZI which are integrated with MoS_2 with a various range of length on the top. To pattern our MoS_2 on Si_3N_4 waveguide, we use lift-off techniques, which a process

of exposing a pattern into photoresist, depositing a thin film and removing the photoresist/thin film stacks (See Section 2.2.2 for experimental details). The patterned Mo is sulfurized at 400 °C in 5 sccm O_2 and 20 sccm H_2S flows.

The transmission spectrum is measured and we extract the losses and coupling coefficients using transmission characteristics (Figure 2-15). As another device architecture, we deposit MoS_2 film on plarnarized waveguide and measure waveguide loss in the range of 1200 – 1550 nm. k value is calculated at waveguide loss of 50 dB/cm using simulation tool with measured parameters (Figure 2-15c). Our synthetic MoS_2 thin films (thickness $\leq$ 5 nm) show different k values measured in NIR band, which demonstrates that k is dependent on device geometry and layer number. Additionally the theoretically predicted value is 0.01 – 0.02 for bulk MoS_2 and 0.001 for monolayer MoS_2. In both case, k values are much smaller than geological bulk crystal and CVD-grown thin film. This means we can improve optical loss properties of these materials by optimizing defect type and density, grain size and thickness. Here we acknowledge that the fabrication and characterization of integrated photonic devices are done by our collaborators: for MZI and ring resonator, Changming Wu in Li's group at University of Washington, for planarized waveguide, Skylar Deckoff-Jones in Hu's group at MIT.

2.4 Conclusion

We show that O_2 gas enhances the formation of crystalline 2H-MoS_2 by sulfurization of metallic Mo. The presence of O_2 does not affect mass transport, such as sulfur diffusion into the film. It does not affect the conversion of Mo from the 0 to the +4 oxidation state, or even the formation of Mo-S bonds. It seems that O_2 specifically catalyzes the formation of Mo-S-Mo bridging bonds, as suggested by molecular dynamics simulations [138], thereby building the backbone of crystalline 2H-MoS_2. The catalytic effect of O_2 accelerates the formation of 2H-MoS_2 at processing temperatures below 400 °C. This is a low processing temperature for MoS_2, especially given that the films formed here are relatively thick. Although the previously-published

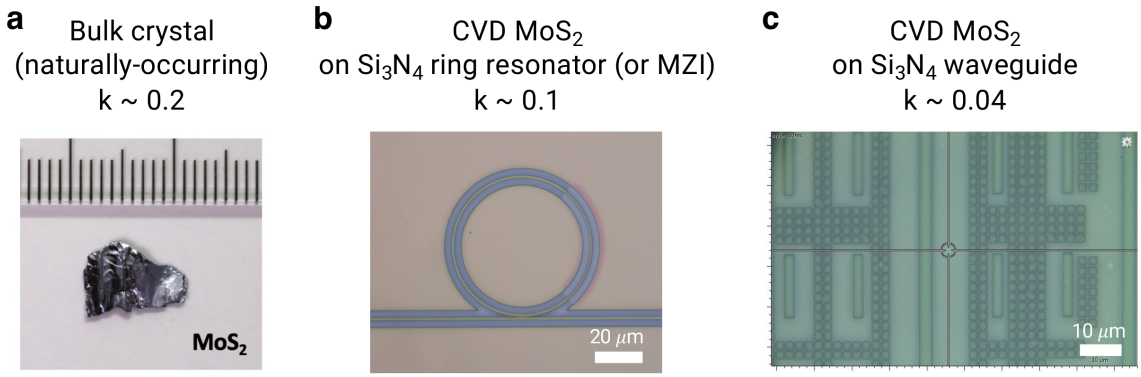

Figure 2-15: **NIR loss index k of MoS_2: geological, bulk crystal and synthetic, polycrystalline thin films.** (a) Photograph of naturally occurring crystal used for spectroscopic ellipsometry measurements. (b) Optical microscope image of Si_3N_4 ring resonator integrated with CVD-grown MoS_2 thin film. Purplish region on the right side of ring resonator is patterned MoS_2 thin film. (c) Optical image of Si_3N_4 waveguide covered with MoS_2 thin film. The devices were made using conventional planar processing, combined with low-temperature, large-area TMD synthesis methods as described in Section 2.2.1.

results of molecular dynamics simulations by Hong *et al.* are suggestive, it is unlikely that the reaction mechanism at-play here is exactly the same as that studied previously, because the gas species and the solid-state boundary conditions are different [138]. Further theoretical and experimental research is needed to determine the exact reaction mechanism by which O_2 accelerates 2H-MoS_2 formation by Mo metal sulfurization in H_2S gas. O_2 gas also affects the MoS_2 film orientation, allowing vertically- and horizontally-oriented films to be made at less than 400 °C. We tentatively attribute this effect to O_2 etching, and its effect on crystal nucleation density. Previous studies have shown that the orientation of MoS_2 films made by metal sulfurization can be affected by Mo metal thickness, but this strain-mediated effect seems unlikely here because the precursor metal film thickness was maintained [147]. The control of orientation of MoS_2 crystallites on a highly-conductive Mo film and by low-temperature processing may be useful for applications of MoS_2 in heterogeneous catalysis and electrochemistry. The two-step process produces films that are smooth and continuous. The process relies on PVD and gas-source sulfurization, and therefore is inherently scalable to wafer-scale and compatible with industrial coating. The crystal quality (*e.g.* grain size) of MoS_2 films made by metal sulfurization likely will

never match that of films obtained by high-temperature MOCVD. However, the two-step approach may be of interest for applications where cost, flexibility, throughout, and large-area uniformity are higher priorities than crystal quality. Further research on catalysts for the formation of MoS_2 and other TMDs by metal sulfurization at low temperature may create new possibilities for industrial applications, such as electrochemical hydrogen evolution [112, 113]. The films studied here are thick, to allow us to distinguish the kinetics of mass transport from the kinetics of sulfurization and 2H-MoS_2 crystallization. It will be interesting to extend this research to the processing of monolayer and few-layer MoS_2 films, and to explore the device fabrication possibilities enabled by large-area and low-temperature MoS_2 coatings.

2.5 Supplementary Information

2.5.1 Sample Processing Information

Table 2.3: **Parameters of Raman peaks for MoS_2 films sulfurized with varying process temperature and O_2 flow extracted from Figure ??.**

$T_{processing}$(°C)		350		375	
Peak		$E_{2g}{}^1$	A_{1g}	$E_{2g}{}^1$	A_{1g}
Peak position (cm^{-1})		378.8±0.5	407.7±0.5	378.7±0.4	407.6±0.4
Width (cm^{-1})	0 O_2	7.93	7.54	6.37	6.53
	1 O_2	6.19	6.54	7.74	7.48
	5 O_2	4.92	6.33	7.46	6.92
	10 O_2	6.62	7.01	7.92	7.24
$T_{processing}$(°C)		400		500	
Peak		$E_{2g}{}^1$	A_{1g}	$E_{2g}{}^1$	A_{1g}
Peak position (cm^{-1})		378.9±0.8	407.6±1.7	378.6±0.6	408.5±1.4
Width (cm^{-1})	0 O_2	7.39	7.25	8.66	7.61
	1 O_2	8.34	8.78	8.96	7.23
	5 O_2	6.65	5.61	8.82	7.89
	10 O_2	8.77	7.02	7.46	9.86

Table 2.4: **Estimated average crystallite size calculated by the Williamson-Hall plot (used pseudo-Voigt fitting). The broadening of XRD peak is attributed to crystallite size and microstrain. Here, we take only size factor into account but exclude micro-strain.**

$T_{process}$ (°C)	O_2 flow rate (sccm)	Crystallite size (nm)
375	0	5.8
	10	7.1
400	0	6.3
	5	5.1
500	0	6.5
	5	5.5

Table 2.5: **Experimental conditions we have carried out to test our hypothesis in chapter 2.**

Sample name	Precursor Mo thickness	Sulfurizing temperature (°C)	O_2 flow rate (sccm) (with 20sccm H_2S)
$CVDMoS_2$_350°C_noO_2 _(16nm or 34nm)Mo	16 or 34nm	350	0
$CVDMoS_2$_350°C_1O_2 _(16nm or 34nm)Mo			1
$CVDMoS_2$_350°C_5O_2 _(16nm or 34nm)Mo			5
$CVDMoS_2$_350°C_10O_2 _(16nm or 34nm)Mo			10
$CVDMoS_2$_375°C_noO_2 _(16nm or 34nm)Mo		375	0
$CVDMoS_2$_375°C_1O_2 _(16nm or 34nm)Mo			1
$CVDMoS_2$_375°C_5O_2 _(16nm or 34nm)Mo			5
$CVDMoS_2$_375°C_10O_2 _(16nm or 34nm)Mo			10
$CVDMoS_2$_400°C_noO_2 _(16nm or 34nm)Mo		400	0
$CVDMoS_2$_400°C_1O_2 _(16nm or 34nm)Mo			1
$CVDMoS_2$_400°C_5O_2 _(16nm or 34nm)Mo			5
$CVDMoS_2$_400°C_10O_2 _(16nm or 34nm)Mo			10
$CVDMoS_2$_500°C_noO_2 _(16nm or 34nm)Mo		500	0
$CVDMoS_2$_500°C_1O_2 _(16nm or 34nm)Mo			1
$CVDMoS_2$_500°C_5O_2 _(16nm or 34nm)Mo			5
$CVDMoS_2$_500°C_10O_2 _(16nm or 34nm)Mo			10

2.6 Contribution Statements

Changming Wu in Mo Li's group at University Washington fabricated ring-resonator and MZI consisted of Si_3N_4 waveguide. Skylar Deckoff-Jones in JJ Hu's group at MIT fabricated planarized waveguide. Yifei Li calculated refractive index of monolayer and bulk MoS_2 using DFT. Akshay Singh measured refractive index of bulk MoS_2 using spectroscopic ellipsometry. Abinash Kumar in James LeBeau's group at MIT performed STEM, HRTEM and CBED.

Chapter 3

Processing of Large Area of TiS_2 Films: Oxygen as Inhibitor

This chapter is reproduced from ref. [60].

Li, Y., Singh, A., Reidy, K., **Jo, S.S.**, Ross, F., Jaramillo, R., "Making Large-Area Titanium Disulfide Films at Reduced Temperature by Balancing the Kinetics of Sulfurization and Roughening", *Adv. Funct. Mater.* **30**, 2003617 (2020), with the permission of Wiley.

3.1 Project Introduction

We have discussed the role of O_2 on MoS_2 formation, which enhanced crystallization of MoS_2 at low concentration of O_2 gas in Chapter 2. However, different transition metal dichalcogenides (TMDs) show different processing challenge. In this Chapter, we will discuss the opposite role of O_2 as a reaction inhibitor in TiS_2 formation. Also, our effort to reduce oxygen background will be described in details.

TMDs feature strong light-matter interaction and a panoply of polymorphs, and therefore are intriguing for development as phase-change materials for integrated photonics applications [3, 23, 103]. Utilizing TMDs in integrated photonic circuit technology will require reliable methods to make and pattern large-area and uniform thin

films. It is also desirable to limit the TMD film processing temperature. TMD film deposition methods often require high temperature, due to various factors, including the high melting point of refractory transition metals, and the often-sluggish kinetics of replacing metal-oxygen bonds by metal-chalcogen bonds (MoS_2 is a notable exception to this trend) [47]. Lower process temperature may be essential for integration to avoid thermal damage to other materials and structures, especially for vertically integrated devices where other low-dimensional materials can be interfaced [148, 149]. Lowering the process temperature may also widen the scope of materials available through alloy design. We suggested that alloys of transition metal sulfides, such as $(Mo,Ti)S_2$, may be attractive as phase-change materials [3]. Stabilizing TMD alloys and avoiding segregation during growth further motivates the drive toward lower processing temperature.

3.2 Experimental Methods

We deposit precursor Ti thin films (thickness < 10 nm) by AJA international Orion 5 magnetron sputtering (base pressure 10^{-5} Torr) on Si/SiO_2, SiN and sapphire substrates. Titanium oxidizes quickly, even in the high vacuum environment of physical vapor deposition (PVD) tools. Therefore, our precursor films are chemically TiO_x, and with roughness approximately 3 Å. We measure precursor film thickness during deposition using a quartz crystal monitor (QCM), using settings for Ti metal, and post-deposition using X-ray reflectivity (XRR) on a Bruker D8 diffractometer. Each of these methods is subject to systematic errors: for QCM we use the material parameters for Ti metal, lacking reliable parameters for TiO_x, whereas XRR data analysis can be complicated by finite film roughness and thickness-dependent layer density. We perform sulfurization in a hot-wall tube furnace reactor at atmospheric pressure, in a flow of between 20 – 100 sccm H_2S and 0 – 200 sccm forming gas (5% H_2, 95% Ar), at temperature up to 900 °C. We use an assortment of techniques including modification of equipment, process, and samples to control the level of trace oxygen in the furnace, and we measure the oxygen level using an electrochemical sensor (Southland

Sensing TO2-1x ppm). We characterize the elemental composition of our films using X-ray photoelectron spectroscopy (XPS, Thermo Scientific K-alpha$^+$, Al Kα source). We determine phase by Raman spectroscopy (Renishaw Invia Reflex Micro Raman) with excitation wavelength 532 nm. We use atomic force microscopy (AFM, Veeco Dimension 3100) to characterize film morphology. We perform transmission electron microscopy (TEM) measurements in both plan view and cross-section geometry. For plan view measurements we grew samples directly on a TEM grid with 50 nm-thick amorphous SiN membranes (Norcada), and we imaged samples using a 200 kV field-emission TEM (JEOL 2010F). For cross-sectional TEM, we prepare samples using a focused ion beam (Helios Nanolab), as described elsewhere [150].

3.3 Results and Discussion

3.3.1 Effect of Temperature and Oxygen Background

We report the synthesis of large-area TiS_2 films using a two-step method of metal deposition by PVD, followed by sulfurization in H_2S gas in a hot-wall tube furnace reactor. This approach is reliable and scalable, since it uses industrially-compatible methods that are easy to implement for large wafers. However, Ti metal is extremely prone to oxidation, and Ti metal films deposited by PVD are more accurately described as TiO_x. Therefore, competition between S and O for Ti bonding orbitals is a central issue.

In Figure 3-1 we show the crystal structures of 1T-TiS_2, selected Ti oxides, and Ti metal. We also show a Richardson-Ellingham diagram for the Ti-O and Mo-O systems. This diagram highlights the extremes of oxygen activity control that are required to avoid Ti oxidation. In contrast, molybdenum oxide does not present an obstacle to the formation of 2H-MoS_2, and may even be a catalytic intermediate [59, 135, 138]. The Richardson-Ellingham diagram represents thermodynamic equilibrium and does not consider TMDs as competing phases, whereas thin film processing is inherently non-equilibrium, and the reacting components in our pro-

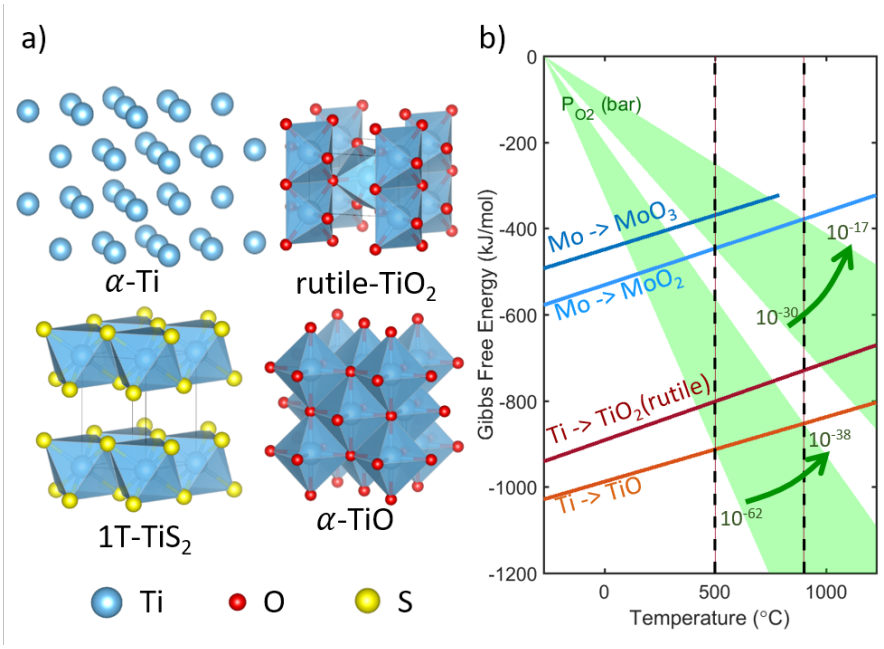

Figure 3-1: **The challenge of out-competing Ti oxidation to make TiS_2 films.** (a) Crystal structures of α-Ti, 1T-TiS_2, α-TiO, and rutile-TiO_2 [5–7]. (b) Richardson-Ellingham diagram illustrating the extreme low values of oxygen activity (represented here by P_{O_2}, labeled in green) needed to suppress Ti oxidation. We also show data for Mo oxidation.

cess include Ti, O, S, and H. Therefore, the oxygen partial pressures indicated in the Richardson-Ellingham diagram are not likely achieved in our process, even in close vicinity to the reacting film. Nevertheless, the Richardson-Ellingham diagram portrays the substantial barrier that Ti-O bonds pose for TiS_2 formation.

In general, high temperature and a highly-reducing environment are needed to substitute S for O and form TiS_2 [57, 151, 152]. In addition to problems with integration, high temperature can lead to film breakup through coarsening, resulting in rough and non-continuous films. Here we find that the process temperature for TiS_2 film formation can be systematically reduced by lowering the level of trace oxygen in the sulfurization process. We are able to achieve large-area and uniform films of 1T-TiS_2 at process temperature as low as 500 °C, with further gains likely through continued improvement in oxygen control.

In Figure 3-2 and Figure 3-3 we show characterization of a typical TiS_2 film sulfurized at 600 °C. For this film the precursor thickness was 3 nm, measured by QCM, and

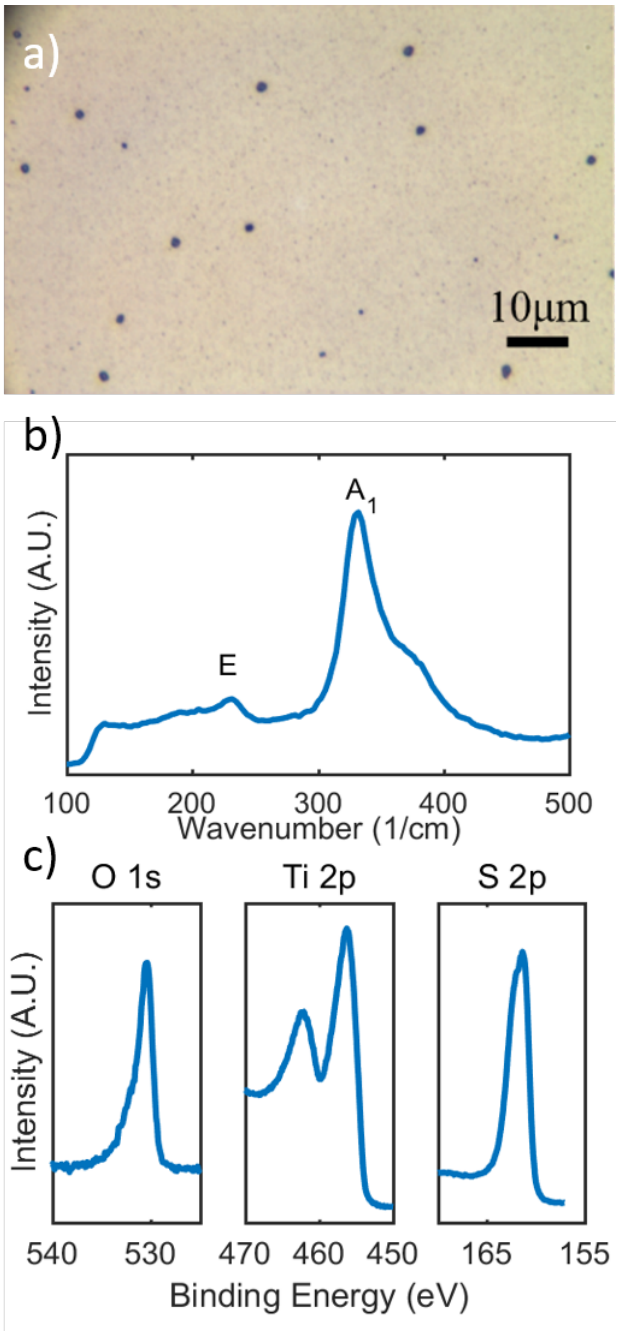

Figure 3-2: **Characterization of a typical TiS_2 film sulfurized at 600°C and $P(O_2) = 40$ppm.** (a) Optical micrograph. (b) Raman spectra showing characteristic modes E and A_1. (c) XPS spectra measured on ion-beam cleaned surface. The Ti 2p and S 2p scan confirm the existence of TiS_2, but the O 1s scan indicates substantial oxygen content remaining.

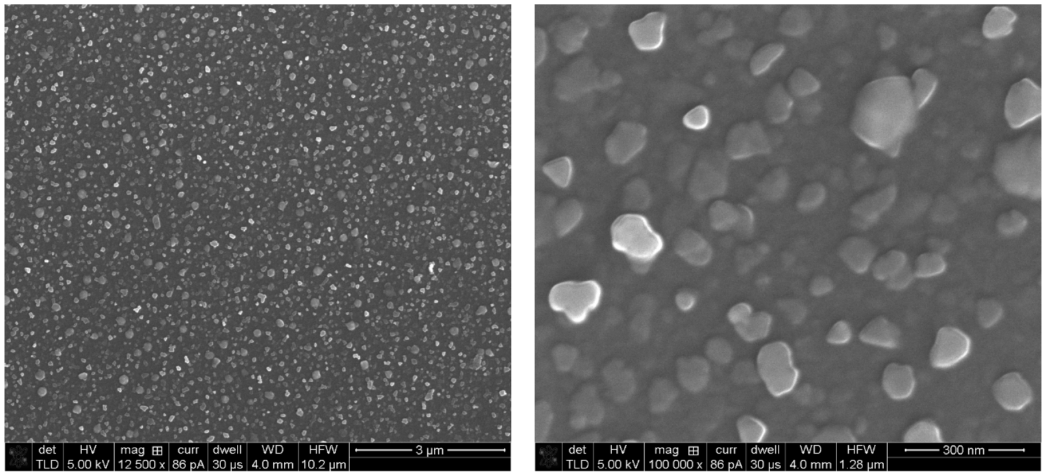

Figure 3-3: SEM images of a TiS_2 film TiS_2_190814, at two magnifications. The film was sulfurized at 600 °C and $P(O_2) = 40$ ppm.

the final TiS_2 film thickness was 10 nm. The characteristic Raman peaks corresponding to the E (332 cm^{-1}) and A_1 (230.5 cm^{-1}) phonons of 1T-TiS_2 are well-defined, and we observe no Raman peaks from competing phases, including the tri-sulfide TiS_3 that sometimes results from low-temperature synthesis [153]. XPS spectra show that the film consists of Ti and S with ratio about 1:2, but also indicate a significant level (*ca.* 10 at. %) oxygen remaining in the film. Since no second crystalline phase is recognized by Raman, XRD, or TEM (below), the oxygen may be incorporated as defects in TiS_2, or in intergranular, amorphous regions. Quantifying the oxygen-to-sulfur ratio using XPS data results in substantial overestimating systematic error, due to differential re-sputtering during depth profiling, and also due to the near-100 % sticking coefficient of background oxygen in the XPS chamber, which is significant even at ultra-high vacuum [154]. The film morphology depends strongly on the sulfurization temperature. Higher-temperature sulfurization results in substantial grain growth and eventually to the formation of disconnected TiS_2 crystals. Lower-temperature sulfurization preserves the planar morphology, and results in smaller grains and smoother films.

We find that lowest-achievable sulfurization temperature depends strongly on the level of trace oxygen in the sulfurization process. Therefore, the process temperature and film morphology depend strongly on the oxygen background. In order to reduce

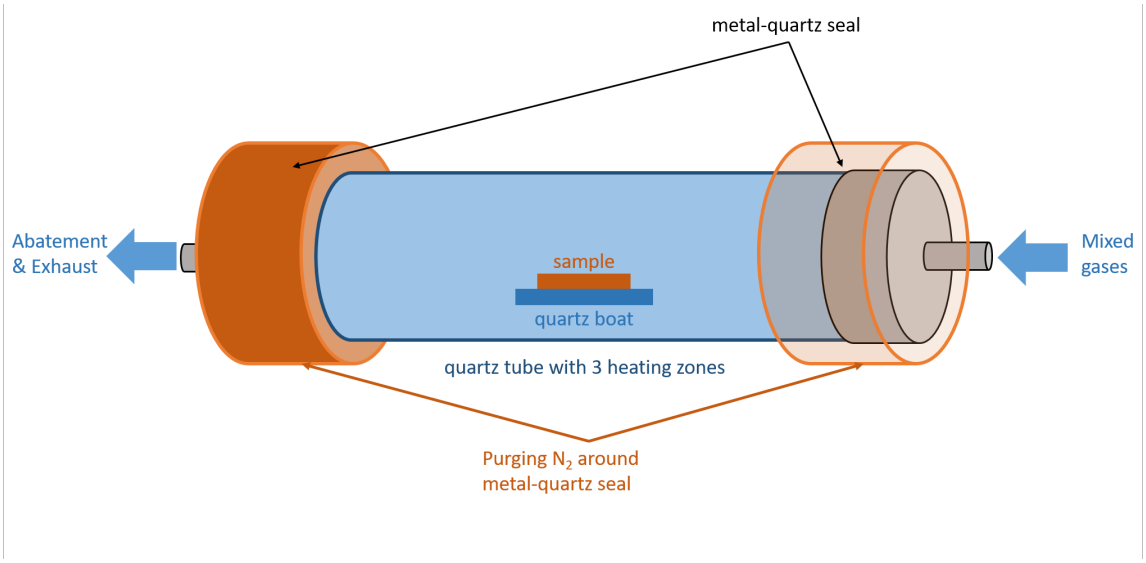

Figure 3-4: **Schematic of sulfurization furnace, including N_2 gas jackets around metal-quartz seal.** N_2 gas constantly flows into the N_2 gas jackets during processing to inhibit oxygen in the air from leaking into our tube furnace system.

oxygen background in our CVD system, we examine that oxygen is mainly leaking around CVD flanges. By installing customized nictrogen jacket, we dramatically decrease oxygen concentration from 4400 ppm to 25 ppm. Figure 3-4 shows the schematic of customized design of our tub furnace CVD system.

In Figure 3-5 we show results of TiS_2 films sulfurized at three different temperatures, between 900 °C and 500 °C and three different oxygen background concentrations, between 4400 and 25 ppm. With a background oxygen concentration of 4400 ppm, a high temperature of 900 °C is required for sulfurization and TiS_2 formation, resulting in substantial coarsening. The resulting sample is no longer a film but a series of isolated TiS_2 particles (Figure 3-5a), and the Raman spectra are position-dependent (Figure 3-5d and Figure 3-6).

We can reduce the background oxygen concentration by installing N_2 gas jackets around the compression seals on our tube furnace, to reduce the O_2 leak rate from the atmosphere. We also deposit a thin gas barrier layer of Mo metal (1 nm) on top of the Ti metal (3 – 10 nm) precursor, in the same deposition chamber, to reduce the rate of Ti metal oxidation during sample transfer. With these changes, the background oxygen concentration is 200 – 1000 ppm (varies throughout the sulfurization process),

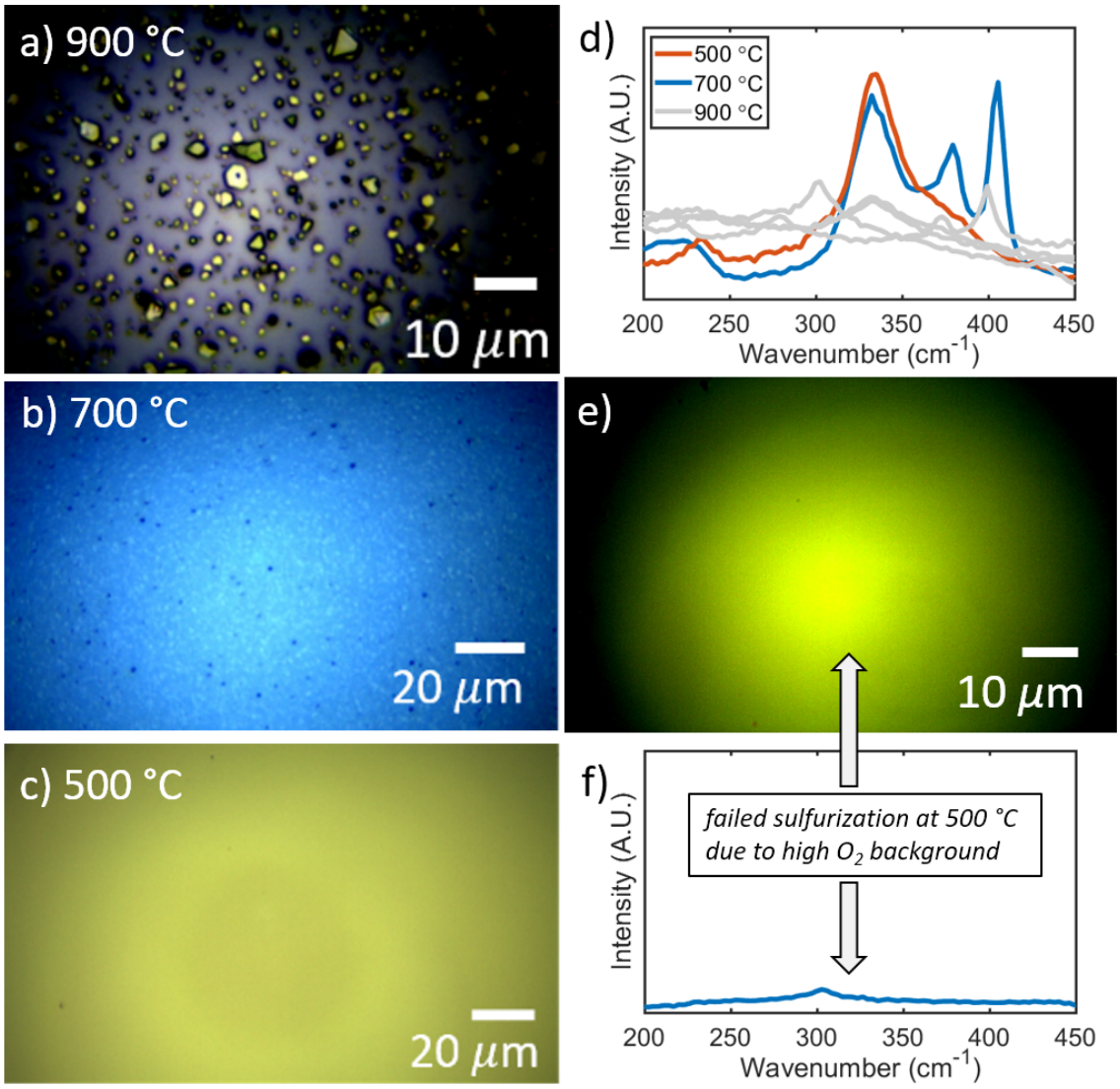

Figure 3-5: **Lowering the sulfurization temperature - thereby improving film morphology – by reducing background oxygen concentration.** (a-c) Optical micrographs of samples sulfurized in three different conditions. (a) Sulfurization at 900 °C for 24 h results in growth of discontinuous, faceted 1T-TiS_2 crystallites. (b) Sulfurization at 700 °C for 2.5 h results in a continuous film with particles visible. (c) Sulfurization at 500 °C for 4 h results in an optically-smooth film. (d) Raman spectra for the samples shown in (a-c). The spectra for the sample processed at 900 °C is position-dependent; we present data from several positions. The MoS_2 peaks (380 and 405 cm^{-1}) for the samples processed at 700 °C and 900 °C are due to the use of a Mo gas barrier layer. (e) Optical micrograph and (f) Raman spectra showing failure of sulfurization at 500 °C for 4 h with insufficiently-reduced O_2 background. The color differences between the different micrographs is due to slightly different film thickness, and lamp changes between experiments.

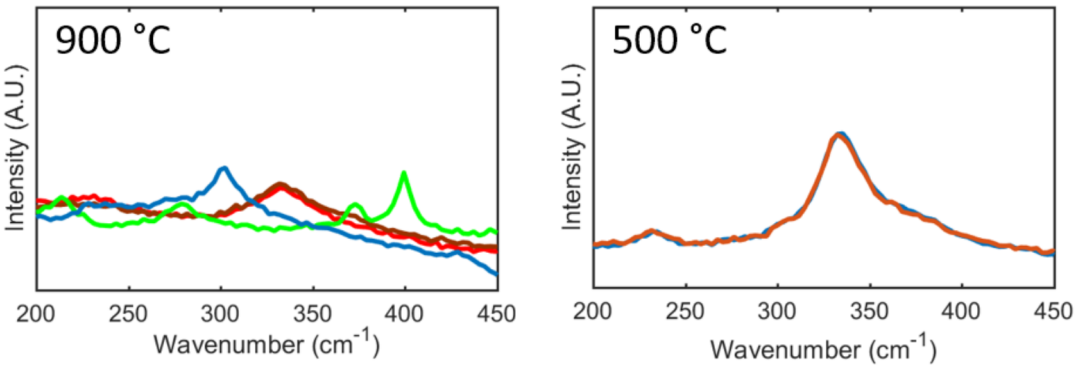

Figure 3-6: Raman spectra measured at multiple points on the same samples shown in Figure 3a-c. The sample sulfurized at 900 °C shows spatial heterogeneity (obvious from the optical micrograph), while the sample sulfurized at 500 °C is uniform

and we can achieve sulfurization at 700 °C. The resulting film is continuous, although sizeable particles are visible under an optical microscope (Figure 3-5b). The Raman spectra confirms the presence of 1T-TiS_2 and 2H-MoS_2, as expected (Figure 3-5d). We can further reduce the background oxygen concentration by extensive purging of the tube before heating, and co-flowing forming gas with H_2S during sulfurization. With these changes, the background oxygen concentration is 25 ppm, and we can achieve sulfurization at 500 °C. In Figure 3-5c-d we present results for a film sulfurized at 500 °C without a Mo barrier layer. The film is optically-smooth and the Raman spectra confirm the 1T-TiS_2 phase. For comparison we also present results for a film sulfurized at 500 °C without the described steps to reduce background oxygen concentration. In this case the TiO_x precursor film remains smooth (Figure 3-5e) and the Raman spectra show no signature of TiS_2 (Figure 3-5f). The results presented in Figures 3-1 and 3-5 clearly show that reducing background oxygen is an effective route to producing large-area and uniform TiS_2 thin films by metal sulfurization.

3.3.2 Role of Mo Barrier Layer

We also note that the Mo barrier layer, used for the sample sulfurized above 700 °C as reported here, is no longer needed to assist TiS_2 formation for sulfurization temperature below 600 °C. This implies that the role of the Mo barrier layer is to slow the formation of new Ti-O bonds in the furnace during sulfurization, rather than

to slow Ti oxidation during sample transfer. For sufficiently low background oxygen concentration in the sulfurization furnace, this barrier layer is no longer needed.

3.3.3 Effect of Precursor

The background oxygen concentration present in the tube furnace is a prime factor in determining the sulfurization results, but details of the TiO_x precursor film are also important, especially the thickness. We measure precursor film thickness by QCM (using settings for Ti metal) during Ti deposition, and by XRR post-deposition. The roughness of the resulting TiS_2 film depends proportionally on the precursor film thickness. We found that for precursor films 1 and 5 nm thick (measured by XRR), sulfurized at 600 °C, the resulting TiS_2 film roughness was 1.7 and 7.6 nm, respectively. For precursor films 3 and 5 nm thick (measured by QCM), sulfurized at 700 °C, the resulting TiS_2 film roughness was 7.2 and 10.3 nm, respectively. These results are consistent with expectations that smoother TiS_2 films result from lower sulfurization temperature and thinner precursors. For the results presented in Figures 3-2 - 3-7, the precursor films were between 3 – 5 nm thick. Raman measurements on the precursor film show no evidence for crystallized Ti or TiO_2; the phase composition is likely a mixture of nanocrystalline Ti and amorphous Ti oxide. Ti oxides (*e.g.* α-TiO and r-TiO_2, shown in Figure 3-1) are non-layered structures built from TiO_6 octahedra, and we assume the same of amorphous Ti oxides [155, 156]. XPS depth profiling suggests that the Ti:O ratio in the precursor film is 1:2 at the surface, but closer to 1:1.5 beneath the surface. This is consistent with TiO_x forming during deposition, and only the topmost surface fully oxidizing to TiO_2 upon air exposure.

3.3.4 Mechanism of Sulfurization and Film Roughening

We turn to TEM to understand the mechanism of sulfurization and film roughening. In Figure 3-7 we show plan views of a film sulfurized at 600 °C and a cross-section view of a film sulfurized at 700 °C. The plan view data show complete coverage, with mostly-flat areas interrupted by vertically-oriented crystallites growing out-of-plane

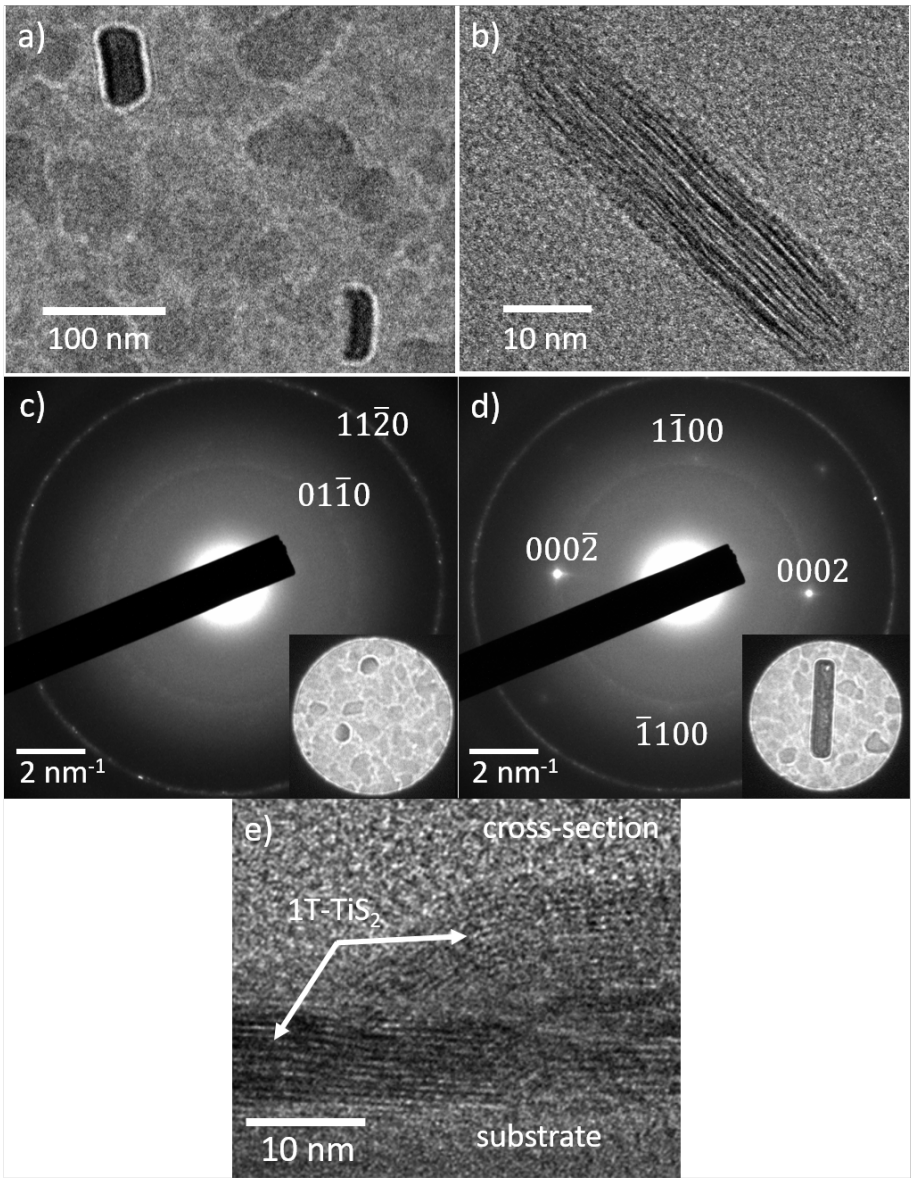

Figure 3-7: **TEM study of 1T-TiS_2 films.** (a-d) Film approximately 10 nm thick, sulfurized at 600 °C for 3 h; the precursor film was 3 nm thick (Ti metal thickness, measured by QCM). (a) Low-magnification plan view shows mostly-flat regions interrupted by vertical outgrowths. (b) High-resolution plan view of a vertically-oriented crystallite. (c) Diffraction pattern of a mostly-flat region of the film (inset). The indexed diffraction rings are consistent with in-plane (0001) texture of the grains. (d) Diffraction pattern a region including a vertically-oriented crystallite (inset). The discrete spots originate from the vertically-oriented crystallite and are consistent with the 1T-TiS_2 phase. The rings originate from the surrounding, mostly-flat film. The diffraction indices correspond to the spots; the ring index assignments are the same as in (c). (e) High-resolution cross-section view of a 1T-TiS_2 film sulfurized at 700 °C for 3 h.

(Figure 3-7a-b). The selected-area electron diffraction (SAED) pattern measured on a mostly-flat region without vertical crystallites (Figure 3-7c) shows $\{01\bar{1}0\}$ and $\{11\bar{2}0\}$ diffraction rings, suggesting that these mostly-flat regions have (0001) in-plane texture, with the basal plane lying flat on the substrate. SAED measured on a vertical crystallite (Figure 3-7d) shows bright single-crystals diffraction spots from the crystallite, in addition to the rings from the surrounding flat regions. The pair of brightest reflections correspond to a d-spacing of 2.85 Å and we index as the $\{0002\}$ diffraction spots with expected spacing. The absence of $\{0001\}$ spots may result from thickness, tilting effect, or a high concentration of stacking faults, corresponding to imperfect registry of adjacent monolayers [157]. The $(1\bar{1}00)$ and $(1\bar{1}02)$ diffraction spots are also apparent. In Figure 3-7e we present a cross-section view that includes a crystallite lying flat on the substrate, and slightly protruding crystallites with different orientations, extending to approximately twice the height of the flat crystallite; this view is typical of the mostly-flat regions, excluding the tall, vertical crystallites and is consistent with the in-plane texture described above. The TEM data therefore indicate a mostly-flat 1T-TiS_2 film, with crystallites of sub-100 nm lateral width lying mostly flat on the substrate, interrupted occasionally by vertically-oriented crystallites that grew out-of-plane. The TEM data provide an explanation for the process by which films roughen during sulfurization. The low surface energy of the basal planes provides a thermodynamic driving force for (0001) texture. This is counteracted by the in-plane stress experienced during the formation of TiS_2 (volume 34.78 cm^3 per mole of Ti) from titanium oxide (18.88 cm^3 per mole of Ti for rutile TiO_2). Furthermore, crystal growth is expected to occur fastest at the layer edges. Therefore, crystallites that nucleate randomly with vertically-oriented edges experience accelerated growth, due to preferential edge growth (kinetic roughening), and to relieve the in-plane stress of the sulfurizing film. In Figure 3-8 we provide a series of simplified illustrations to describe TiS_2 film formation by sulfurzation.

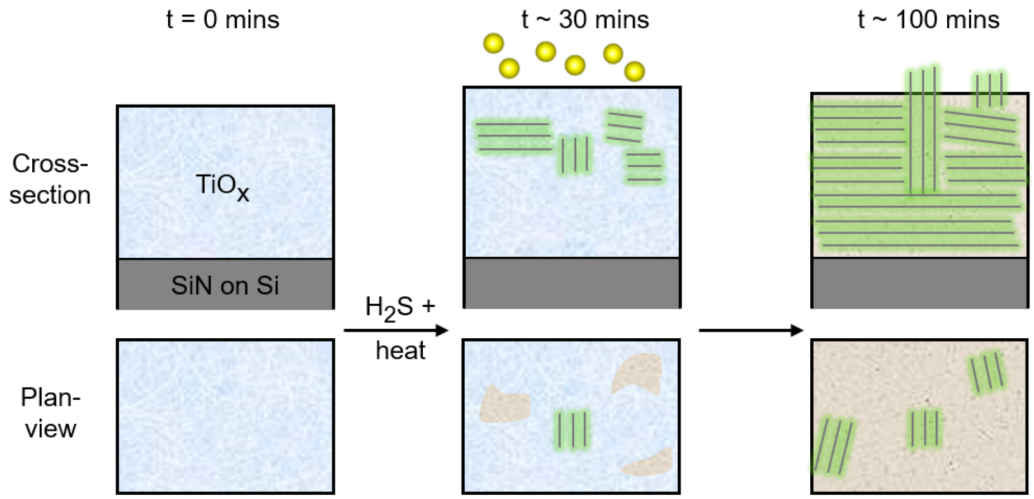

Figure 3-8: Schematic of TiS_2 film formation by sulfurization, visualized in cross-section and plan-view geometry. The concentration of vertically-oriented crystallites is exaggerated for illustration purposes.

3.4 Conclusion

We conclude that film roughening during sulfurization results from the nucleation and growth of TiS_2 crystallites with initially-random orientation, under the competing influences of a preferred orientation, film stress, and anisotropic growth kinetics. Nucleation and growth of TiS_2 requires overcoming the kinetic barrier of replacing Ti-O bonds by Ti-S bonds. With high oxygen background levels this kinetic barrier is persistent, and requires high sulfurization temperature to overcome. Lower oxygen background levels enable lower sulfurization temperature, presumably by lowering the rate at which new Ti-O bonds form during phase transformation.

Here we synthesized large-area, single-phase 1T-TiS_2 films via a two-step method with sulfurization temperature as low as 500 °C. Based on the trends that we report, we expect that lower-temperature processing should be achievable through further reduction in O_2 background levels, and perhaps also by reducing the oxygen content in the TiO_x precursor film. We also predict that film roughness could be further reduced by lowering the sulfurization rate, for instance by reducing the H_2S process gas pressure.

Low-temperature film processing is desirable for integration and for stabilizing designer alloys. It is not a likely route to make single crystal films. Therefore, devices

requiring single crystal TMD layers – such as transistors or quantum emitters – may rely on layer transfer to enable integration, since the TMD growth conditions are rather extreme. However, for many technologies, polycrystalline films do not present an obstacle. For refractive, sub-band gap applications in integrated photonics, such as phase-modulators, chemical purity that controls sub-band gap absorption may be more important than grain size. Besides integrated photonics, the approach that we develop here for film deposition may be useful for optical meta-materials, tribology, and electrochemistry.

3.5 Supplementary Information

3.5.1 Additional Design to Reduce Oxygen Concentration in CVD System

I describe how and how much we lower the oxygen background in our tube furnace system in chapter 3. Here I report the detailed design of the nitrogen jacket. The nitrogen jacket consists of three parts, including main body of unlined paint can with lid, silicon rubber mold for tight sealing between the can and the quartz tube and nitrogen gas tube with regulator (Figure 3-9). Water jet is employed to make holes on the lid, one for a feed-through at the center (d $\approx$ 1.92cm) and three more for screws around the flange (d $\approx$ 0.92 cm) as illustrated in Figure 3-9a. SBR rubber push-in grommet of d $\approx$ 1.92cm is used for the hold at the center to tightly seal around the feed-through. We also water jet out a hole of d 0.4 cm on the side wall where is close to the flange, for a push-to-connect tube fitting which is eventually connect with a gas tube and a regulator (Figure 3-9b). The bottom part of the can is cut with Dremels and the silicon rubber mold is placed to make sealing around the tube. Figure 3-10 shows how the nitrogen jacket is incorporated into the system. During the growth process, nitrogen gas constantly flows into the nitrogen jacket to prevent oxygen in the air from leaking into the tube. The gas pressure of nitrogen gas is controlled by a simple valve regulator without gas gauge.

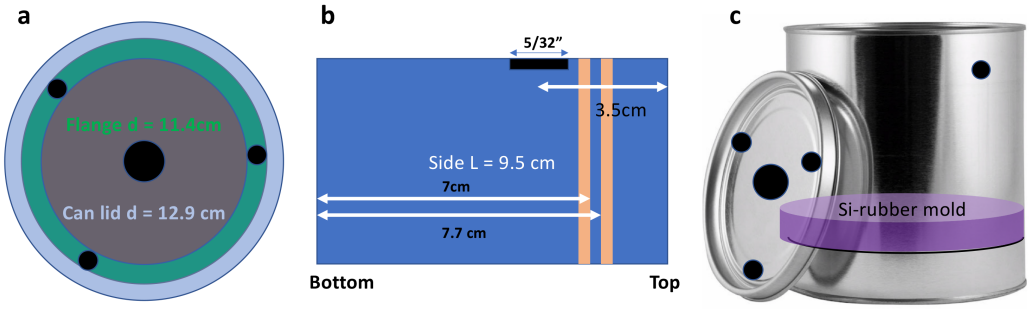

Figure 3-9: **Mechanical drawing of the nitrogen jacket.** (a) Top view of the can lid. The outer diameter of can and flange is 12.9 cm and 11.4 cm, respectively. (b) Side view of the paint can. The orange parts show where the vacuum flange is located. (c) A photo preview with illustrations. The black line shows where to cut the can with Dremels.

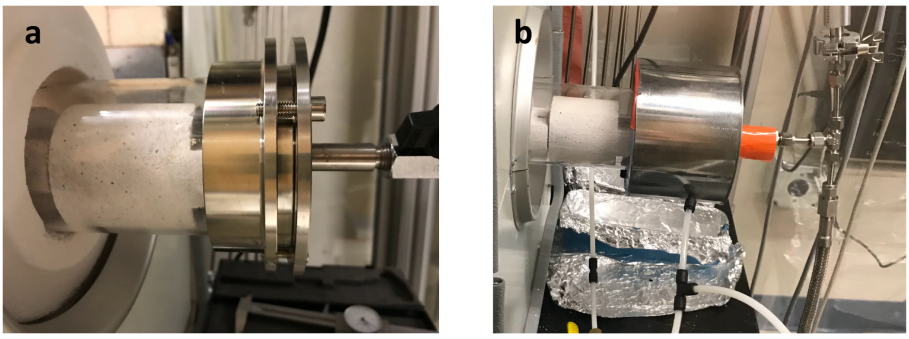

Figure 3-10: **Photograph of the flange of CVD furnace.** (a) Before and (b) after installing the nitrogen jacket around the flange where is the leaking point.

3.6 Contribution Statements

Yifei Li and Akshay Singh designed the idea and synthesized TiS_2 film and characterized with Raman and XPS. Kate Reidy in Frances Ross's group at MIT carried out TEM and electron diffraction measurement.

Chapter 4

Process-Dependent Native Oxide Metrology using Spectroscopic Ellipsometry: Native Oxidation in Ambient Condition

This chapter is reprinted with permission from ref. [158].

Jo, S.S., Singh, A., Yang, L., Tiwari, S.C., Hong, S., Krishnamoorthy, A., Sales, M.G., Oliver, S.M., Fox, J., Cavalero, R.L., Snyder, D.W., Vora, P.M., McDonnell, S.J., Vashishta, P., Kalia, R.K., Nakano, A., Jaramillo, R., "Growth Kinetics and Atomistic Mechanisms of Native Oxidation of ZrS_x Se_{2-x} and MoS_2 Crystals", *Nano Lett.* **20**, 8592–8599 (2020), Copyright 2020 American Chemical Society.

4.1 Project Introduction

A thorough understanding of the processing and properties of native oxides is essential for designing semiconductor devices. This is no less true for nanomaterials than it is for legacy semiconductors such as silicon, for which control and understanding of the native oxide was a seminal achievement of 20th century materials science. Layered transition metal dichalcogenides (TMDs) nominally have inert, fully-passivated

surfaces, but it is well-known that this is an oversimplification and that many TMDs oxidize readily. As interest grows in applications of TMDs in microelectronics, photonics, and optoelectronics, so too does the importance of developing predictive materials processing methods that take into account the native oxide [3, 23, 59, 159–161]. The stability of TMDs in ambient conditions has been studied for decades [84, 85, 87, 89, 162–173]. It is known that stability against oxidation increases as the chalcogen element changes from Te, to Se, to S, and that TMDs including group-4 transition metals are particularly unstable in air [84, 162, 164]. Monolayers are less stable than few-layer and bulk crystals, but the basal surfaces of monolayer MoS_2 and $MoSe_2$ are stable against chemisorption in ambient conditions, and oxidation of few-layer WS_2 is self-limiting [85, 86, 89, 162, 165, 166, 171, 174]. Oxidation preferentially begins at defects such as chalcogen vacancies and grain boundaries, can be accelerated by illumination, and may be facilitated by organic absorbates [85, 87, 162, 163, 166, 174, 175]. The effects of humidity on oxidation have also been studied [167–170]. For instance, the oxidation rate of pulverized MoS_2 at elevated temperature has been found to depend on relative humidity and particle size [170]. It has been shown that H_2O is a milder oxidizing agent than O_2 for oxidation of epitaxially-grown monolayer MoS_2 at elevated temperature [171]. These results suggest that H_2O may be a catalyst for spontaneous oxidation in humid air. TMD oxidation has also been studied in harsh environments typical of device processing, such as exposure to ozone or etchant [169, 172, 176–178]. Here we report on the growth kinetics and atomic mechanisms of native oxidation in ambient conditions of freshly-cleaved surfaces of bulk single crystals of ZrS_xSe_{2-x} alloys and MoS_2. We find that the Zr-based TMDs oxidize readily, with the rate increasing with Se content. Meanwhile, MoS_2 seems to oxidize not at all in air on a laboratory time scale. We quantify the oxide growth rate with sub-nm resolution using spectroscopic ellipsometry (SE) [179]. SE represents an improvement in thickness resolution and measurement time over other methods used to observed TMD oxidation, such as atomic force microscopy, optical microscopy, and Raman spectroscopy [84, 89, 163, 164]. Our results are unique in quantifying oxidation of a TMD alloy series, and may be particularly useful for pro-

cessing electronic devices from Zr-based TMD nanomaterials [82]. Further, we use first principles-validated reactive molecular dynamics (RMD) simulations to illustrate the atomistic mechanism of oxidation of ZrS_xSe_{2-x}, and to understand the stability of MoS_2. We find that oxygen favorably chemisorbs on the ZrS_2 surface, and then moves readily into the crystal lattice by a mechanism of Zr-O bond switching, facilitated by successive redox transitions at the S sites. At short times, the interaction between O and S is indirect, mediated by the Zr atoms. The rate-limiting step for oxide growth is the formation and out-diffusion of SO_2. In contrast, we find the oxidation of MoS_2 is kinetically inhibited by a large energetic barrier to O_2 dissociative adsorption, even though chemisorbed oxygen is thermodynamically preferred [86]. These results are enabled by the development of a force field that can describe Zr-Mo-S-O interactions, an advance over previous work using first principles-informed RMD simulations based on ReaxFF reactive force fields to study the Mo-S-O system [180].

4.2 Experimental Methods

4.2.1 Tape-Time Processing

We study bulk crystals of ZrS_xSe_{2-x} alloys and MoS_2. ZrS_xSe_{2-x} crystals spanning the full composition range from $ZrSe_2$ (x = 0) to ZrS_2 (x = 2) are obtained by chemical vapor transport synthesis in sealed quartz ampoules using high-purity sulfur and selenium powders mixed with zirconium lump pieces. Iodine was employed as a transport agent at a concentration of 5 mg/cm^3 to facilitate the growth of cm-scale flakes. The chalcogenide source molar stoichiometry was varied to control the alloy composition. The ZrS_xSe_{2-x} binary system is isomorphic and forms a full solid solution in the 1T structure (space group: $P\bar{3}m1$, #164) [181]. We study naturally-occurring MoS_2 crystals (2H structure, space group: $P6_3/mmc$, #194) received from the Smithsonian Institution (catalog number NMNH B3306). In Figure 4-1 we show photographs of several of the crystals studied. We use adhesive tape (3M, Scotch) to create newly-exposed and oxide-free surfaces by mechanical cleaving. We affix the

freshly-cleaved crystals on the tape to a glass slide for inspection. We then use SE to monitor the native oxidation process as a function of time, from minutes to days. The entire process, from mechanical cleaving to SE measurements, is performed in typical laboratory ambient conditions: temperature ∼20 °C, and relative humidity ∼50%.

4.2.2 Characterization Method

While we carry out SE measurement, the surface of freshly exfoliated TMD films are optically smooth as well as the formed oxide are, which enables us to model the data measured by SE. Because SE requires flat and reflective surfaces. We here present surface morphology measurements on oxidized crystals, to confirm that the surfaces remain flat and uniform after the oxide formation. In Figure 4-2 and 4-3 we present scanning electron microscopy (SEM) and atomic force microscopy (AFM) data measured on ZrS_xSe_{2-x} and MoS_2 crystals that were held in ambient conditions for over ten months. The results show that the surfaces remain smooth and uniform, and therefore appropriate for SE analysis as we perform in this work.

We perform SE measurements on the (001) basal planes which are perpendicular to the optic axis by using a UV-NIR Vase ellipsometer from J. A. Woollam in the photon energy range 1.25 to 6.5 eV (wavelength range 992 to 190 nm). However, we only report results between 1.25 and 5 eV, due to large depolarization outside of this range (Figure 4-5). This ellipsometer uses an automatic rotating analyzer and an auto-retarder. We use focusing optics to generate a measurement spot approximately 300 μm in diameter, and we perform all measurements on mirror-smooth surfaces. We carry out all measurements at a fixed angle-of-incidence of 70°. TMDs are highly anisotropic, but also have very large ordinary refractive indices - they are optically very dense for light propagating perpendicular to the basal plane. As a result, incident light is refracted strongly downward inside the crystals, and our SE measurements are sensitive only to the ordinary refractive index [23]. Our samples are opaque over the photon energy range used in this study, and therefore our data are not affected by scatter from the back surface, which would require special care in analysis [3].

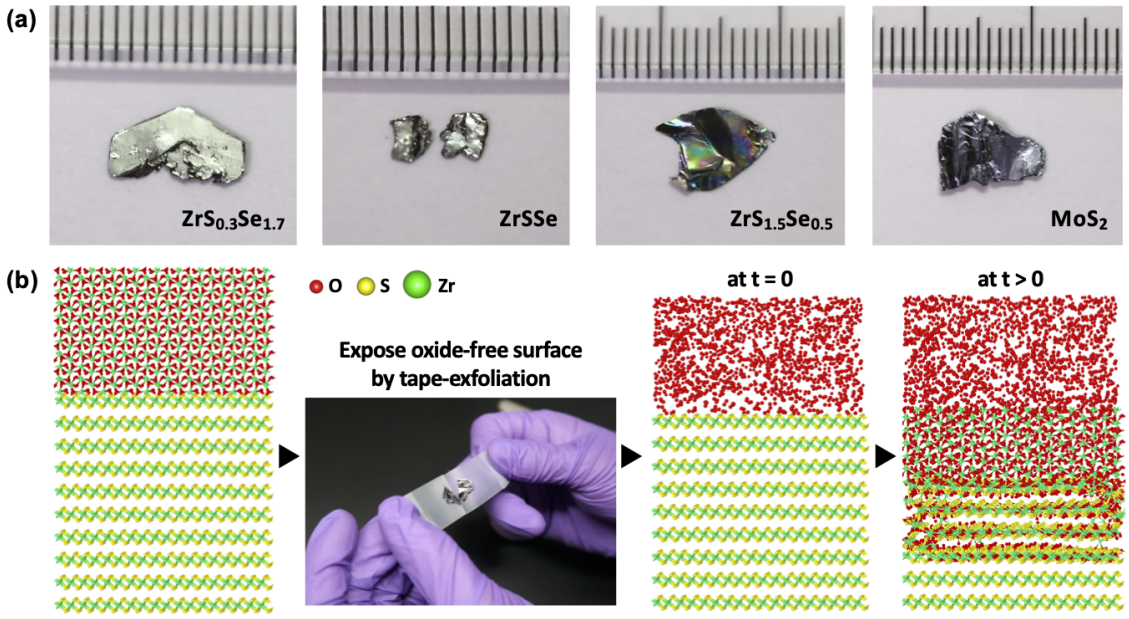

Figure 4-1: **Illustration of tape-time processing** (a) Photographs of select TMD bulk crystals used in this study; ruler gradation = 1 mm. (b) Illustration of tape-time processing for oxidation rate measurements, shown for 1T-ZrS_2. SE measurements are performed on the newly-exposed basal plane as it oxidizes.

We complement our SE experiments with X-ray photoelectron spectroscopy (XPS) measurements of an atmosphere-exposed MoS_2 surface. A geological MoS_2 crystal from SPI Supplies is mechanically cleaved and kept in a sample container. After a year in atmosphere, XPS spectra of the MoS_2 surface are obtained using a monochromated Al Kα X-ray source (1486.7 eV) at 300 W and a Scienta Omicron R3000 analyzer at a pass energy of 50 eV. The ultra-high vacuum system for XPS characterization used in this work is described elsewhere [182].

4.3 Computational Methods

4.3.1 Optical Modelling – Oxide and Surface Roughness

SE measures the complex reflectance ratio $\rho = \frac{r_p}{r_s} = tan\Psi e^{i\Delta}$; r_p and r_s are the amplitude Fresnel reflection coefficients for p- and s-polarized light, respectively, and ρ is parameterized by the ellipsometry amplitude $tan\Psi$ and angle Δ. The effective

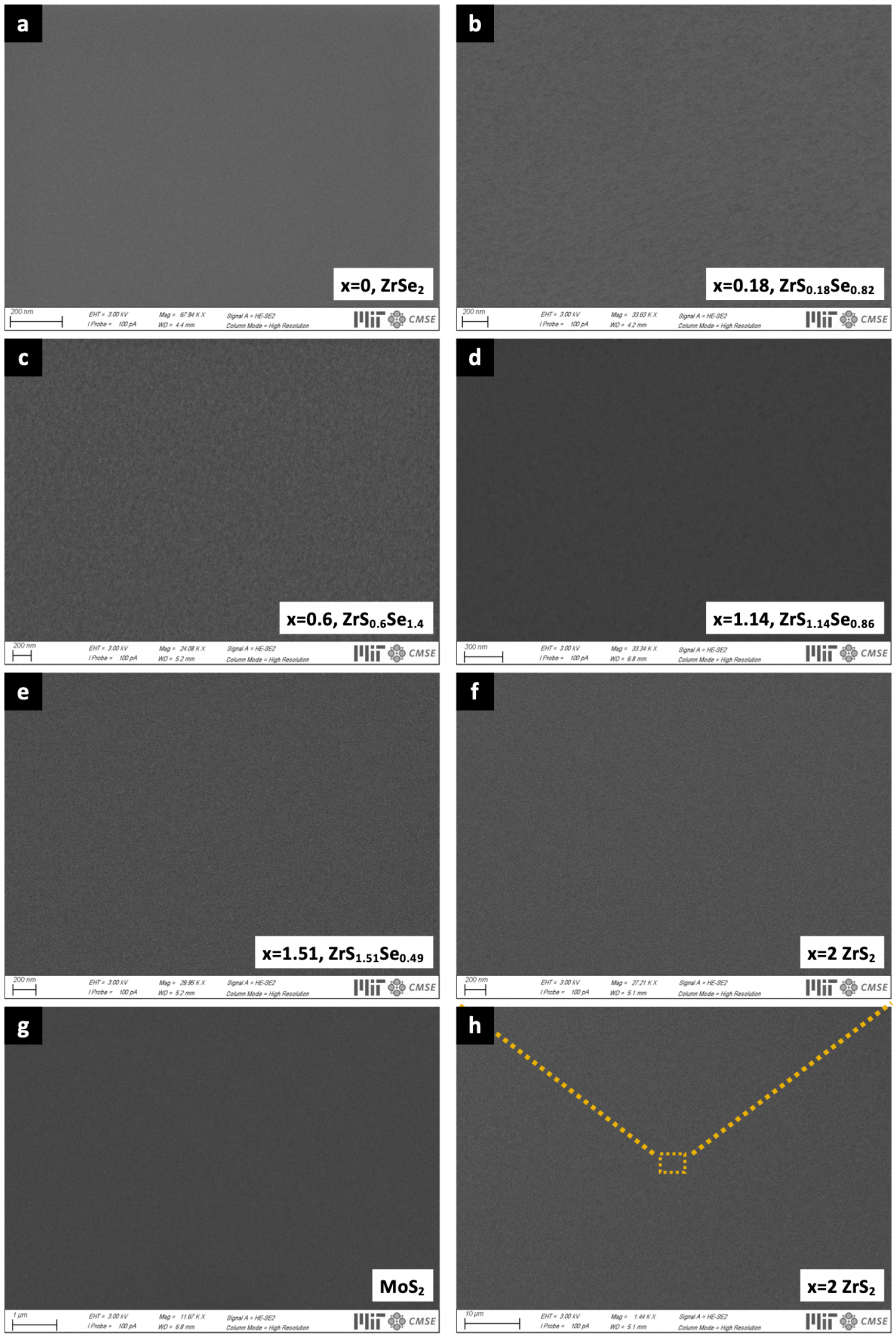

Figure 4-2: SEM images of surface morphology of ZrS_xSe_{2-x} and MoS_2 crystals kept in ambient conditions for over ten months after exfoliation. The surfaces are flat and homogenous. (f) corresponds to the dotted region in (h).

dielectric constant is determined by calculating the complex dielectric constant (ε_2^{eff}) by direct inversion of SE data, ρ and the angle of incidence (Φ): $\varepsilon_2^{eff} = sin^2(\Phi)(1 + tan^2(\Psi)(\frac{1-\rho}{1+\rho})^2)$.

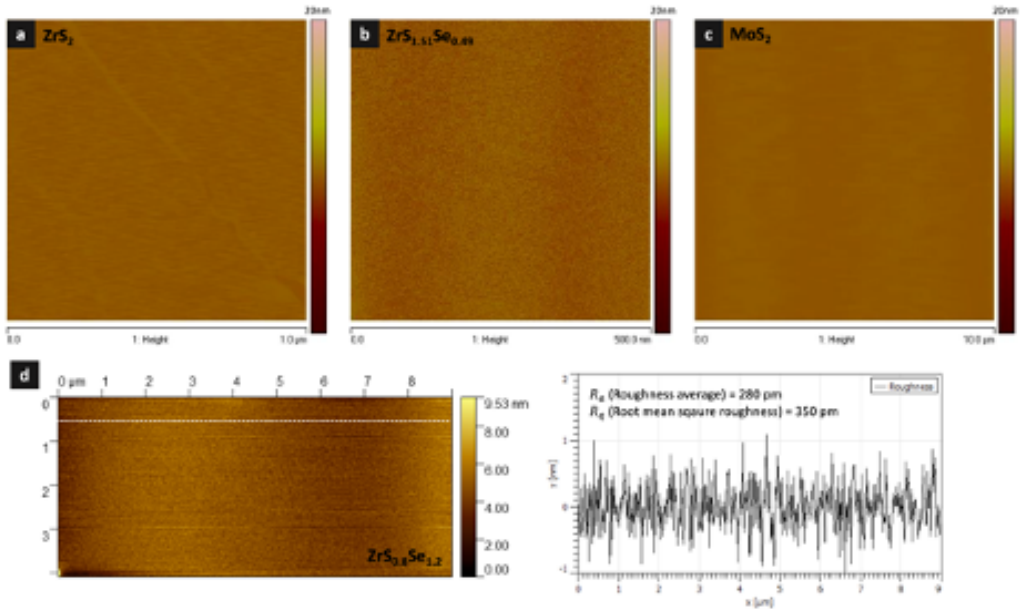

Figure 4-3: Tapping-mode AFM images of ZrS_xSe_{2-x} and MoS_2 crystals showing smooth and uniform surfaces, without island formation. The root mean square (RMS) roughness of the $ZrS_{0.8}Se_{1.2}$ surface in panel (d) is 0.35 nm; the shown profile is taken along the white dotted line.

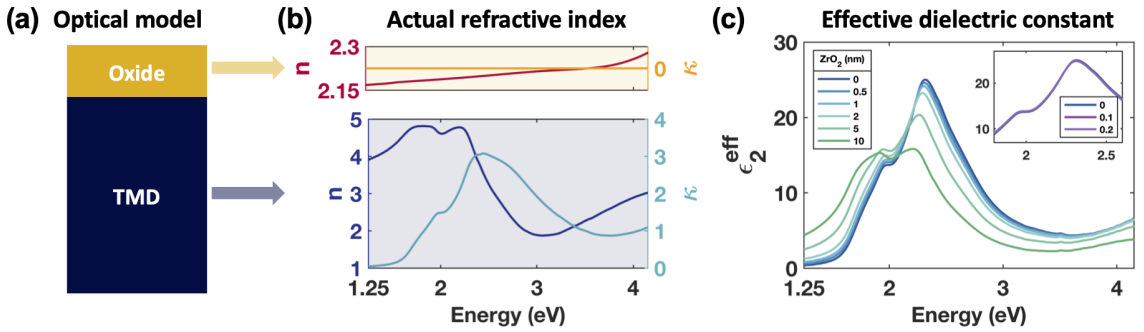

Figure 4-4: **Modeling and interpreting the SE data.** (a) Schematic (not to scale) of the model used. (b) Complex refractive index of ZrO_2 (top) and $ZrSe_2$ (bottom). (c) Simulated ε_2^{eff} for a $ZrSe_2/ZrO_2$ model with varying ZrO_2 thickness (0, 0.5, 1, 2, 5, 10 nm). (Inset) Magnified view of the simulated ε_2^{eff} of $ZrSe_2$ with oxide thickness 0, 0.1 and 0.2 nm showing that the change in ε_2^{eff} is indistinguishable.

We use SE analysis software (Semilab) to perform model-based analysis of the SE data. We consider two competing sample models, presented in Figure 4-5. We use an optical model consisting of three layers – air, thin oxide layer, and semi-infinite bulk crystal – to estimate the oxide thickness. However, the main part is the two-layered structure consisted of thin oxide layer and semi-infinite bulk crystal part. Each part

has its own actual refractive index. We assume the dielectric properties of the oxide and underlying crystal are not changing over time. Also, the thickness of bulk does not change as semi-infinite solid but overlying oxide thickness changes. If we consider the two-layer structure as one component, it gives us effective dielectric constant and it changes with the thickness of oxide. The spectra show obvious difference in the regime where the oxide thickness is over 2 angstroms. But they are indistinguishable where the oxide thickness is below 2 angstroms. The SE analysis software includes a data library for wide range of materials, including optical data (n, κ) for ZrO_2, but not for MoO_3. Therefore, we use (n, κ) data for MoO_3 as found in the scientific literature [82]. We fit the data by letting the oxide thickness vary in the model.

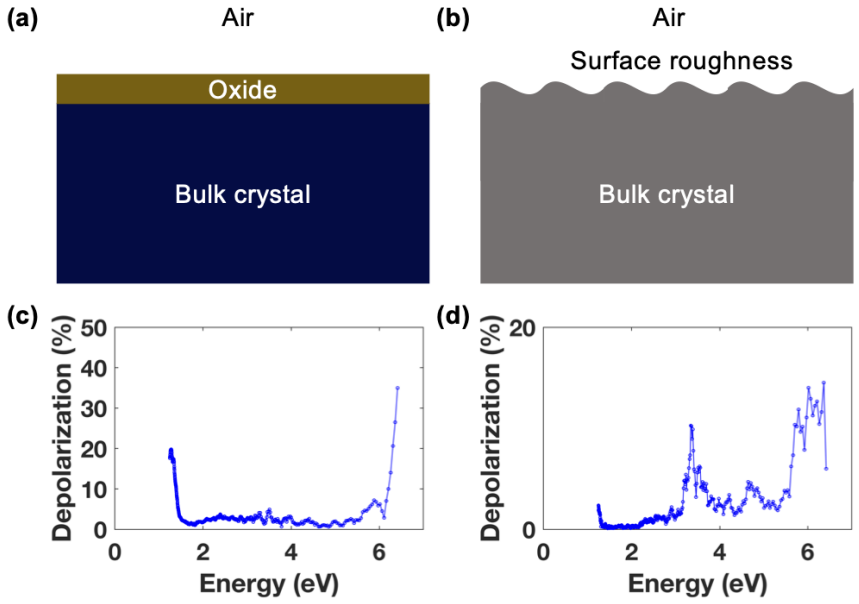

Figure 4-5: **Competing models used to analyze SE data.** (a) Layered model used to estimate the native oxide thickness formed on the surface of a bulk crystal upon air exposure. (b) Layered model used to account for the effect of surface roughness on the bulk crystal data. Depolarization measurement on (c) MoS_2 and (d) the select ZrS_xSe_{2-x} alloy (x = 0.8).

In the limit of very thin oxide layers, an alternative model of a semi-infinite bulk crystal with a rough surface (Figure 4-5b) also yields a satisfactory fit to the data. We analyze this model using the Bruggeman effective medium approximation to account for surface roughness. We use a diffusion phase model with two phases (air and crystal), setting them in equimolar composition (50:50). The Bruggeman model

includes a polynomial, the order of which depends on the number of components. Therefore, we use the model to quadratic order. This alternate model is not effective for analyzing the SE data measured on $Zr(S,Se)_2$ alloys, for which the oxide grows quickly and to a substantial thickness. However, for MoS_2 the data is equivalently well-fit by both models. This is reflected in the data presented in Figure 4-5b, with oxide thickness below the experimental resolution. These same SE data are equivalently well modeled using the roughness model, with surface roughness of 2 Å , which is confirmed by atomic force microscopy. For the cleaved surfaces reported here, this is a minor distinction because there is no oxide growth and the surface is very smooth. The choice of model becomes more important for rougher samples or those with unknown overlayers, as can be the case for un-cleaved geological samples [23]. We also show depolarization data measured on MoS_2 and a representative ZrS_xSe_{2-x} alloy (x = 0.8) in the photon energy range 1.25 – 6.5 eV (wavelength range 992 – 190 nm). The depolarization is high (> 15%) in the energy range above 5 eV. The depolarization effect is caused by multiple reasons; (1) incident angle variation originating from focusing of the probe light; (2) wavelength variation caused by the finite spectral resolution of monochromator; (3) surface light scattering caused by a large surface roughness of a sample; (4) thickness inhomogeneity of layers in the structure; (5) backside reflection in a thick substrate [183]. It is common when sample's lateral dimensions is smaller than collimated beam. Therefore, in the main text we report results only in the energy range 1.25 – 5 eV where the depolarization is less than 15 %.

4.3.2 Reactive Molecular Dynamics Simulation Methods

We perform RMD simulations based on the ReaxFF reactive force field to study the oxidation of ZrS_2 and MoS_2 slabs. A ReaxFF parameter set for Mo/O/S interactions in the MoS_2 oxidation was taken from Hong et al [138]. Another ReaxFF parameter set for Zr/O interactions was successfully developed by van Duin et al [184]. We then merged these two parameter sets into a single force field. We further developed this force field for Zr/O/S interactions by comparing with quantum mechanical (QM)

calculations. Our newly-developed Mo/Zr/O/S force field can be found in the SI. The SI also includes the validation of the Mo/Zr/O/S force field against QM data sets and QMD simulations. We perform RMD simulations in the canonical (NVT) ensemble, where the temperature is controlled by a Nose-Hoover thermostat, with a temperature-damping constant of 100 fs. We numerically integrate the equations of motion with a time step of 1 fs. The lateral dimensions of the MoS_2 simulation cell are 46.83 $\times$ 40.36 Å^2, and the simulated system contains 4 monolayers of MoS_2 stacked vertically. Similarly, the lateral dimensions of the ZrS_2 simulation cell are 53.52 $\times$ 46.35 Å^2, and the simulation cell contains 4 monolayers of ZrS_2. The two outer layers are exposed to O_2 gas. We apply periodic boundary conditions in the lateral directions. Each simulation contains 768 metal atoms (Mo or Zr) and 1536 S atoms, to which we add 2000 O_2 molecules.

4.4 Results and Discussion

4.4.1 Time-Dependent SE Results

In Figure 4-6 we present the imaginary component of the effective dielectric constant (ε_2^{eff}) measured on single-crystal ZrS_xSe_{2-x} alloys as a function of time after cleaving, measured by SE. The effective dielectric constant accurately represents the material only for a uniform, semi-infinite sample with an intimate and smooth sample-air interface, hence the qualifier "effective" (see chapter 4.3.1). The time-dependence of the data is a straightforward clue that the actual sample structure is more complicated, and changes in time as the samples are exposed to air. Comparing the results for $ZrSe_2$ (Figure. 4-6a) to the results for ZrS_2 (Figure. 4-6f), we see that the sulfide is more air-stable. The peaks in the ε_2^{eff} spectra derive from the lowest-lying direct, allowed optical transitions and excitons (X_Γ, X_L, X_A), which blue-shift with sulfur content across the ZrS_xSe_{2-x} series [28].

The interpretation of the ε^{eff} data presented in Figure 4-6 deserves some discussion. In the presence of a native oxide, ε^{eff} is not an accurate estimate of the

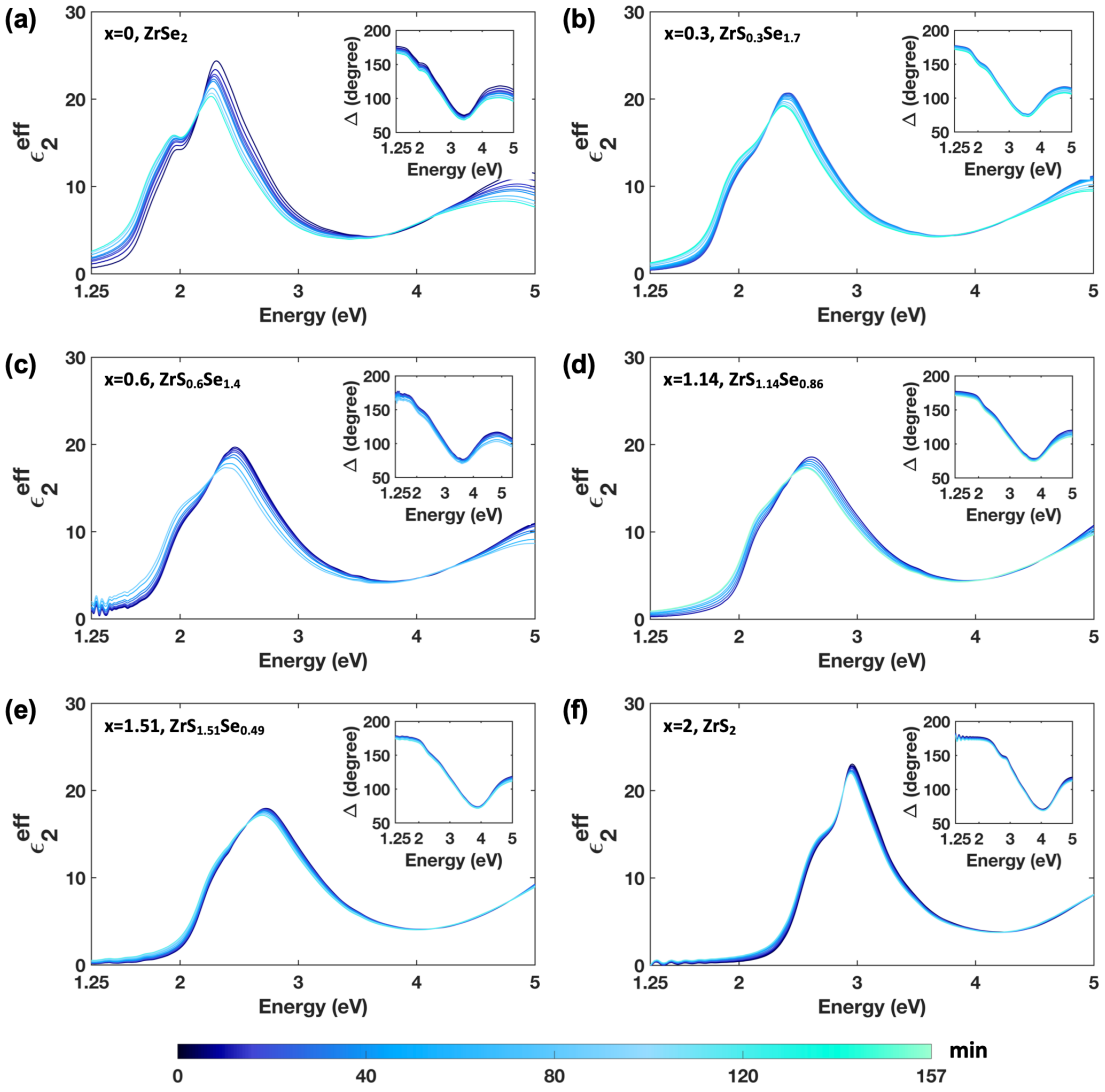

Figure 4-6: **Imaginary part of the effective dielectric constant (ε_2^{eff}) measured by SE.** ε_2^{eff} as a function of time in ambient conditions after exposing a fresh surface, for six compositions: (a) $ZrSe_2$, (b) $ZrS_{0.3}Se_{1.7}$, (c) $ZrS_{0.6}Se_{1.4}$, (d) $ZrS_{1.14}Se_{0.86}$, (e) $ZrS_{1.51}Se_{0.49}$, (f) ZrS_2. The insets show the SE amplitude (Δ) for the same data series. The color bar at the bottom indicates the exposure time after cleaving.

actual dielectric response of the underlying crystal. In this case, the actual dielectric constant must be determined through modeling and regression (Section. 4.3.1). We assume that the dielectric properties of the oxide and the underlying crystal are unchanging in time, and that the time dependence of the data derives from increasing oxide thickness. We assume that the oxide is a dielectric with refractive index spectra equal to that of ZrO_2 (using reference data) or MoO_3 [185]. We use this model to analyze the experimental data, leading to the thickness-time results presented below. To aid interpretation of the ε^{eff} data presented in Figure 4-6, we simulate ε_2^{eff} for different oxide thickness, all else held constant (Figure 4-4). We see that ε_2^{eff} overestimates (underestimates) the extinction coefficient ($\kappa = -\sqrt{\varepsilon_2}$) well below (well above) the exciton resonances. We also see that ε_2^{eff} suggests a red-shift of the exciton resonances with increasing oxide thickness. This is a subtle effect of light interacting with a multi-layer sample with absorption resonances; it does not imply a change to the exciton spectrum structure of the underlying crystal. The simulated ε_2^{eff} spectra also indicate the ability of SE to resolve oxide thickness down to 2 Å, below which the spectra cease changing. This is comparable to a metal-oxygen bond length.

In Figure 4-7 we show SE time-series data recorded after cleaving a fresh surface of MoS_2. In contrast to the results for ZrS_xSe_{2-x}, the results for MoS_2 show no apparent change, even after many days of exposure. This suggests that a pristine MoS_2 surface does not spontaneously oxidize in air on laboratory time scales. If freshly-cleaved MoS_2 does maintain a pristine surface in air, then the effective dielectric constant is an accurate estimate of the optical properties of the material. In Figure 4-7a we show the complex dielectric constant ($\varepsilon_1 - i\varepsilon_2$), and in Figure 4-7b we show the complex refractive index ($n - i\kappa$). The optical transitions characteristic of MoS_2 excitons A ($\approx$ 1.8 eV), B ($\approx$ 2.1 eV), C ($\approx$ 2.7 eV) and D ($\approx$ 3.1 eV) are clearly observed in the loss spectra (ε_2 and κ). We note the small loss coefficient, $\kappa < 0.05$, for photon energy near and below the indirect band gap of 1.29 eV. This value is lower than our previously-reported value of $\kappa \approx 0.2$, which we determined from SE measurements on geological crystals from the same batch but without cleaving [23]. This illustrates the sensitivity of SE to surface conditions, including roughness. The

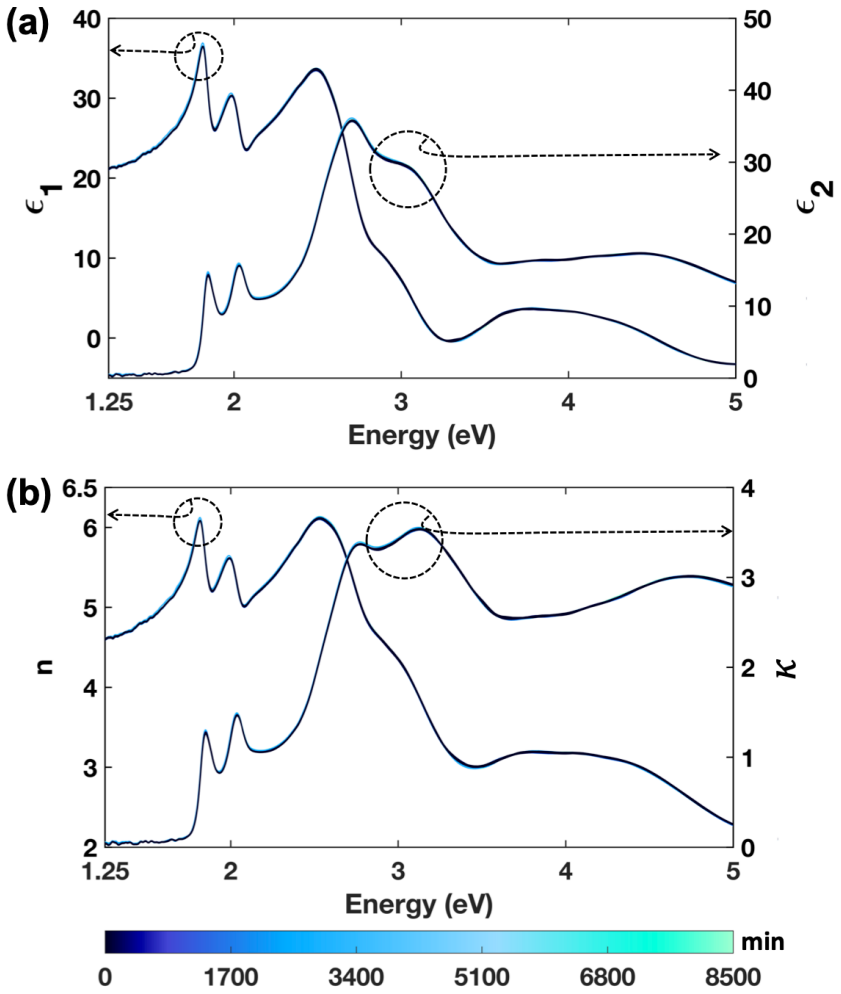

Figure 4-7: **Effective optical constants of MoS_2.** Complex dielectric constant (a) and refractive index (b) of MoS_2 determined by SE measurements on a freshly-cleaved surface. The color series indicates the time elapsed between cleaving the surface and taking the SE data. The spectra recorded at times between 6 and 8,498 min overlap and are barely distinguishable. This time-invariance suggests that the freshly-exposed MoS_2 surface is stable in air on laboratory time scales.

value of the loss coefficient that we measure here is comparable to what we measure on waveguide-integrated synthetic MoS_2 thin films ($\kappa \approx 0.04 - 0.1$, unpublished), and approaches our theoretical predictions for ideal, bulk MoS_2 ($\kappa \approx 0.01$ - 0.02) [23, 59], as discussed in Section 2.3.5. These value bode well for refractive, low-loss applications of MoS_2 in integrated photonics [12]. This metrology is simple and easy to apply to other material system. We investigate WS_2, WSe_2 and HfS_2 and they show similar behavior as MoS_2, meaning they are air stable (Figure 4-8) and .

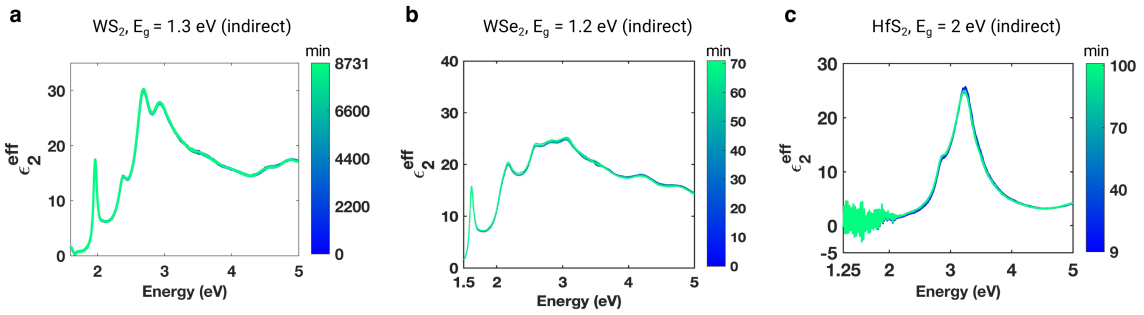

Figure 4-8: **Effective optical constants of WS_2, WSe_2 and HfS_2.** Measured ε_2^{eff} over time in ambient conditions after mechanical exfoliation: (a) WS_2, (b) WSe_2, (c) HfS_2. The color bar indicates the exposure time after exfoliation.

4.4.2 Kinetics of Native Oxidation: ZrS_2 and MoS_2

In Figure 4-9a-b we plot the time-dependence of the growth of native oxide on ZrS_xSe_{2-x} and MoS_2. The oxidation of Se-rich ZrS_xSe_{2-x} starts immediately after cleaving and the oxide grows approximately logarithmically in time, showing no sign of stopping within the 160 min observation window. S-rich samples oxidize more slowly; for ZrS_2 the oxidation process appears to stop above $\approx$ 1 nm of oxide thickness.

We further discuss the applicability of established kinetic models to interpret our results. There are two widely-used kinetic models for oxide growth: the Deal-Grove linear-parabolic model, and Fick's diffusion model. The Deal-Grove model considers three phenomena, with corresponding rates: arrival of oxidizing molecules on the surface, diffusion through the forming oxide layer, and reaction at the interface of the oxide and underlying, unoxidized material. Of these, the arrival of oxidizing

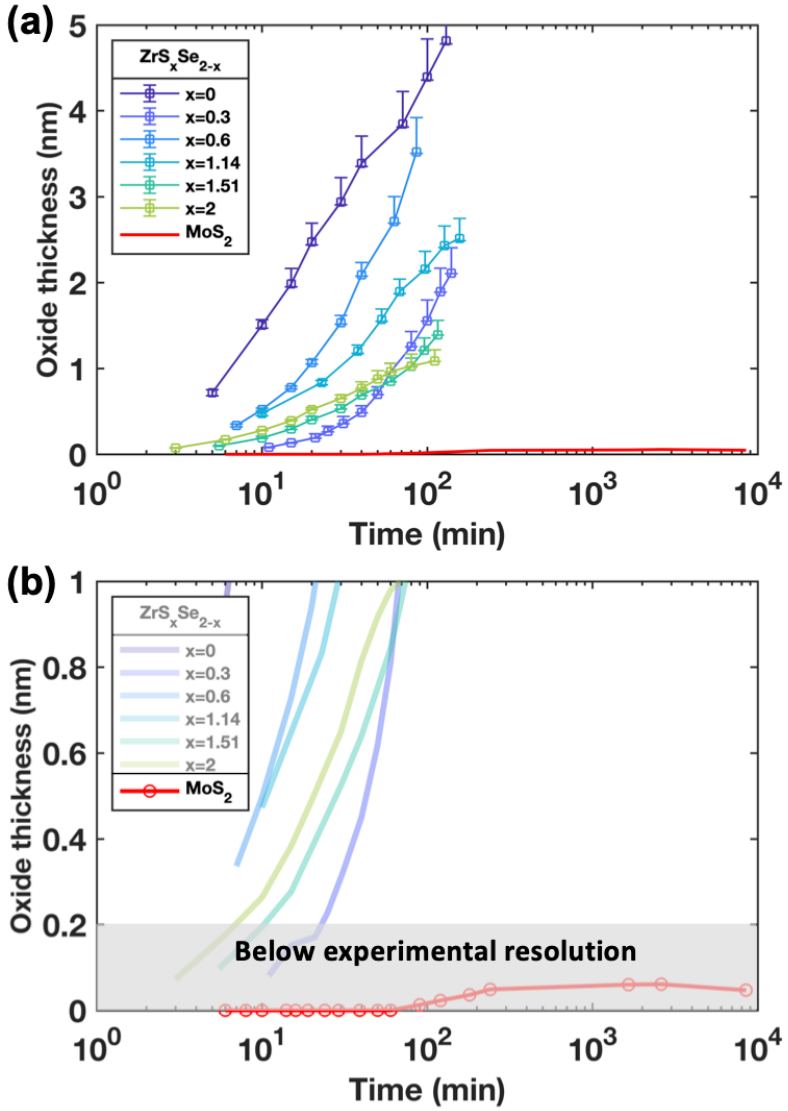

Figure 4-9: **Time-thickness of native oxide plot of MoS_2 and ZrS_xSe_{2-x}.** Kinetics of native oxide formation on freshly-cleaved ZrS_xSe_{2-x} and MoS_2. (a) Oxide thickness vs. exposure time for ZrS_xSe_{2-x} alloys; from blue to light green, x=0, x=0.3, x=0.6, x=1.14, x=1.51, x=2. The error bars represent systematic errors in the model and nonlinear regression procedure. It reflects ± 5% error in initial guess of oxide thickness and 10% error in surface roughness of oxide. (b) Plot of oxide thickness vs. exposure time for MoS_2. The model-based data analysis infers an oxide thickness that is below the experimental resolution of ≈ 2 Å, which is indicated by the grey region.

molecules is not a rate-determining step in ambient conditions, and this rate can be safely ignored. The rate law relating oxide thickness (d) and time (t) is

$$t - t_0 = \frac{B}{A}(d - d_0) + \frac{1}{B}(d^2 - {d_0}^2)$$

where t_0 = initial time, A and B are linear and parabolic growth rates, d_0 = oxide thickness at t_0. Since we start from an oxide free surface (*i.e.* for $t_0 = 0, d_0 = 0$), the equation simplifies to

$$t = \frac{B}{A}d + \frac{1}{B}d^2$$
$$\frac{t}{d} = \frac{B}{A} + \frac{1}{B}d.$$

This linear-parabolic model predicts that a plot of $\frac{t}{d}$ vs. d will be a straight line with a positive intercept, as we present in Figure 4-10a. In Figure 4-10b we plot in this way the data for ZrS_xSe_{2-x} compositions x = 0 and x = 2. We see that the linear-parabolic model does not apply to either of these data sets.

We also evaluate the Fick's diffusion model, which predicts the oxide growth in time as $d = \sqrt{2Dt}$, where D = diffusion coefficient. This model can be thought of as a simplification of the linear-parabolic model, wherein the reaction at the interface is not a rate-determining step. In this model, the oxygen diffusion through the forming oxide is usually taken to be the rate-determining step. We present the model of diffusion-limited growth in Figure 4-10c, showing a straight line on a plot of d vs. $\sqrt{t}$. In Figure 4-10d we plot in this way our data for several compositions, and we see that the data does not conform to Fick's model. The data for x =0, 0.3 (not shown here), 1.14, and 2 may be consistent with two growth regimes with different diffusion rates: for short (long) times, D is large (small), and oxide grows faster (slower). We speculate this could results from growth rate determined initially by in-diffusion of oxygen, and at later times by the formation and out-diffusion of SO_2. However, this behavior is not seen clearly in the thickness-time data for all samples.

The non-applicability of either model to our data may be expected from the differences between oxidizing an element (such as Si) and oxidizing a compound (such as ZrS_2), and from the RMD simulation results. For TMDs such as ZrS_2, the growth of a

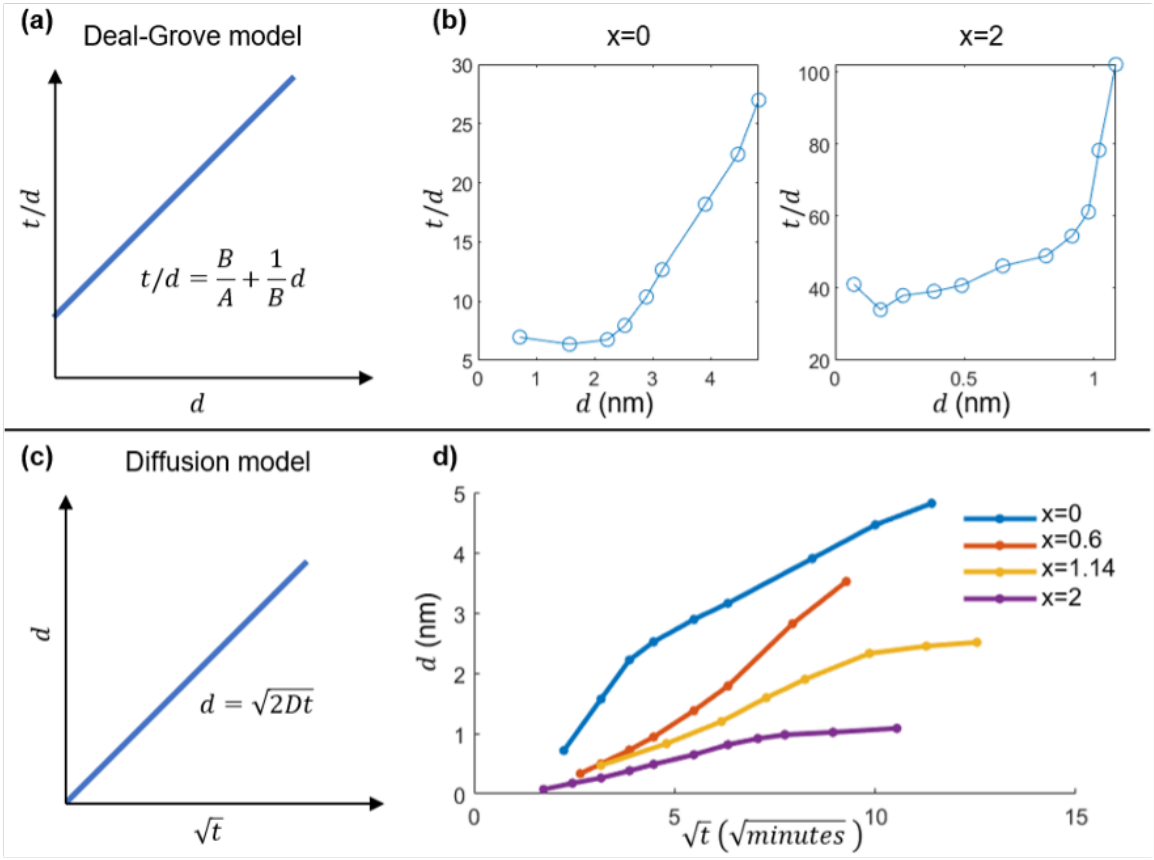

Figure 4-10: **Evaluation of rate models for modelling the native oxide growth kinetics of ZrS_xSe_{2-x} alloys.** Top (a-b): Deal-Grove, linear-parabolic model. Bottom (c-d): Fick's diffusion model. (a) The linear-parabolic model predicts a straight line when plotting t/d vs. d. (b) Plots of $\frac{t}{d}$ vs. d for compositions x = 0 and x = 2. These plots show that oxide growth does not follow the linear-parabolic rate model. (c) Fick's diffusion model predicts a straight line when plotting d vs. $\sqrt{t}$. (d) Plots of $dvs.\sqrt{t}$ for compositions x = 0, 0.6, 1.14, and 2. None of the data is well-modeled by a single diffusion rate.

native oxide is accompanied by sulfur loss, such as sublimation of SO_2, which process adds complexity that is not captured by simple models. At short times, the growth of an intermediate oxysulfide layer may indeed be limited by the in-diffusion of oxygen, which moves by the Zr-O bond-switching mechanism described above. However, at later times (*e.g.* by t = 1.5 ns in the simulation at 1500 K) the rate-limiting process is the formation and out-diffusion of SO_2. This is a complicated reaction-diffusion process involving many stages of bond breaking and reformation.

We find that MoS_2 barely oxidizes in air after cleaving, if at all. Our SE modeling and data analysis is consistent with an oxide thickness of ≈ 1 Å forming within 5 hrs after cleaving, and remaining stable after 6 days on air exposure, as we show in Figure 4-9b. However, this result is below the experimental sensitivity, and therefore our data is also consistent with a stable and pristine MoS_2 surface. To distinguish between these two scenarios – incipient oxidation, or a stable and pristine MoS_2 surface – we turn to XPS. As we show in Figure 4-11, the O 1s spectrum shows no detectable Mo-O bonding (530.2 eV for MoO_3), and the S 2p spectrum shows no S-O bonding (167 eV for SO_2), indicating that the MoS_2 surface is not oxidized. These XPS results were obtained from a geological MoS_2 crystal that was mechanically cleaved and then exposed to ambient conditions for a year. Both SE and XPS show that the surface of MoS_2 is stable and non-reactive in typical laboratory conditions, as has been reported previously [84, 86].

4.4.3 Atomistic Mechanism of Native Oxide Formation

To understand the rapid oxidation of Zr-based TMDs compared to MoS_2, we perform RMD simulations of the oxidation of MoS_2 and ZrS_2 slabs. The simulation volume consists of four TMD layers. While this is far thinner than the bulk crystals that we study experimentally, it is sufficient to study the key atomic-scale mechanisms, and still requires substantial computational resources. We simulate oxidation in an oxygen partial pressure of 1.16 kbar and at 800 K, to accelerate the process; as a result, the timescales of oxidation observed in simulation are not expected to match those observed in experiment. In Figure 4-12 we show the initial simulation setup

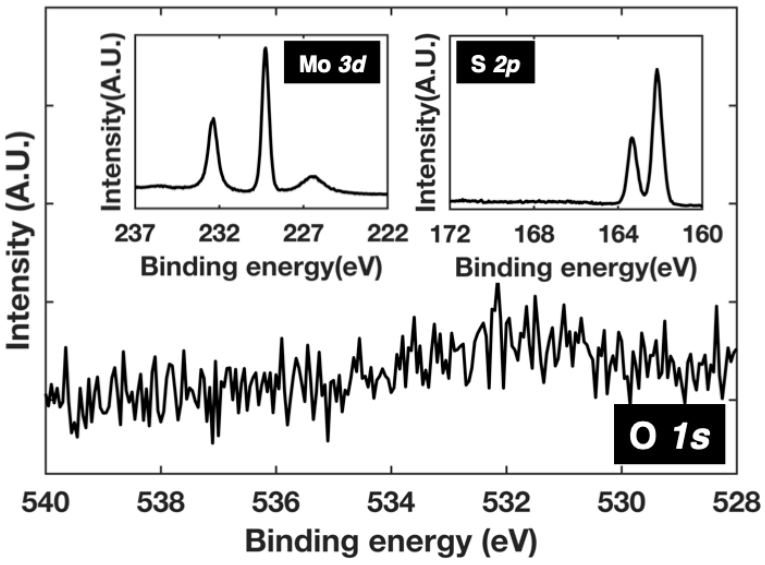

Figure 4-11: **High resolution XPS scan of O-1s, Mo-3d and S-2p peaks of MoS_2.** XPS O-1s peak and (inset) Mo-3d peak and S-2p peak for a MoS_2 crystal stored in laboratory ambient conditions for a year after cleaving. No oxygen signal is detected.

(at time t = 0 ns) and the final snapshot (t = 2.5 ns) for MoS_2 and ZrS_2 oxidation. The simulation box is periodic in the $\langle 100 \rangle$ and $\langle 010 \rangle$ directions (*i.e.* in-plane). The simulations show that ZrS_2 oxidizes extensively. To quantify the extent of oxidation, we show the total numbers of M-S, M-O, O-O, and S-O bonds (M = Mo or Zr). The increase in Mo-O with oxidation time is negligible compared to the rapid increase of Zr-O bonds. Concurrently, we observe a notable decrease in O-O bonds in the ZrS_2 simulation, suggesting scission of O-O bonds followed by formation of Zr-O bonds. The bond counting data in Figure 4-12f suggest that ZrS_2 oxidation progresses in two stages. During the first 0.1 ns, the number of Zr-O bonds rises rapidly, followed by much slower increase at longer times. The rapid initial reaction may be explained by energetically-favored O_2 adsorption on the ZrS_2 surface [186]. The rapid increase in the number of Zr-O bonds is not accompanied by a similarly rapid decrease in the number of Zr-S bonds, as we discuss below. The subsequent, slower process of Zr-O bond formation represents the growth of an amorphous oxy-sulfide that largely eliminates the van der Waals (vdW) gaps. In contrast, we observe almost no decrease of O-O bonds in the MoS_2 simulation. This suggests that MoS_2 remains mostly inert

and stable in the simulated environment.

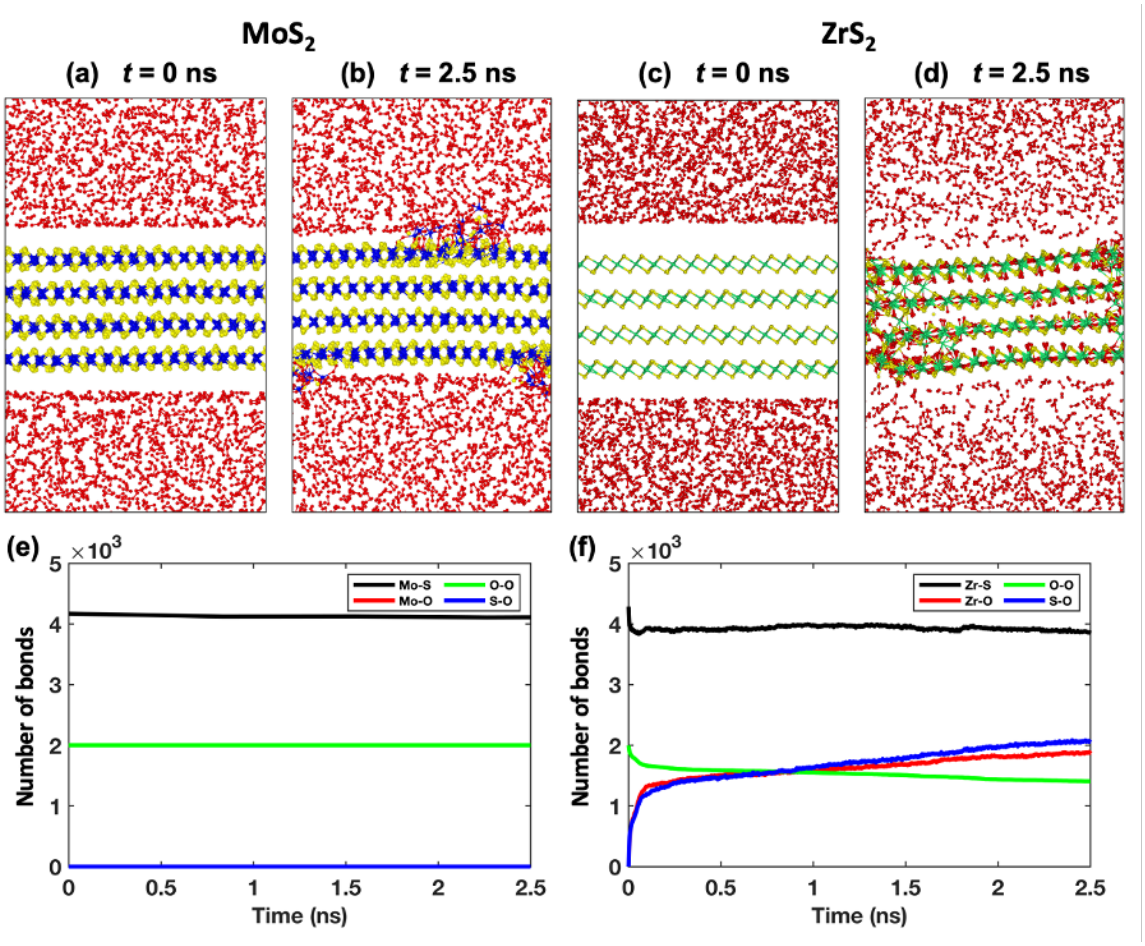

Figure 4-12: **RMD simulations of MoS_2 and ZrS_2 oxidation.** Snapshots of (a-b) MoS_2 oxidation and (c-d) ZrS_2 oxidation at time t = 0 and 2.5 ns, respectively. Spheres represent individual atoms: blue (Mo), green (Zr), yellow (S) and red (O). Time evolution of corresponding bond count for (e) MoS_2 and (f) ZrS_2 oxidation.

We also find that the presence of a grain boundary substantially accelerates oxidation of ZrS_2, as expected. The grain boundary includes metal-terminated edges, which are known to accelerate oxidation compared to chalcogen-terminated edges. In Figure 4-13b-c we compare the simulation results after 1.5 ns of oxidation for the models with and without a grain boundary. Near the grain boundary, the layered crystal structure has largely been eliminated by aggressive oxidation after 1.5 ns. Farther from the grain boundary, and in the model without a grain boundary, there is substantial oxygen content after 1.5 ns, but the layered crystal structure remains intact. The oxidation rates of the models with and without grain boundaries can be

quantitatively compared by counting Zr-O and S-O bonds, as shown in Figure 4-13d-e. The initial, steep rise in the Zr-O and S-O bond counts is similar in both cases. This corresponds to adsorption, as discussed above. The subsequent, slower rise in the Zr-O and S-O bond counts is faster in the presence of a grain boundary. This can be understood as a result of fast oxygen transport along the grain boundary. As a result, oxygen is present at the "entrance" to vdW gaps in higher concentration than the case without the grain boundary. Therefore, the total concentration of oxygen within the vdW gaps, and concurrent rise in Zr-O and S-O bond counts, is faster with the grain boundary present.

We analyze the process of ZrS_2 oxidation in detail by considering atomic trajectories. We find that oxidation proceeds in six steps:

(1) adsorption of O_2 molecules on the ZrS_2 surface;

(2) dissociation of O_2 on ZrS_2 surface, and formation of Zr-O bonds;

(3) Zr pushed into van der Waals gaps between TMD layers, due to formation of new Zr-O bonds;

(4) formation of inter-layer Zr-S and Zr-O bonds, resulting in breakdown of the layered crystal structure;

(5) oxygen transport laterally within and vertically between layers by a mechanism of Zr-O bond switching;

(6) formation and out-diffusion of SO_2.

In Figure 4-14a-b we show the cross-section and top-down view of the simulation at t = 2 ps, illustrating steps 1-2. We indicate O_2 adsorption sites with black rectangles. We find that the adsorption of O_2 on the ZrS_2 basal surface is energetically-favorable, with adsorption energy E_{ads} = -0.006 eV per O_2 molecule, which we calculate by density function theory (DFT) simulations of a ZrS_2 surface-O_2 molecule system. In contrast, we find no stable, relaxed energetic minimum for a MoS_2 surface-O_2 molecule system, indicating that the adsorption energy is positive. Constrained MD simulations paint a similar picture, that O_2 adsorption is favorable on ZrS_2 but unfavorable on MoS_2 (See Chapter 4.6).

After rapid adsorption of O_2, we observe O-O bond breaking and the formation

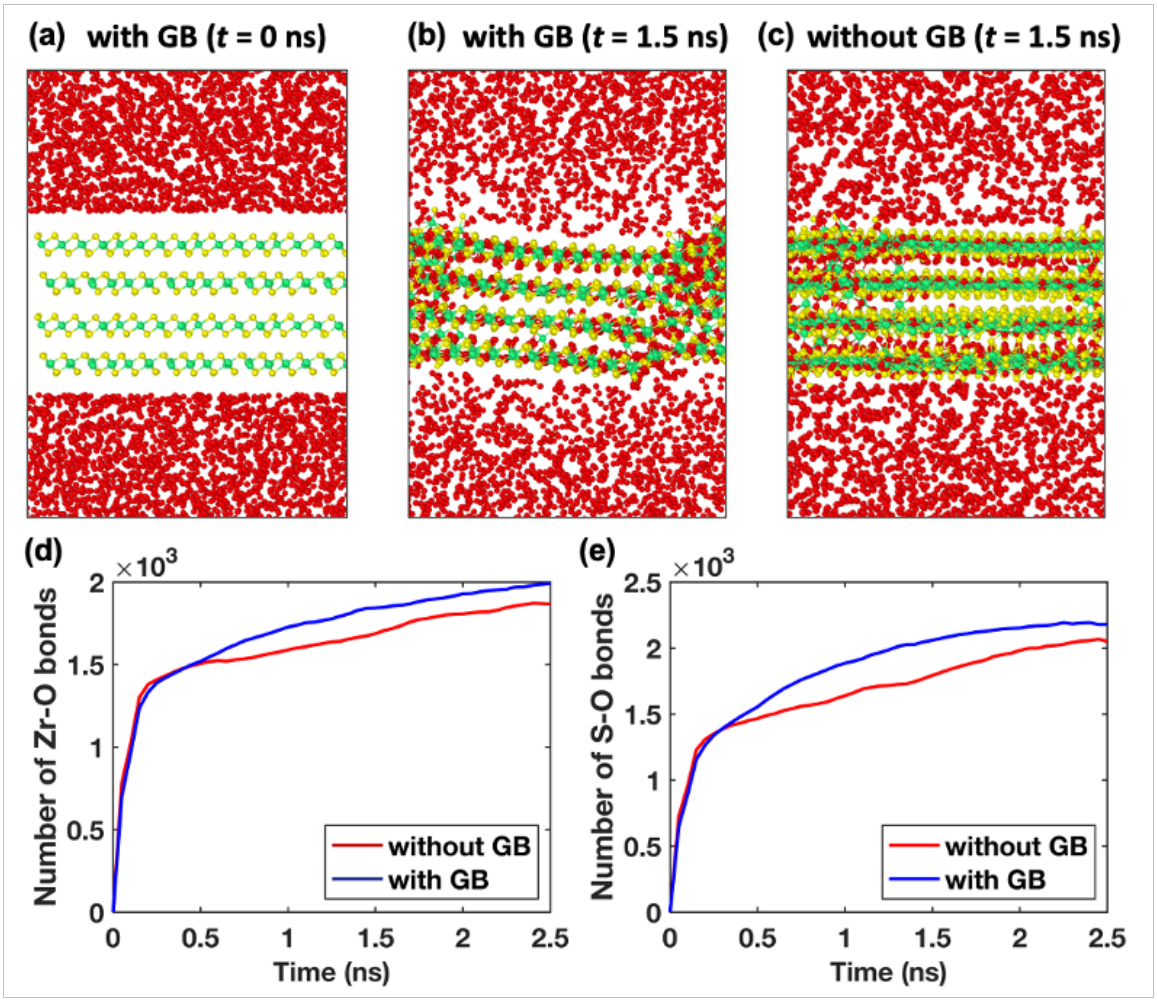

Figure 4-13: **RMD simulations of ZrS_2 oxidation in the presence of a grain boundary.** (a-b) Snapshots of the simulation at time t = 0 and 1.5 ns, respectively. (c) Snapshot at t =1.5 ns of oxidation of ZrS_2 without a grain boundary. (d-e) Time dependence of the number of Zr-O and S-O bounds for ZrS_2 oxidation with (blue) and without (red) a grain boundary.

of Zr-O bonds. We also observe 2- and 3-coordinated oxygen atoms on the ZrS_2 surface after O-O bond breakage, corresponding to 2-coordinated bridge oxygen, and 3-coordinated oxygen that are seeds for zirconia growth. A similar process was proposed for the oxidation of monolayer ZrS_2 [173].

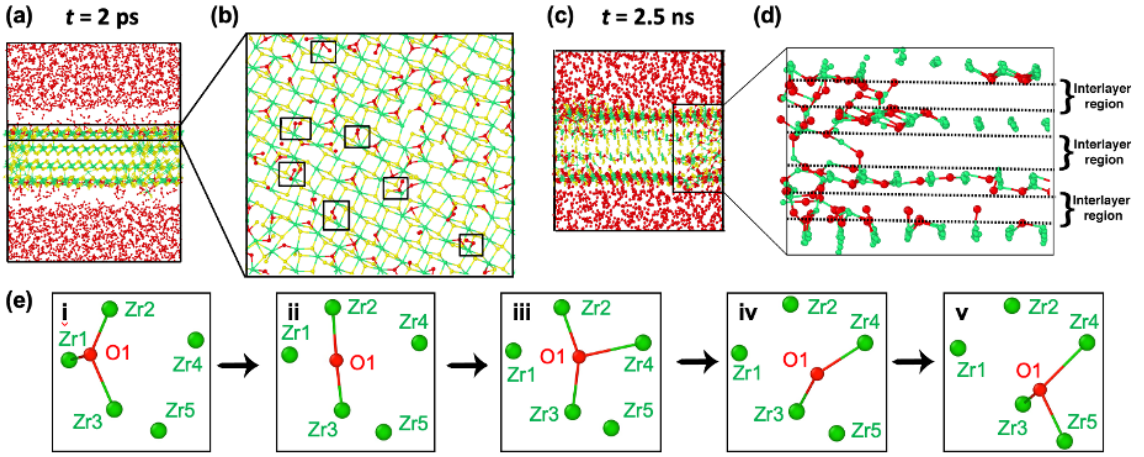

Figure 4-14: **Atomistic mechanisms of ZrS_2 oxidation.** Cross section (a) and top-down (b) views at t = 2 ps, showing O_2 adsorption and Zr-O bond formation that involves both 2- and 3-fold coordinated oxygen atoms (enclosed by black rectangles). Cross section (c) and close-up (d) view at t = 2.5 ns, showing the formation of an amorphous matrix and the closing of the van der Waals gaps; S atoms are not shown in (d) for clarity. (e) Oxygen transport mechanism of Zr-O bond switching, including oxygen switching between 2- and 3-fold coordination: (i-ii) breakage of Zr1-O1 bond and decrease in coordination number (3→2); (ii-iii) formation of Zr4-O1 bond and increase in coordination number (2→3); (iii-iv) breakage of Zr2-O1 bond and reduced coordination number (3→2); (iv-v) formation of Zr5-O1 bond and coordination number recovery (2→3).

Following the initial formation of Zr-O bonds, Zr moves from the top layer into the interlayer region. The protrusion of Zr atoms results in the collapse of the vdW gap between ZrS_2 layers by the formation of new, interlayer Zr-S and Zr-O bonds, resulting in amorphous, non-layered material. This is illustrated by a simulation view at t = 2.5 ns, presented in Figure 4-14c-d. The close-up in Figure 4-14d highlights the inter-layer Zr atoms and bonds. The expansion of these disordered regions into the vdW gaps provides pathways for oxygen transport further into the ZrS_2 crystal. We find that oxygen transport proceeds by a process of Zr-O bond switching, illustrated step-by-step in Figure 4-14e, in which Zr and O atoms are numbered and S atoms

are omitted for clarity. The coordination of oxygen atom O1 first changes from 3 to 2 by the breakage of the Zr1-O1 bond. The subsequent creation of a new Zr4-O1 bond restores the 3-fold coordination. A similar process continues when the Zr2-O1 bond is broken and a new Zr5-O1 bond is formed. Oxygen thus traverses the system by successive breaking and forming Zr-O bonds. This bond-switching mechanism for oxygen transport is akin to Grotthuss mechanism which plays essential roles in various processes in oxides [181, 182, 187]. It is interesting that this process is not correlated with a decrease in the number of Zr-S bonds. This suggests that S atoms act as spectators during these initial steps of Zr-O bond formation, amorphization, and oxygen transport, and that charge neutrality is maintained by successive redox transitions at the S sites. The intermediate phase is therefore a zirconium oxysulfide, with mixed-valence sulfur ions. The thermodynamic end-products of ZrS_2 oxidation are ZrO_2 and SO_2; therefore, the oxidation state of sulfur goes from S^{2-} to S^{4+}. It is interesting that the oxidation of sulfur is mediated initially through the Zr site. These processes are also observed in first-principles QMD simulations (see chapter 4.6), thus validating these atomistic mechanisms of ZrS_2 oxidation. The last step in the oxidation of ZrS_2 is the formation and out-diffusion of SO_2. Our simulation at 800 K does not extend for long enough time to observe this process. Simulations performed at a much higher temperature of 1500 K do observe the formation and out-diffusion of SO_2 molecules (See Chapter 4.6).

4.5 Conclusion

Our results provide quantitative guidance for designing and processing semiconductor devices based on ZrS_xSe_{2-x} and MoS_2, and identify the atomistic-scale mechanisms of bonding and phase transformations in layered materials with competing anions. Direct, atomic-scale experimental testing of the mechanisms illustrated here by molecular dynamics may require extensive use of methods of chemical spectroscopy with Å-level depth resolution, including variable-angle photoelectron spectroscopy, and possibly the development of tools to resolve bond forming and breaking on ultra-fast

time scales. It will be interesting to extend our methods to study the oxidation of thin films produced by various methods, especially including wafer-scale processes that will be essential for device fabrication, and in different conditions [59]. This is especially pertinent if native oxides are discovered to have beneficial passivating or functional properties, as they do for legacy semiconductors [82].

4.6 Supplementary Information

4.6.1 O_2 Adsorption Energy on MoS_2 and ZrS_2 Surfaces by Quantum-Mechanical Calculation

To understand the favorable adsorption of O_2 on the surface of ZrS_2, we perform first-principles constrained MD simulations. We calculated electronic states using the projector augmented-wave (PAW) method within the framework of DFT [188]. For the exchange-correlation energy, we used the generalized gradient approximation (GGA) based on the PBE functional [189]. We construct a simulation cell consisting of 3-layered $Zr_{48}S_{96}$ and $Mo_{48}S_{96}$ systems. To reproduce the adsorption process on the surface of MS_2 (M = Zr, Mo), we constrain the interatomic distance between M and O atoms ($r_{\text{M-O}}$) (Figure 4-15ab), and we gradually decrease $r_{\text{M-O}}$ during the simulations in steps of 0.3 Å. We use the QMD simulation results to calculate changes in the free energy (ΔF) of the metal-oxygen bond by integrating a Lagrange multiplier $\lambda(r)$ along the constrained distance $r = r_{\text{M-O}}$:

$$\Delta F(r) = \int_{r_0}^{r} < \lambda(r') > \, dr' \quad \text{(S1)}$$

$\lambda(r)$ is obtained by averaging over the last 1000 steps of the QMD simulation for each $r_{\text{M-O}}$ value. Further details of this procedure can be found in Misawa et al [190]. Figure 4-15c shows the calculated change in free energy for Zr-O and Mo-O bond. We observe that O_2 adsorption on MoS_2 surface is prevented by a large energy barrier. For ZrS_2 the energy barrier is much smaller, and there is a local energy minimum between 2 – 2.5 Å, which we interpret as a metastable state for adsorbed O_2. We observe a similar trend in ReaxFF simulations.

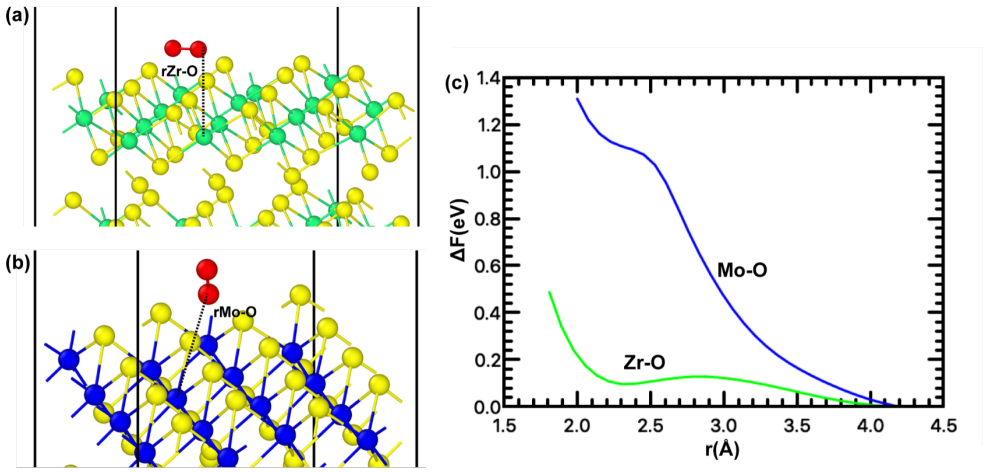

Figure 4-15: Simulation cells containing the (a) ZrS_2, and (b) MoS_2 surface with an O_2 molecule. The interatomic distances are shown by dotted black lines. (c) Change in free energy as a function of distance for Zr-O (green line) and Mo-O (blue line).

4.6.2 Validation of ZrS_2 Force Field by Quantum Molecular Dynamics Simulation

To validate the RMD simulation of ZrS_2 oxidation, we perform first-principles QMD simulation within the framework of DFT [191–193]. We used the generalized gradient approximation (GGA) based on the PBE functional with PAW formalism for QMD simulation [188, 189]. The QMD simulation contains $Zr_{48}S_{96}$ slab and 72 O_2 molecules with similar setup as reactive molecular dynamics as shown in Figure 4-16a. We perform simulations up to 6 ps at a temperature of 1200 K. Figure 4-16b shows the snapshot of the final configuration after 6 ps. In the final configuration, we observe the oxidation of surface layers very similar to RMD simulation in the main text. Due to Zr-O bond formation, Zr atoms in the top layer are pushed into the underlying van der Waals gap, or out of the top surface. This distortion destroys the layered crystal structure of ZrS_2, creating a disordered region. A disordered region can be observed between first and second layers in Figure 4-16b. Similar disordered region were observed in RMD simulation as shown in Figure 4-14d in the chapter 4, thus validating the presence of new channel for oxygen diffusion in disordered region.

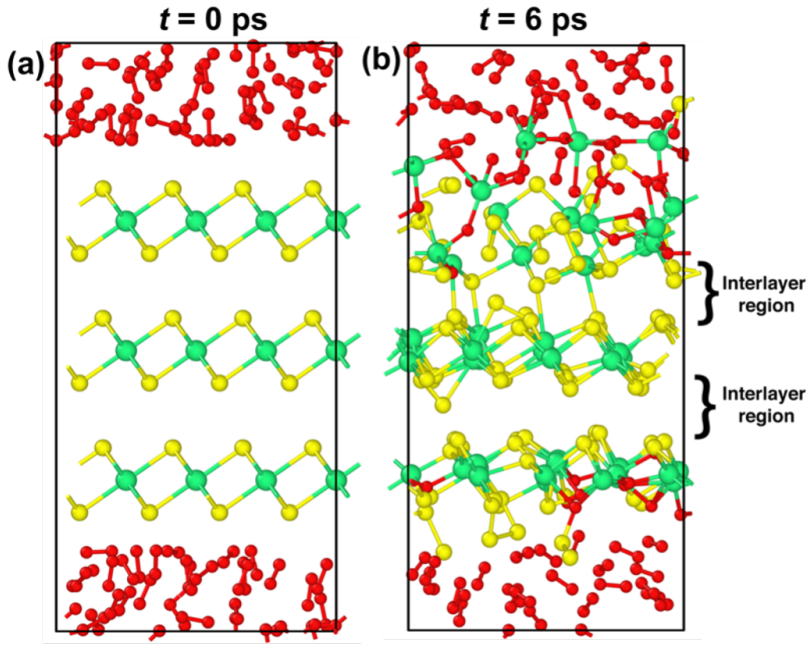

Figure 4-16: Initial and final configurations of QMD simulation to study ZrS_2 oxidation. (a) Initial system with 48 Zr (green), 96 S (yellow) and 144 O (red) atoms. (b) Final configuration after 6 ps.

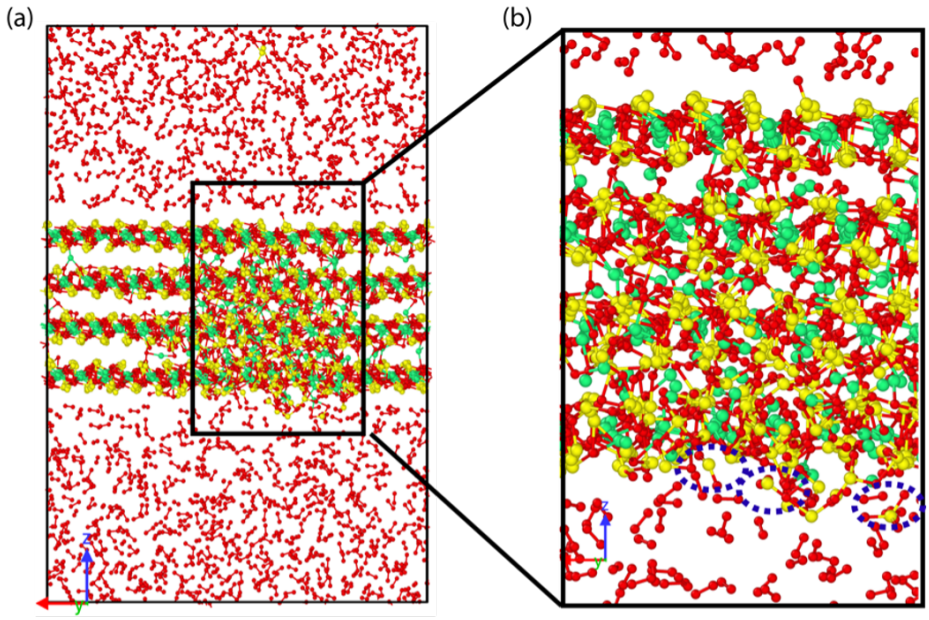

Figure 4-17: (a) Snapshot of RMD simulation to study ZrS_2 oxidation at 1500 K after 2.5 ns. (b) Close-up view of disordered region. The formed SO_2 molecules is highlighted by blue dotted circles.

4.6.3 ZrS_2 Oxidation at 1500 K

We perform RMD simulation to study the oxidation of ZrS_2 at higher temperature (1500 K), to further accelerate the oxidation process. The initial simulation setup is maintained the same as for the 800 K simulation presented in the chapter 4. In Figure 4-17a we show the final configuration after 2.5 ns at 1500 K; Figure 4-17b is a close-up view of the same configuration. In Figure 4-17a, we observe the formation of disordered region, which is similar to the simulation at 800 K. In Figure 4-17b, we also observe the formation of SO_2 molecules, which are not observed at 800 K due to the slow formation rate.

To further validate the adsorption and reactivity of O_2 on ZrS_2 surface, we compare intermediate structures formed on the surface layer of ZrS_2 slab at an earlier stage of ReaxFF RMD and first-principles QMD simulations. In Figure 4-18ab we show close-up views of the top surface layer simulated by QMD and RMD, respectively. In both simulations we observe the formation of 2-coordinated bridging oxygen and 3-coordinated oxygen atoms.

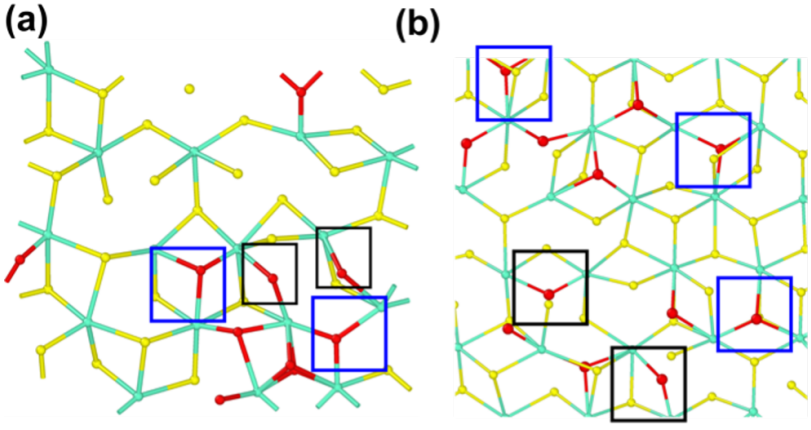

Figure 4-18: Comparison of oxygen intermediates formed in QMD (a) and RMD (b) simulations. Blue and black boxes highlight 3-coordinated oxygen and 2-coordinated bridge oxygen, respectively.

4.7 Contribution Statements

Liqiu Yang, Subodh C Tiwari, Arvind Krishnamoorthy in Priya Vashishta and Rajiv Kalia and Aiichiro Nakano's group at University of Southern California and Sungwook Hong at California State University carried out molecular dynamics calculation. Maria Sales in Stephen McDonnell's group measured XPS of bulk MoS_2 which was exfoliated and exposed to air for air.

Chapter 5

Controlled Native Oxide Growth on Single Crystalline MoS_2 for Microelectronics: Native Oxidation in Aggressive Condition

5.1 Project Introduction

We studied the growth kinetics and mechanisms in Chapter 4 in ambient condition and briefly discussed the importance of native oxide in semiconductor industry. In this Chapter, we develop processing method to directly grow high quality native oxide from transition metal dichalcogenides (TMDs), which is in aggressive condition rather than ambient condition. It would not have been possible for Si to dominate semiconductor technology without high-quality native insulator, SiO_2, as its gate dielectric. Whereas electronic and optical properties of layered materials (LMs) have been widely studied, study on processing of native oxidation of LMs remains elusive and properties of the oxide are still largely unknown. Moreover, systematic knowledge of native oxide in LMs which is directly relevant to semiconductor device processing is lacking although oxide quality on semiconductor dramatically changes device performance.

LM-based device research mostly uses atomic layer deposition (ALD) high-k insulators (k = 16 $\sim$ 20) such as Al_2O_3, HfO_2 and ZrO_2 which often result in the formation of charge traps at the interface between the deposited insulator and LM. The poor interface quality limits to achieve high performance complementary metal-oxide-semiconductor (CMOS) transistors with low operation voltage, low interface state density, reduced gate leakage current and high breakdown voltage. As a benchmark, low standby power CMOS requires a leakage current of below 1.5×10^2 A cm^{-2} and interface state density of below $\sim 10^{10}$ cm^{-2} eV^{-1} [194]. It is also known that directly depositing dielectrics on chemically inert surfaces of LMs is challenging, requiring surface functionalization using high energy process, reactive species or seeding layer. The high energy and reactive process, such as ultraviolet-ozone [195], electron beam irradiation [196], remote forming gas (5% H_2 in N_2) plasma [197], remote O_2 plasma [198], provide nucleation sites by increasing defect density or creating chemically-active surface layer. The seeding layer made of organic self-assembled monolayers [199] or a epitaxial monolayer molecular crystal [194] facilitates adsorption, resulting in conversion of hydrophobic surface to hydrophilic surface. However, deposited oxide films often face interface states and defects due to the inherent limitation of film deposition such as roughness and material damage occurred during the process. Additionally the extra film deposition process is cost-ineffective. Furthermore, all of these methods are quite different from the method used in Si technology. The high quality of SiO_2 is directly grown on Si substrate using wet oxidation or dry oxidation method rather than depositing SiO_2 film.

In this regard, there has been efforts to make native oxide on its semiconducting counterpart. It has been proven that $HfSe_2$ or $ZrSe_2$ transistors with its native oxide show good device performance (low hysteresis, on/off ratio of $> 10^6$, on$-$current of 30 μA/μm) by suppressing the thermal activation of interfacial trap states [82]. High performance Bi_2O_2Se field-effect transistors is demonstrated by converting few layers of Bi_2O_2Se to Bi_2SeO_5 in layer-by-layer manner upon thermal oxidation [200]. Beyond the thermal oxidation, MoO_3/MoS_2 heterostructure has been demonstrated using O_2 plasma, enabling layer-by-layer oxidation [201]. However, most of plasma oxidation

study on two-dimensional materials focus on layer-thinning, etching and stability [202–205] rather than investigating growth mechanism, interface quality from both morphological and electronic perspective, electronic and optical properties of native oxide and device performance.

In this chapter, our objective is to study growth kinetics of native oxidation of TMDs, particularly MoS_2 due to three reasons of that (1) we have a large geological MoS_2 crystal obtained from Smithsonian Institution, (2) bulk MoS_2 indirect band gap of 1.29 eV is very close to that of Si ($\sim$ 1.12 eV) and (3) MoO_3 is well-known as an efficient hole injection layer and its high work function could lower contact resistance of MoS_2 [206, 207]. Both thermal oxidation and non-thermal oxidation method are employed to make MoO_3/MoS_2 stack. Our main focus is in understanding the oxide growth mechanism of each method and controlling the relative rates of oxidation of MoS_2 to MoO_3 and volatilization of MoO_3. We identify mass transport mechanism in thermal oxidation, revealing that MoO_3 volatilization and vapor transport is a major challenge to make thin, conformal native oxide films on MoS_2 by thermal oxidation. To overcome these drawbacks, non-thermal oxidation using oxygen plasma processing is adopted at room temperature which enables to minimize vaporization of MoO_3. The preliminary data of O_2 plasma oxidation shows thin amorphous MoO_3 conformally covering MoS_2 even along the side wall, indicating O_2 diffuses into MoS_2 bulk and forms native oxide layer.

5.2 Experimental Methods

5.2.1 Thermal Annealing Process

Thermal oxidation process to grow SiO_2 films has been studied for decades, which is now well-known and well-understood. There are two thermal oxidation methods which are dry oxidation using oxygen gas and wet oxidation using water vapor or steam. Herein, we mainly focus on dry oxidation so thermal oxidation throughout this chapter refers to dry oxidation.

To find optimal processing method to directly grow continuous MoO_x layer on MoS_2 single crystal, three different thermal annealing methods are adopted: (1) tube furnace, (2) box furnace and (3) rapid thermal annealing (RTA) furnace. We first prepare the free-standing MoS_2 sample of $\leq$ 1 cm x 1 cm by cleaving the bulk counterpart using single-edge razor blade. Then the surface of MoS_2 is mechanically exfoliated using adhesive tape (3M, Scotch) at slow speed so as to obtain as large terrace of oxide-free surface as we are able to.

Atmospheric pressure chemical vapor deposition (CVD) with 1.5 inch quartz tube is employed to grow MoO_3 on single crystal MoS_2 substrate. The freshly exfoliated free-standing MoS_2 sample is placed in the center of the furnace to minimize the difference in set temperature (T_{set}) and actual temperature (T_{actual}). The system is pumped downed for 20 min and then the base pressure of 0.01 Torr is acquired. In the next step, the valve connected to the oil pump is closed and the tube is filled with a gas mixture of O_2 of 10 sccm and N_2 of 40 sccm until the overall gas pressure of the system reaches at atmospheric pressure. The sample is heated up to set temperature of 500 °C at the maximum ramping rate of the furnace ($\sim$ 15 °C/min) with an oxygen partial pressure (P_{O2}) of 0.2 atm and then annealed for 1 hr. To limit vaporization of MoO_3 during the cooling process, the sample is cooled down to room temperature while maintaining the same oxygen atmosphere.

The oxidation rate of MoS_2 depends on oxygen concentration, temperature, humidity and defect concentration. In addition to O_2 environment condition, H_2O in air could be a catalyst for oxidation at elevated temperature [171]. MoO_3 is grown onto MoS_2 over a range of temperatures from 350 to 500 °C by the box furnace in laboratory ambient condition of $P_{O2} \sim 0.2$ atm and relative humidity of $\sim$ 50 %. The heating rate is $\sim$ 10 °C/min. The temperature is maintained at the growth temperature over various duration (1, 5, 30 and 60 min). As soon as the growth is done, the box furnace is turned off and naturally cooled down to room temperature overnight.

Lastly, we use RTA system (AS-One, ANNEALSYS) which has fast ramp rate of 20 °C/sec and fast cooling rate of $\sim$ 1 °C/sec. There are several advantages of using RTA which are short processing time (manufacturable) and high ramp and cooling

rate. In addition, we can flow high purity process gases with mass flow controller and also can easily switch over between various process gases. The high heating rate is favorable in our experiment because MoO_3 is highly volatile. We expect to minimize the vaporization causing surface morphology perturbation by using fast ramp rate, which does not give atoms enough time to move around during ramping. The cleaved MoS_2 crystal is loaded directly onto susceptor without extra substrate, followed by pumping chamber down to ≤ 5 torr. Gas mixture of N_2 and O_2 is purged until the system reaches at atmospheric pressure. A series of P_{O2} is investigated by controlling the ratio of N_2 to O_2 while maintaining the total gas flow of 1000 sccm. For example, we introduce N_2 of 600 sccm and O_2 of 400 sccm for $(P_{O2}) = 0.4$. The RTA chamber is heated up to 450 °C and the sample is annealed at the temperature for several conditions of duration; 1 min, 5 min, 10 min, 20 min and 30 min. Once the annealing process is done, the chamber is cooled down to 100 °C at which we can safely open the chamber to unload sample.

5.2.2 Oxygen Plasma Treatment

In addition to thermal oxidation, MoO_x film is grown using an oxygen plasma system (AutoGlow) at room temperature. We choose oxygen plasma cleaner to test the idea of plasma oxidation of MoS_2. Thus, the experimental condition we use in this chapter is highly preliminary and needs to be further optimized using plasma system having better controllability over oxygen pressure (oxygen gas flow rates), radio frequency (RF) power (plasma power), duration, background pressure (vacuum) and substrate temperature. The RF power input heats electrons and gives energy to ionize [208]. Increase in gas pressure leads to increase collision frequency and decrease the plasma density. Therefore, the plasma density (= ion density = electron density) is determined by the balance between RF power and gas pressure. To reveal oxidation kinetics of plasma oxidation of MoS_2 and the effect of each parameter on oxidation process, the oxide thickness can be investigated by changing the aforementioned parameters. MoS_2 crystal is placed in a plasma chamber and the chamber is pumped down until the pressure drops to the desired base pressure of $0.5 \sim 1.0$ torr. The

surface is exposed to the plasma generated at the RF power of 100 W for 2 min, 150 W for 2 min, 150 W for 10 min and 200 W for 10 min in sequence. Between each plasma process, the sample is taken out to the air and investigated with optical microscope to look at visible change in color or morphology.

5.2.3 Graphene Growth and Wet Transfer

In low-pressure CVD system, monolayer graphene is synthesized on Cu foil (25 μm thick) pre-cleaned with acetic acid. The cleaning process is an essential step to remove common impurities on the foils, enabling to grow high quality monolayer graphene. The pre-cleaned Cu foil is placed in 1 inch quartz tube and the CVD system is pumped down for 30 min. The quartz chamber is heated up to 1035 °C with ramping rate of $\approx$ 35 °C. While ramping up, 50 standard cubic centimeter (sccm) of H_2 gas (P $\approx$ 1.5 Torr) is used as an input gas to create reducing environment limiting the formation of amorphous carbon with dangling bonds. After the temperature is stabilized at 1035 °C, the Cu foil is annealed for 30 min in order to increase the Cu grain size and smoothen the surface. In the growth step 6 sccm of methane (CH_4) gas is introduced at 1035 °C for 40 min, which is followed by cooling process to room temperature under 40 sccm of H_2 and 6 sccm of CH_4 to prevent as-synthesized graphene from oxidizing and hydrogenation reactions.

We mask MoS_2 surface with CVD-grown monolayer graphene, that allows us to determine what mass transport route is taken during thermal annealing process. The graphene is transfered onto free-stranding MoS_2 crystal using conventional wet transfer method. The procedure is described as below.

(1) A 4.5 wt% solution of poly(methyl methacrylate) dissolved in anisole (PMMA, 950K, A9, MicroChem) is spin-coated onto as-grown graphene/Cu stack at 2500 rotations per minute (RPM) for 60 s as a carrier material and then baked in a box furnace at 80 °C for 15 min.

(2) The Cu foil is etched out by copper etchant (*i.e.* iron chloride ($FeCl_3$) aqueous solution, CE-100, Transene Company Inc.) for 15 min, resulting in floated PMMA/graphene stack on the surface of the etchant.

(3) The PMMA/graphene stack is rinsed with de-ionized (DI) water, 10 wt% hydrochloric acid (HCl) soluton (ACS grade, Hydrochloric Acid 36.5 - 38 %, VWR, Analytical) and DI water. HCl solution eliminates the etchant residue in the form of metallic salt and DI water in the last step removes the HCl residue.

(4) The rinsed PMMA/graphene stack is scooped out onto the free-standing MoS_2 crystal at room temperature and then is dried overnight in the fume hood to gently evaporate residual water trapped at the interface and finally to form conformal contact between graphene and MoS_2. If target substrate is flat such as Si/SiO_2 wafer, compressed N_2 gas blow can replace the overnight drying step. We find that peel-off or rip-off of graphene occurs even with the gentle drying step by N_2, due to uneven and curved surface features of MoS_2.

(5) The overall PMMA/graphene/MoS_2 stack is immersed in acetone solvent at room temperature for 20 min and then washed with isopropyl alcohol (IPA).

5.2.4 Mechanically Exfoliated Graphite and CAB-mediated Transfer

We use mechanically exfoliated graphite to partially mask MoS_2 for the same purpose as dictated in the previous Section 5.2.3. The main differences between mechanically exfoliated graphite and monolayer CVD graphene are thickness and defect density. Whereas mechanically exfoliated crystal does not have grain boundary, CVD-grown poly crystalline monolayer suffers from high grain boundary densities.

We intentionally use thick graphite not only to eliminate the possibility of remote epitaxy growth through mono- or bi-layer graphene but also to make the graphene pattern visible under optical microscope and scanning electron microscope (SEM). Graphite is exfoliated on a pre-cleaned Si/SiO_2 substrate using scotch tape and adhesive tape (Nitto Denko America Inc. 3195MS). Then the exfoliated graphite flake is transferred onto MoS_2 using cellulose acetate butyrate (CAB)-mediated transfer method [209]. The transfer is based on water intercalation happening in between a hydrophilic Si/SiO_2 substrate and hydrophobic graphite flake embedded in hydropho-

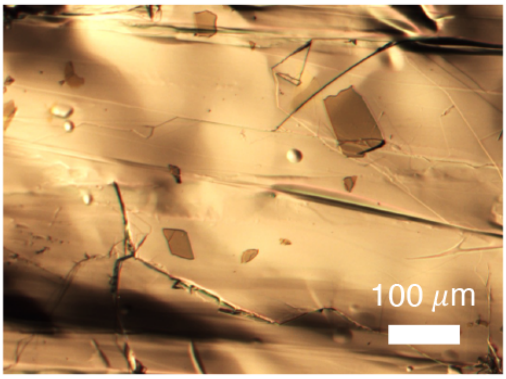

Figure 5-1: **Graphene patches on MoS_2 crystal.** Optical microscope image of mechanically exfoliated graphite transferred onto MoS_2 bulk crystal.

bic polymer. The full details of the process is described below.

(1) CAB solution (20 wt%) is prepared by dissolving 10 g CAB in 40 ml ethyl acetate. The exfoliated graphite onto SiO_2 stack is spin-coated with the CAB solution at 1500 rpm for 60 s with an acceleration of 300 rpm/s, followed by baking at 80 °C for 6 min.

(2) CAB around the flake of interest is cut in a rectangle with enough margin by using a scalpel. A droplet of DI water is added over the cut line. The water droplet intercalate between substrate and CAB, resulted in lifting-off the rectangular CAB layer embedding graphite flake from the substrate.

(3) MoS_2 crystal is placed on a optical microscope stage to find terrace and then the graphite/CAB stack is transferred to the region of interest subsequently.

(4) To improve adhesion between graphite and MoS_2, the sample is baked at 140 °C (T_g of CAB $\sim$ 130 °C) for 15 min. After cooling down the sample, the sample is put into acetone for 15 min and rinsed with IPA.

Figure 5-1 shows the resulting exfoliated crystals on free standing MoS_2 crystal with various thickness.

5.2.5 Characterization Methods

Morphology of MoO_x crystallite is analyzed using an optical microscope and high-resolution SEM (Zeiss Merlin). The SEM plan-view images are mainly collected in

high resolution secondary electron imaging mode. Graphene/MoS_2 specimens are examined using an in-lens secondary electron detector to achieve even higher image resolution of 1.4nm at accelerating voltage of 1 kV. Comparing to out-lens detector (Everhart-Thornley detector), in-lens detector shows less background of indirect secondary electron produced on chamber walls [210]. We characterize the MoO_x phase and crystallinity using Raman spectroscopy (Reinshaw Invia Reflex Micro Raman) at room temperature, with a 532 nm laser excitation source with an optical intensity of $6.5\mu W/\mu m^2$ to minimize the sample degradation attributed to the thermal effect of laser. The minimum achievable spot size of Raman is theoretically diffraction-limited which is simply defined by the laser wavelength and microscope objective.

$$\text{Laser spot diameter} = 1.22\ \lambda\ /\ \text{NA}$$

where λ is the wavelength of the laser and NA is the numerical aperture.

Our Raman microscope objectives have a specification as follow: NA of 50x is 0.75, NA of LWD100x is 0.75 and NA of 100x is 0.9. We use LWD100x for data collection which the theoretical spot size is $\sim$ 865 nm with a 532 nm laser. As complementary method, high resolution transmission electron microscopy (HR-TEM, JEOL 2100 and JEOL 2010) and scanning transmission electronic microscopy (STEM) is also used to determine the phase of MoO_x of whether it is amorphous or crystalline (if so, which crystalline phase). Cross-sectional TEM samples are prepared by focused ion beam (FIB) with electron beam and Ga ion (Ga^+) source. We perform HR-TEM at electron beam energy of 80 and 200 kV. Compositional analysis and chemical states is done using X-ray photoelectron spectroscopy (XPS, Nexsa G2 Surface Analysis System, ThermoFisher Scientific), with a monochromatic aluminum Kα X-ray source (spot size $\sim$ 100 μm), and pass energy of 200 eV and 50 eV for survey scans and for high-resolution scans, respectively. Before collecting XPS spectra, we use monatomic Ar ion beam with 1000 eV for 30 s to remove surface adsorbates such as hydrocarbon. Although crystalline MoO_3 is a n-type wide band-gap semiconductor with a gap of 3.2 eV [211] not a insulator, amorphous molybdenum oxysulfide could be less conductive and charges could build up on the surface. After each scan is done, thus,

electron flood gun is used to neutralize positive surface charge accumulated on the surface and avoid unexpected peak shifts caused by the surface charging. Combined with XPS, we use energy dispersive X-ray analysis (EDS or EDX) to identify the elemental composition and visualize the spatial distribution of elements as a map with an operating electron energy of $5 \sim 15$ kV. EDS detector (Oxford Instruments) attached in JOEL 7900F SEM is utilized. Electron energy loss spectroscopy (EELS) spectrum is acquired on Themis Z STEM at 200 kV. The energy resolution, measured as the full width at half maximum of the zero loss peak (ZLP), is 0.7 eV with an energy dispersion of 0.15 eV/pixel (overview spectra), and 0.05 eV/pixel (fine structure). This 0.15 eV dispersion allows the recording of the Mo-M2,3 and O-K edges on the same spectra. All spectra is first x-ray removed and aligned by the ZLP using the Gatan software. Background subtraction is performed in the pre-edge energy window for each spectra. The multiple scattering is then removed by Fourier-ratio deconvolution with the aligned low-loss spectrum obtained for the same region of the sample.

5.3 Results and Discussion

5.3.1 Growth Mechanism of Thermal Oxide of MoS_2 crystal: Thermal Oxidation

We oxidize the freshly exfoliated MoS_2 crystals in ambient box furnace while varying processing temperature and holding other conditions constant (See Section 5.2.1), in order to investigate temperature effect on growth mechanism of thermal oxide, and further on morphology and composition of resulting oxide. Processing temperature is chosen based on the fact that (1) volatilization process of MoO_3 is dominant above 550 °C [212] and (2) Mo undergoes oxidation into orthorhombic MoO_3 excluding MoO_2 and the non-stoichiometric oxides above 350 °C [213].

In Figure 5-2, SEM indicates that thermal oxide processed above 450 °C is highly faceted, discrete and elongated hexagon-shaped crystalline plates. Raman spectra indicates that the phase of the resulting oxide is α-MoO_3 [214, 215]. The unit cell of

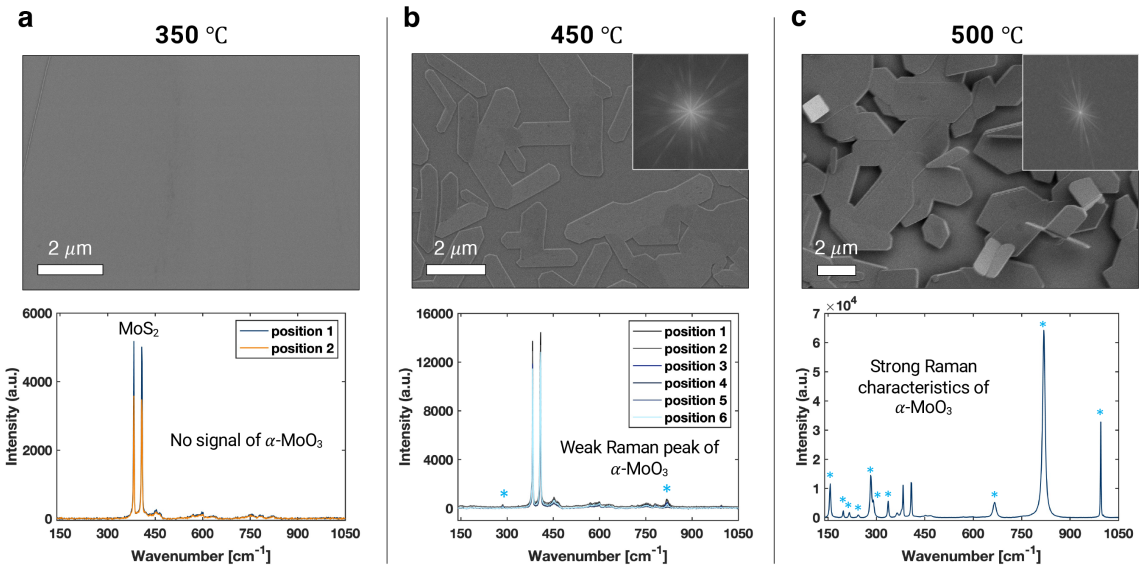

Figure 5-2: **Processing temperature effect on oxide formation.** SEM images and Raman spectra of freshly-exfoliated bulk MoS_2 oxidized at (a) 350 °C, (b) 450 °C and (c) 500 °C for 1 hr in ambient air. Insets in (b) and (c) show 2D Fourier transform pattern of MoO_3 processed with edge detection filter, which reveals dodecagon pattern.

α-MoO_3 is orthorhombic with lattice constants a = 0.394 nm, b = 1.386 nm and c = 0.369 nm and is composed of double-layers of MoO_6 stacked together along [010] by van der Waals force [213].

Combining the crystal shape and phase identification, we find that the large face of crystal is (010) plane which is the stoichiometric surface with the lowest surface energy. The preferential growth direction corresponding to long axis is [100] or [001] because {100} and {001} planes have high surface energy and chemical activity [213, 216]. We note that oxide crystallites annealed at 450 °C are observed mostly near active sites such as layer-edge and step-edge. In contrast, MoO_3 crystallites oxidized at 500 °C are found throughout the crystal not limited to edge site, including (010) plane faces. Three types of growth mode of MoO_3 are found relative to the location on MoS_2 surface: (1) Near layer-edge, crystallite in long strip shape are found along the layer-edge, (2) in the terrace near layer-edge, in-plane hexagonal crystallite similar to 450 °C result are found and (3) in the terrace far from the layer-edge, out-of-plane crystallites are dominant which the elongated direction of [100] or [001] is orthogonal to MoS_2

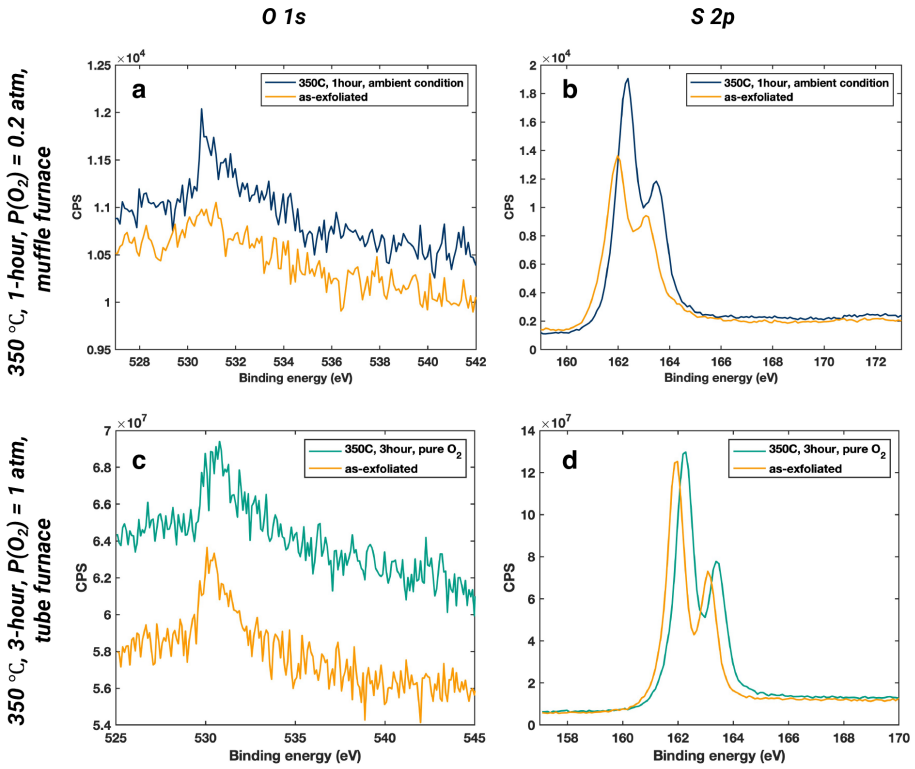

Figure 5-3: **High resolution XPS spectra of O 1s and S 2p peaks collected on thermally oxidized MoS_2 at 350 °C.** (a)-(b) O 1s and S 2p core emission, respectively, for a freshly-exfoliated sample (yellow) and a sample annealed in ambient air for 1 hr. (c)-(d) O 1s and S 2p core emission, respectively, for a freshly-exfoliated sample (yellow) and a sample annealed in pure O_2 at 1 atm for 3 hr.

basal plane. We infer thermal annealing at 500 °C increases S vacancies on the terrace, leading to high nucleation density even on relatively inert terrace region. To identify the angular relationship of overlying MoO_3 with underlying MoS_2, we extract the edge of crystallites using a edge detection filter and perform the fast Fourier transform (FFT) (insets in Figure 5-2b-c). The FFT dodecagon pattern explains that MoO_3 is formed on 2H-MoS_2 (hexagonal phase) with identical angular relationship via van der Waals epitaxy [207]. The reciprocal two-dimensional lattice of α-MoO_3 is rhombus and α-MoO_3 grown on MoS_2 shows three possible orientation, resulting in 12-fold pattern [207]. Please note that FFT pattern of 500 °C sample is weak because the merged crystallites obscure the edge detection step. On the contrary, MoO_3 grown on amorphous SiO_2 is randomly oriented without any angular preference due to an abundance of dangling-bonds existed on SiO_2 as shown in Figure 5-7a. The crystal

shape of MoO_3 on SiO_2 is regular-hexagon not elongated hexagon-shape found in MoO_3 grown on MoS_2 (signature of van der Waals epitaxy) [217]. It has been proved that MoO_3 can be expitaxially deposited on crystalline LMs [207, 217, 218] but what leads the epitaxial growth has not been clearly identified. Therefore, further advanced study such as in-situ TEM is required to understand the epitaxial growth mechanism of whether it is driven by minimization of strain energy and surface energy, and to investigate nucleation sites among various candidates of V_s, V_{Mo}, atop Mo and S atom.

MoS_2 oxidized at 350 °C does not result in perceptible oxidation, as evidenced by XPS studies (Figure 5-3), SEM and Raman (Figure 5-2), whereas oxidation at 450 °C already results in discrete MoO_3 crystallite formation. We oxidize the sample in even harsher oxidation condition in pure O_2 environment for extended processing time ($\sim$ 3 hr). No morphology change is observed and O 1s spectrum does not show any detectable sign of Mo-O bonding and S-O bonding, revealing that the MoS_2 surface is not oxidized.

The composition of thermal oxide grown at 450 °C and 500 °C are measured by EDS mapping and EDS spectrum. As shown in EDS elemental mapping in Figure 5-4 and Figure 5-5c, overlying MoO_3 contains strong O peak. Mo and S peaks are found throughout the region of interest which is attributed to the exposed underlying MoS_2 and the overlapping of Mo Lα and S Kα complicate the elemental analysis. The STEM cross-sectional image of MoS_2 oxidized at 500 °C shows that overall thickness of MoO_3 layer is $\sim$ 230 nm consisted of 30 $\sim$ 100 nm-thick MoO_3 blocks and void between them (Figure 5-5). Figure 5-5b confirms that the oxide blocks have faceted sidewalls and are separated by boundaries of lower atomic number. The blocks are not strongly crystalline as evidenced by a weak diffraction signal from atomic layers parallel to the film surface. The vertical lines underneath MoO_3 in Figure 5-5a and the dark shadow below void in Figure 5-5b are artifacts from FIB.

We further investigates the chemical features of MoO_3 layered on MoS_2 by measuring the fine structure of EELS edges (Figure 5-6). The EELS spectrum shows sharp Mo M edge peak at 382 eV and O K edge peak at 531.2 eV, featuring Mo^{6+}

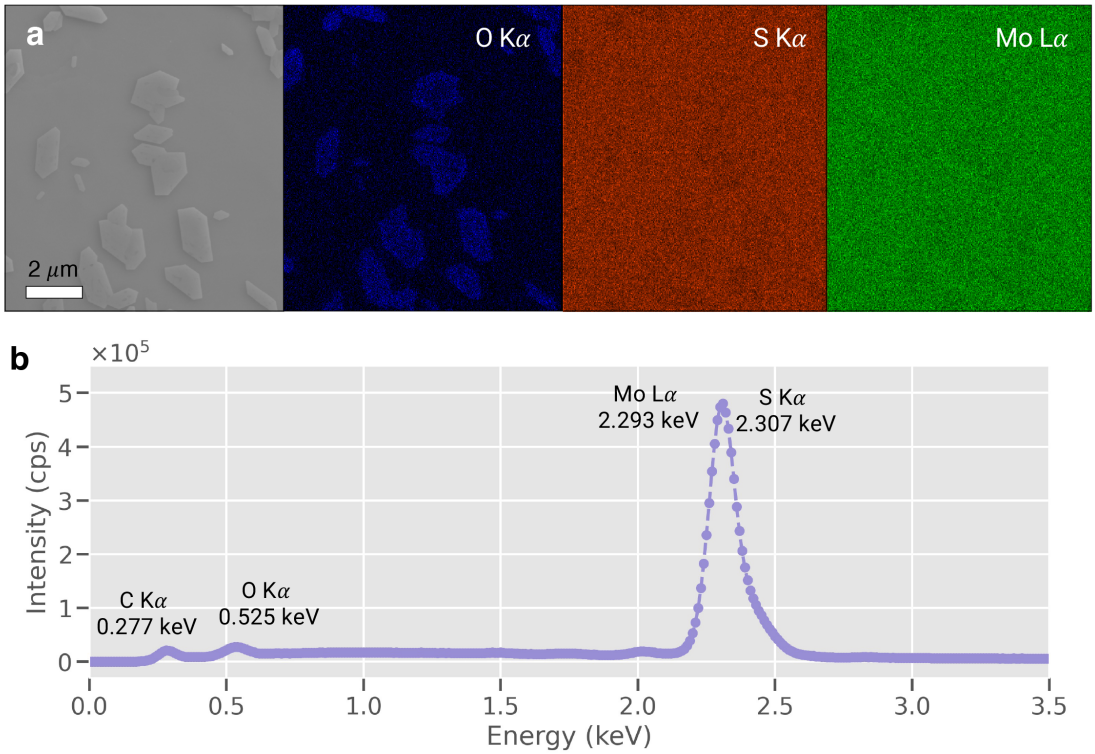

Figure 5-4: **Elemental analysis of freshly-exfoliated MoS_2 oxidized at 450 °C and 0.2 atm O_2 for 1 hr.** (a) EDS mapping and elemental analysis, including O, S and Mo. (b) The corresponding EDS spectrum.

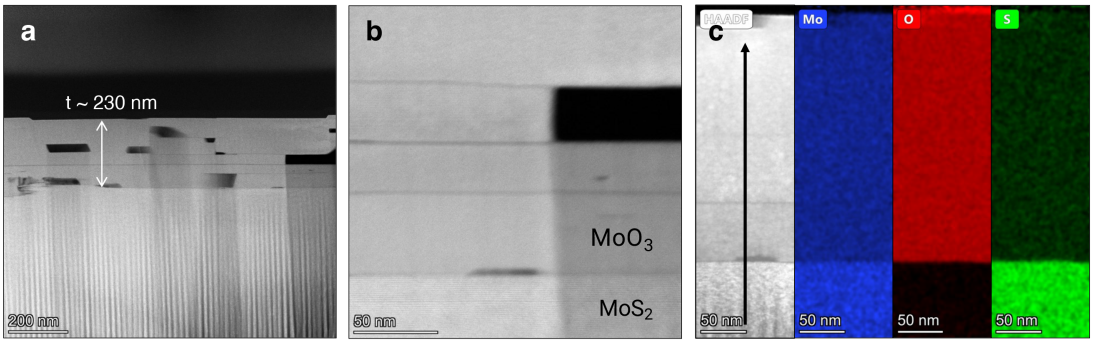

Figure 5-5: **Structural characterization and compositional analysis for MoO_3 crystallite grown on MoS_2.** (a) Cross-sectional STEM images of freshly exfoliated MoS_2 crystal oxidized at 500 °C and P(O_2 = 0.2 atm for 1 hr. The sample is prepared by FIB and the linear structures in MoS_2 are an artifact of the FIB process which is known as curtaining. Thickness of the non-uniform MoO_3 is ∼ 230 nm. (b) STEM cross section shows visible lattice planes of MoS_2, thick MoO_3 block and some voids. The darker shaded region beneath the void is an artifact caused by milling. (c) EDS elemental mapping image and Mo, O and S distribution in the sample.

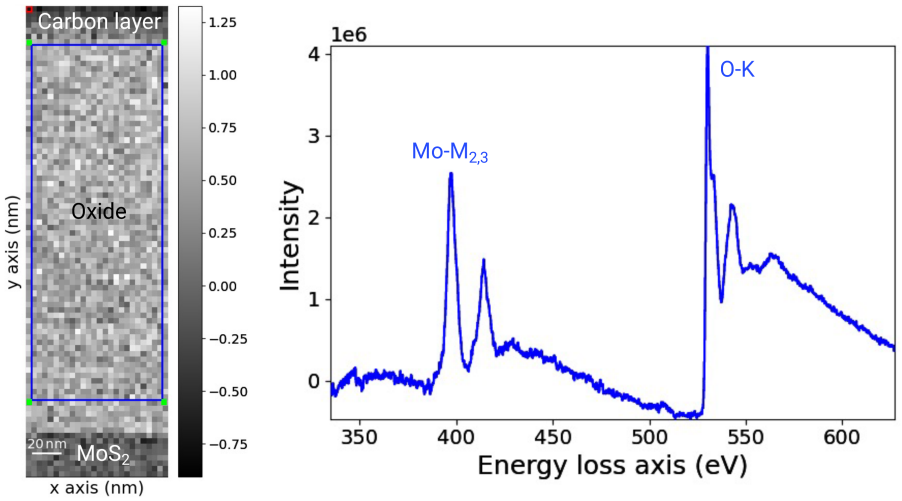

Figure 5-6: **EELS spectrum of MoO_3 grown on MoS_2 crystal at 500 °C and 0.2 atm O_2 for 1hr.** The oxygen fine structure suggests that oxide is MoO_3 with some oxygen vacancies.

and O_2- of MoO_3, whereas the the spectrum measured from MoS_2 does not show the signature of oxygen peak [219]. The small shoulder of O K edge peak at 532.5 eV indicates the presence of oxygen vacancies [220] which could be generated during thermal annealing process.

To understand the mass transport mechanism (vapor phase transport vs. solid state diffusion) and oxidation mechanism (layer-by-layer growth vs. nucleation, growth and coalescence), we carefully design three experiments:

(1) The freshly-exfoliated MoS_2 crystal is sandwiched between pre-cleaned Si/SiO_2 wafers. The top wafer is placed face down on MoS_2 surface with micro-gap.

(2) CVD monolayer graphene is transferred onto the MoS_2 crystal and covers the whole surface (for experimental method, see Section 5.2.3).

(3) Mechanically exfoliated thick graphites are transferred onto the MoS_2 and used as a patterned mask (see Section 5.2.4).

The prepared stacks are annealed at 500 °C and 0.2 atm O_2 for 1hr in simple box furnace (See Section 5.2.1). Figure 5-7 shows SEM images of hexagon-shaped MoO_3 crystals grown on Si/SiO_2 wafer, monolayer graphene and patterned graphite, suggesting that MoO_3 is formed by vapor phase growth. Similar mechanism has been found in previous research that van der Waals epitaxial growth of MoO_3 can be

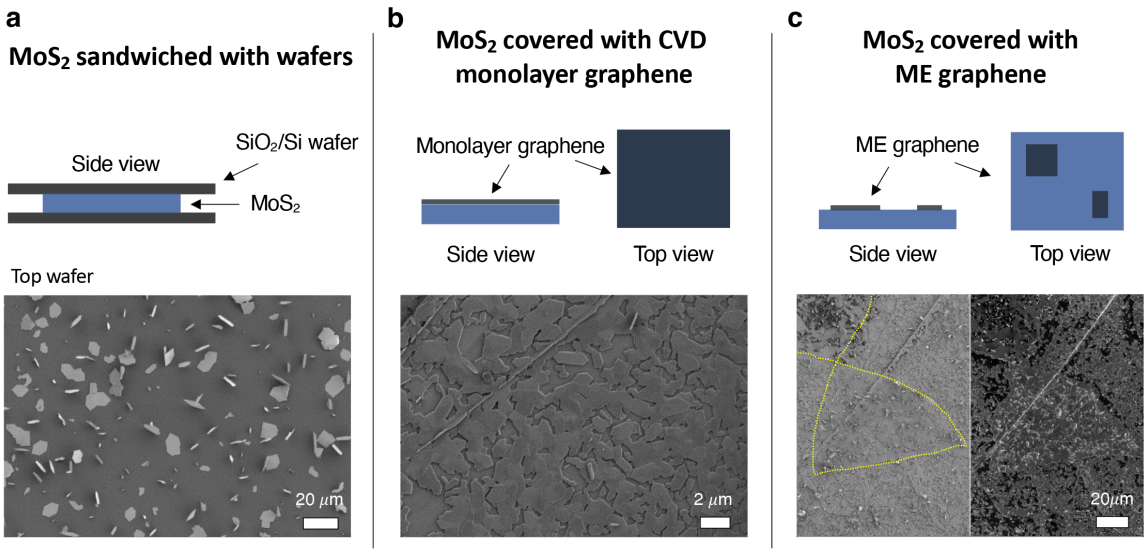

Figure 5-7: **Experimental design to identify mass transport mechanism.** Illustration of the method used and resulting SEM images. (a) MoS_2 crystal is sandwiched between Si/SiO_2 wafers, (b) CVD-grown monolayer graphene is transferred onto MoS_2 and (c) mechanically-exfoliated graphite flakes are placed on MoS_2. Surface of MoS_2 crystal is exfoliated using adhesive tape before oxidation processing which anneals samples at 500 °C and 0.2 atm O_2 for 1hr. SEM images show that MoO_3 crystallite grown on Si/SiO_2 wafer which is placed face-down on top surface of MoS_2 with micro-gap. And MoO_3 grows over the monolayer graphene and mechanically exfoliated graphite flake.

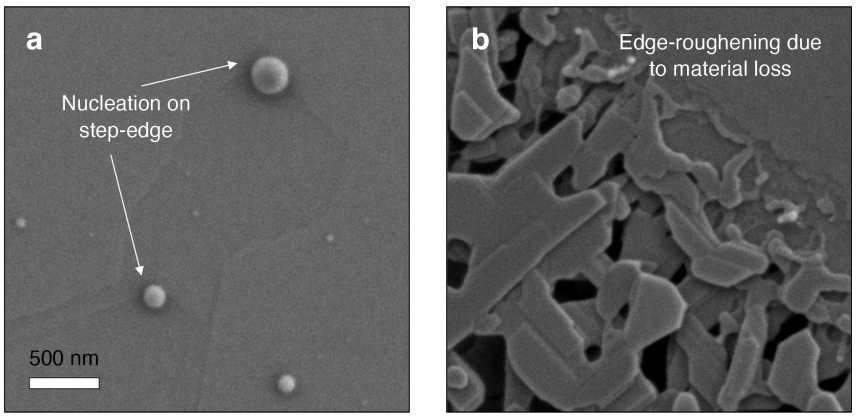

Figure 5-8: **Trace of vaporization and nucleation of thermally oxidized MoS_2 at 500 °C, 0.2 atm O_2 for 1 hr.** SEM images of showing (a) nuclei formation on step-edge and (b) edge-roughening due to vaporization of MoO_3 which is preferentially formed along the crystal layer-edge.

done on highly-oriented crystalline LMs using Mo metal instead of MoS_2 [217, 218]. We propose the growth mechanism of thermal oxidation that firstly MoS_2 surface is

oxidized into MoO_x, secondly, the MoO_x is sublimated and re-deposited on the MoS_2 surface through nucleation, growth and coalescence. MoO_3 grown on monolayer and graphite flakes have larger grain size than one grown on MoS_2. The average grain size (D) is estimated of D(MoS_2) < D(monolayer graphene) < D(bulk graphite). We believe that high defect densities (sulfur vacancies) of MoS_2 generated during thermal annealing increase the nucleation density, leading to smaller grain size. The bulk graphite shows good thermal stability than monolayer in air, resulted in the most intact surface with the least active site [221].

During thermal annealing at 500 °C in air, MoS_2 is etched with edges with zigzag-terminated or armchair-terminated as represented in Figure 5-8. The step-edges serve as preferred nucleation sites by reducing energy barrier of nuclei formation. In heterogenous nucleation, the step-edge shows smaller energy barrier than terrace because the required surface free energy ($\Delta G = \gamma A$, where γ = surface energy/unit area, A = total surface area) to form nuclei is smaller on the step-edge with smaller surface area. The predominant vaporization occurs in edge sites of MoS_2, which is evidenced by faceted edge structure (Figure 5-8).

To minimize the sublimation of MoO_3 and investigate the time evolution of morphology as a function of annealing time, RTA annealing is adopted and the bulk MoS_2 crystal is annealed at 450 °C, $P(O_2)$ = 0.2 atm at different growth times: 1 min, 5 min and 10 min. SEM images of resulting MoO_3 crystal (Figure 5-9) show that the initial shape of crystal is square which is consistent with the predicted equilibrium morphology of MoO_3 [216], followed by anisotrpic growth along preferential growth direciton of [100] or [001], followed by coalescence of individual crystal.

With temperature and duration control, we investigate the effect of oxygen partial pressure on MoO_3 formation. Because high volatilization rate of MoO_x interferes with making conformal, continuous and uniform MoO_3 thin film on MoS_2, we oxidize the MoS_2 crystal at higher oxygen pressure (*i.e.* $P(O_2)$ = 0.4 atm) than atmospheric condition (*i.e.* $P(O_2)$ = 0.2 atom). In Figure 5-10, high oxygen pressure enables in-plane oxide growth with high surface coverage, providing uniform and continuous oxide film. The film coverage increases with growth time meaning fully-covered MoO_3

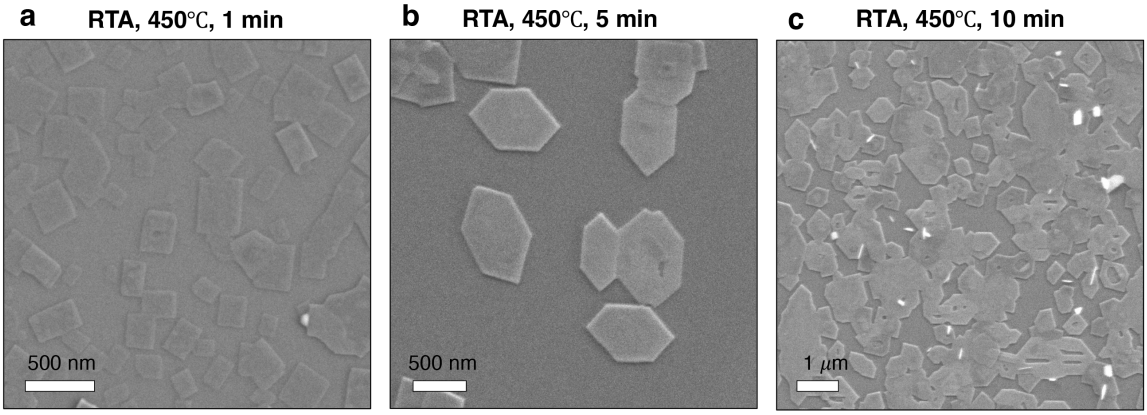

Figure 5-9: **Morphology evolution of MoO_3 crystallite as function of processing time.** SEM images of freshly-exfoliated MoS_2 crystal oxidized at 450 °C and 0.2 atm O_2 for (a) 1 min, (b) 5 min and (c) 10 min. Note that RTA system is employed for fast heating rate of 20 °C/sec, preventing unnecessary material's loss from occurring during the extended ramp period.

could be obtained by increasing the growth time. We note that thermal oxidation over 30 min in RTA system is not viable due the the equipment limitation. Figure 5-10c shows some holes in the oxide film resulting from merging of different crystals and these hole can be filled up by extending the growth time.

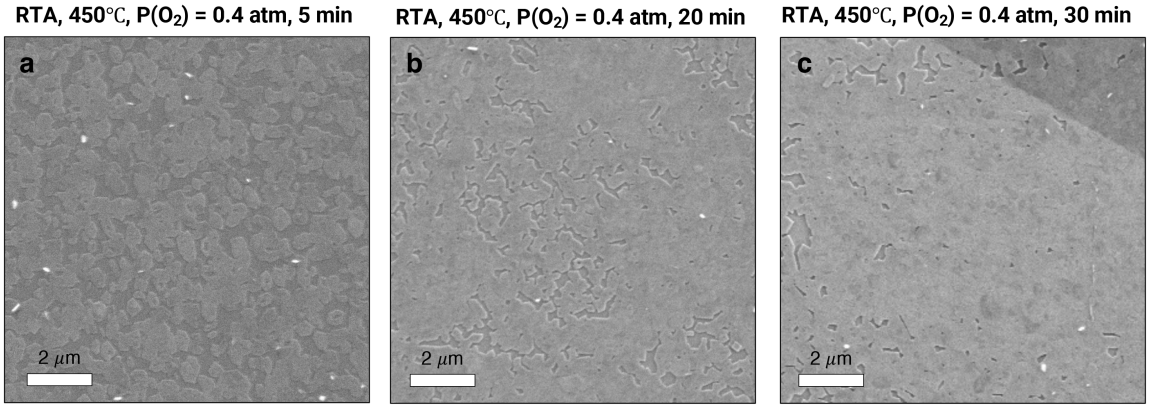

Figure 5-10: **The effect of O_2 pressure on morphology of thermal oxide.** SEM images of freshly-exfoliated MoS_2 crystal oxidized at 450 °C and 0.4 atm O_2 for (a) 5 min, (b) 20 min and (c) 30 min, indicating that MoO_3 grows laterally rather than forming protruded crystalline along out-of-plane direction. With processing time increases, MoO_3 domains close the surface of MoS_2 through lateral growth and coalescence with other grains.

Based on all the evidence above, we conclude that MoO_3 formed by thermal oxidation is a volatile oxide, and is used as a precursor for MoS_2 thin film growth by

vapor transport. Therefore, we hypothesize that the oxidation process proceeds as: (1) MoO_x formation, accompanied by sulfur release into the vapor phase, (2) MoO_x evaporation and re-condensation, (3) MoO_x attachment on oxide nucleation sites, (4) MoO_3 crystal growth. To test this hypothesis, we carry out a series of experiments with modified substrates on which MoO_3 crystals could form only through vapor transport of the Mo precursor. The results clearly demonstrated that MoO_x evaporation is a key step in the observed thermal oxidation process leading to structures such as shown in Figure 5-2. Given these results, making conformal, thin native oxide films requires enhancing the rate of MoO_x formation relative to the rate of MoO_x volatilization, requiring non-thermal method.

5.3.2 O_2 Plasma-generated MoO_3: Plasma Oxidation

RF plasma is employed to make continuous and conformal MoS_2/MoO_3 stack as non-thermal oxidation method (for method see Section 5.2.2). Figure 5-11a-b shows continuous, smooth and uniform MoO_3. The presence of oxygen throughout the surface is confirmed by EDS map and EDS spectrum (inset in Figure 5-11c), featuring O Kα peak as marked with blue. Although the EDS spectrum is taken at electron beam energy of 2.5 kV which is much lower than minimum recommended energy for EDS of $\sim$ 5 kV, it is chosen to increase signal from light element (here, oxygen) and exclude Mo Lα and S Kα features originated from underlying bulk MoS_2. Cross-sectional STEM is conducted on MoS_2 crystal oxidized using plasma, to confirm the formation of MoO_3 and understand the process of MoS_2 oxidation, at an accelerating voltage of 80 kV to reduce knock-on damage in MoS_2/MoO_3 stack. Visible degradation in MoS_2 is observed at electron beam energy of 200 kV. The bright field STEM images (Figure 5-11d) clearly show the double-layered structure comprised of MoS_2 and MoO_3. The plasma-generated MoO_3 is conformally formed on curved MoS_2 surface with the thickness of $\sim$ 4 nm. In Figure 5-12, high-resolution STEM imaging of the plasma-generated MoO_3 indicates growth of an amorphous oxide. We use EDS elemental mapping to identify the elemental composition and to visualize the spatial distribution of elements (Figure 5-11e), revealing oxygen resides in structurally amorphous

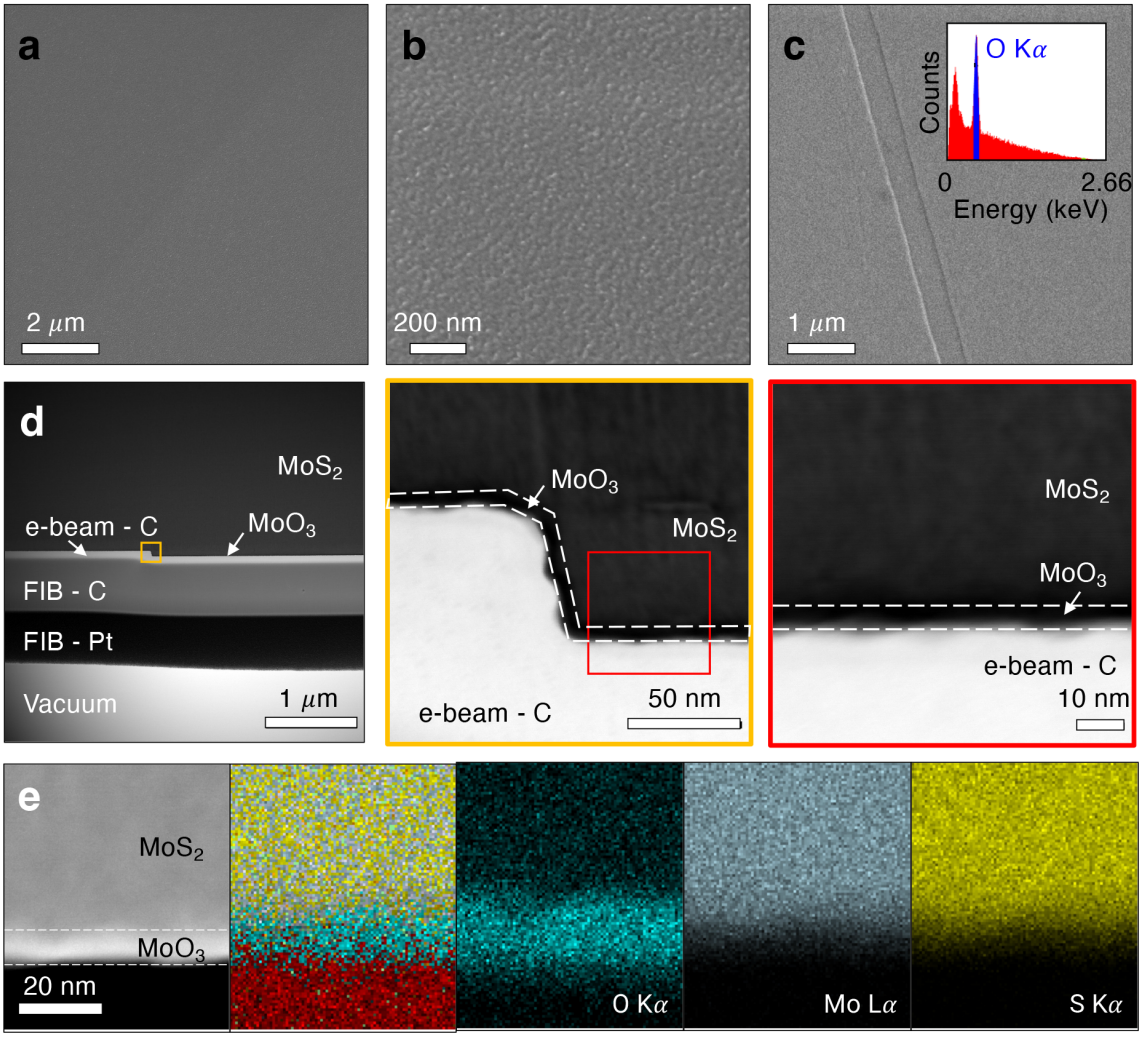

Figure 5-11: **Morphology, structure and composition analysis of plasma-generated MoO_3/MoS_2.** SEM (a-b) in-lens and (c) high-resolution secondary electron images of the oxygen plasma-processed MoS_2 film at three magnifications. The inset shows EDS spectrum collected in the region of interest. Blue peak corresponds to O Kα and red peak in the lower energy regime corresponds to Mo Mα and S Lα. (d) Cross sectional STEM images demonstrating a thin, conformal native oxide formed on MoS_2 by O_2 plasma. (e) STEM-EDS element mapping of O Kα, Mo Lα and S Kα, showing the layer structure qualitatively, indicating displacement of S by O in oxide layer. We note that the same sample is used for SEM, STEM and EDS shown in (a)-(e).

regions.

The overlap of Mo L and S K emission peaks complicates quantitative analysis. We semi-quantitatively identify the oxide composition using a line scan across the specimen, demonstrating the spectral evolution across the MoS_2/MoO_3 stack is pro-

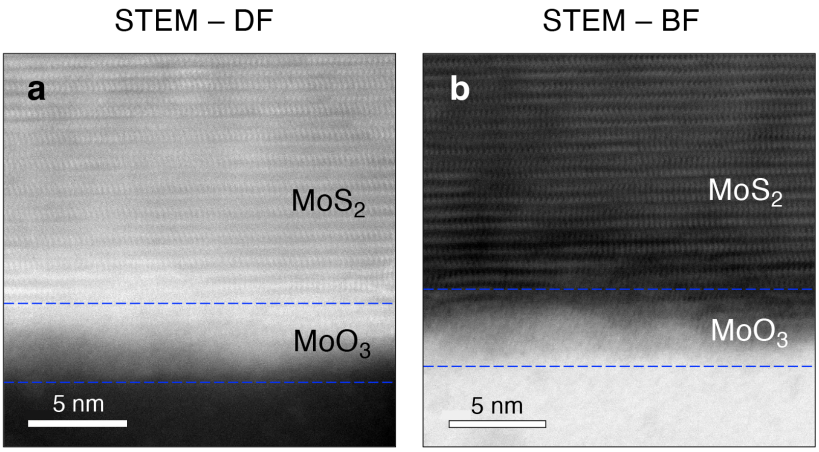

Figure 5-12: **Identification of oxide phase.** High-resolution STEM cross sections of plasma-generated MoO_3/MoS_2. (a) Dark field STEM cross section showing vivid lattice fringe of MoS_2 and hazy region of MoO_3, featuring plasma-generated MoO_3 is amorphous.

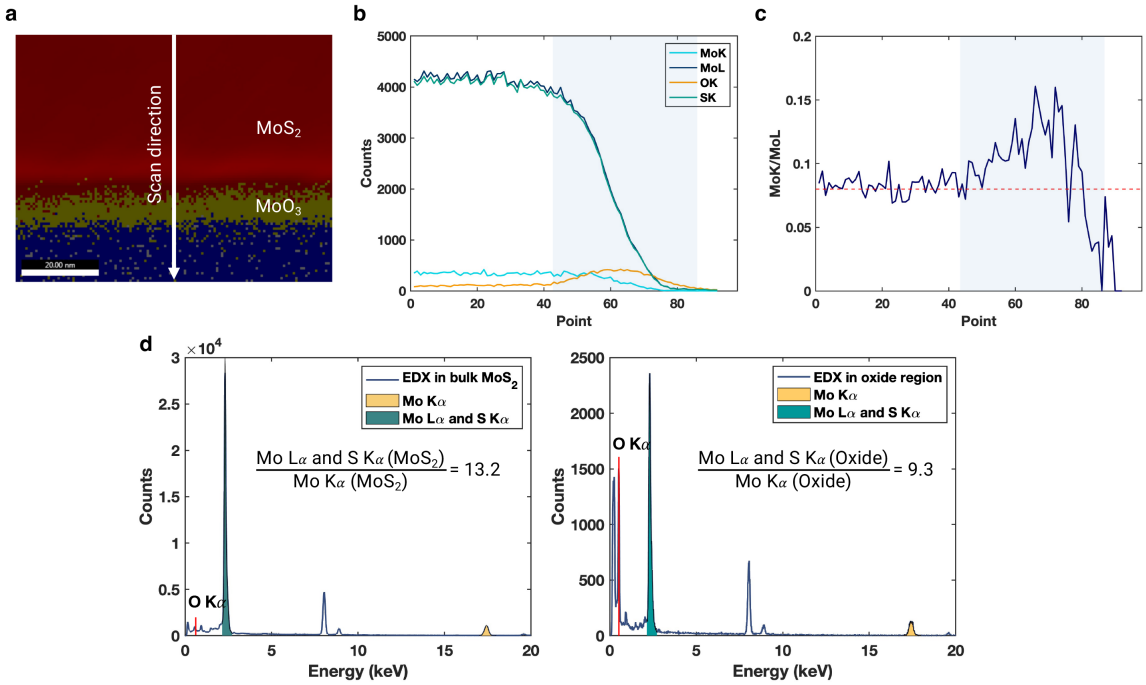

Figure 5-13: **Composition analysis of plasma-generated MoO_3.** EDS data lines-cans analyzed to determine native oxide composition. (a) False-color image showing line scan. (b) EDS spectra intensity for Mo K, Mo L, O K, and S K emission. (c) Ratio of Mo K to Mo L (which is combined with S K) intensity. The peak in the oxide region indicates a decrease in sulfur concentration in this layer. (d) Individual EDS spectra collected in (left) bulk MoS_2 and (right) oxide area. The equation is to calculate the ratio of the area beneath Mo L (which is combined with S K) to the area beneath Mo K. The decrease in the ratio suggests less sulfur in oxide.

vided in Figure 5-13. We assume the same amount of Mo in both region of MoO_3 and MoS_2 and the ratio of Mo K to Mo L (included S K) should be constant if there is no composition change across the sample. However, the peak in the oxide (shaded region in Figure 5-13c) is observed which infers sulfur is deficient in the oxide layer. In similar concept, we compare the area under the Mo K and Mo L (which is combined with the S K) peaks in EDS spectra as shown in 5-13d, also demonstrating the sulfur concentration in oxide is relatively lower than in MoS_2.

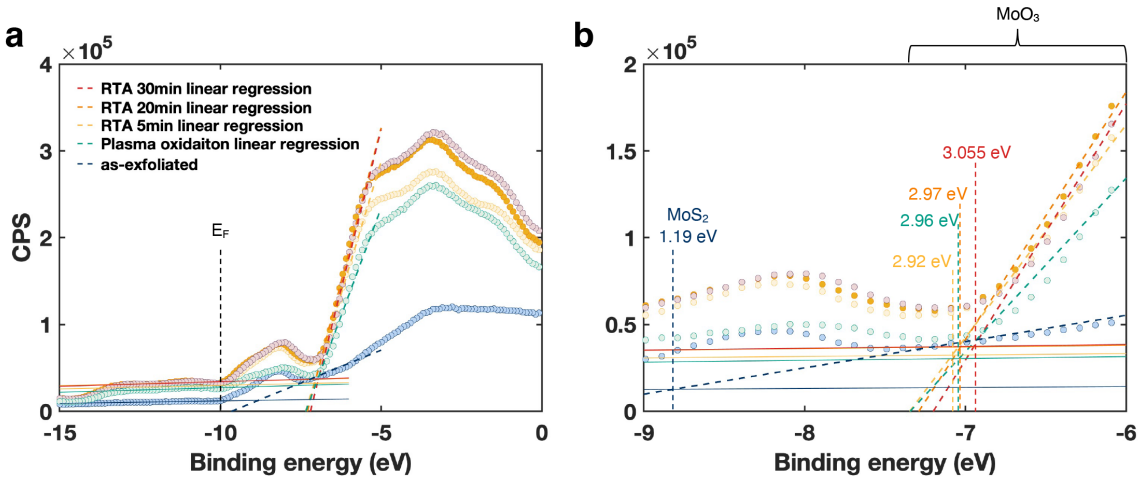

Figure 5-14: **UPS characterization of MoS_2 and MoO_3.** (a) UPS spectra of the low binding energy regime (valence region) near the Fermi level for as-exfoliated MoS_2(meaning the surface is freshly-exfoliated with scotch tape) and MoO_3 processed in various oxidation conditions. (b) Magnified image near the Fermi energy (Here, it is located at -10 eV because we bias samples with 10 V. For conducting samples, 10V bias shifts UPS spectra by around 10 eV).

We investigate the electronic properties of thermal oxide and plasma-generated oxide using ultraviolet photoelectron spectroscopy (UPS) with spot size of 2 mm, HeII source (40.81 eV), and the sample is biased with 10 V leading a measured spectrum shift by 10 eV. Consequently, -10 eV corresponds to Fermi energy. The valence band edge of as-exfoliated bulk MoS_2 is 1.18 eV below Fermi level and it is known that indirect band gap of bulk MoS_2 is 1.29 eV, suggesting MoS_2 is n-type semiconductor. Thermally oxidized MoS_2 have the valence band edge at 2.92, 2.99 and 3.055 eV. The more oxide forms as annealing period increases, resulted in shift of valence band edge to further down from fermi energy level (Figure 5-14b). The valence band edge of

plasma-generated oxide is 2.96 eV which is comparable to thermally oxidized MoS_2 at 450 °C, $P(O_2)$ = 0.4 atm for 20 min. The metallic feature around -8 eV appears due to surface contamination or something else.

5.4 Conclusion

In conclusion, we demonstrate the role of various process parameters involved in thermal oxidation of MoS_2 such as annealing temperature, oxygen partial pressure, heating rate and annealing duration. We find that MoO_3 is grown on MoS_2 by van der Waal epitaxy and the continuous closed thin MoO_3 can be formed at 450 °C, $P(O_2)$ = 0.4 atm for longer than 30 min in RTA system with high ramp rate to minimize the surface perturbation. It is proved that thermal oxidation mechanism is based on nucleation, growth and coalescence with the source from MoO_x sublimation. However, it seems to difficult to find a sweet spot having balance between MoO_x formation rate and MoO_x volatilization rate. To overcome the challenges associated with thermal process, we adopt non-thermal oxidation method, RF plasma oxidation. Our results on plasma-generated oxide include extensive study of SEM, HR-TEM, STEM, Raman, XPS and UPS. Taken together, these results suggest that plasma-generated oxide is a conformal, continuous and amorphous thin film ($\sim$ 4 nm) indicating oxidation occurs in bulk MoS_2 by reacting with oxygen. We also demonstrate the electronic structure, focusing on the difference between fermi energy and valence band edge. The valence band edge (2.96 eV) of plasma-generated MoO_3 is comparable to thermal oxide (2.99 eV).

5.5 Contribution Statements

Kate Reidy in Frances Ross's group at MIT transferred mechanically exfoliated graphite on bulk MoS_2 and performed STEM and EELS on MoO_3 grown on MoS_2 at 500 °C in box furnace. Jules Gardener and Austin Akey at Harvard University carried out STEM, HR-TEM and cross-sectional EDS.

Chapter 6

Photonic Platforms using In-Plane Optical Anisotropy

This chapter is adapted with permission from ref. [222].

Jo, S.S., Wu, C., Zhu, L., Yang, L., Li, M., Jaramillo, R., "Photonic Platforms Using In-Plane Optical Anisotropy of Tin (II) Selenide and Black Phosphorus", *Adv. Photonics Res.* **2**, 2100176 (2021), with the permission of Wiley.

6.1 Project Introduction

In this Chapter, we introduce how we can use dielectric anisotropy of group IV-monochalcogenides to modulate phase of signal light on several photonic devices using photonic simulation tool. After we navigate the opportunities in integrated photonics using computation, we will discuss the experimental efforts to change the crystal structure of group IV-monochalcogenides using linearly polarized light. Layered and two-dimensional (2D) semiconductors interact strongly with light and feature a variety of crystalline structures that, at least in principle, can be switched quickly and with low energy input. This suggests a variety of applications of 2D materials for active optical phase modulation in photonic integrated circuits (PICs). Many 2D semiconductors feature band gap in the range of 1 – 2 eV, and therefore are favorable for refractive near-infrared (NIR) applications [12]. All layered materials are strongly

Table 6.1: **Selection of layered and 2D materials with substantial optical anisotropy within individual layers. In this work we consider devices using SnSe and bP; our results suggest similar applications of other materials.**

Material	a (Å)	b (Å)	Space Group	Reference
SnO	3.66	4.03	P_{mmn}	Zhou et al. [47]
SnSe	4.28	4.40	P_{m2_1n}	Zhou et al. [8]
SnS	4.08	4.31	P_{m2_1n}	Xiong et al. [227]
GeSe	3.59	5.73	P_{m2_1n}	Zhou et al. [228]
GeS	3.64	4.52	P_{m2_1n}	Xiong et al. [227]
bP	3.30	4.63	P_{mna}	Wei et al. [229]

birefringent, with refractive index much higher for electric field polarization within the layers (ordinary) than perpendicular (extraordinary) [223, 224]. Here we focus on 2D materials that are substantially triaxial, with low optical symmetry within individual layers [225, 226]. Among layered and 2D materials there are many with substantial optical anisotropy within individual layers, including the group-IV monochalcogenides MX (M = Ge or Sn, X = S or Se) and black phosphorous (bP). We study whether the optical anisotropy within individual layers can be used to switch light in PIC devices, provided that a mechanism is available to switch the crystal orientation (*i.e.* the domain pattern). We use numerical device modeling to study how confined light interacts with these layered materials with varying crystal orientation, and to simulate several device concepts. Our results may be broadly applicable to 2D materials with ferroelectric and ferroelastic crystal structures (Table 6.1).

6.2 Ferroelastic Switching using In-Plane Optical Anisotropy

Our work is inspired by a theoretical prediction of non-thermal transformations between crystalline domains in ferroelastic 2D materials driven by light and in-plane dielectric anisotropy [8, 101, 228]. In Figure 6-1a we illustrate energetically-degenerate ferroelastic domains in monolayer tin (II) selenide (SnSe). The structure has a rectangular unit cell, with lattice constants a = 4.275 Å (zig-zag direction) and b = 4.401 Å

(armchair direction). The predicted switching effect is due to the substantial in-plane anisotropy of the dielectric tensor ε_{ij}. The dielectric energy for an applied electric field $\underline{\mathrm{E}}$ depends on the polarization, and this polarization-dependence generates a torque on the crystal. For sufficiently-strong electric field and dielectric anisotropy, theory predicts a barrier-less transformation between ferroelastic domain types [8]. For materials that are ferroelectric and ferroelastic, both terms linear in $\underline{\mathrm{E}}$ (*i.e.* ferroelectric polarization) and quadratic in $\underline{\mathrm{E}}$ (*i.e.* dielectric polarization) may contribute to this effect. However, the linear term only contributes for low-frequency applied electric field, for which the crystal structure can follow the phase of the applied field. For high-frequency applied electric field, appropriate for switching triggered by optical pulses (*i.e.* light-controls-light), only the dielectric energy $\varepsilon_{ij}\mathrm{E_i E_j}$ remains. Therefore, this effect is general for materials with anisotropic dielectric tensors. Theory predicts opto-mechanical switching occurring on a time scale of picoseconds, and with optical energy input on the scale of 0.001 $\mathrm{aJ/nm^3}$ [8]. Therefore, this opto-mechanical effect may be competitive for photonic modulators operating at high bandwidth and with low power consumption.

Here we study devices based on switching ferroelastic domains in SnSe and bP, and operating in NIR and short-wavelength infrared (SWIR). The band gap ($\mathrm{E_g}$) of SnSe in bulk and monolayer forms is 0.9 and 1.6 eV, respectively, and is indirect in both cases [22]. For bP, $\mathrm{E_g}$ is 0.3 and 2 eV for bulk and monolayer forms, and is direct in both cases [88]. Optical anisotropy is enhanced near absorption resonances, so we design our devices to operate near $\mathrm{E_g}$ [8]. The complex dielectric tensors for SnSe and bP in bulk and monolayer forms are not well-established experimentally. Therefore, for consistency throughout this work we use refractive index data predicted by density functional theory (DFT). DFT has well-known systematic errors in predicting the energy of excited states, often resulting in under-estimation of $\mathrm{E_g}$. However, the predicted complex dielectric response is more accurate than excited-state energies because DFT produces accurate solutions for electron crystal wave functions, which are used to calculate the dielectric response in the random phase approximation (RPA) [230]. In other words, DFT-predicted $n(\lambda)$ and $k(\lambda)$ data are often inaccurate in the

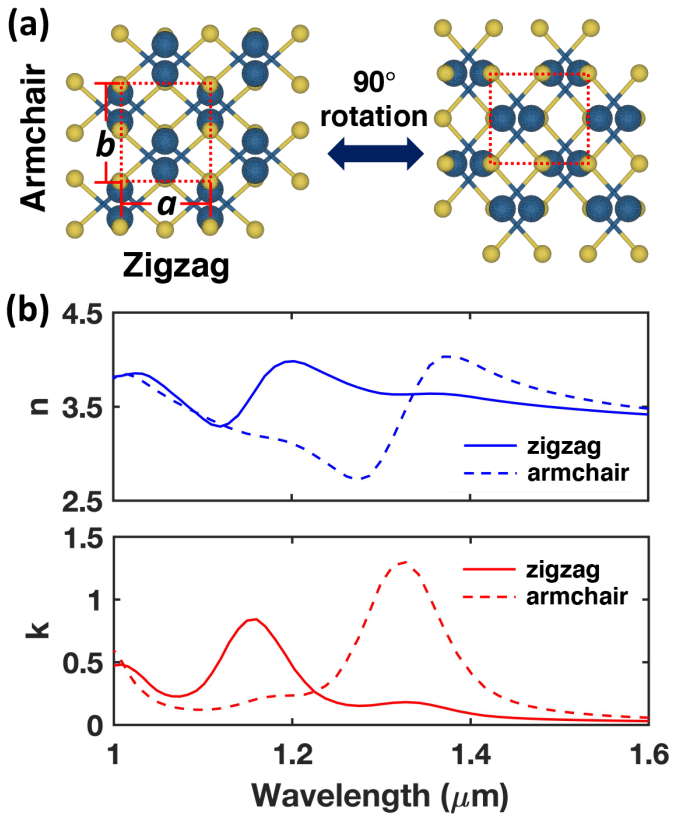

Figure 6-1: **In-plane optical anisotropy for monolayer SnSe.** (a) Top view of SnSe crystal structure showing the rectangular 2D unit cell with zig-zag (short axis) and armchair (long axis) directions. (b) Complex refractive index of monolayer SnSe for electric field polarized along the zig-zag and armchair directions, predicted by theory [8]. Theory under-estimates the band gap, which is in fact at 1.6 eV. Therefore, in real monolayer SnSe, the loss peaks (here seen in the NIR) would occur below 800 nm. Note that calculated n and k values are likely consistent with measured values but the spectral range could change due to the limitation of calculation.

abscissa, but acceptable in the ordinate: the features associated with band-to-band transitions (such as the SnSe absorption resonances between 1 – 1.4 μm in Figure 6-1b) may be rigidly shifted along the energy (horizontal) axis to match experiment [231]. In this work the optical properties of SnSe are as-calculated by DFT, and our simulated devices operate near DFT-predicted absorption resonances. Real devices will likely be designed to operate at higher photon energy, at or below the experimental E_g. The calculated optical properties for bP used here include a band gap correction, and therefore the operating photon energy range for the simulated bP devices is more accurate than for the simulated SnSe devices. We study the usefulness of the

optical anisotropy of layered materials with ferroelastic domains; we do not consider the mechanism of switching between domains, as we and others did in earlier work [8, 101, 228]. Both optical phase control and the domain switching mechanism rely on the anisotropic dielectric tensor. When an optical pulse in the visible-NIR is used for domain switching, only the electronic contribution to the dielectric response (ε_{ij}^{elec}, sometimes referred to as the optical dielectric constant, or ε_{∞}) is important. The anisotropy of the dielectric response of triaxial layered and 2D materials is often enhanced at low frequency; for instance, for SnS, ε_{ij} at low frequency is predicted to vary between 35 and 52 (values normalized to the susceptibility of free space) with varying electric field polarization within the layers [232]. In principle, low-frequency dielectric anisotropy could allow domain switching by direct current electric fields, but in practice the required field strengths are attainable only with laser fields.

6.3 Properties of and Devices based on Monolayer SnSe

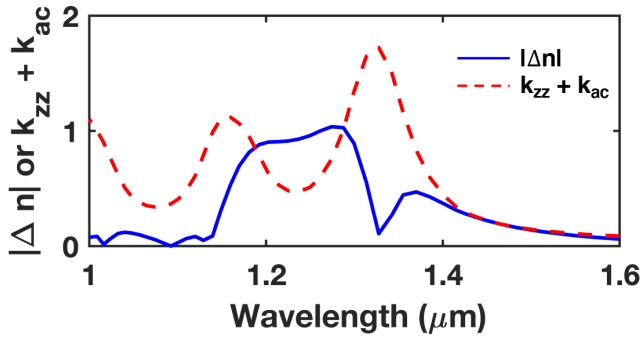

Figure 6-2: Difference in real refractive index of monolayer SnSe, $|\Delta n|=|n_{zz} - n_{ac}|$ and sum of imaginary refractive index $k_{zz} + k_{ac}$. Note that calculated n and k values are likely consistent with measured values but the spectral range could change due to the limitation of calculation.

SnSe is a layered material, but has relatively high exfoliation energy, and as a result has not been widely studied in monolayer form [9, 233, 234]. Therefore, we use the published, theoretically-predicted complex refractive index of monolayer SnSe in

our device simulations [8]. We present in Figure 6-1b the real (n) and imaginary (k) refractive indices along the zig-zag (ZZ) and armchair (AC) directions, and in Figure 6-2 the difference $|\Delta n| = |n_{zz} - n_{ac}|$ and the sum $\sum k = k_{zz} + k_{ac}$ between these directions. A high figure of merit (FoM) is required to efficiently modulate the phase of light with small propagation loss. There are at least two different FoM expressions encountered in the literature on phase-change materials for photonics: either $|\Delta n|/|\Delta k|$ and $|\Delta n|/|\sum k|$. In this work, we use the second expression of FoM $= |\Delta n|/\sum k$ to capture the usefulness of ferroelastic domain switching for controlling optical phase with low loss. For monolayer SnSe, a maximum FoM ≈ 2 is achieved at wavelength $\lambda = 1.24$ μm, at which $|\Delta n| = 0.93$ and $\sum k = 0.47$; see Figure 6-3 [8]. For reference, the widely-studied phase-change material $Ge_2Sb_2Te_5$ exhibits $|n_c - n_a| \sim 2.7$ and $k_c + k_a \sim 2.1$ in the range 1.2 - 1.6 μm [100, 235, 236]. We note that the expression $|\Delta n|/|\Delta k|$ often appears in the literature as a FoM for phase-change materials for photonics as aforementioned. This is particularly useful for proposed applications that use optical absorption in one of the states, such as switchable attenuators. However, it can mislead for designing low-insertion-loss devices, because it can obscure optical loss. According to this definition, ferroelastic switching in monolayer SnSe has a FoM of 152 at the wavelength of 1.23 μm for SnSe, with $|\Delta n| \sim 0.91$ and $|\Delta k| \sim 0.006$ (Figure 6-3a). In other words, the monolayer SnSe shows large refractive contrast and limited absorption contrast at 1.23 μm, according to theoretically-calculated optical properties. However, we believe that the second FoM expression is more broadly useful, as it emphasizes the value of low insertion loss in both configurations. In Figure 6-3c-d we similarly plot the FoM for bulk bP, calculated using both expressions with n, k values illustated in Figure 6-4.

We use the optical properties of monolayer SnSe to simulate an optical switch based on a silicon nitride (Si_3N_4) ring resonator integrated with a patch of monolayer SnSe that can switch between different ferroelastic domains (Figure 6-5a). The Si_3N_4 waveguide has width and thickness of 1 μm and 0.22 μm, respectively, and the SnSe layer thickness is 9 Å. The ring resonator has a bending radius of 50 μm and a realistic quality factor (Q) of 2×10^5 [237, 238].

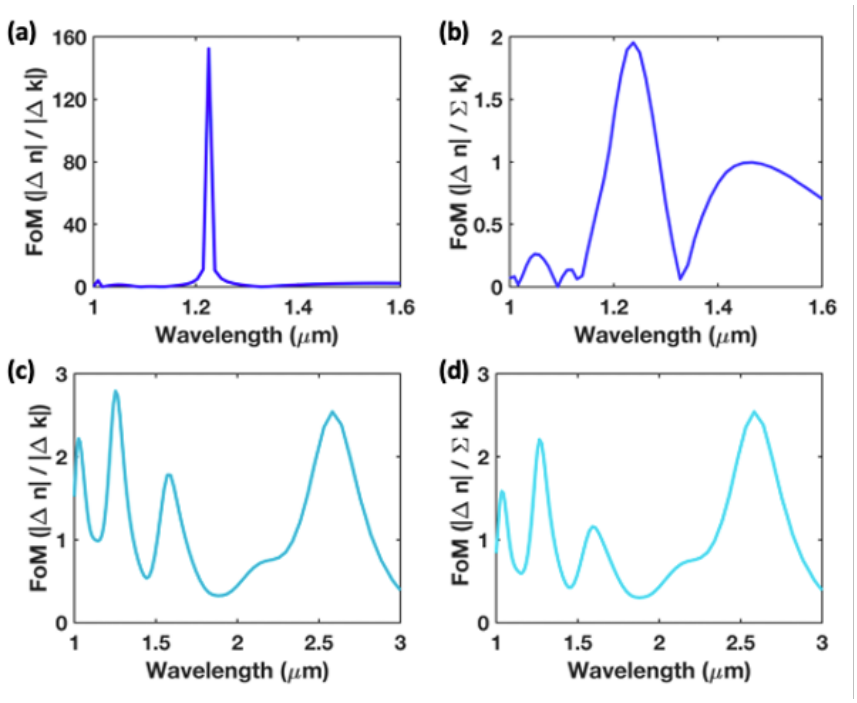

Figure 6-3: The FoM of (a-b) monolayer SnSe and (c-d) bulk bP in NIR range calculated using two different expressions. Note that calculated n and k values are likely consistent with measured values but the spectral range could change due to the limitation of calculation.

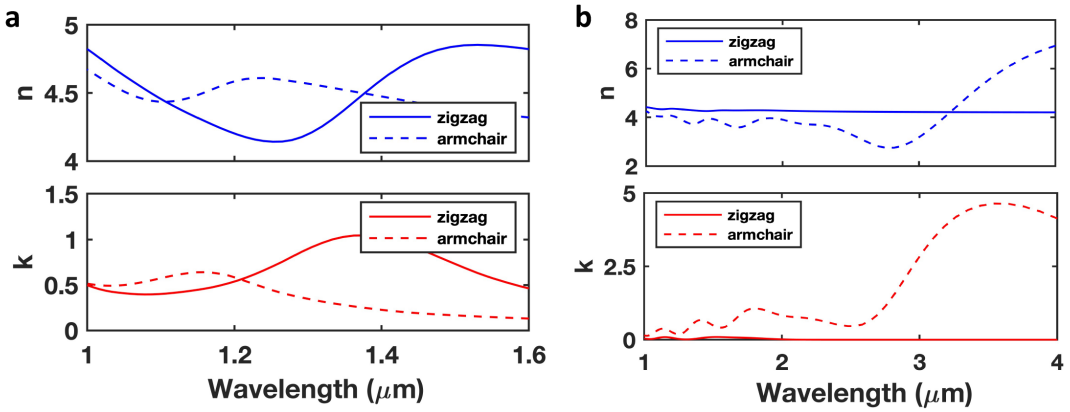

Figure 6-4: Real (n) and imaginary (k) refractive index of bulk (a) SnSe and (b) bP.

The guided optical modes couple evanescently to the SnSe monolayer. One principal axis of the monolayer SnSe (ZZ or AC) is aligned with the direction of light propagation ($\hat{z}$), and the other principal axis is aligned with $\hat{x}$. We choose the TE_0 mode, for which $\underline{E}$ for the guided light is directed mainly along $\hat{x}$. The ring is designed to be near-critically coupled to the bus waveguide when the SnSe zig-zag axis

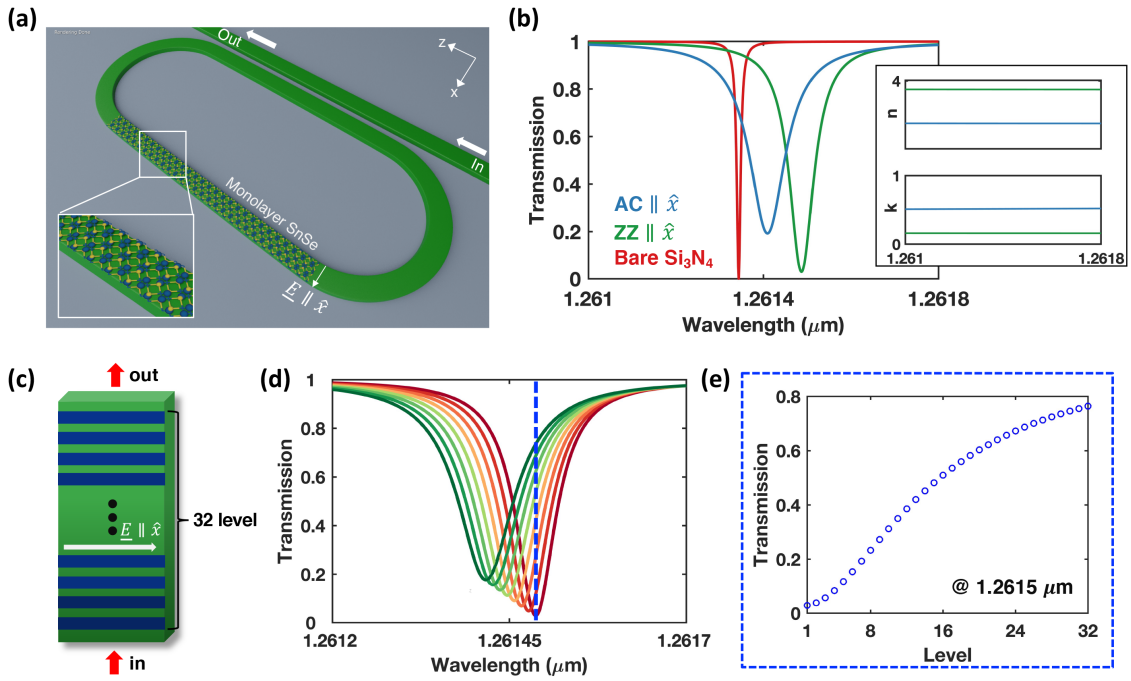

Figure 6-5: **Simulating a switchable ring-resonator using a monolayer SnSe active layer.** (a) Device illustration (not to scale). (b) Transmission spectra for resonator without SnSe (red), resonator with SnSe ZZ ∥ x̂ (green), and SnSe AC ∥ x̂ (blue). Simulations are for the TE_0 mode with E ∥ x̂. (Inset) The refractive index data $n(\lambda)$ and $k(\lambda)$ used for the simulation. Data are shown for E ∥ ZZ (green) and E ∥ AC (blue), and are effectively constant within the simulation window: $n_{AC} = 2.76$, $n_{ZZ} = 3.75$, $k_{AC} = 0.51$, $k_{ZZ} = 0.16$. (c) Schematic illustration (not to scale) of 32 × 1 array of monolayer SnSe patches, to simulate a multi-level device. (d) Variation in device transmission as the 32 SnSe patches are sequentially switched between ZZ ∥ x̂ and AC ∥ x̂ configurations. Dark red (far right) represents the case of all 32 patches aligned with ZZ ∥ x̂; dark green (far left) represents the case of all 32 patches aligned with AC ∥ x̂. (e) Transmission at $\lambda = 1.2615$ μm (indicated in (d) by blue dotted line) as the patches are sequentially switched from ZZ ∥ x̂ to AC ∥ x̂.

is aligned with $\hat{x}$ (ZZ $\parallel \hat{x}$). When the ferroelastic domain is switched, the resonance shifts, providing a means to control the transmission along the bus waveguide. We optimize the length of the SnSe patch and the coupling coefficient (defined as the ratio of electric field amplitudes in the bus waveguide and in the resonator) to optimize the transmission on/off ratio while minimizing insertion loss.

To optimize the performance of the SnSe integrated micro-ring modulator, we calculate the insertion loss and the modulation depth as a function of the coupling coefficient as well as the monolayer SnSe length. We use the following equation:

$$T = \left|\frac{a - re^{-i\varphi}}{1 - rae^{i\varphi}}\right|^2 = \frac{r^2 + a^2 - 2r \times a cos\varphi}{1 + r^2a^2 - 2r \times a cos\varphi'}$$

T is the transmission, r, a and φ represent the single-pass electrical field amplitude transmission, amplitude self-coupling coefficient and the single-pass phase shift respectively (Figure 6-6). We assume that the modulator works at the on-resonance wavelength when the crystal orientation ZZ $\parallel \hat{x}$ as shown in Figure 6-5b, which leads to an "Off" state with the transmission T_{Off}. Once the crystal orientation switches, the device is switch to an "On" state with the transmission T_{On}. The insertion thus is defined as -T_{on} (in dB), and the modulation depth is defined as T_{On}/T_{Off} (in dB). The star in Figure 6-6 labels the parameters used, which aims to obtain a high modulation depth with an acceptable insertion loss.

In Figure 6-5b we show the transmission spectra for an SnSe patch length of 35 μm; the inset shows the $n(\lambda)$ and $k(\lambda)$ data used in the simulation. The device has a broader linewidth and higher insertion loss for AC $\parallel \hat{x}$. At $\lambda = 1.2615$ μm, the difference in transmission between ZZ $\parallel \hat{x}$ and AC $\parallel \hat{x}$ is 0.74. This large dynamic range suggests the possibility of designing a multi-level device. To simulate such a device, we place a 32×1 array of monolayer SnSe patches on the waveguide, where each patch has area 1.1 x 1.2 μm^2 (Figure 6-5c). By sequentially switching the patches between ZZ $\parallel \hat{x}$ and AC $\parallel \hat{x}$ configurations, we simulate a device with 32 discrete transmission levels (Figure 6-5d).

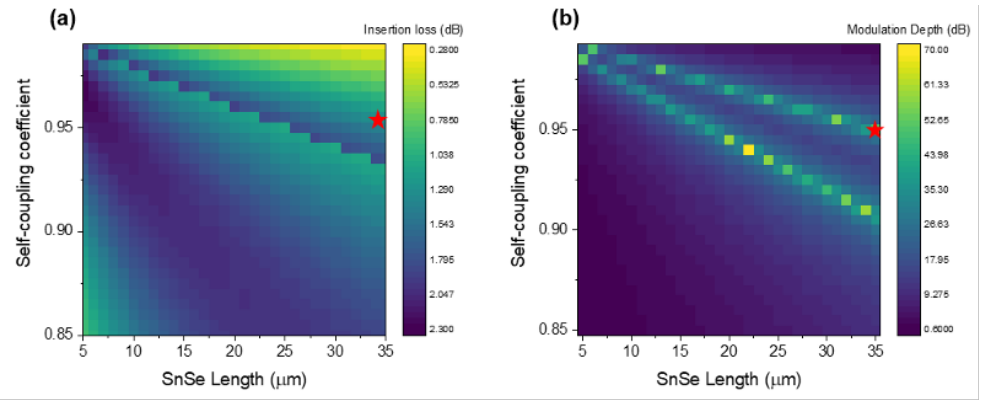

Figure 6-6: **Optimizing the transmission on/off ratio of the Si_3N_4 ring resonator with integrated monolayer SnSe.** (a) The insertion loss as a function of the coupling coefficient and the SnSe length. (b) The modulation depth as a function of the coupling coefficient and the length of the SnSe. The parameters used in the main text are shown as the star.

6.4 Properties of and Devices based on Bulk SnSe

We also simulate devices using bulk (*i.e.* many-layer thick) SnSe. As for the monolayer case, we use published, theoretically-predicted refractive index data [239]. Using this data, we find that bulk SnSe features a FoM of 0.68 at $\lambda = 1.55$ μm, with $\Delta n = 0.50$ and $\sum k = 0.73$. Δn is smaller for bulk than for monolayer SnSe, but the larger interaction volume allows devices with shorter interaction length.

In Figure 6-7a we show the results of a simulated Si_3N_4 ring resonator with a bulk SnSe active layer, working the telecommunications C-band ($\lambda \approx 1530 - 1565$ μm). The Si_3N_4 waveguide has thickness 0.22 μm and width 1.2 μm, and the SnSe active layer has thickness 10 nm and interaction length of 4 μm. Compared to monolayer SnSe, the larger interaction volume produces a larger shift in the resonance position, but the device also has higher optical loss. Due to the large width of the resonance for of ZZ $\parallel \hat{x}$, the maximum transmission contrast (found at the local minimum for AC $\parallel \hat{x}$) is 0.52, which is 30% smaller than the maximum contrast for monolayer SnSe. It is noteworthy that polarization-dependent optical response shows the opposite behavior in monolayer and bulk SnSe; *i.e.*, in the monolayer case AC $\parallel \hat{x}$ is lossier, but in the bulk case ZZ $\parallel \hat{x}$ is lossier.

We also design an asymmetrical 1×2 switch integrated with bulk SnSe as shown

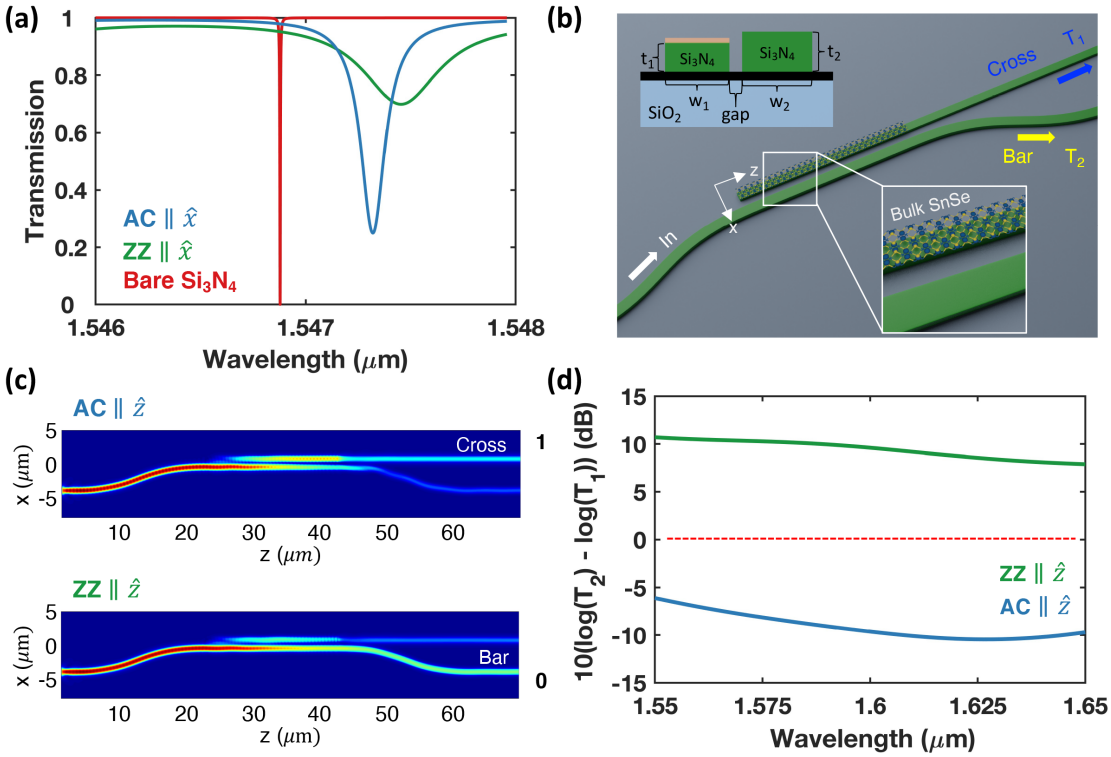

Figure 6-7: **Simulating a switchable ring-resonator and a 1 × 2 switch using a bulk SnSe active layer.** (a) Transmission spectrum for a bare ring resonator (red), resonator with bulk SnSe with ZZ ∥ x̂ (green), and resonator with AC ∥ x̂ (blue); the geometry is as shown in Figure 6-5a. (b) Schematic of 1 × 2 directional coupler. Port 1 is the cross-port and port 2 is the bar-port. The insets show a cross-section view and a representation of a waveguided with integrated SnSe (not to-scale). (c) Representative simulated data at $\lambda = 1600$ nm; the colors indicate optical power. (d) The loss contrast between bar-port (T_2) and cross-port (T_1) for ZZ ∥ ẑ (green) and AC ∥ ẑ (blue).

in Figure 6-7b. The 1 × 2 switch relies on the asymmetric coupling between a Si_3N_4 ridge waveguide and a bulk SnSe-on-Si_3N_4 hybrid waveguide operating in the TM mode, for which $\underline{E}$ is parallel with light propagation direction ($\hat{z}$). To optimize the geometry, we simulated the hybrid eigenmode supported by the asymmetrically-coupled waveguides using the frequency-domain finite-element (FDTD) method.

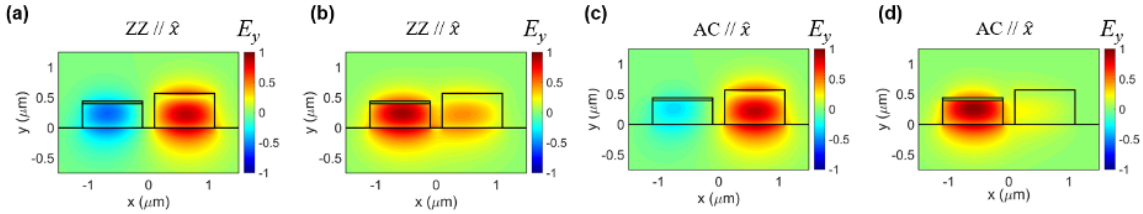

Figure 6-8: **Design the mode coupling of the bulk SnSe integrated 1 × 2 switch.** This image shows the cross section structure corresponding to Figure 6-7. Normalized electrical field E_y profiles of the supermodes in the two-coupled-waveguide system when the crystal orientation of bulk SnSe is in (a-b) ZZ ∥ x̂ and (c-d) AC ∥ x̂. (a), (c) show the antisymmetric mode and (b), (d) show the symmetric mode. Due to the large mode index mismatch when AC ∥ x̂ the coupling strength between two waveguides is low, resulting in two isolated modes.

The widths of the strip waveguide and the hybrid waveguide are optimally chosen to make their mode effective indices equal when the ZZ axis of the SnSe is aligned with the x-axis of the waveguide (see Figure 6-8 and Section 6.7.1). Figure 6-8a-b shows the electrical field E_y distribution for the hybrid TM mode, the mode strongly coupled between two waveguides. Therefore, the input TM-polarized light will be evanescently coupled to the cross port completely for an appropriate coupling length. Meanwhile, when the crystal orientation switches, the large contrast in effective index between the two waveguides results in substantial phase mismatch, resulting in two isolated modes as shown in Figure 6-8c-d.

The cross-port waveguide is set to be 1 μm wide (w_1) and 400 nm tall (t_1), and it is fully covered by SnSe with thickness of 40 nm. The bar-port waveguide has a width (w_2) of 1.2 μm and a height (t_2) of 540 nm, and is separated from the cross-port by a 200 nm gap, with a waveguide-to-waveguide coupling length of 20 μm. When the SnSe AC axis is aligned with the direction of light propagation (AC ∥ $\hat{z}$, ZZ ∥ x̂), the phase-matching condition is satisfied, and light incident from the ridge waveguide

couples into the hybrid waveguide (Port 1), leading to the cross-switch state (Figure 6-7c, top). When the ferroelastic domain switches, the phase-matching condition is altered, leading to the bar-switch state (Figure 6-7c, bottom). In Figure 6-7d we show the contrast between the bar-port and the cross-port, 10(log(T_2) - log(T_1)), where T_2 and T_1 correspond to the transmitted power at the bar-port and cross-port, respectively. The device shows a large contrast upon ferroelectric domain switching, from -10 to 10 dB, over a large bandwidth. Although this performance is not good enough to completely change the light propagation path, it can be used as an effective modulator.

6.5 Properties of and Devices Based on Bulk bP

bP is a widely-studied material due to its potential usefulness for electronic and mid-IR photonic applications [240–242]. Here we simulate a ring resonator and a directional coupler using bulk bP, as we do above for SnSe. Like SnSe, the crystal structure of bP is orthorhombic and consists of puckered honeycomb layers with inversion symmetry, with a rectangular in-plane unit cell as shown in Figure 6-9a. We show $|\Delta n|$=$|n_{zz} - n_{ac}|$ and sum $k_{zz} + k_{ac}$ for bulk bP in Figure 6-9b and the FoM for bulk bP is calculated using methods described previously (Figure 6-3) [243]. For bulk bP, a maximum FoM ≈ 2.5 is achieved at wavelength $\lambda = 2.58$ μm, at which $|\Delta n| = 1.15$ and $\sum k = 0.45$. Based on this FoM data, we choose to simulate devices operating at $\lambda \approx 2.5$ μm. As noted in Section , the theoretical data for bP includes a band gap correction (unlike the theoretical data used for SnSe), and therefore the operating wavelength range simulated here may accurately match future experiments.

We design a ring resonator to be critically coupled to the bus waveguide when the ZZ axis of bP is aligned with the direction of light propagation (AC $\parallel \hat{x}$, as illustrated in Figure 6-5a). The resulting device has a Si_3N_4 waveguide 1.6 μm wide and 330 nm thick, with a bending radius of 100 μm. A bP layer 10 nm thick fully covers the waveguide for an interaction length of 5 μm. We present in Figure 6-9c the device transmission spectrum. The resonance shifts shorter wavelength and develops more

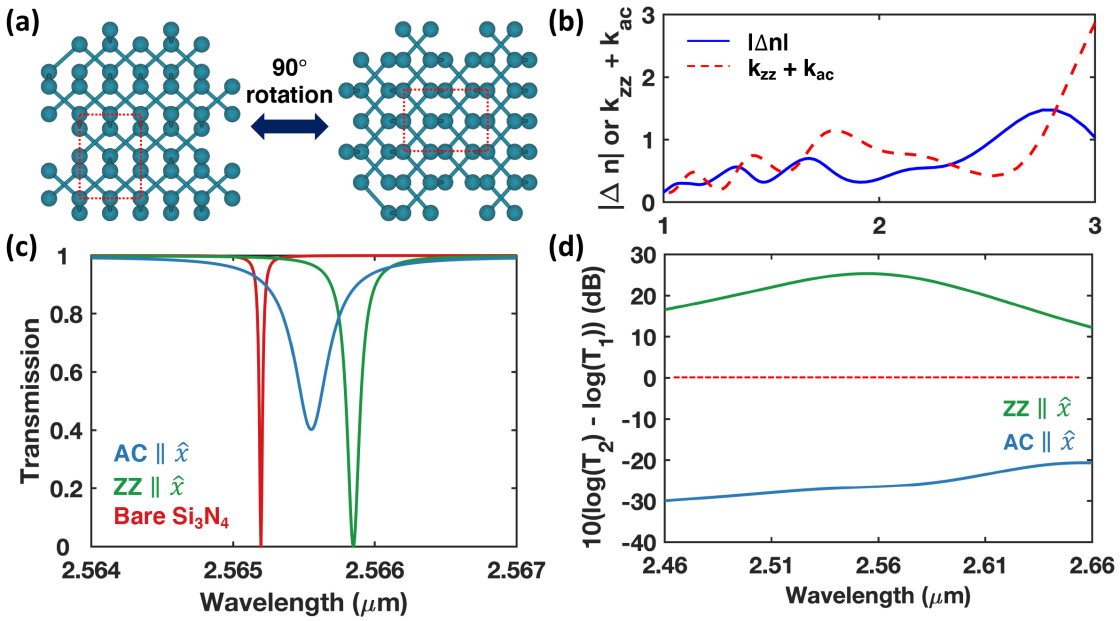

Figure 6-9: **Simulating devices based on bP.** (a) Crystal structure of a single layer of bP, showing ferroelastic domains related by 90° rotation. (b) Difference $|\Delta n|=|n_{zz}-n_{ac}|$ and sum $k_{zz}+k_{ac}$ for bulk bP, determined by first-principles calculations. (c) Transmission spectrum for a bare ring resonator (red), resonator with bulk bP with ZZ ∥ x̂ (green), and resonator with AC ∥ x̂ (blue); the geometry is as shown in Figure 6-5a. (d) The loss contrast between bar-port (T_1) and cross-port (T_2) for ZZ ∥ x̂ (green) and AC ∥ x̂ (blue) for a 1 × 2 directional coupler using bulk bP.

optical loss upon switching from ZZ ∥ x̂ to AC ∥ x̂. This is due to the anisotropy in effective mass: the AC axis has smaller effective mass than the ZZ axis, and as a result bP shows anisotropic plasmonic dispersion [240]. The transmission contrast between the two bP orientations reaches 0.88 at the wavelength of the ZZ ∥ x̂ resonance. The on/off ratio is as large as 85 dB, with an insertion loss of 0.53 dB.

We also simulate a 1×2 switch for the TE_0 mode using bulk bP, similar in geometry to that pictured in Figure 6-7b. The Si_3N_4 waveguide is 400 nm thick and 2 μm wide, and the bar-port and the cross-port are separated by a gap of 300 nm. Unlike the case presented in Figure 6-7b, here both the cross-port and the bar-port are covered with a bP layer 30 nm thick and 20 μm long. In Figure 6-9d we present the contrast 10(log(T_2) - log(T_1)) between the two configurations ZZ ∥ x̂ and AC ∥ x̂. The device has a switching contrast of ≈ 50 dB at 2.56 μm.

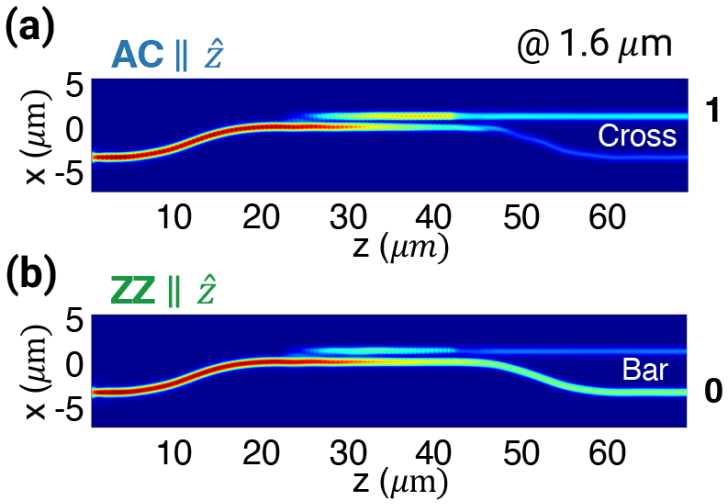

Figure 6-10: FDTD simulation results showing the mode evolution (top view) when the bP crystal orientation (a) ZZ ∥ ẑ and (b) AC ∥ ẑ, which corresponds to a cross or a bar state of the 1 × 2 switch.

The design method for SnSe switch, described above in Section 6.4, also works for designing switches using bP and operating in the TE_0 mode. As an example, we simulate a 1 × 2 switch based on bulk bP-integrated coupled waveguides (see Figure 6-9 for the device geometry). Here, we design the symmetrical two-coupled-waveguide geometry with bP integrated on top. If orientations of both bP flakes are aligned as ZZ ∥ x̂, the two waveguides are coupled, and light incident from the bar waveguide

switches to the cross port. If the bP flake in the cross waveguide is switched to the AC $\parallel \hat{\mathrm{x}}$ direction, then the two waveguides are isolated due to the large mode-index mismatch, the incident light remains in the bar waveguide.

6.6 Conclusion

We have shown that the orientation of the in-plane crystal structure of layered and 2D materials with low symmetry – specifically the triaxial materials SnSe and bP – has a substantial impact on device performance when integrated into photonic integrated ring resonators and 1×2 switches. Theory predicts that the crystal orientation (*i.e.* the ferroelastic domain structure) of such materials can be switched through an ultra-fast, non-thermal, and lower-power method by strong electric fields, due to dielectric anisotropy [8]. Should such predictions be borne out in experiment, then triaxial layered and 2D materials may become quite useful for light-controls-light mechanisms in photonic integrated circuits. Our results may be broadly applicable to layered and 2D materials with ferroelectric and ferroelastic crystal structures, which number more than the two studied here.

6.7 Supplementary Information

6.7.1 Geometry of Simulated Photonic Devices

Here we report geometry of photonic devices we use for simulation in chapter 5.

6.8 Contribution Statements

Changming Wu in Mo Li's group at University of Washington did photonic simulation using Lumerical.

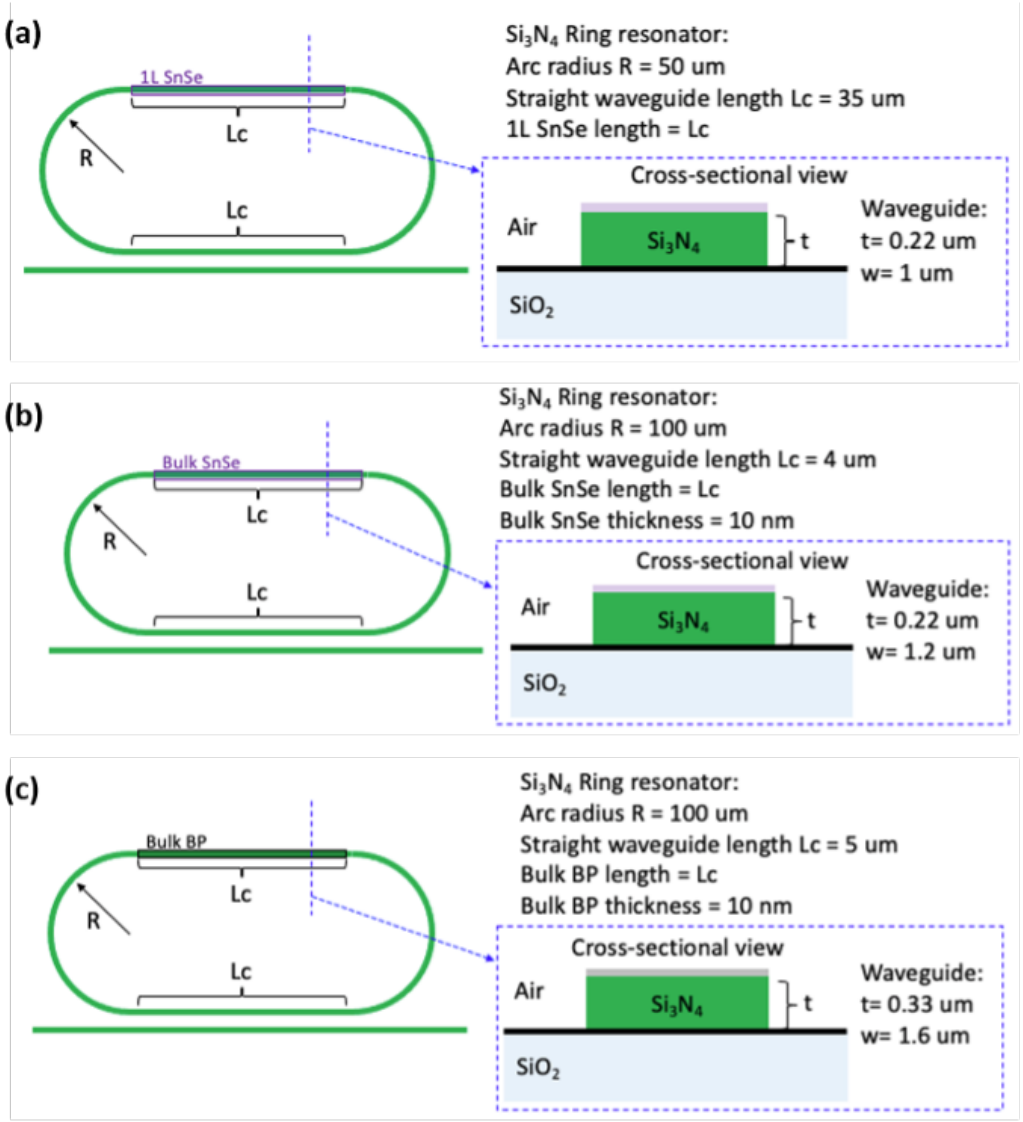

Figure 6-11: Geometry of simulated Si_3N_4 ring resonators, with integrated (a) monolayer SnSe, (b) bulk SnSe, and (c) bulk bP.

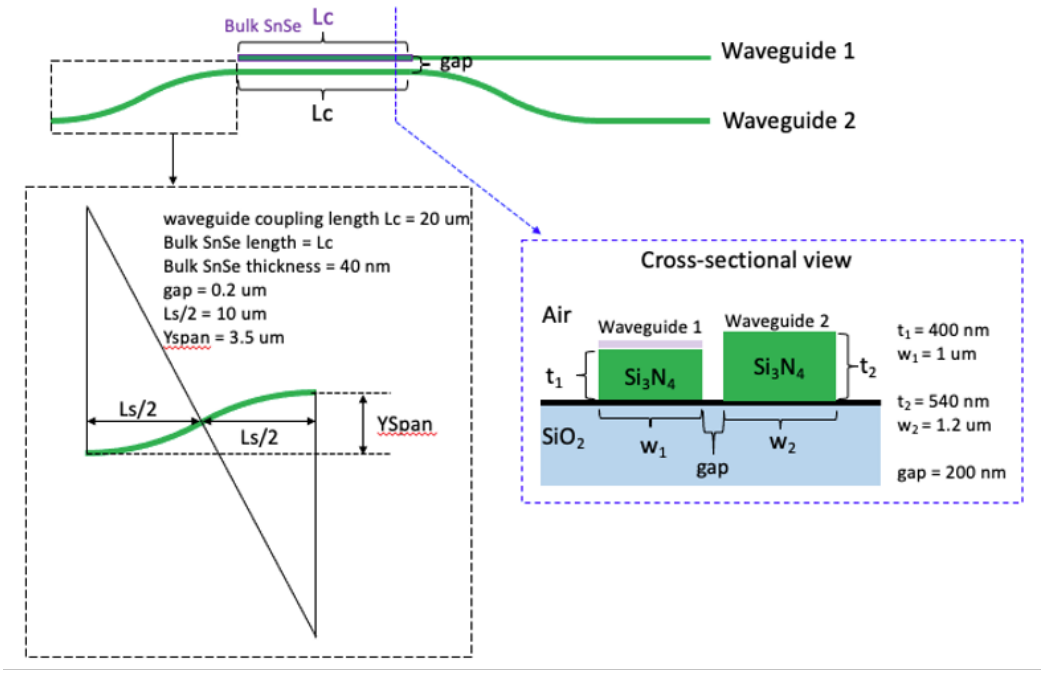

Figure 6-12: Geometry of 1x2 switch integrated with bulk SnSe.

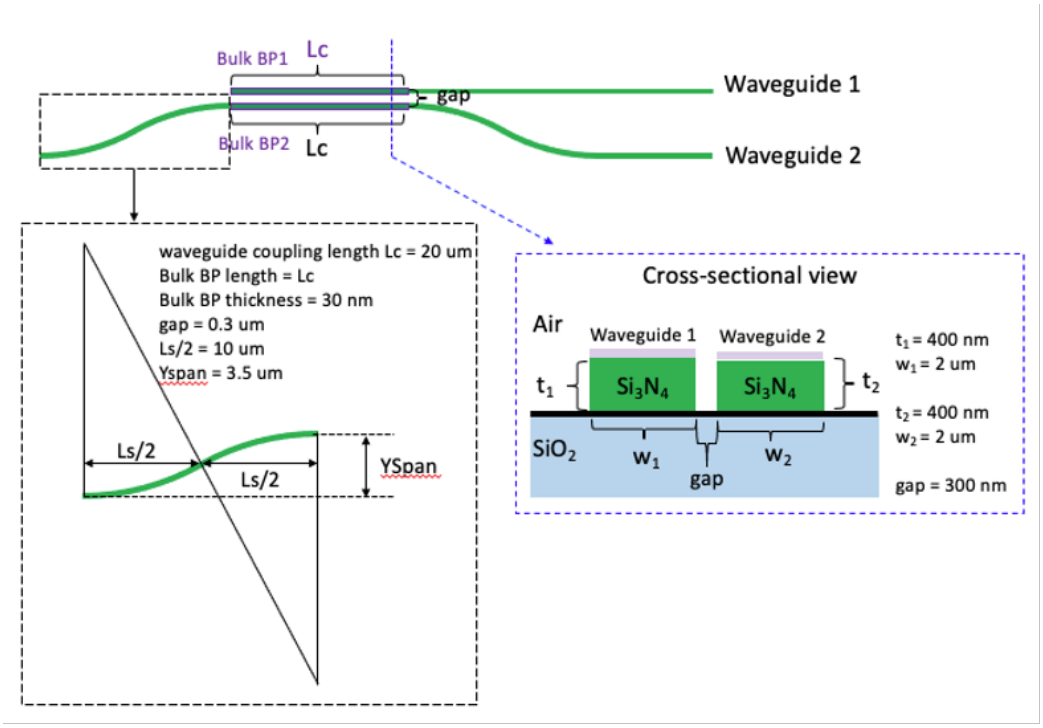

Figure 6-13: Geometry of 1x2 switch integrated with bulk bP.

Chapter 7

In-Plane Optical Anisotropy of SnSe and Experimental Design for Light-Induced Ferroelastic Domain Switching

7.1 Project Introduction

In Chapter 6, we theoretically demonstrate that phase of signal light can be tuned using the in-plane dielectric anisotropy of tri-axial layered materials (LMs) such SnSe and bP, and evaluate the device performance (ring resonators and directional coupler) when integrated with GeS-type LMs using a photonic simulation tool. In this chapter, we develop a sample preparation method, investigate facile methods to determine crystal orientation and demonstrate free-space THz pulse-driven barrierless, opto-mechanical switching. There has been few reports on experimental observation of phase transition in SnSe. Huang *et al.* observed nonthermal lattice instability induced by above-gap photoexcitation in SnSe [244], proving the phase transition from P_{nma} (thermodynamically stable phase at room temperature) to I_{mmm} (non-equilibrium phase), which is accompanied by a low frequency A_g phonon softening.

The photoinduced transient phase transition from P_{nma} to C_{mcm} (thermodynamically stable phase at high temperature) is also demonstrated at room temperature in a few hundreds of femtosecond, which is driven by the displacive exciation of coherent A_g phonons [245]. However, these phase transition mechanism is different from what we try to demonstrate in this chapter which is inspired by our collaborator's theoretical paper [8]. We use group IV-monochalcogenide with broken in-plane symmetry thus shows tri-axial optical properties, which resulting in large in-plane optical anisotropy. This chapter shows you how we can use the large in-plane optical anisotropy to induce phase transition called a domain switching. Among various available tri-axial material systems which can be used for the domain switching, we chose SnSe which orthorhombic narrow band gap semiconductor with distorted rock salt lattice structure. The theoretical study suggests new barrierless switching mechanism. The ground state potential energy curve without external electric field shows two stable structural variants with rectangular symmetry which are called variant 1 and variant 2. And the high symmetry state referred as SP acts as an energy barrier between two states. However, if we apply electric field, the additional second order term including dielectric functions ($-\frac{1}{2} \cdot E^* \cdot \varepsilon^1(\omega_0) \cdot E$) asymmetrically changes the energy curve, enabling second order phase transition without barrier. Due to the minus sign in the additional term, barrier-less switching occurs from small susceptibility state (which is high energy state) to high susceptibility state. For example, at 1.43 eV of photon energy, variant 1 has dielectric function of 53 along zigzag direction and 36 along armchair direction. Therefore, when we apply y-polarized light, armchair switches into zigzag within few pico-seconds. In short, dielectric anisotropy can be used for non-thermal, barrierless, field-driven domain switching and we describe experimental efforts to confirm this prediction. Note that it has recently demonstrated that strong electric field can shift a martensitic phase boundary in ZrO_2 with large dielectric anisotropy, which is similar behavior but we would like to observe this martensitic transition in SnSe using linearly polarized light instead of applying voltage [246].

7.2 Experimental Methods

7.2.1 Mechanical Exfoliation

Mechanical exfoliation is the simplest method to get the atomically thin nanosheets of LMs, which enables us to study physical fundamentals with the best quality of the nanosheets with low concentration of structural defects [247, 248]. However, this top down method has several drawbacks resulted from the stochastic process. It lacks control of the number of layers, flakes size, the locations of the nanosheet flakes and low yield of monolayer flakes, limiting their practical applications. Finding desired crystal flakes with a desirable thickness and lateral size is time-consuming process as it requires to repeat numerous exfoliation steps and look for the favorable flake from a number of randomly distributed flakes under optical microscope, until you find THE flake. Although LMs are weakly bounded by van der Waals force, some materials show stronger interlayer coupling than others. Thus the following key parameters should be optimized based on the exfoliation energy of materials; surface pre-treatment of target substrate, type of exfoliation tape (adhesive force strength, how much polymer residue it leaves, if it is thermal release tape or not), temperature, duration, contact angle, pressure, speed and so on. For these reasons, mechanical exfoliation is mostly used for research purpose rather than industrial use. Therefore, an essential prerequisite for practical applications is the development of reliable synthetic method for large area SnSe thin film, which is not covered in this thesis.

SnSe is prepared by the mechanical exfoliation method to test the opto-mechanical phase transition predicted by calculation [8]. Unfortunately, it is challenging to obtain monolayer SnSe flakes due to its high interlayer binding energy, which limits the research scope. SnSe features the strong interlayer ionic bonding and large electron distribution by lone pair electron in Sn [249]. And a strong charge transfer between adjacent layers results in large interlayer binding energy and thus the strong interlayer coupling, which is stronger than van der Waals interaction (Figure 7-1) [10, 233]. Chowdhury *et al.* have calculated the formation energy of monolayer group IV-monochalcogenides, MX (M = Si, Ge, Sn and X = S or Se), indicating the ex-

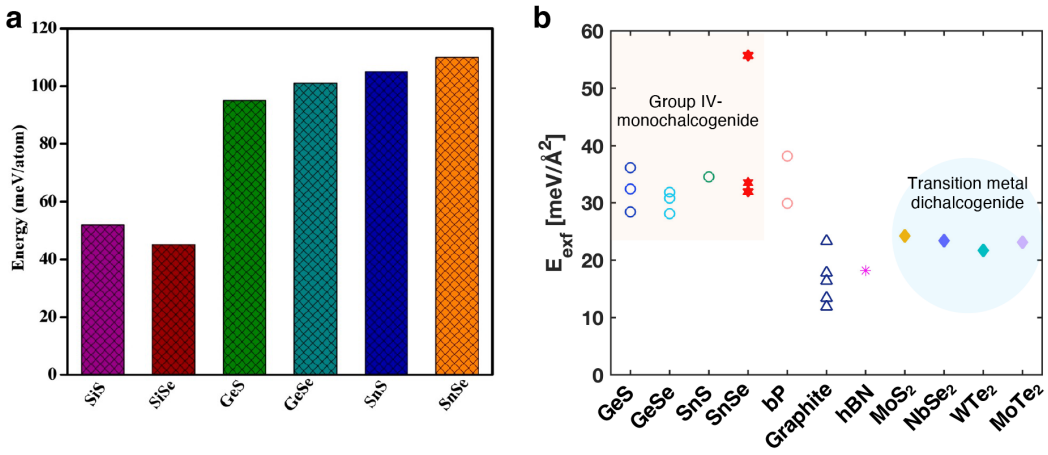

Figure 7-1: **Large exfoliation energy of group IV-monochalcogenides.** (a) Formation energies of monolayer group IV-monochalcogenides from their corresponding bulk counterparts. Reprinted (adapted) with permission from [9]. Copyright 2017 American Chemical Society. (b) The exfoliation energies of group-IV monochalcogenides with other 2D materials. Reproduced from [10], with the permission of AIP Publishing.

foliation energy of monolayer SnSe from the bulk SnSe is the highest among other MXs [9]. Figure 7-1 shows the exfoliation energies of MX materials, transition metal dichalcogenides, black phosphorus and graphite, indicating that MXs have significantly large exfoliation energy compared to other 2D materials. Although monolayer SnSe has been successfully synthesized using bottom-up methods of molecualr beam epitaxy (crystal size $\sim$ 100 nm) [250] and chemical vapor deposition followed by nitrogen etching (crystal size $\sim$ tens of μm) [251], the thinnest SnSe flake obtained by mechanical exfoliation is $\sim$ 70 nm with a crystal size of tens of μm [234].

Figure 7-2: **Mechanical exfoliation of SnSe crystal.** (a) Photograph of bulk SnSe crystal, (a) Photograph of cleaved crystals on a scotch tape, (b) Optical microscopy image of exfoliated SnSe crystals of various thickness.

As we discuss the difficulty to obtain a desirable SnSe flake (as thin and large as possible) above, we optimize the mechanical exfoliation technique for strongly-bounded SnSe crystals, as described below. Note that SnSe crystal (Figure 7-2a) is synthesized by Bridgman crystal growth method by Kanatzidis group at Northwestern University. Also, two different types of tape are used in this process: a scotch tape and blue tape.

(1) Use a scotch tape (3M), having a large adhesive force than Nitto tape (Nitto, SPV 224PR-MJ LB) known as a blue tape, to nicely spread/lay out flakes with a tweezer. Figure 7-2 represents the resulting tiles made of delaminated crystals which are still shiny.

(2) Exfoliate SnSe crystals with a blue tape by attaching the blue tape on the scotch tape with original crystal tile, and then gently press and rub the surface of the tape with the backside of the tweezer. Repeat this process with new blue tape and the original scotch tape until the flakes look greyish when looking at the exfoliated flakes on the tape using the white light in the room. Please note that lateral size of crystal gets smaller as we repeat the exfoliation process. Hence we need to find the balance between thickness and lateral size of flakes by controlling the frequency of exfoliation.

(3) To increase the surface adhesion of oxidized silicon substrate, use O_2 plasma or UV-ozone treatment for 5 min. Put the scotch tape (or blue tape) on the chip and place the entire substrate/tape embedding the crystal flakes stack (we call it a chip) on the hot place at 80 °C for 1 min. Take out the chip from the hot plate and nicely rub the tape with finger or backside (flat side) of the tweezer to remove the bubbles. Do not press hard that could break the exfoliated flakes.

(4) Wait few minutes before peel off the tape and lastly peel off quite slowly.

Through this method, we can obtain the SnSe flakes as thin as 10 nm-thick but the lateral size is quite small (≤ 2 μm). We mostly use THz pulses for light-induced phase switching, requiring a THz enhancement structure to reach the electric field threshold. In this case, the less O_2 plasma exposure is the better pick up the target flake later. However, if we adopt a OPA-derived near infrared (NIR) or mid-IR laser

as a pump, the metamaterials is not necessary because the laser power itself is strong enough to drive the switching, enabling easier sample preparation. In this case, we can use O_2 for 10 min to maximize the interaction between the crystals and substrate, resulting in high yield and large crystal size. But this method generates lots of thick bulk crystals on the substrate rather than 2D flakes. We can thin down these thick flakes (Figure 7-3a) to mono- and few-layers of crystals (Figure 7-3b) by adopting a polymer stamp to further exfoliate the flakes on Si/SiO_2 substrate.

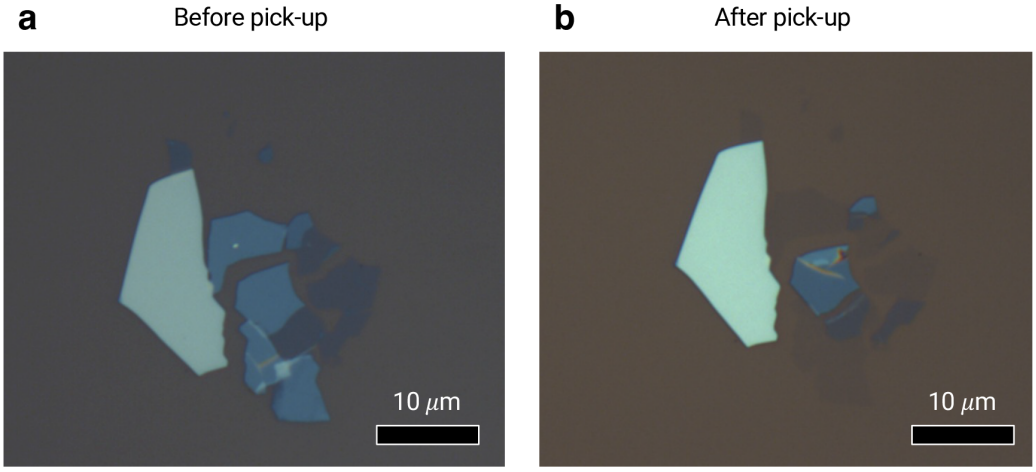

Figure 7-3: **Idea of thinning down the exfoliated SnSe crystals on Si/SiO_2.** Optical images of (a) as-exfoliated SnSe flakes and (b) thin-downed SnSe flakes using a polymer stamp. The color contrast between (a) and (b) clearly indicates that the polymer stamp delaminates the flakes rather than picks up the whole crystals.

7.2.2 THz Metamaterial Fabrication

The required electric field to induce the opto-mechanical switching is $\sim$ 15 MV/cm, which is much stronger than the peak strength of our single-cycle THz pulses ($\sim$ 300 kV/cm) generated from fundamental 800 nm pulse derived from an Ti:Sapphire amplified laser system (Coherent Legend Elite Duo) through a process known as optical rectification, requiring THz field enhancement structure. We fabricate the THz metamaterial can be fabricated using a standard photolithography and lift-off process. To dehydrate the fused silica substrate and improve adhesion of photoresist, we employ hexamethyldisilizane (HDMS) vacuum oven (YES-TA) to make HMDS

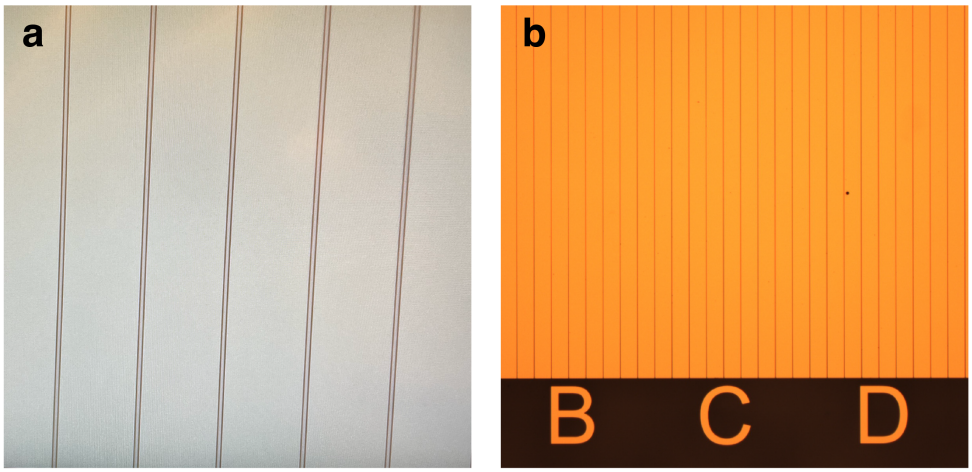

Figure 7-4: **Optical images of THz metamaterial made of Au.** THz metamaterial on the fused silica wafer (a) After develop and before metal deposition, (b) Resulting Au metamaterial consisted of Au strip with a width of 50μm and 2μm gap.

layer on the substrate. PMGI lift-off photoresist is spin-coated on the fused silica substrate at 3500 rmp for 60 s, followed by soft-baking at 230 °C for 5 min on a hotplate. Then positive photoresist AZ3312 is spin-coated on the sample at 3500 rpm for 60 s (resulitng photoreis thickness $\sim$ 1.2 μm), soft-baked at 112 °C for 90 s on a hot plate. The sample should be cool down to evaporate the solvent (anisole) and get reliable resulting pattern, especially for small feature size $<$ 1 μm. The pattern is exposed to the double-layered photoresist using the a maskless aligner MLA-150 with the 375 nm diode laser and a dose of 180 mJ/cm^2. After the UV exposure, the sample is post-basked at 112 °C for 60 s. The post exposure bake helps to smoothen out the roughness occurred by standing wave effect on photoeresist. Then the sample is developed in AZ300MF for 75 s and hard-baked at 90 °C for 3 min on a hot plate, helping to have better adhesion and harden resist. A thin film of 10nm Cr as an adhesion layer and subsequent 90nm Au is deposited onto the sample using electron beam evaporator. The sample is soak in NMP at 80 °C overnight for lift-off process, rinsed by isopropyl alcohol (IPA) and dried by nitrogen gun. The PMGI lift-off resist ensures smooth and clean lift-off of the metal thin film, extending the limits of lift-off processing with high resolution of $<$ 0.25 μm, which is beyond where single layer photoresist can achieve. Figure 7-4 shows the finished metamaterial fabricated by the

processing described in this section.

7.2.3 Dry Transfer for vdW Heterostructure

Strong linearly polarzied electric is required to drive the phase transition in SnSe, where the critical electric field is > 2.9 MV/cm for monolayer SnSe at incident energy $\hbar w_0 = 0.963$eV [8]. Even the single-pulse laser could easily damage the materials by heating, breaking bond and then removing atoms by photon absorption[252]. In our switching experiment, the laser with the wavelength of below band gap is used which the thermal damage would be minimized. We can thin down and pattern the layered materials using laser [253, 254]. It has proved that hexagonal boron nitride (hBN) is a good encapsulation material for high performance device because it is atomically flat and has relatively low charge trap and large band gap (for bulk hBN, indirect band gap = 6.08 eV [255]; for monolayer hBN, direct band gap = 6.47 eV [256]) preventing from optically interfering with the signal from the sample. Also, it is a good chemical passivation layer because it is impermeable to all gases and liquids [257], for example protecting air-sensitive materials from oxidation in an ambient condition and from field-induced charge emission from the underlying gold substrates [258]. Thus we encapsulate the exfoliated SnSe flakes with hBN to not only protect the crystals but also improve the adhesion with gold metamaterial enhancing THz fields using a dry transfer method, which is a deterministic technique to fabricate van der Waal heterostructure on the pre-fabricated metamaterial using a polymer stamp via precise pick-up and drop-down steps. We note that the interaction between the exfoliated flakes and Si/SiO_2 substrate plays a critical role in this technique, requiring to find the sweet spot of O_2 plasma treatment time on the substrate. O_2 plasma makes a surface of Si/SiO_2 substrate to hydrophilic and thus more adhesive, enabling to obtain the mechanically exfoliated LMs with large lateral size at high density. However, the increased in interaction between the substrate and the flake makes the pickup process challenging. If you use O_2 plasma, the adhesion force becomes larger meaning you cannot pick up from SiO_2 substrate to transfer your flake onto metamaterials.

We first prepare a polymer stamp made of polydimethylsiloxane (PDMS, SYL-

GARD 184 Silicone Elastomer Kit) and polycarbonate (PC). In many cases of vdW heterostructure fabrication, polypropylene carbonate (PPC) is used instead of PC but we choose PC because it is more adhesive. Due to the challenging in SnSe exfoliation in Section 7.2.2, O_2 plasma treatment is necessary to obtain the mechanically exfoliated SnSe on SiO_2/Si substrate, requiring stronger pick-up force. PDMS is prepared from a solution with a ratio of 20:1 of Sylgard 184 pre-polymer to curing agent, stored in vacuum desiccator for *sim* 24 hr for degassing and curing. The PC solution is prepared by dissolving 0.6 g PC beads in 9.6 g chloroform. The cured PDMS cut into 2 x 2 mm^2 and then placed on a glass slide. The PC thin film is prepared using drop casting method as follow: (1) drop solution on the glass slide and cover with another glass slide, (2) separate them by sliding over each other, (3) leave both glass slides with the polymer side as faced up in ambient condition for 5 min to evaporate the residual solvent, (4) cut the film into square shape of 1 x 1 cm_2 and (5) place the PC film onto a double-sided tape with a hole punched into it as a window. As last step, the prepared PC/double-sided tape is gently attached onto glass slide/PDMS, and remove the extra scotch tape on the backside of the glass slide in order to secure a clear view under optical microscope.

The as-prepared polymer stamp is loaded upside down on a micromanipulator (transfer arm) that can precisely position in x, y and z directions. The exfoliated hBN on Si/SiO_2 is fixed on the microscope stage equipped with a heating system and vacuum holder. After finding the target flake, the heating microscope stage is set to 70 °C and then the polymer stamp is lowered into conformal contact with the target flake. After the stamp completely covers the crystal for 1 min, cool down the sample to 60 °C and retract the micromanipulator slowly to lift the resulting stamp/target hBN crystal stack. The glass/PDMS/hBN stack is baked at the baking temperature between 50 $\sim$ 80 °C. The previously picked-up hBN crystal is aligned over the next target SnSe crystal and the pick-up process is repeated but at 130 °C for the SnSe crystal and the overall stacked structure is lifted off at 60 °C. Please not that it is important to slowly drop down the stamp/hBN stack (at speed of $\sim$ 2 μm/min and at a tilted angle) to avoid air bubbles and non-conformal contact. To place the resulting

van der Waals assembly, the gold metamaterial on fused silica wafer is placed on the heating stage and the temperature sets to 80 °C. The overall stack of hBN/SnSe adhered to the stamp is dropped down and make a conformal contact to the target substrate, followed by heating up to 165 °C for few minutes and then cool down to 80 °C in order to release the hBN/SnSe assembly from the polymer stamp. The hBN/SnSe crystal onto silica substate is soaked in acetone for 10 min and rinsed by IPA to remove the PC residue.

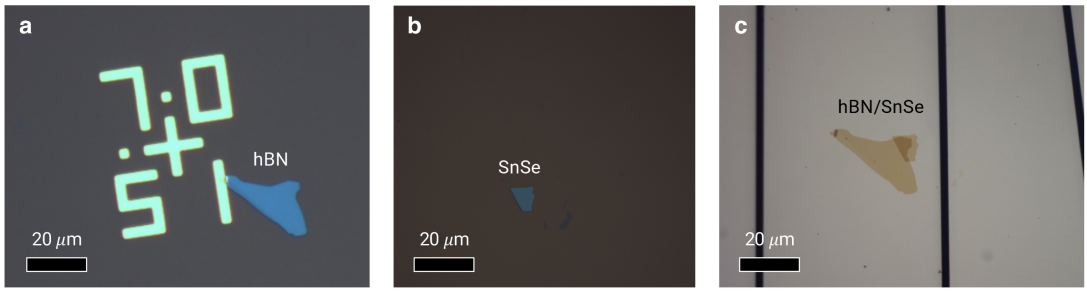

Figure 7-5: **Optical microscoopy images of hBN, SnSe and hBN/SnSe heterostructure.** (a) As-exfoliated hBN, (b) as-exfoliated SnSe, (c) hBN/SnSe heterostructure on Si/SiO_2 substrate after drop-down step.

Figure 7-5c shows that the SnSe flake encapsulated with hBN is placed on the gold strip. The heterostructure is supposed to be located on top of a gap between gold strips but it is challenging to align such as small flake (lateral size < 4 μm) using PDMS/PC stamp due to refraction and diffraction of light. In the future, this could be resolved by using better light source with higher intensity, finding a method to obtain SnSe flakes with large enough lateral size of > 20 μm, using modified transfer method with higher precision [259].

7.3 Results and Discussion

7.3.1 Identifying Crystallographic Orientations

SnSe is the orthorhombic IV-VI compound semiconductor (α-SnSe), having a layered structure with a distorted rock-salt lattice structure and the space group of P_{nma} at room temperature [260]. Owing to the distorted layered structure and the broken mir-

ror symmetry with respect to (110) plane, it displays the anharmonic and anisotropic bonding. In particular, the SnSe crystal consists of two-atom thick SnSe layers with strong covalent Sn-Se bonding within the bc-plane, and stacked together by van der Waals Sn-Se interaction between adjacent planes along the a-axis. Herein, each axis is defined as in the following; the direction perpendicular to the 2D bc-plane as the a-axis, the buckled zigzag direction as the b-axis, the armchair direction as the c-axis. Each atom forms six heteropolar bonds. When we take a look at only one Sn atom, there are three nearest and strongest bonds and the two second-nearest ones in the same double layers. The last sixth nearest neighboring atom resides in the adjacent double layers. This structural anisotropy results in highly-anisotropic optical, electrical and thermoelectric properties. For example, the zigzag geometry is flexible so that it can dissipate lateral phonons transport [260, 261]. As a consequence of intrinsically low lattice thermal conductivity along the zigzag direction, a high ZT (where Z is the figure of merit and T is absolute temperature, indication of the efficiency of thermoelectric materials) along the zigzag direction has been reported which is attributed to the layered structure and strong lattice anharmonicity [261].

The driving force of the opto-mechanics driven martensitic transition is an anisotropic dielectric function, which enables a second order phase transition. To align the linearly polarized light to the crystal orientation with high ε_1, we first need to identify the in-plane crystal orientation in bulk SnSe and exfoliated flakes. Among numerous characterization techniques, we choose the general area detector diffraction system (GADDS) for bulk SnSe single crystals, and polarization-dependent reflectivity measurement using femtosecond laser and angle-resolved polarized Raman spectroscopy for exfoliated SnSe flakes.

We use GADDS to gain information of in-plane orientation of bulk SnSe, which allows us to further measure its anisotropic optical properties using spectroscopic ellipsometer or FT-IR spectroscopy. The bulk SnSe sample is mounted on the sample stage with a double-sided tape and subsequently the surface is exfoliated with an adhesive tape to remove the native oxide layer or chemical adsorbates from the air. GADDS 2D x-ray diffraction (XRD) patterns is recorded with symmetric scans in

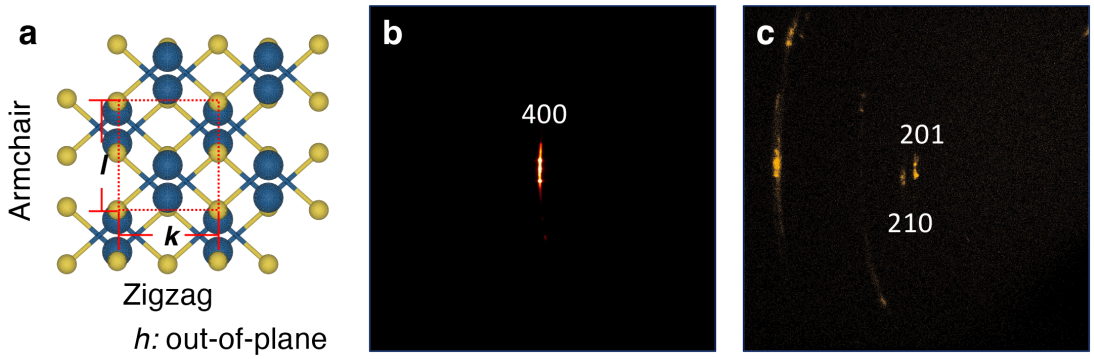

Figure 7-6: **Crystal structure and 2D GADDS x-ray diffraction patterns of bulk SnSe crystals.** (a) Top view of SnSe crystal structure showing the rectangular 2D unit cell with zigzag (k, short axis) and armchair (l, long axis). Note that h is out-of-plane direction. (b-c) 2D GADDS x-ray diffraction patterns of bulk SnSe crystals.

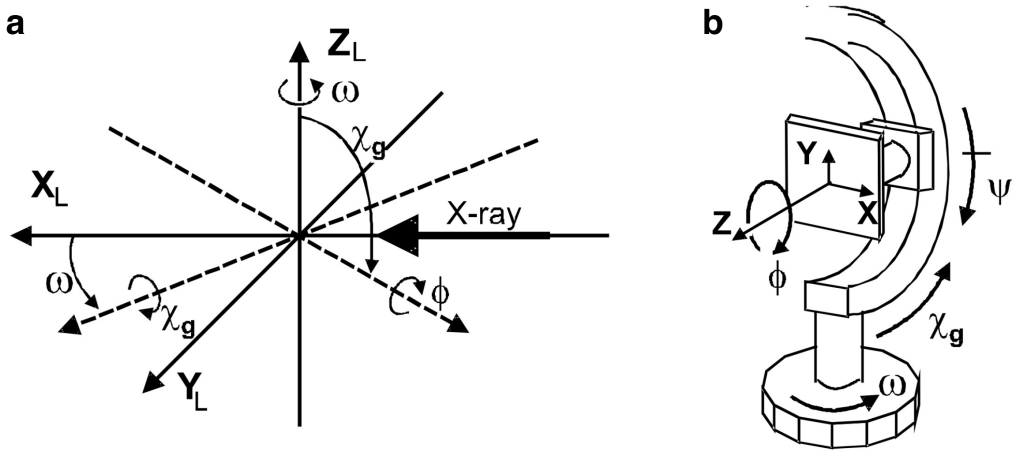

Figure 7-7: **Geometry related to GADDS XRD system - sample rotation and translation.** (a) Available rotation axes ($\omega, \chi_g, \psi, \phi$) in X_L, Y_L and Z_L coordinates, (b) Relationship among all rotation axes and translation axes. Image is adapted with permission from [11].

Bragg-Brentano geometry using Bruker Cobalt Source D8 with GADDS ($\lambda_{Co} = 0.179$ nm). Figure 7-7 summarizes the crystal structure of rectangular unit cell of SnSe crystals and the 2D XRD results. The sample shows evident out-of-plane (400) peak at $2\theta = 36.255°$ (Figure 7-7b). The in-plane (201) peak at $2\theta = 29.486°$ is found by a ϕ scan at $\psi = 52.327°$, indicating armchair direction (See Figure 7-7 for geometry of XRD system.). The weak (210) peak is also found next to (201) peak. The elongated peak shape suggests that SnSe crystal is not single crystal nor poly crystal but well-textured poly crystal.

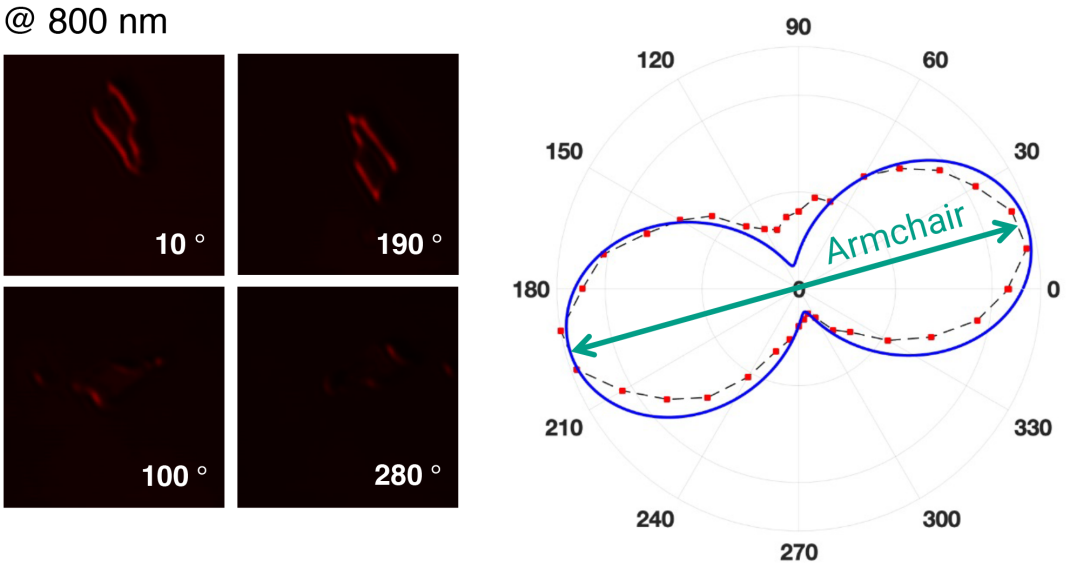

Figure 7-8: **Optical microscope reflectivity images of the SnSe flakes.** (a) The reflective polarization resolved optical microscope image of the SnSe flake with sample rotation angles from 0° to 350° with 10° rotation steps. The 800 nm femtosecond laser is used as a light source and the polarizaiton direction is vertical. (b) Angular dependence of the reflectivity intensities measured using 800 nm femtosecond laser under parallel polarization configuration.

Although XRD is a powerful technique to characterize power or bulk crystalline materials, it cannot be employed for exfoliated crystalline flake of few μm crystal size due to mm-sized spot and the lack of optical microscope. The freshly-exfoliated SnSe sample are prepared by micromechanical exfoliation method (See Section 7.2.1), then transferred onto oxygen-plasma cleaned Si/SiO_2. The thickness of SnSe flake is $\sim$ 123 nm which is confirmed by atomic force microscopy (Figure 7-9a). Thanks to the strong in-plane anisotropic optical response, the crystal orientation is determined using two characterization method: polarization dependent reflectivity measurement and angle-resolved polarized Raman spectroscopy using laser with diffraction-limited spot and optical microscope. The polarization dependent reflectivity is measured with a femtosecond laser of 800 nm and rotating sample stage. The incident light is linearly polarized and we rotate the sample with the angular step size of 10°. Figure 7-8 shows polarization dependent reflectivity optical microscopy images and the corresponding polar plot of reflectivity intensity versus rotation angle, confirming armchair

direction of the flakes. We measure ellipsometric angles of bulk SnSe and calculate the reflectivity using the measured values, featuring armchair direction shows high reflectivity at 800 nm. We have not studied deeper on irregular reflectivity over the flakes showing only reflective along the edge, requiring further study. However this method is less convenient than polarized Raman (will discuss shortly) due to the lack of rotational polarizer.

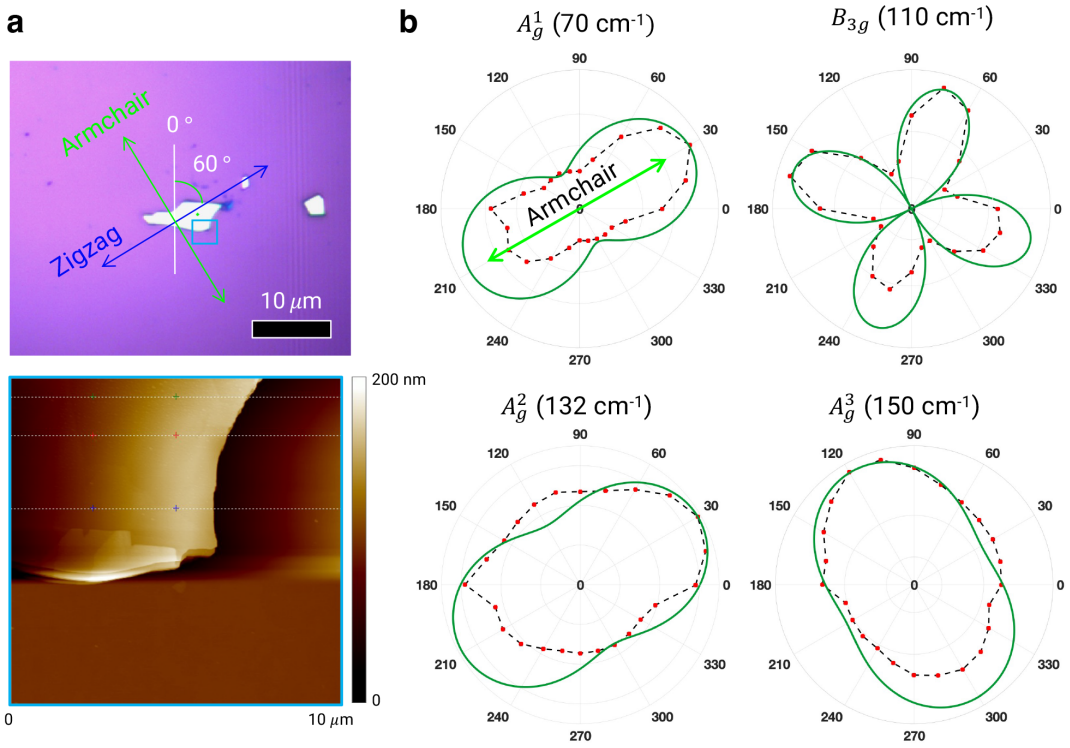

Figure 7-9: **Angle-resolved polarized Raman spectroscopy.** (a) Optical image of the freshly exfoliated SnSe flake on Si/SiO_2 and AFM surface scan images corresponding to the blue box in optical microscope image. The average thickness of the flake is $\sim$ 123 nm $\pm$ 3 nm. (b) Polarized Raman diagrams of the SnSe flake in (a) with different polarizer rotation angles excited using a 532 nm laser under parallel-polarization configuration. Note that in-plane crystallographic orientation of the SnSe flake are marked with green line (armchair) and bule line (zigzag), which is rotated by 90° from each other.

Angle-resolved polarized Raman spectroscopy is an another tool to identify the crystal orientation of anisotropic crystals, featuring the anisotropic light-matter interaction in mechanically exfoliated SnSe flakes. We use the polarized Raman to measure Raman spectra as function of the polarizer rotation angle under parallel polarization

configuration with the 532 nm laser. The 0 degree line in Figure 7-9a indicates the polarization direction and the polarizer is rotated in counterclockwise direction by 15°. The most commonly discussed Raman vibrational modes in SnSe crystals are the A_g^1, B_{3g}, A_g^2 and A_g^3 at 70, 110, 132 and 150 cm^{-1}, respectively. Figure 7-9 shows obvious angle dependence of Raman intensities at particular Raman mode. In other words, the Raman modes are highly sensitive to crystal orientation of SnSe, allowing us to easily determine the orientation of exfoliated flakes [262].

7.3.2 Critical Electric Field for Barrierless Switching

We evaluate the important experimental parameters with regard to the opto-mechanics driven martensitic transition in bulk SnSe crystals using experimental values of complex dielectric constants ($\varepsilon = \varepsilon_1$ - iε_2) of bulk SnSe. The dielecric constants of the bulk SnSe crystal is measured in the spectral range of 200 nm $\sim$ 24 μm using spectroscopic ellipsometer and we use the published dielectric functions for the far-IR wavelength range (30 $\sim$ 400 μm) [263, 264]. For the spectral range of 200 nm to 1 μm, we perform SE measurements on the (001) basal planes which are perpendicular to the optic axis at a fixed angle-of-incidence of 70° by using a UV-NIR Vase ellipsometer from J. A. Woollam. Mark at Tufts University measures IR optical properties of bulk SnSe using the IR-VASE ellipsometer in the wavelength range of 2 μm to 24 μm. There are two energetically degenerate states (See Figure 6-1a for crystal structure), which is two 90°-orientation variants. Throughout this chapter, we refer the rectangular unit cell with zigzag direction along x-axis to the orientation variant 1 (FE_1, left in Figure 6-1a) and the the unit cell rotated by 90° from variant 1 to the orientation variant 2 (FE_2, right in Figure 6-1a). We assume the energy barrier between two domains is same as the energy predicted in the theoretical paper [8], which is back-calculated Δu using the critical electric field strength (E_{crit}) and the corresponding ε_1.

$$\Delta u(w_0, t) = \tfrac{1}{2}\Delta E^2 \cdot \varepsilon_1(w_0) \cdot \varepsilon_0$$
$$\Delta u_{crit} = 2.3 \text{ meV/f.u.}$$

Using the energy barrier value and experimentally measured ε_1 of bulk SnSe, the

critical electric field is estimated. In Figure 7-10, the shaded regions represent the spectral range where the critical electric field is experimentally achievable by strong optical pump or adopting electric field enhancement structure. The optomechanics driven phase transition occurs from orientation variant with small ε_1 to another with large ε_1, varying over wide spectral range. Therefore, the linearly polarized electric field should be aligned with the crystal orientation with small ε_1 to observe any changes in Raman or reflectivity intensities. The color bar in Figure 7-10 indicates the switching direction. For example, for green block, zigzag direction shows larger ε_1 than armchair direction in the wavelength regime. Thus, the linearly x-polarized electric field needs to be aligned with armchair direction for induce martensitic transition from FE 1 to FE 2. The transition can be verified with Raman dynamical probe or reflectivity dynamical probe.

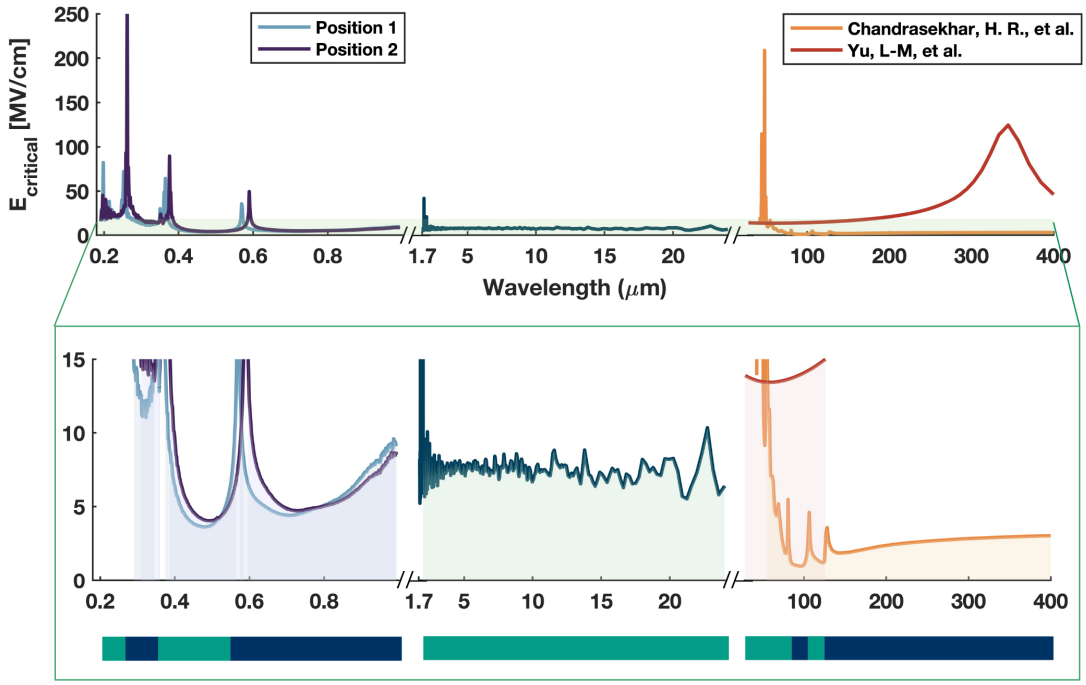

Figure 7-10: **Critical electric field required to drive the opto-mechanical switching.** Green box provides the experimentally achievable regime of electric field < 15 MV/cm. Shaded area corresponds to possible wavelength range for switching experiments. The color bar on the bottom indicates the switching direction; (dark blue) phase transition from zigzag $\parallel \hat{x}$ to armchair $\parallel \hat{x}$, (green) phase transition from armchair to zigzag $\parallel \hat{x}$ at where $\hat{x}$ means x-polarized light.

7.3.3 Switching Experiments: Single-Shot THz Pump Probe Spectroscopy

Single-shot Thz pump probe spectroscopy in a reflection geometry is adopted to demonstrate the proof-of-concept of light-induced martensitic transition in SnSe. Single-shot spectroscopy is chosen to avoid sample degradation which conventional pump-probe methods often encounter, and to observe the non-volatile change in SnSe. We assume single-pulse optical damage threshold limit for monolayer SnSe is similar or higher order of magnitude to monolayer MoS_2 of $\sim$ 50 mJ/cm^2 (2.5 mW) [252]. In our case, we use a laser with the energy of below-band gap of SnSe thus optical damage threshold limit with this would be higher. A stronger pump pulse (herein, THz pump) is employed to induce the elastic energy change in SnSe system, enabling second order transition from high energy state to low energy state. A weaker probe pulse (herein, reflectivity probe) is used to monitor the Thz pump-induced phase transition (*i.e.* change in optical properties) of SnSe at some delay relative to the pump pulse. We use transient reflectivity measurement (*i.e.* the optical probe measuring reflectivity change) which is sensitive to changes to refractive index ($n - i\kappa$) of SnSe.

The freshly exfoliated SnSe flake ($\sim$ 30 nm) is transferred onto a gold metamaterial using CAB-medicated transfer method (See Section 5.2.4 for the method). The microslits consist of Au strip with a width of 98 μm and thickness of 200 nm placed on a fused silica wafer, each strip is separated with the gap of 2μm from another (Figure 7-11b). The single shot THz source has a peak strength of 300 kV/cm, which is enhanced up to the 2 orders of magnitude in the capacitive gaps. The THz pump is peaked at 0.6 THz ($\sim$ 500 μm) and has a bandwidth of $\sim$ THz (*i.e.* 0.1 $\sim$ 1.1 THz) and repetition rate of 1 kHz. The visible probe is centered at 800 nm and is focused down using 50x objective which the spot size is a few micrometer or less. We use time-to-frequency encoding to encode the temporal information (*i.e.* τ) onto one probe pulse and subsequently read it out on a single-shot basis. We chirp our ultrafast probe pulse to be very long (herein, $\sim$ 30 ps), and then overlap it with a

relatively short THz pump pulse (herein, $\sim$ 1 ps). Because the probe is chirped, different frequencies of the probe pulse overlaps with the pump at various relative time delays spanning the whole 30 ps range. The pump-probe trace becomes embedded on the spectra of the probe pulse, which can then be read out using a spectrometer.

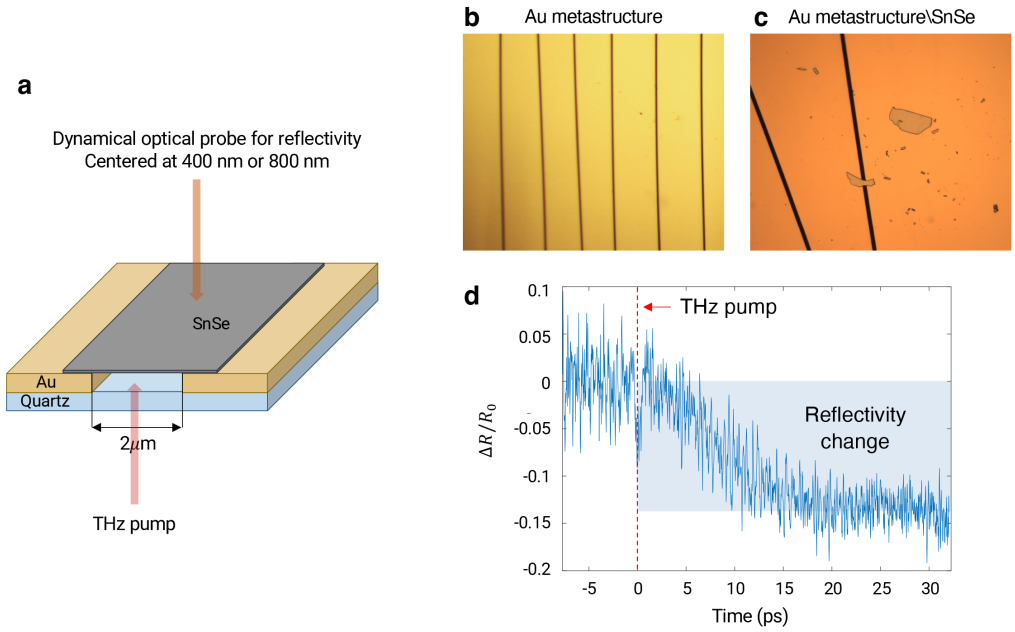

Figure 7-11: **Single shot THz switching experiment set-up and results.** (a) Schematics of switching experiments set-up. Optical images of Au metamaterial (b) without and (c) with SnSe flakes. (d) The transient-photoexcitation-induced-reflectivity changes ($\Delta R/R_0$) in SnSe at ambient condition. The red dotted line indicates when THz pump excites the sample.

As depicted in Figure 7-11, a back illumination geometry is employed which THz optics for THz pump and optical microscopy setup for visible probe are on opposite sides of the sample. The THz field is polarized perpendicular to the gold strips. Figure 7-11d shows THz pulse-driven phase transition in SnSe, with the THz pump field exceeding the critical electric field (See Section 7-10) at where energy barrier disappears, which is linearly polarized to $\hat{x}$. Upon exposure to a single high-field strength THz pulse, the reflectivity drops 10 $\sim$ 15 % within 10 $\sim$ 20 ps before plateauing. This results is highly preliminary and further measurements are necessary to confirm that this signal persists on even longer time scales. However this slow feature suggests that it could be a phase transition from armchair $\parallel \hat{x}$ to zigzag $\parallel \hat{x}$ perhaps not

dissimilar to that observed in two-dimensional transition metal dichalcogenides. This issue can be mitigated by applying a protective layer, for example encapsulating with hBN layers (hBN/SnSe/hBN heterostructure) because hBN adhere to the gold better. Unfortunately, we were not able to confirm the result with a static measurement because once the flake is exposed to a single THz pulse, it would simply fall off due to the strong field strength which is commonly observed phenomena when working with small flakes.

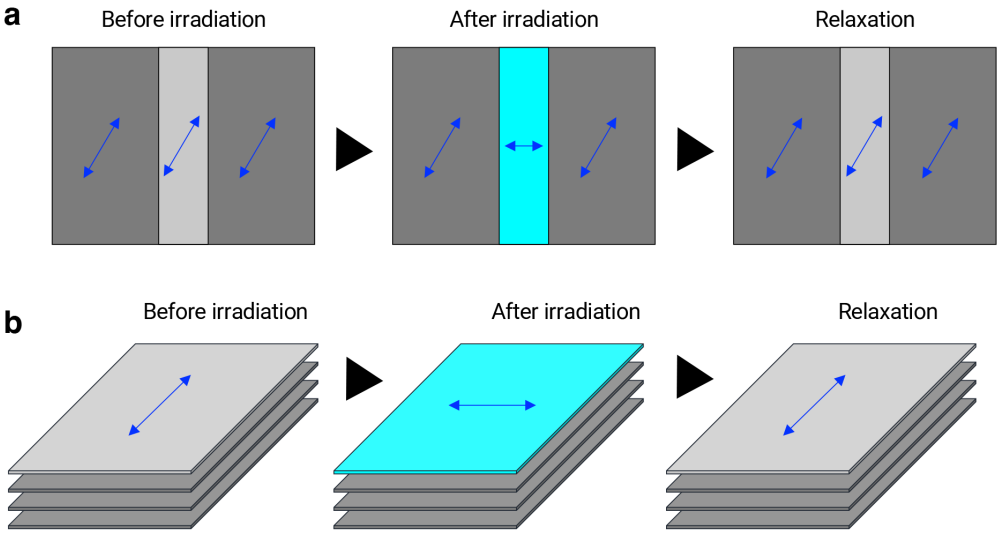

Figure 7-12: **Illustration of possible scenario of mechanical constraints.** (a) Surrounding domains where not exposed to THz pulse could rotate the switched area back to original geometry. (b) Upon THz irradiation, only topmost surface could response and intact underlying layers could apply shear stress to the switched layer.

Another concern is the mechanical constraints which the initial theoretical paper did not take into consideration. The opto-mechanical switching prediction is based on the assumption of strain-free monolayer SnSe. There are two types of strain constraints existed in this geometry. Only the parts of SnSe placed on the empty gap are irradiated with linearly polarized THz pump. Neighboring domain are not excited and could apply shear force the switched area, resulting in relaxation (Figure 7-12a). Figure 7-12b describes the mechanical constraint from another layers. Due to the exfoliation challenge in SnSe, our SnSe samples have thickness of 30 nm which opens up possibility that only surface layer can be switched upon THz illumination

but underlying layered-planes remain same. We have not tested if it is permanent or reversible change and if it it reversible what relaxation time is (transient vs. long-lived).

In the future, we could use femtosecond stimulated Raman spectroscopy (FSRS) because Raman scattering provides strcutual informaiton as we discussed in Section 7.3.1. Note that FSRS spectra are polarized because it uses polarized laser. This way, we can monitor changes in the Raman peaks as the new phase grows and this would be highly illuminating with regards to the underlying mechanism. Furthermore, we can maximize the change by aligning crystallographic orientation with high dielectric constant (real part, ε_1) to the direction across the micro-gap ($\parallel \hat{x}$).

7.4 Conclusion

We conduct single THz pump probe spectroscopy on the mechanically exfoliated SnSe flakes with a thickness of 30 nm to demonstrate the opto-mechanical properties of GeS-type materials. The preliminary result of a THz-induced phase transition in bulk SnSe is obtained using single shot spectroscopy with reflection geometry. The reflectivity change following THz excitation ($\sim$ 15 %) suggests the phase transition from armchair $\parallel \hat{x}$ to zigzag $\parallel \hat{x}$ within $\sim$ 20 ps. This is the first experimental demonstration proving the phenomenon of that anistropic dielectric properties of GeS-type VI-VI monochalcogenide can be used for barrier-less, martensitic transition upon linearly-polarized light exposure. Combined with the theoretical prediction made in Chapter 6, this new light-controls-light mechanisms can be further studied in photonic device with waveguided pump light rather than free space pump laser. The prospects are particularly promising for on-chip low-loss photonic switches integrated with tri-axial layered materials.

7.5 Contribution Statements

Qian Song in Riccardo Comin's group at MIT did polarized Raman measurement. Frank Gao and Zhuquan Zhang in Keith Nelson's group at MIT performed the single-shot ThZ pump probe measurement.

Chapter 8

Conclusions and Outlook

8.1 Conclusions

In this thesis, I investigated and developed techniques to make van der Waals (vdW) layered materials (LMs) more applicable in integrated photonics and microelectronics, particularly transiton metal dichalcogenides (TMDs, MX_2) and group IV-VI monochalcogenides (GeS-type, MX) which providing strong, non-perturbative optical phase modulation.

This thesis began by describing the unique structural and resulting novel optical properties of LMs and LMs as an emerging phase change materials for low loss intergrated photonics, thus motivating further research in (1) wafer-scale and low temperature processing methods, (2) air stability and native oxidation of LMs for semiconductor technology and (3) anisotropic optical properties of LMs enabled for optical phase shifters controlled by light.

In Chapter 2, low temperature processing as low as 400 °C was demonstrated using the oxygen gas (O_2) as a reaction catalyst. I corroborated that O_2 gas enhanced the formation of crystalline 2H-MoS_2 and changed the orientation of MoS_2 crystallite by sulfurization of metallic Mo. Our low temperature two-step process produced films that were smooth and continuous on various substrate. Furthermore, k (imaginary part of refractive index) of our chemical vapor deposition MoS_2 was measured on few different types of photonic devices, featuring low optical loss ($k < 0.1$).

In Chapter 3, I confirmed that O_2 acted as an inhibitor in TiS_2 formation resulting into high sulfurization temperature of 900 °C. Large-area TiS_2 thin films at temperature as low as 500 °C was successfully synthesized by significantly reducing oxygen background during sulfurization. This dependence resulted from the fact that Ti-O bonds presented a substantial kinetic and thermodynamic barrier to TiS_2 formation. I concluded that lowering the sulfurization temperature was important to make smooth films, and to enable integration of TiS_2 into device technology.

In Chapter 4, I provided quantitative guidance for designing and processing semiconductor devices based on ZrS_xSe_{2-x}, MoS_2, WS_2, WSe_2 and HfS_2 with sub-nm resolution using spectroscopic ellipsometry, and identified the atomistic-scale mechanisms of bonding and phase transformations in layered materials with competing anions. I found that the Zr-based TMDs oxidized readily, with the rate increasing with Se content. Meanwhile, MoS_2 was not oxidized at all in air on a laboratory time scale. I demonstrated that oxygen favorably chemisorbed on the ZrS_2 surface, and then moved readily into the crystal lattice by a mechanism of Zr-O bond switching, facilitated by successive redox transitions at the S sites. The rate-limiting step for oxide growth was the formation and out-diffusion of SO_2.

In Chapter 5, I demonstrated the role of the various process parameters involved in thermal oxidation of MoS_2 and thus found MoO_3 was grown on MoS_2 by vapor phase transport vdW epitaxy through nucleation, growth and coalescence process, which raising the issue with finding a sweet spot between MoO_x formation rate and MoO_x volatilization rate. The plasma-generated oxide was a conformal, continuous and amorphous thin film ($\sim$ 4 nm) indicating oxidation occured in bulk MoS_2 by reacting with oxygen.

In Chapter 6, I showed that the orientation of the in-plane crystal structure of two dimensional (2D) LMs with low symmetry – specifically the triaxial materials SnSe and bP – had a substantial impact on device performance when integrated into photonic integrated ring resonators and 1 $\times$ 2 switches. Theory predicted that the crystal orientation (*i.e.* the ferroelastic domain structure) of such materials can be switched through an ultra-fast, non-thermal, and lower-power method by strong

electric fields, due to dielectric anisotropy. Should such predictions be borne out in experiment, then triaxial layered and 2D materials may become quite useful for light-controls-light mechanisms in photonic integrated circuits. Our results may be broadly applicable to layered and 2D materials with ferroelectric and ferroelastic crystal structures, which number more than the two studied here.

In Chapter 7, I conducted single THz pump probe spectroscopy on the mechanically exfoliated SnSe flakes with a thickness of 30 nm to demonstrate the opto-mechanical properties of GeS-type materials. The preliminary result of a THz-induced phase transition in bulk SnSe was obtained using single shot spectroscopy with reflection geometry. The reflectivity change following THz excitation ($\sim$ 15 %) suggested the phase transition from armchair $\parallel \hat{x}$ to zigzag $\parallel \hat{x}$ within $\sim$ 20 ps. This was the first experimental demonstration proving the phenomenon of that anisotropic dielectric properties of GeS-type VI-VI monochalcogenides can be used for barrier-less, martensitic transition upon linearly-polarized light exposure.

Overall, this thesis studied large area processing (synthesis of semiconductor), native oxide formation (insulator for semiconductor technology) and the proof-of-concepts of optical switches (applications using semiconductor) to demonstrate the usefulness and competitiveness of LMs in current semiconductor technology particularly in photonic integrated circuits.

8.2 Outlook

I end this thesis by proposing several promising directions as an extension of this thesis.

8.2.1 Device Characterization based on LMs Produced at Low Temperature

I proposed low temperature processing expanding compatibility of LMs with modern silicon integrated circuit technology, from font-end-of-line to back-end-of-line integra-

tion. Our low temperature processed MoS_2 film is chemically pure and nanocrystalline with high grain boundary density. But the optical loss is still low, which suggesting our wafer-scale, patternable MoS2 is a good candidate for low loss photonics.

Thus future study requires to design, fabricate devices and further investigate device performance as function of processing parameters of other transition metal chacogenides. The crystalline quality including gain size, layer number, uniformity of layer orientation and defect density should be improved to achieve low loss, high charge confinement and high Δn for optical phase shifters (ring resonator, directional coupler, MZI etc). Many open questions remain, however, including about the advantage of resultant polycrystalline film in martensitic transformation discussed in Chapter 7, whether grain boundaries are of benefit to reduce/relax the stress induced by the transition.

8.2.2 Thermal and Non-Thermal Oxidation of Epitaxial 2D Layered Materials

Thermal oxidation and non-thermal oxidation study in this thesis are limited to exfoliated bulk MoS_2 crystals which the distinctive surface features complicate to identify the clear kinetic pathway taken. When it comes to native oxide as a high quality functional material, it offers electrically beneficial interface by suppressing interfacial trap states. To demonstrate the advantages, the native oxide should be grown on homogeneous, flat and continuous wafers to remove these unnecessary surface factors and further make device with the resultant LMs/oxide stacks. This requires using epitaxy LMs wafers to make electrically high quality interface between LMs and its counterpart oxide, and is currently under development in our group. I proved that thermal oxide of MoS_2 formed by vapor transport phase growth due to the high volatilization of MoO_3, meaning the interface quality could be very different from that of Si/SiO_2. Therefore, for epitaxy MoS_2 wafer, plasma oxidation study on the correlation between processing parameters and structural/functional (particularly, electrical and dielectric properties of the oxide) characterization needs to be conducted first.

8.2.3 Optical Switching of SnSe Obtained by Bottom-Up Method

Chapter 6 and 7 showed how in-plane anisotropy can be used for low loss optical switches and how anistropic dielectric functions can induce barrier-less, ultra-fast, martensitic transformation. Another interesting, longer-term research direction is to further extend the switching experiments using different optical set-up and monolayer SnSe synthesized by bottom-up method such as molecular beam epitaxy and chemical vapor deposition. Due to the high exfoliation energy of SnSe, I was not able to achieve monolayer SnSe by mechanical exfoliation and the underlying layers could increase the strength of required electric field, which could be overcome using bottom-up method, making the calculated value more close to the actual value required for experimental realization. By adopting other available optical pump selections, THz enhancement structure may not be necessary and thus the whole grain or thin film which smaller than laser spot size can be switched without strain constraints resulted from surrounding domains. Once the switching behavior is confirmed in SnSe, we can expand the material selection and prove this switching mechanism is widely applicable to 2D GeS-type LMs.

Bibliography

[1] Momma, K. & Izumi, F. Vesta 3 for three-dimensional visualization of crystal, volumetric and morphology data. *Journal of applied crystallography* **44**, 1272–1276 (2011).

[2] Wang, N. *et al.* Design of ultra-compact optical memristive switches with gst as the active material. *Micromachines* **10**, 453 (2019).

[3] Li, Y., Singh, A., Krylyuk, S., Davydov, A. & Jaramillo, R. Near-infrared photonic phase-change properties of transition metal ditellurides. In *Low-Dimensional Materials and Devices 2019*, vol. 11085, 110850T (International Society for Optics and Photonics, 2019).

[4] Li, J. *et al.* High-performance graphene-integrated thermo-optic switch: design and experimental validation. *Optical Materials Express* **10**, 387–396 (2020).

[5] Banus, M., Reed, T. & Strauss, A. Electrical and magnetic properties of tio and vo. *Phys. Rev. B* **5**, 2775 (1972).

[6] Chianelli, R., Scanlon, J. & Thompson, A. Structure refinement of stoichiometric tis2. *Mater. Res. Bull* **10**, 1379–1382 (1975).

[7] Wood, R. The lattice constants of high purity alpha titanium. *Proc. Phys. Soc. (1958-1967)* **80**, 783 (1962).

[8] Zhou, J., Xu, H., Li, Y., Jaramillo, R. & Li, J. Opto-mechanics driven fast martensitic transition in two-dimensional materials. *Nano Lett.* **18**, 7794–7800 (2018).

[9] Chowdhury, C., Karmakar, S. & Datta, A. Monolayer group iv–vi monochalcogenides: low-dimensional materials for photocatalytic water splitting. *The Journal of Physical Chemistry C* **121**, 7615–7624 (2017).

[10] Chang, K. & Parkin, S. S. Experimental formation of monolayer group-iv monochalcogenides. *Journal of Applied Physics* **127**, 220902 (2020).

[11] He, B. B. *Two-Dimensional X-Ray Diffraction - Geometry Conventions* (2009).

[12] Singh, A. *et al.* Refractive uses of layered and two-dimensional materials for integrated photonics. *ACS Photonics* **7**, 3270–3285 (2020).

[13] Leuthold, J., Koos, C. & Freude, W. Nonlinear silicon photonics. *Nat. Photonics* **4**, 535–544 (2010).

[14] Chai, Z. *et al.* Ultrafast all-optical switching. *Adv. Opt. Mater.* **5**, 1600665 (2017).

[15] Subbaraman, H. *et al.* Recent advances in silicon-based passive and active optical interconnects. *Opt. Express* **23**, 2487–2511 (2015).

[16] Nikolova, D. *et al.* Scaling silicon photonic switch fabrics for data center interconnection networks. *Opt. Express* **23**, 1159–1175 (2015).

[17] Reed, G. T., Mashanovich, G., Gardes, F. Y. & Thomson, D. Silicon optical modulators. *Nat. Photonics* **4**, 518–526 (2010).

[18] Soref, R. & Bennett, B. Electrooptical effects in silicon. *IEEE J. Quantum Electron.* **23**, 123–129 (1987).

[19] Janner, D., Tulli, D., García-Granda, M., Belmonte, M. & Pruneri, V. Micro-structured integrated electro-optic linbo3 modulators. *Laser Photonics Rev.* **3**, 301–313 (2009).

[20] Mak, K. F., Lee, C., Hone, J., Shan, J. & Heinz, T. F. Atomically thin mos 2: a new direct-gap semiconductor. *Physical review letters* **105**, 136805 (2010).

[21] Butler, S. Z. *et al.* Progress, challenges, and opportunities in two-dimensional materials beyond graphene. *ACS nano* **7**, 2898–2926 (2013).

[22] Shi, G. & Kioupakis, E. Anisotropic spin transport and strong visible-light absorbance in few-layer snse and gese. *Nano Lett.* **15**, 6926–6931 (2015).

[23] Singh, A. *et al.* Near-infrared optical properties and proposed phase-change usefulness of transition metal disulfides. *Appl. Phys. Lett* **115**, 161902 (2019).

[24] Greenaway, D. L. & Nitsche, R. Preparation and optical properties of group iv–vi2 chalcogenides having the cdi2 structure. *Journal of Physics and Chemistry of Solids* **26**, 1445–1458 (1965).

[25] Gregora, I., Velickỳa, B. & Závětová, M. Refractive index of crystalline and amorphous ges. *physica status solidi (b)* **104**, K95–K100 (1981).

[26] Banai, R. *et al.* Ellipsometric characterization and density-functional theory analysis of anisotropic optical properties of single-crystal α-sns. *Journal of Applied Physics* **116**, 013511 (2014).

[27] Wang, X. & Lan, S. Optical properties of black phosphorus. *Advances in Optics and photonics* **8**, 618–655 (2016).

[28] Oliver, S. M. *et al.* Phonons and excitons in zrse 2–zrs 2 alloys. *J. Mater. Chem. C.* **8**, 5732–5743 (2020).

[29] Wang, Y. *et al.* Composition-tunable 2d snse 2 (1- x) s 2x alloys towards efficient bandgap engineering and high performance (opto) electronics. *Journal of Materials Chemistry C* **5**, 84–90 (2017).

[30] Evans, B. & Young, P. Optical absorption and dispersion in molybdenum disulphide. *Proceedings of the Royal Society of London. Series A. Mathematical and Physical Sciences* **284**, 402–422 (1965).

[31] Wilson, J. A. & Yoffe, A. The transition metal dichalcogenides discussion and interpretation of the observed optical, electrical and structural properties. *Advances in Physics* **18**, 193–335 (1969).

[32] Liu, H.-L. *et al.* Optical properties of monolayer transition metal dichalcogenides probed by spectroscopic ellipsometry. *Applied Physics Letters* **105**, 201905 (2014).

[33] Li, Y. *et al.* Measurement of the optical dielectric function of monolayer transition-metal dichalcogenides: Mos 2, mo s e 2, ws 2, and ws e 2. *Physical Review B* **90**, 205422 (2014).

[34] Funke, S. *et al.* Imaging spectroscopic ellipsometry of mos2. *Journal of Physics: Condensed Matter* **28**, 385301 (2016).

[35] Rha, S.-K. *et al.* Improved tin film as a diffusion barrier between copper and silicon. *Thin Solid Films* **320**, 134–140 (1998).

[36] Takamura, Y., Jain, S., Griffin, P. & Plummer, J. Thermal stability of dopants in laser annealed silicon. *Journal of Applied Physics* **92**, 230–234 (2002).

[37] Qin, S. Dopant deactivation and reactivation study of advanced doping technologies. In *2014 International Workshop on Junction Technology (IWJT)*, 1–7 (IEEE, 2014).

[38] Tang, A. *et al.* Toward low-temperature solid-source synthesis of monolayer mos2. *ACS Applied Materials & Interfaces* **13**, 41866–41874 (2021).

[39] Sedky, S., Witvrouw, A., Bender, H. & Baert, K. Experimental determination of the maximum post-process annealing temperature for standard cmos wafers. *IEEE transactions on Electron Devices* **48**, 377–385 (2001).

[40] Takeuchi, H., Wung, A., Sun, X., Howe, R. T. & King, T.-J. Thermal budget limits of quarter-micrometer foundry cmos for post-processing mems devices. *IEEE transactions on Electron Devices* **52**, 2081–2086 (2005).

[41] Bae, S. *et al.* Roll-to-roll production of 30-inch graphene films for transparent electrodes. *Nature nanotechnology* **5**, 574–578 (2010).

[42] Kobayashi, T. *et al.* Production of a 100-m-long high-quality graphene transparent conductive film by roll-to-roll chemical vapor deposition and transfer process. *Applied Physics Letters* **102**, 023112 (2013).

[43] Xin, H., Zhao, Q., Chen, D. & Li, W. Roll-to-roll mechanical peeling for dry transfer of chemical vapor deposition graphene. *Journal of Micro and Nano-Manufacturing* **6** (2018).

[44] Hong, N. *et al.* Roll-to-roll dry transfer of large-scale graphene. *Advanced Materials* 2106615 (2021).

[45] Zhang, J. *et al.* Scalable growth of high-quality polycrystalline mos2 monolayers on sio2 with tunable grain sizes. *ACS Nano* **8**, 6024–6030 (2014).

[46] Bhimanapati, G. R. *et al.* Recent advances in two-dimensional materials beyond graphene. *ACS Nano* **9**, 11509–11539 (2015).

[47] Zhou, J. *et al.* A library of atomically thin metal chalcogenides. *Nature* **556**, 355–359 (2018).

[48] Sutter, E., Zhang, B., Sun, M. & Sutter, P. Few-layer to multilayer germanium (ii) sulfide: synthesis, structure, stability, and optoelectronics. *ACS Nano* **13**, 9352–9362 (2019).

[49] Xue, D.-J. *et al.* Gese thin-film solar cells fabricated by self-regulated rapid thermal sublimation. *J. Am. Chem. Soc.* **139**, 958–965 (2017).

[50] Xu, Y. *et al.* Epitaxial nucleation and lateral growth of high-crystalline black phosphorus films on silicon. *Nat. Commun* **11**, 1–8 (2020).

[51] Maiti, R. *et al.* A semi-empirical integrated microring cavity approach for 2d material optical index identification at 1.55 μm. *Nanophotonics* **8**, 435–441 (2019).

[52] Wei, G., Stanev, T. K., Czaplewski, D. A., Jung, I. W. & Stern, N. P. Silicon-nitride photonic circuits interfaced with monolayer mos2. *Appl. Phys. Lett.* **107**, 091112 (2015).

[53] Kang, K. *et al.* High-mobility three-atom-thick semiconducting films with wafer-scale homogeneity. *Nature* **520**, 656–660 (2015).

[54] Bade, B. P., Garje, S. S., Niwate, Y. S., Afzaal, M. & O'Brien, P. Tribenzyltin (iv) chloride thiosemicarbazones: novel single source precursors for growth of sns thin films. *Chem. Vap. Depos.* **14**, 292–295 (2008).

[55] Boscher, N. D., Carmalt, C. J., Palgrave, R. G. & Parkin, I. P. Atmospheric pressure chemical vapour deposition of snse and snse2 thin films on glass. *Thin Solid Films* **516**, 4750–4757 (2008).

[56] Eichfeld, S. M. *et al.* Highly scalable, atomically thin wse2 grown via metal–organic chemical vapor deposition. *ACS Nano* **9**, 2080–2087 (2015).

[57] Chang, H. & Schleich, D. Tis2 and tis3 thin films prepared by mocvd. *J. Solid State Chem.* **100**, 62–70 (1992).

[58] Tarasov, A. *et al.* Highly uniform trilayer molybdenum disulfide for wafer-scale device fabrication. *Adv. Funct. Mater* **24**, 6389–6400 (2014).

[59] Jo, S. S. *et al.* Formation of large-area mos2 thin films by oxygen-catalyzed sulfurization of mo thin films. *J. Vac. Sci. Technol. A: Vac. Surf. Films* **38**, 013405 (2020).

[60] Li, Y. *et al.* Making large-area titanium disulfide films at reduced temperature by balancing the kinetics of sulfurization and roughening. *Adv. Funct. Mater* **30**, 2003617 (2020).

[61] Krbal, M. *et al.* 2d mose2 structures prepared by atomic layer deposition. *Phys Status Solidi – Rapid Res Lett* **12**, 1800023 (2018).

[62] Kim, S. B., Sinsermsuksakul, P., Pike, R. D. & Gordon, R. G. Synthesis of n-heterocyclic stannylene (sn (ii)) and germylene (ge (ii)) and a sn (ii) amidinate and their application as precursors for atomic layer deposition. *Chem. Mater.* **26**, 3065–3073 (2014).

[63] Drozd, V. *et al.* Ald synthesis of snse layers and nanostructures. *J. Phys. D J PHYS D APPL PHYS* **42**, 125306 (2009).

[64] Kim, W. *et al.* Atomic layer deposition of gese films using hgecl3 and [(ch3) 3si] 2se with the discrete feeding method for the ovonic threshold switch. *Nanotechnology* **29**, 365202 (2018).

[65] Nam, T. & Kim, H. Atomic layer deposition for nonconventional nanomaterials and their applications. *J. Mater. Res.* **35**, 656–680 (2020).

[66] Yeo, S. *et al.* Low-temperature direct synthesis of high quality ws2 thin films by plasma-enhanced atomic layer deposition for energy related applications. *Appl. Surf. Sci* **459**, 596–605 (2018).

[67] Basuvalingam, S. B. *et al.* Low-temperature phase-controlled synthesis of titanium di-and tri-sulfide by atomic layer deposition. *Chem. Mater.* **31**, 9354–9362 (2019).

[68] Mattinen, M. *et al.* Van der waals epitaxy of continuous thin films of 2d materials using atomic layer deposition in low temperature and low vacuum conditions. *2D Mater.* **7**, 011003 (2019).

[69] Oviroh, P. O., Akbarzadeh, R., Pan, D., Coetzee, R. A. M. & Jen, T.-C. New development of atomic layer deposition: processes, methods and applications. *Science and technology of advanced materials* **20**, 465–496 (2019).

[70] Indirajith, R., Srinivasan, T., Ramamurthi, K. & Gopalakrishnan, R. Synthesis, deposition and characterization of tin selenide thin films by thermal evaporation technique. *Curr. Appl. Phys.* **10**, 1402–1406 (2010).

[71] Liu, S.-C. *et al.* Tuning the optical absorption property of gese thin films by annealing treatment. *Phys. Status Solidi – Rapid Res. Lett.* **12**, 1800370 (2018).

[72] Patel, S., Aparimita, A., Sripan, C., Ganesan, R. & Naik, R. Thermal annealing induced ag diffusion into ges thin film: Structural and optical property study. In *AIP Conf Proc.*, vol. 2115, 030276 (AIP Publishing LLC, 2019).

[73] Bashkirov, S., Gremenok, V. & Ivanov, V. Physical properties of sns thin films fabricated by hot wall deposition. *Semiconductors* **45**, 749–752 (2011).

[74] Yang, Z. *et al.* Field-effect transistors based on amorphous black phosphorus ultrathin films by pulsed laser deposition. *Adv. Mater.* **27**, 3748–3754 (2015).

[75] Serna, M. I. *et al.* Large-area deposition of mos2 by pulsed laser deposition with in situ thickness control. *ACS Nano* **10**, 6054–6061 (2016).

[76] Hamada, M. *et al.* High hall-effect mobility of large-area atomic-layered polycrystalline zrs 2 film using uhv rf magnetron sputtering and sulfurization. *IEEE J. Electron Devices Soc.* **7**, 1258–1263 (2019).

[77] Rajan, A., Underwood, K., Mazzola, F. & King, P. D. Morphology control of epitaxial monolayer transition metal dichalcogenides. *Phys. Rev. Mater.* **4**, 014003 (2020).

[78] Yue, R. *et al.* Nucleation and growth of wse2: enabling large grain transition metal dichalcogenides. *2D Mater.* **4**, 045019 (2017).

[79] Pacuski, W. *et al.* Narrow excitonic lines and large-scale homogeneity of transition-metal dichalcogenide monolayers grown by molecular beam epitaxy on hexagonal boron nitride. *Nano Lett.* **20**, 3058–3066 (2020).

[80] Henini, M. *Molecular beam epitaxy: from research to mass production* (Elsevier, 2012).

[81] Tiefenbacher, S., Sehnert, H., Pettenkofer, C. & Jaegermann, W. Epitaxial films of ws2 by metal organic van der waals epitaxy (mo-vdwe). *Surf. Sci.* **318**, L1161–L1164 (1994).

[82] Mleczko, M. J. *et al.* Hfse2 and zrse2: Two-dimensional semiconductors with native high-κ oxides. *Sci. Adv.* **3**, e1700481 (2017).

[83] Jaramillo, R. *et al.* Transient terahertz photoconductivity measurements of minority-carrier lifetime in tin sulfide thin films: Advanced metrology for an early stage photovoltaic material. *Journal of Applied Physics* **119**, 035101 (2016).

[84] Mirabelli, G. *et al.* Air sensitivity of mos2, mose2, mote2, hfs2, and hfse2. *J. Appl. Phys.* **120**, 125102 (2016).

[85] Liu, H., Han, N. & Zhao, J. Atomistic insight into the oxidation of monolayer transition metal dichalcogenides: from structures to electronic properties. *RSC Adv.* **5**, 17572–17581 (2015).

[86] Kc, S., Longo, R. C., Wallace, R. M. & Cho, K. Surface oxidation energetics and kinetics on mos2 monolayer. *J. Appl. Phys.* **117**, 135301 (2015).

[87] Li, Q., Zhou, Q., Shi, L., Chen, Q. & Wang, J. Recent advances in oxidation and degradation mechanisms of ultrathin 2d materials under ambient conditions and their passivation strategies. *J. Mater. Chem. A.* **7**, 4291–4312 (2019).

[88] Castellanos-Gomez, A. Black phosphorus: narrow gap, wide applications. *J. Phys. Chem.* **6**, 4280–4291 (2015).

[89] Ye, F. *et al.* Environmental instability and degradation of single-and few-layer wte2 nanosheets in ambient conditions. *Small* **12**, 5802–5808 (2016).

[90] Ahluwalia, G. K. *Applications of chalcogenides: S, Se, and Te* (2017).

[91] Ríos, C. *et al.* Integrated all-photonic non-volatile multi-level memory. *Nature photonics* **9**, 725–732 (2015).

[92] Makino, K., Tominaga, J. & Hase, M. Ultrafast optical manipulation of atomic arrangements in chalcogenide alloy memory materials. *Opt. Express* **19**, 1260–1270 (2011).

[93] Wuttig, M. & Yamada, N. Phase-change materials for rewriteable data storage. *Nat. Mater.* **6**, 824–832 (2007).

[94] Le Gallo, M. & Sebastian, A. An overview of phase-change memory device physics. *J. Phys. D J PHYS D APPL PHYS* **53**, 213002 (2020).

[95] Wu, C. *et al.* Low-loss integrated photonic switch using subwavelength patterned phase change material. *Acs Photonics* **6**, 87–92 (2018).

[96] Nukala, P., Lin, C.-C., Composto, R. & Agarwal, R. Ultralow-power switching via defect engineering in germanium telluride phase-change memory devices. *Nat. Commun.* **7**, 1–8 (2016).

[97] Duerloo, K.-A. N., Li, Y. & Reed, E. J. Structural phase transitions in two-dimensional mo-and w-dichalcogenide monolayers. *Nature communications* **5**, 1–9 (2014).

[98] Lin, Y.-C., Dumcenco, D. O., Huang, Y.-S. & Suenaga, K. Atomic mechanism of the semiconducting-to-metallic phase transition in single-layered mos 2. *Nature nanotechnology* **9**, 391–396 (2014).

[99] Zhang, F. *et al.* Electric-field induced structural transition in vertical mote 2-and mo 1–x w x te 2-based resistive memories. *Nature materials* **18**, 55–61 (2019).

[100] Zhang, Y. *et al.* Broadband transparent optical phase change materials for high-performance nonvolatile photonics. *Nat. Commun.* **10**, 1–9 (2019).

[101] Xu, H., Zhou, J., Li, Y., Jaramillo, R. & Li, J. Optomechanical control of stacking patterns of h-bn bilayer. *Nano Res.* **12**, 2634–2639 (2019).

[102] Yu, Y. *et al.* Giant gating tunability of optical refractive index in transition metal dichalcogenide monolayers. *Nano letters* **17**, 3613–3618 (2017).

[103] Datta, I. *et al.* Low-loss composite photonic platform based on 2d semiconductor monolayers. *Nat. Photonics* **14**, 256–262 (2020).

[104] Li, Y., Duerloo, K.-A. N., Wauson, K. & Reed, E. J. Structural semiconductor-to-semimetal phase transition in two-dimensional materials induced by electrostatic gating. *Nat. Commun.* **7**, 1–8 (2016).

[105] Radisavljevic, B. & Kis, A. Mobility engineering and a metal–insulator transition in monolayer mos 2. *Nat. Mater.* **12**, 815–820 (2013).

[106] Lee, H. S. *et al.* Mos2 nanosheet phototransistors with thickness-modulated optical energy gap. *Nano Lett.* **12**, 3695–3700 (2012).

[107] Splendiani, A. *et al.* Emerging photoluminescence in monolayer mos2. *Nano Lett.* **10**, 1271–1275 (2010).

[108] Lopez-Sanchez, O., Lembke, D., Kayci, M., Radenovic, A. & Kis, A. Ultrasensitive photodetectors based on monolayer mos 2. *Nat. Nanotechnol* **8**, 497–501 (2013).

[109] Radisavljevic, B., Radenovic, A., Brivio, J., Giacometti, V. & Kis, A. Single-layer mos 2 transistors. *Nat. Nanotechnol* **6**, 147–150 (2011).

[110] Braga, D., Gutiérrez Lezama, I., Berger, H. & Morpurgo, A. F. Quantitative determination of the band gap of ws2 with ambipolar ionic liquid-gated transistors. *Nano Lett.* **12**, 5218–5223 (2012).

[111] Perera, M. M. *et al.* Improved carrier mobility in few-layer mos2 field-effect transistors with ionic-liquid gating. *ACS Nano* **7**, 4449–4458 (2013).

[112] Li, G. *et al.* All the catalytic active sites of mos2 for hydrogen evolution. *J. Am. Chem. Soc.* **138**, 16632–16638 (2016).

[113] Voiry, D. *et al.* Conducting mos2 nanosheets as catalysts for hydrogen evolution reaction. *Nano Lett.* **13**, 6222–6227 (2013).

[114] Liu, G. *et al.* Mos 2 monolayer catalyst doped with isolated co atoms for the hydrodeoxygenation reaction. *Nat. Chem.* **9**, 810–816 (2017).

[115] Samnakay, R., Jiang, C., Rumyantsev, S., Shur, M. & Balandin, A. Selective chemical vapor sensing with few-layer mos2 thin-film transistors: comparison with graphene devices. *Appl. Phys. Lett* **106**, 023115 (2015).

[116] Kumar, R., Goel, N. & Kumar, M. Uv-activated mos2 based fast and reversible no2 sensor at room temperature. *ACS Sens.* **2**, 1744–1752 (2017).

[117] Lee, Y.-H. *et al.* Synthesis of large-area mos2 atomic layers with chemical vapor deposition. *Adv. Mater* **24**, 2320–2325 (2012).

[118] Kang, K. N., Godin, K. & Yang, E.-H. The growth scale and kinetics of ws 2 monolayers under varying h 2 concentration. *Sci. Rep.* **5**, 1–9 (2015).

[119] Park, W. *et al.* Photoelectron spectroscopic imaging and device applications of large-area patternable single-layer mos2 synthesized by chemical vapor deposition. *ACS Nano* **8**, 4961–4968 (2014).

[120] Shi, Y., Li, H. & Li, L.-J. Recent advances in controlled synthesis of two-dimensional transition metal dichalcogenides via vapour deposition techniques. *Chem. Soc. Rev.* **44**, 2744–2756 (2015).

[121] Salazar, N., Beinik, I. & Lauritsen, J. V. Single-layer mos 2 formation by sulfidation of molybdenum oxides in different oxidation states on au (111). *Phys. Chem. Chem. Phys* **19**, 14020–14029 (2017).

[122] Wu, C.-R., Chang, X.-R., Wu, C.-H. & Lin, S.-Y. The growth mechanism of transition metal dichalcogenides by using sulfurization of pre-deposited transition metals and the 2d crystal hetero-structure establishment. *Sci. Rep.* **7**, 1–8 (2017).

[123] Cain, J. D., Shi, F., Wu, J. & Dravid, V. P. Growth mechanism of transition metal dichalcogenide monolayers: the role of self-seeding fullerene nuclei. *ACS Nano* **10**, 5440–5445 (2016).

[124] Pyeon, J. J. *et al.* Wafer-scale growth of mos 2 thin films by atomic layer deposition. *Nanoscale* **8**, 10792–10798 (2016).

[125] Jurca, T. *et al.* Low-temperature atomic layer deposition of mos2 films. *Angew. Chem. Int. Ed.* **56**, 4991–4995 (2017).

[126] Valdivia, A., Tweet, D. J. & Conley Jr, J. F. Atomic layer deposition of two dimensional mos2 on 150 mm substrates. *J. Vac. Sci. Technol. A: Vac. Surf. Films* **34**, 021515 (2016).

[127] Browning, R. *et al.* Atomic layer deposition of mos2 thin films. *Mater. Res. Express* **2**, 035006 (2015).

[128] Tan, L. K. *et al.* Atomic layer deposition of a mos2 film. *Nanoscale* **6**, 10584–10588 (2014).

[129] Jin, Z., Shin, S., Han, S.-J., Min, Y.-S. *et al.* Novel chemical route for atomic layer deposition of mos 2 thin film on sio 2/si substrate. *Nanoscale* **6**, 14453–14458 (2014).

[130] Andrzejewski, D. *et al.* Improved luminescence properties of mos2 monolayers grown via mocvd: role of pre-treatment and growth parameters. *Nanotechnology* **29**, 295704 (2018).

[131] Cwik, S. *et al.* Direct growth of mos2 and ws2 layers by metal organic chemical vapor deposition. *Adv. Mater. Interfaces* **5**, 1800140 (2018).

[132] Zhan, Y., Liu, Z., Najmaei, S., Ajayan, P. M. & Lou, J. Large-area vapor-phase growth and characterization of mos2 atomic layers on a sio2 substrate. *Small* **8**, 966–971 (2012).

[133] Choudhary, N., Park, J., Hwang, J. Y. & Choi, W. Growth of large-scale and thickness-modulated mos2 nanosheets. *ACS Appl. Mater. Interfaces* **6**, 21215–21222 (2014).

[134] Keller, B. D. *et al.* Process control of atomic layer deposition molybdenum oxide nucleation and sulfidation to large-area mos2 monolayers. *Chem. Mater.* **29**, 2024–2032 (2017).

[135] Chen, W. *et al.* Oxygen-assisted chemical vapor deposition growth of large single-crystal and high-quality monolayer mos2. *J. Am. Chem. Soc.* **137**, 15632–15635 (2015).

[136] Yu, H. *et al.* Wafer-scale growth and transfer of highly-oriented monolayer mos2 continuous films. *ACS Nano* **11**, 12001–12007 (2017).

[137] Zhou, H. *et al.* Thickness-dependent patterning of mos 2 sheets with well-oriented triangular pits by heating in air. *Nano Res.* **6**, 703–711 (2013).

[138] Hong, S. *et al.* Chemical vapor deposition synthesis of mos2 layers from the direct sulfidation of moo3 surfaces using reactive molecular dynamics simulations. *J. Phys. Chem. C* **122**, 7494–7503 (2018).

[139] Tate, M. W. *et al.* High dynamic range pixel array detector for scanning transmission electron microscopy. *Microsc. Microanal* **22**, 237–249 (2016).

[140] Cheng, Y. *et al.* Van der waals epitaxial growth of mos 2 on sio 2/si by chemical vapor deposition. *RSC Adv.* **3**, 17287–17293 (2013).

[141] Patterson, T. A., Carver, J. C., Leyden, D. E. & Hercules, D. M. A surface study of cobalt-molybdena-alumina catalysts using x-ray photoelectron spectroscopy. *The Journal of Physical Chemistry* **80**, 1700–1708 (1976).

[142] Conner, G. Combination analysis of metal oxides using esca, aes, and sims. *J. Vac. Sci. Technol.* **15**, 343–347 (1978).

[143] Choi, J.-G. & Thompson, L. Xps study of as-prepared and reduced molybdenum oxides. *Appl. Surf. Sci.* **93**, 143–149 (1996).

[144] Klug, H. & Alexander, L. X-ray diffraction procedures for polycrystalline and amorphous materials, wiley, new york 1974.

[145] Veeramalai, C. P. *et al.* Enhanced field emission properties of molybdenum disulphide few layer nanosheets synthesized by hydrothermal method. *Appl. Surf. Sci.* **389**, 1017–1022 (2016).

[146] Heo, S., Ishiguro, Y., Hayakawa, R., Chikyow, T. & Wakayama, Y. Perspective: Highly ordered mos2 thin films grown by multi-step chemical vapor deposition process. *APL Mater.* **4**, 030901 (2016).

[147] Jung, Y. *et al.* Metal seed layer thickness-induced transition from vertical to horizontal growth of mos2 and ws2. *Nano Lett.* **14**, 6842–6849 (2014).

[148] Shulaker, M. M. *et al.* Three-dimensional integration of nanotechnologies for computing and data storage on a single chip. *Nature* **547**, 74–78 (2017).

[149] Yu, W. J. *et al.* Vertically stacked multi-heterostructures of layered materials for logic transistors and complementary inverters. *Nature Mater.* **12**, 246–252 (2013).

[150] Zhao, Z. *et al.* Cathodoluminescence as an effective probe of carrier transport and deep level defects in droop-mitigating ingan/gan quantum well heterostructures. *Appl. Phys. Express* **12**, 034003 (2019).

[151] Pore, V., Ritala, M. & Leskelä, M. Atomic layer deposition of titanium disulfide thin films. *Chem. Vap. Depos.* **13**, 163–168 (2007).

[152] Gao, Z. *et al.* In situ-generated volatile precursor for cvd growth of a semimetallic 2d dichalcogenide. *ACS Appl. Mater. Interfaces* **10**, 34401–34408 (2018).

[153] Talib, M., Tabassum, R., Islam, S. & Mishra, P. Influence of growth temperature on titanium sulphide nanostructures: from trisulphide nanosheets and nanoribbons to disulphide nanodiscs. *RSC Adv.* **9**, 645–657 (2019).

[154] McDonnell, S., Smyth, C., Hinkle, C. L. & Wallace, R. M. Mos2–titanium contact interface reactions. *ACS Appl. Mater. Interfaces* **8**, 8289–8294 (2016).

[155] Martin, N., Rousselot, C., Rondot, D., Palmino, F. & Mercier, R. Microstructure modification of amorphous titanium oxide thin films during annealing treatment. *Thin solid films* **300**, 113–121 (1997).

[156] Salama, T. M., Tanaka, T., Yamaguchi, T. & Tanabe, K. Exafs/xanes study of titanium oxide supported on sio2: A structural consideration on the amorphous state. *Surf. Sci.* **227**, L100–L104 (1990).

[157] Onoda, M., Saeki, M. & Kawada, I. Stacking faults in nonstoichiometric titanium sulfide. *Physica B+ C* **105**, 200–204 (1981).

[158] Jo, S. S. *et al.* Growth kinetics and atomistic mechanisms of native oxidation of zrs x se2–x and mos2 crystals. *Nano Lett.* **20**, 8592–8599 (2020).

[159] Jariwala, D., Sangwan, V., Lauhon, L., Marks, T. & Hersam, M. Emerging device applications for semiconducting two-dimensional transition metal dichalcogenides. *ACS nano* **8**, 1102–1120 (2014).

[160] Wang, Q. H., Kalantar-Zadeh, K., Kis, A., Coleman, J. N. & Strano, M. S. Electronics and optoelectronics of two-dimensional transition metal dichalcogenides. *Nat. Nanotechnol* **7**, 699–712 (2012).

[161] McDonnell, S. J. & Wallace, R. M. Atomically-thin layered films for device applications based upon 2d tmdc materials. *Thin Solid Films* **616**, 482–501 (2016).

[162] Gao, J. *et al.* Aging of transition metal dichalcogenide monolayers. *ACS nano* **10**, 2628–2635 (2016).

[163] Sahoo, P. K. *et al.* Probing nano-heterogeneity and aging effects in lateral 2d heterostructures using tip-enhanced photoluminescence. *Opt. Mater. Express* **9**, 1620–1631 (2019).

[164] Cruz, A., Mutlu, Z., Ozkan, M. & Ozkan, C. S. Raman investigation of the air stability of 2h polytype hfse2 thin films. *MRS Commun.* **8**, 1191–1196 (2018).

[165] Pető, J. *et al.* Spontaneous doping of the basal plane of mos 2 single layers through oxygen substitution under ambient conditions. *Nat. Chem.* **10**, 1246–1251 (2018).

[166] Spychalski, W. L., Pisarek, M. & Szoszkiewicz, R. Microscale insight into oxidation of single mos2 crystals in air. *J. Phys. Chem. C.* **121**, 26027–26033 (2017).

[167] Budania, P. *et al.* Long-term stability of mechanically exfoliated mos 2 flakes. *MRS Commun.* **7**, 813–818 (2017).

[168] Kang, J. *et al.* Solvent exfoliation of electronic-grade, two-dimensional black phosphorus. *ACS nano* **9**, 3596–3604 (2015).

[169] Su, C. *et al.* Waterproof molecular monolayers stabilize 2d materials. *Proc. Natl. Acad. Sci. U.S.A.* **116**, 20844–20849 (2019).

[170] Ross, S. & Sussman, A. Surface oxidation of molybdenum disulfide. *J. Phys. Chem.* **59**, 889–892 (1955).

[171] Grønborg, S. S. *et al.* Basal plane oxygen exchange of epitaxial mos2 without edge oxidation. *2d Mater.* **6**, 045013 (2019).

[172] Yamamoto, M. *et al.* Self-limiting layer-by-layer oxidation of atomically thin wse2. *Nano Lett.* **15**, 2067–2073 (2015).

[173] Li, Q. *et al.* Unveiling chemical reactivity and oxidation of 1t-phased group vi disulfides. *Phys. Chem. Chem. Phys.* **21**, 17010–17017 (2019).

[174] Kotsakidis, J. C. *et al.* Oxidation of monolayer ws2 in ambient is a photoinduced process. *Nano Lett.* **19**, 5205–5215 (2019).

[175] Ly, T. H. *et al.* Observing grain boundaries in cvd-grown monolayer transition metal dichalcogenides. *ACS nano* **8**, 11401–11408 (2014).

[176] Zheng, X. *et al.* A homogeneous p–n junction diode by selective doping of few layer mose 2 using ultraviolet ozone for high-performance photovoltaic devices. *Nanoscale* **11**, 13469–13476 (2019).

[177] Zheng, X. *et al.* Controlled layer-by-layer oxidation of mote2 via o3 exposure. *ACS Appl. Mater. Interfaces* **10**, 30045–30050 (2018).

[178] Zheng, X. *et al.* Enormous enhancement in electrical performance of few-layered mote 2 due to schottky barrier reduction induced by ultraviolet ozone treatment. *Nano Res.* **13**, 952–958 (2020).

[179] Morita, M., Ohmi, T., Hasegawa, E., Kawakami, M. & Ohwada, M. Growth of native oxide on a silicon surface. *J. Appl. Phys.* **68**, 1272–1281 (1990).

[180] Hong, S. *et al.* Computational synthesis of mos2 layers by reactive molecular dynamics simulations: initial sulfidation of moo3 surfaces. *Nano Lett.* **17**, 4866–4872 (2017).

[181] Nomura, K.-i., Chen, Y.-C., Kalia, R. K., Nakano, A. & Vashishta, P. Defect migration and recombination in nanoindentation of silica glass. *Appl. Phys. Lett* **99**, 111906 (2011).

[182] Shimojo, F., Ohmura, S., Kalia, R. K., Nakano, A. & Vashishta, P. Molecular dynamics simulations of rapid hydrogen production from water using aluminum clusters as catalyzers. *Phys. Rev. Lett.* **104**, 126102 (2010).

[183] Halagačka, L., Postava, K. & Pištora, J. Analysis and modeling of depolarization effects in mueller matrix spectroscopic ellipsometry data. *Procedia Materials Science* **12**, 112–117 (2016).

[184] Van Duin, A. C., Merinov, B. V., Jang, S. S. & Goddard, W. A. Reaxff reactive force field for solid oxide fuel cell systems with application to oxygen ion transport in yttria-stabilized zirconia. *J. Phys. Chem. A.* **112**, 3133–3140 (2008).

[185] Vos, M. F., Macco, B., Thissen, N. F., Bol, A. A. & Kessels, W. Atomic layer deposition of molybdenum oxide from (n t bu) 2 (nme2) 2mo and o2 plasma. *J. Vac. Sci. Technol. A: Vac. Surf. Films* **34**, 01A103 (2016).

[186] Li, Q. *et al.* Thermodynamics and kinetics of an oxygen adatom on pristine and functionalized graphene: insight gained into their anticorrosion properties. *Phys. Chem. Chem. Phys.* **21**, 12121–12129 (2019).

[187] Agmon, N. The grotthuss mechanism. *Chem. Phys. Lett.* **244**, 456–462 (1995).

[188] Blöchl, P. E. Projector augmented-wave method. *Phys. Rev. B* **50**, 17953 (1994).

[189] Perdew, J. P., Burke, K. & Ernzerhof, M. Generalized gradient approximation made simple. *Phys. Rev. Lett.* **77**, 3865 (1996).

[190] Misawa, M. *et al.* Reactivity of sulfur molecules on moo3 (010) surface. *J. Phys. Chem* **8**, 6206–6210 (2017).

[191] Car, R. & Parrinello, M. Unified approach for molecular dynamics and density-functional theory. *Phys. Rev. Lett.* **55**, 2471 (1985).

[192] Hohenberg, P. & Kohn, W. Inhomogeneous electron gas. *Phys. Rev.* **136**, B864 (1964).

[193] Kohn, W. & Sham, L. J. Self-consistent equations including exchange and correlation effects. *Phys. Rev.* **140**, A1133 (1965).

[194] Li, W. *et al.* Uniform and ultrathin high-κ gate dielectrics for two-dimensional electronic devices. *Nature Electronics* **2**, 563–571 (2019).

[195] Azcatl, A. *et al.* Mos2 functionalization for ultra-thin atomic layer deposited dielectrics. *Applied Physics Letters* **104**, 111601 (2014).

[196] Xiao, M., Qiu, C., Zhang, Z. & Peng, L.-M. Atomic-layer-deposition growth of an ultrathin hfo2 film on graphene. *ACS applied materials & interfaces* **9**, 34050–34056 (2017).

[197] Wang, X. *et al.* Improved integration of ultra-thin high-k dielectrics in few-layer mos2 fet by remote forming gas plasma pretreatment. *Applied Physics Letters* **110**, 053110 (2017).

[198] Yang, J. *et al.* Improved growth behavior of atomic-layer-deposited high-k dielectrics on multilayer mos2 by oxygen plasma pretreatment. *ACS applied materials & interfaces* **5**, 4739–4744 (2013).

[199] Alaboson, J. M. *et al.* Seeding atomic layer deposition of high-k dielectrics on epitaxial graphene with organic self-assembled monolayers. *Acs Nano* **5**, 5223–5232 (2011).

[200] Li, T. *et al.* A native oxide high-κ gate dielectric for two-dimensional electronics. *Nature Electronics* **3**, 473–478 (2020).

[201] Ko, T. Y. *et al.* On-stack two-dimensional conversion of mos2 into moo3. *2D Materials* **4**, 014003 (2016).

[202] Zhu, H. *et al.* Remote plasma oxidation and atomic layer etching of mos2. *ACS applied materials & interfaces* **8**, 19119–19126 (2016).

[203] Wu, J. *et al.* Layer thinning and etching of mechanically exfoliated mos2 nanosheets by thermal annealing in air. *Small* **9**, 3314–3319 (2013).

[204] Yamamoto, M., Einstein, T. L., Fuhrer, M. S. & Cullen, W. G. Anisotropic etching of atomically thin mos2. *The Journal of Physical Chemistry C* **117**, 25643–25649 (2013).

[205] Brown, N. M., Cui, N. & McKinley, A. An xps study of the surface modification of natural mos2 following treatment in an rf-oxygen plasma. *Applied surface science* **134**, 11–21 (1998).

[206] Cai, L. *et al.* Rapid flame synthesis of atomically thin moo3 down to monolayer thickness for effective hole doping of wse2. *Nano letters* **17**, 3854–3861 (2017).

[207] Yoon, A., Kim, J. H., Yoon, J., Lee, Y. & Lee, Z. Van der waals epitaxial formation of atomic layered α-moo3 on mos2 by oxidation. *ACS applied materials & interfaces* **12**, 22029–22036 (2020).

[208] Daniel M. Dobkin, M. K. Z. *Principles of Chemical Vapor Deposition* (Springer, 2003).

[209] Schneider, G. F., Calado, V. E., Zandbergen, H., Vandersypen, L. M. & Dekker, C. Wedging transfer of nanostructures. *Nano letters* **10**, 1912–1916 (2010).

[210] Joseph I. Goldstein, P. E. D. C. J. C. E. L. E. L. L. S. J. R. M., Dale E. Newbury. *Scanning Electorn Microscopy and X-Ray Microanalysis* (Springer, 2003).

[211] Carcia, P. & McCarron Iii, E. Synthesis and properties of thin film polymorphs of molybdenum trioxide. *Thin Solid Films* **155**, 53–63 (1987).

[212] Smolik, G. R., Petti, D. A., Mccarthy, K. A. & Schuetz, S. T. Oxidation, volatilization, and redistribution of molybdenum from tzm alloy in air. Tech. Rep., Idaho National Engineering and Environmental Lab., Idaho Falls, ID (US) (2000).

[213] Floquet, N., Bertrand, O. & Heizmann, J. Structural and morphological studies of the growth of moo 3 scales during high-temperature oxidation of molybdenum. *Oxidation of metals* **37**, 253–280 (1992).

[214] Dieterle, M., Weinberg, G. & Mestl, G. Raman spectroscopy of molybdenum oxides part i. structural characterization of oxygen defects in moo 3- x by dr uv/vis, raman spectroscopy and x-ray diffraction. *Physical Chemistry Chemical Physics* **4**, 812–821 (2002).

[215] Yao, D. D. *et al.* Electrodeposited α-and β-phase moo3 films and investigation of their gasochromic properties. *Crystal growth & design* **12**, 1865–1870 (2012).

[216] Sun, S. *et al.* First principles investigation of the surface stability and equilibrium morphology of moo3. *Applied Surface Science* **467**, 753–759 (2019).

[217] Molina-Mendoza, A. J. *et al.* Centimeter-scale synthesis of ultrathin layered moo3 by van der waals epitaxy. *Chemistry of Materials* **28**, 4042–4051 (2016).

[218] Kim, J. H. *et al.* van der waals epitaxial growth of single crystal α-moo3 layers on layered materials growth templates. *2D Materials* **6**, 015016 (2018).

[219] Lajaunie, L., Boucher, F., Dessapt, R. & Moreau, P. Quantitative use of electron energy-loss spectroscopy mo-m2, 3 edges for the study of molybdenum oxides. *Ultramicroscopy* **149**, 1–8 (2015).

[220] Li, Y. *et al.* Oxygen vacancy-rich moo 3- x nanobelts for photocatalytic n 2 reduction to nh 3 in pure water. *Catalysis Science & Technology* **9**, 803–810 (2019).

[221] Nan, H. Y. *et al.* The thermal stability of graphene in air investigated by raman spectroscopy. *Journal of Raman Spectroscopy* **44**, 1018–1021 (2013).

[222] Jo, S. S. *et al.* Photonic platforms using in-plane optical anisotropy of tin (ii) selenide and black phosphorus. *Adv. Photonics Res.* 2100176 (2021).

[223] Yang, H. *et al.* Optical waveplates based on birefringence of anisotropic two-dimensional layered materials. *ACS Photonics* **4**, 3023–3030 (2017).

[224] Ermolaev, G. *et al.* Giant optical anisotropy in transition metal dichalcogenides for next-generation photonics. *Nat. Commun.* **12**, 1–8 (2021).

[225] C. Gomes, L. & Carvalho, A. Electronic and optical properties of low-dimensional group-iv monochalcogenides. *J. Appl. Phys.* **128**, 121101 (2020).

[226] Doha, M. H. *et al.* Integration of multi-layer black phosphorus into photoconductive antennas for thz emission. *J. Appl. Phys.* **128**, 063104 (2020).

[227] Xiong, F., Zhang, X., Lin, Z. & Chen, Y. Ferroelectric engineering of two-dimensional group-iv monochalcogenides: The effects of alloying and strain. *J. Materiom.* (2018).

[228] Zhou, J. & Zhang, S. Terahertz optics-driven phase transition in two-dimensional multiferroics. *npj 2D Mater. Applic.* **5**, 1–8 (2021).

[229] Wei, Q. & Peng, X. Superior mechanical flexibility of phosphorene and few-layer black phosphorus. *Appl. Phys. Lett.* **104**, 251915 (2014).

[230] Gajdoš, M., Hummer, K., Kresse, G., Furthmüller, J. & Bechstedt, F. Linear optical properties in the projector-augmented wave methodology. *Phys. Rev. B* **73**, 045112 (2006).

[231] Saha, S., Sinha, T. & Mookerjee, A. Electronic structure, chemical bonding, and optical properties of paraelectric batio 3. *Phys. Rev. B* **62**, 8828 (2000).

[232] Stevanović, V. *et al.* Variations of ionization potential and electron affinity as a function of surface orientation: The case of orthorhombic sns. *Appl. Phys. Lett.* **104**, 211603 (2014).

[233] Song, H.-Y. & Lü, J.-T. Density functional theory study of inter-layer coupling in bulk tin selenide. *Chemical Physics Letters* **695**, 200–204 (2018).

[234] Cho, S.-H. *et al.* Multi-layer snse nanoflake field-effect transistors with low-resistance au ohmic contacts. *Nanoscale Res. Lett.* **12**, 1–6 (2017).

[235] Wu, C. *et al.* Programmable phase-change metasurfaces on waveguides for multimode photonic convolutional neural network. *Nat. Commun.* **12**, 1–8 (2021).

[236] Shportko, K. *et al.* Resonant bonding in crystalline phase-change materials. *Nat. Mater.* **7**, 653–658 (2008).

[237] Gondarenko, A., Levy, J. S. & Lipson, M. High confinement micron-scale silicon nitride high q ring resonator. *Opt. Express* **17**, 11366–11370 (2009).

[238] Levy, J. S., Foster, M. A., Gaeta, A. L. & Lipson, M. Harmonic generation in silicon nitride ring resonators. *Opt. Express* **19**, 11415–11421 (2011).

[239] Melendez, J. J., Gonzalez-Romero, R. L. & Antonelli, A. Quasiparticle bands and optical properties of snse from an ab initio approach. *Comput. Mater. Sci.* **152**, 107–112 (2018).

[240] Liu, Z. & Aydin, K. Localized surface plasmons in nanostructured monolayer black phosphorus. *Nano Lett.* **16**, 3457–3462 (2016).

[241] Guo, Q. *et al.* Black phosphorus mid-infrared photodetectors with high gain. *Nano Lett.* **16**, 4648–4655 (2016).

[242] Chen, C. *et al.* Widely tunable mid-infrared light emission in thin-film black phosphorus. *Sci. Adv.* **6**, eaay6134 (2020).

[243] Tran, V., Soklaski, R., Liang, Y. & Yang, L. Layer-controlled band gap and anisotropic excitons in few-layer black phosphorus. *Phys. Rev. B* **89**, 235319 (2014).

[244] Huang, Y. *et al.* Observation of a novel lattice instability in ultrafast photoexcited snse. *Physical Review X* **12**, 011029 (2022).

[245] Han, Y. *et al.* Photoinduced ultrafast symmetry switch in snse. *The Journal of Physical Chemistry Letters* **13**, 442–448 (2022).

[246] Lai, A. & Schuh, C. A. Direct electric-field induced phase transformation in paraelectric zirconia via electrical susceptibility mismatch. *Physical Review Letters* **126**, 015701 (2021).

[247] Novoselov, K. S. *et al.* Electric field effect in atomically thin carbon films. *science* **306**, 666–669 (2004).

[248] Hong, J. *et al.* Exploring atomic defects in molybdenum disulphide monolayers. *Nature communications* **6**, 1–8 (2015).

[249] Sarkar, A. S. & Stratakis, E. Recent advances in 2d metal monochalcogenides. *Advanced Science* **7**, 2001655 (2020).

[250] Chang, K. *et al.* Microscopic manipulation of ferroelectric domains in snse monolayers at room temperature. *Nano letters* **20**, 6590–6597 (2020).

[251] Jiang, J. *et al.* Two-step fabrication of single-layer rectangular snse flakes. *2D Materials* **4**, 021026 (2017).

[252] Paradisanos, I., Kymakis, E., Fotakis, C., Kioseoglou, G. & Stratakis, E. Intense femtosecond photoexcitation of bulk and monolayer mos2. *Applied Physics Letters* **105**, 041108 (2014).

[253] Castellanos-Gomez, A. *et al.* Laser-thinning of mos2: on demand generation of a single-layer semiconductor. *Nano letters* **12**, 3187–3192 (2012).

[254] Hu, L., Shan, X., Wu, Y., Zhao, J. & Lu, X. Laser thinning and patterning of mos 2 with layer-by-layer precision. *Scientific reports* **7**, 1–9 (2017).

[255] Cassabois, G., Valvin, P. & Gil, B. Hexagonal boron nitride is an indirect bandgap semiconductor. *Nature photonics* **10**, 262–266 (2016).

[256] Wickramaratne, D., Weston, L. & Van de Walle, C. G. Monolayer to bulk properties of hexagonal boron nitride. *The Journal of Physical Chemistry C* **122**, 25524–25529 (2018).

[257] Cao, Y. *et al.* Quality heterostructures from two-dimensional crystals unstable in air by their assembly in inert atmosphere. *Nano letters* **15**, 4914–4921 (2015).

[258] Dean, C. R. *et al.* Boron nitride substrates for high-quality graphene electronics. *Nature nanotechnology* **5**, 722–726 (2010).

[259] Rosser, D., Fryett, T., Saxena, A., Ryou, A. & Majumdar, A. High-precision local transfer of van der waals materials on nanophotonic structures. *Optical Materials Express* **10**, 645–652 (2020).

[260] Shi, W. *et al.* Tin selenide (snse): growth, properties, and applications. *Advanced Science* **5**, 1700602 (2018).

[261] Zhao, L.-D. *et al.* Ultralow thermal conductivity and high thermoelectric figure of merit in snse crystals. *Nature* **508**, 373–377 (2014).

[262] Xu, X. *et al.* In-plane anisotropies of polarized raman response and electrical conductivity in layered tin selenide. *ACS applied materials & interfaces* **9**, 12601–12607 (2017).

[263] Yu, L.-M. *et al.* Infrared optical constants of orthorhombic iv-vi lamellar semiconductors refined by a combined study using optical and electronic spectroscopies. *Physical Review B* **47**, 16222 (1993).

[264] Chandrasekhar, H., Humphreys, R., Zwick, U. & Cardona, M. Infrared and raman spectra of the iv-vi compounds sns and snse. *Physical Review B* **15**, 2177 (1977).